Limiting techniques for the discontinuous Galerkin method on unstructured meshes

by

KRISHNADUTT

A thesis
presented to the University of Waterloo
in fulfillment of the
thesis requirement for the degree of
Doctor of Philosophy
in
Applied Mathematics

Waterloo, Ontario, Canada, 2022

Examining Committee Membership

The following served on the Examining Committee for this thesis. The decision of the Examining Committee is by majority vote.

Supervisor(s):	Lilia Krivodonova Professor, Dept. of Applied Mathematics, University of Waterloo
Internal Member:	Anita Layton Professor, Dept. of Applied Mathematics, University of Waterloo
Internal Member:	Sander Rhebergen Professor, Dept. of Applied Mathematics, University of Waterloo
Internal-External Member:	Justin Wan Professor, Dept. of Computer Science, University of Waterloo
External-External(s):	Dmitri Kuzmin Professor, Faculty of Mathematics, Technical University of Dortmund

Author's Declaration

I hereby declare that I am the sole author of this thesis. This is a true copy of the thesis, including any required final revisions, as accepted by my examiners.

I understand that my thesis may be made electronically available to the public.

Abstract

Many complex phenomena like shock-shock interactions, shock-vortex interactions, stratified flows, etc., are governed by nonlinear hyperbolic conservation laws. Higher order numerical schemes like the discontinuous Galerkin (DG) method are increasingly being used in computational fluid dynamics (CFD) codes to solve such conservation laws. Oscillations often develop in the numerical solutions obtained using higher-order methods. These spurious oscillations can lead to numerical instabilities and eventual degradation of the solution. Slope limiting is one of the mechanisms used to suppress such oscillations, and thus, stabilize the numerical solution. Slope limiters were originally introduced for finite volume (FV) methods, where the reconstructed slope in an element is modified to prevent oscillations while maintaining second-order accuracy and stability of the numerical solution. Limiters tailored specifically for the DG method have also been proposed. However, developing efficient higher order limiting techniques for the DG method on unstructured meshes remains an open problem. Many factors influence the design of a suitable limiter for the DG method, e.g., the domain discretization involved, the basis functions used to approximate the solution, the choice of limiting directions, and the neighborhood used to reconstruct the solution coefficients, to name a few.

In this work, we propose high-order moment limiters for the DG method on unstructured two-dimensional (triangular, quadrilateral, curvilinear triangular) and three-dimensional (tetrahedral) meshes. The limiters work by relating the solution coefficients (moments) to directional derivatives along specified directions and limiting said directional derivatives independently using a one-dimensional slope limiter. The limiting is performed hierarchically starting at the highest moment and stops on reaching a set of moments/derivatives that remains unchanged, thereby preventing overlimiting.

To use available computational resources efficiently, simulations often employ run-time adaptive mesh refinement strategies. In this thesis, we present a high-order limiter for the DG method on nonconforming triangular meshes that arise in such adaptive computations. Moreover, we also propose a simple algorithm to update the reconstruction stencil of elements in an adaptively refined triangular mesh. Our algorithm is implemented entirely on the graphics processing unit (GPU) and avoids race conditions.

We provide numerical examples to show that limited solutions retain the theoretical rate of convergence and are robust in the presence of discontinuities. Finally, we perform wall clock studies to analyze the performance of the proposed limiter for the computational cost involved in executing the limiter.

Acknowledgements

I would like to thank my supervisor, Lilia, for her continued guidance and support throughout my time in Waterloo. Next, I would like to thank Andrew for his valuable time and for helping me out with the code. Finally, I would like to thank Abdullah, Harley, and Michael for showing me, by example, what kindness can be.

Table of Contents

List of Figures

List of Tables

Chapter 1

Introduction

Nonlinear hyperbolic conservation laws can be used to model several complex physical phenomena like shock-vortex interactions, stratified flows, flows around a turbine, etc. Closed-form analytical solutions do not exist for many of these problems, thus making it necessary to rely on numerical simulations to obtain approximate solutions. Many of these simulations, for example modeling atmospheric flows for weather forecasting, simulations of oceanic surface waves and their interaction with coastlines, etc. involve large variations in length and time scales. Moreover, we require high accuracy in the numerical solution to efficiently capture complex phenomena over such large scales. Using traditional techniques like a simple finite volume (FV) formulation often prove to be computationally expensive, especially to achieve the required high accuracy of the solution. Therefore, higher order numerical schemes are being progressively used in computational fluid dynamics (CFD) codes to solve nonlinear conservation laws. Due to its compact computational stencil and ease in handling adaptive refinement (of both the computational element and the polynomial numerical approximation of the solution in an element) over complex geometries, the discontinuous Galerkin (DG) method offers an attractive alternative to traditional schemes.

Numerical solutions obtained from high order methods often develop spurious oscillations near solution discontinuities which can lead to numerical instabilities and eventual degradation of the solution. For example, consider the linear advection equation

$$\mathbf{u}_t + a_1 \frac{\partial}{\partial x}\mathbf{u} + a_2 \frac{\partial}{\partial y}\mathbf{u} = 0, \tag{1.1}$$

with $(a_1, a_2) = (1, 0)$ and the initial condition $u(\mathbf{x}, 0) = \mathbf{u}_0(\mathbf{x})$ given by

$$\mathbf{u}_0(\mathbf{x}) = \begin{cases} 1.0, & |x| \leq 0.25, |y| \leq 0.25, \\ 0.0, & \text{otherwise}, \end{cases} \tag{1.2}$$

in the domain $\Omega = [-1,1] \times [-1,1]$. Figure 1.1 compares the cross-section of the exact solution of the advecting square pulse at $t = 0.5$ with the numerical solution obtained using a second order DG approximation. We can clearly observe spurious oscillations, also referred to as "Gibbs oscillations", near the discontinuities at $x = 0.25$ and $x = 0.75$. These spurious oscillations are undesired as they often lead to numerical instabilities and reduced accuracy in regions where solution is smooth. The issue is further exacerbated

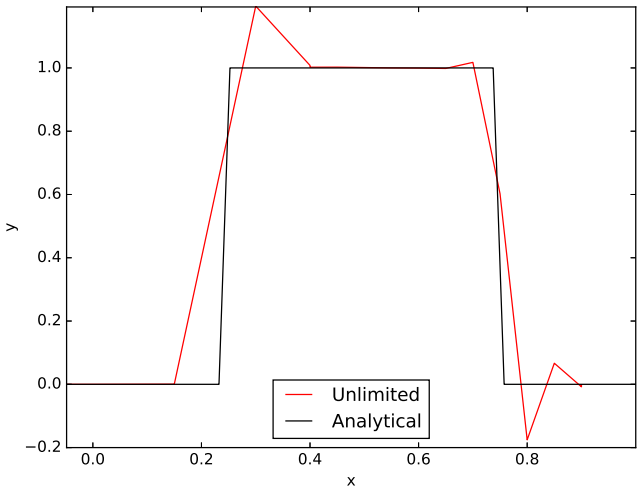

Figure 1.1: Cross-section at $y = 0.5$ of an advecting square pulse at $t = 0.5$, obtained with a second order numerical approximation.

for nonlinear hyperbolic conservation laws, where the presence of oscillations can lead to nonlinear instabilities. Consider the Noh test case [3] for the two-dimensional Euler system of equations given by

$$\frac{\partial}{\partial t}\begin{pmatrix}\rho\\ \rho u\\ \rho v\\ E\end{pmatrix} + \frac{\partial}{\partial x}\begin{pmatrix}\rho u\\ \rho u^2 + p\\ \rho uv\\ (E+p)u\end{pmatrix} + \frac{\partial}{\partial y}\begin{pmatrix}\rho v\\ \rho uv\\ \rho v^2 + p\\ (E+p)v\end{pmatrix} = 0, \tag{1.3}$$

where ρ is the density, ρu and ρv are the x- and y-direction momenta, E is the energy, and the pressure, p, is given by the equation of state $p = (\gamma - 1)\left(E - \frac{\rho}{2}(u^2 + v^2)\right)$. The test case involves the time evolution of a symmetric circular shock structure. Figure 1.2 shows how spurious oscillations have severely deteriorated the numerical approximation of density, obtained using a second order DG approximation. In certain situations, these oscillations can potentially lead to nonphysical values for the numerical solution, for example, negative

values for density, energy, and/or pressure. Therefore, it is imperative that we suppress such spurious oscillations and stabilize the solution.

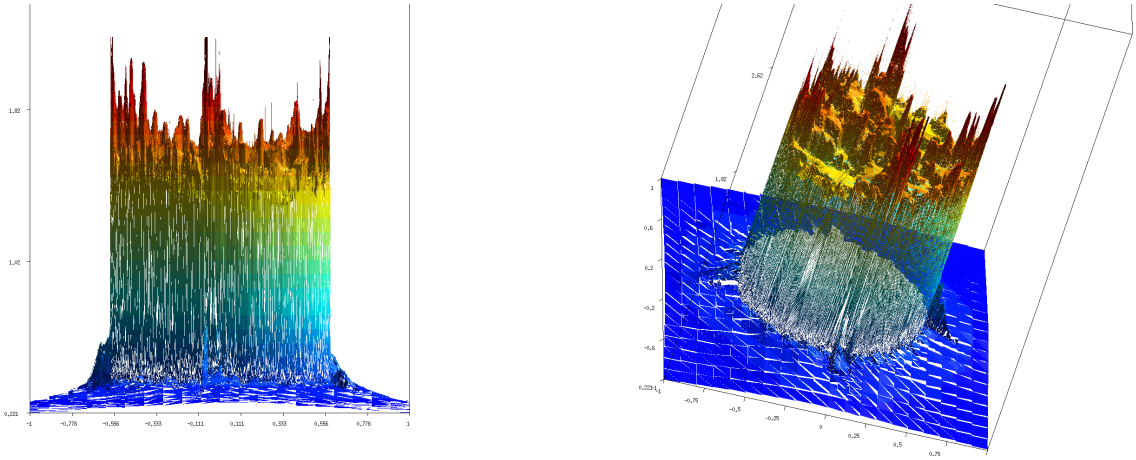

Figure 1.2: Numerical solution (density) at $t = 2.$ for the Noh test case with a second order DG approximation.

Designing efficient and robust techniques to control such spurious oscillations near solution discontinuities remains one of the challenges in developing robust higher order methods for solutions of nonlinear hyperbolic conservation laws. Several techniques have been successfully developed to suppress numerical oscillations resulting from higher order discretizations employed in traditional methods like finite volume methods, finite difference methods, etc. Many of these techniques, for example, artificial viscosity methods [4, 5], flux limiters [4, 6, 1], spectral filters [7, 8, 9], weighted essentially non oscillatory (WENO) reconstruction [10, 11], and slope limiters [12, 1, 13, 14] have been successfully applied to the DG formulation.

1.1 Slope Limiters

Slope limiting, originally proposed for FV methods, is one of the techniques used to suppress oscillations by controlling the gradient of the solution in an element. It is a natural limiting method for second order formulations, especially in the context of FV methods as it involves reconstructing the slope without altering the average value in an element. For example, consider the one-dimensional hyperbolic conservation law given by

$$\frac{\partial}{\partial t}u + \frac{\partial}{\partial x}f(u) = 0. \tag{1.4}$$

Let the approximate linear solution U_i in an element Ω_i be

$$U_i = \overline{U}_i + \hat{U}_i \cdot (\mathbf{x} - \mathbf{x}_0), \tag{1.5}$$

where $\overline{U}_i$ is the solution average in Ω_i, $\hat{U}_i$ is the gradient of the solution in the element, and $\mathbf{x}_0$ is the element centroid. As shown in Figure 1.3, slope limiting reconstructs the

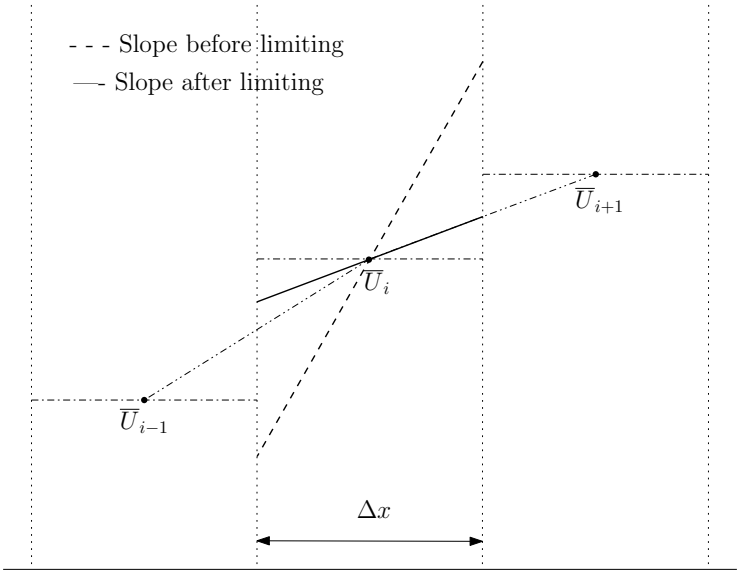

Figure 1.3: Reconstruction of the slopes of the solution using slope limiting.

slope of the solution resulting in a modified solution given by

$$\tilde{U}_i = \overline{U}_i + \phi(R)\hat{U}_i \cdot (\mathbf{x} - \mathbf{x}_0), \tag{1.6}$$

where $R = \dfrac{\overline{U}_{i+1} - \overline{U}_i}{\overline{U}_i - \overline{U}_{i-1}}$ is the ratio of the forward and backward differences in $\overline{U}$. Figure 1.4 shows some of the commonly used one-dimensional slope limiters.

Efficient limiters [6, 15, 16, 17] based on the total variation diminishing (TVD) property have been successfully developed for second order methods in one-dimension. However, TVD schemes reduce solution accuracy near smooth extrema [18] to first order and, thus, are at most second order accurate. Through numerical examples, it was shown in [19] that limiters based on the TVD property on two-dimensional Cartesian grids can achieve an accuracy of at most first-order. Recently, using an isotropic definition for total variation, it was shown numerically in [20] that the limited second order DG solutions of two-dimensional hyperbolic equations are TVD in the means. However, due to a limited theoretical basis for the TVD property in high dimensions, most practical limiters were

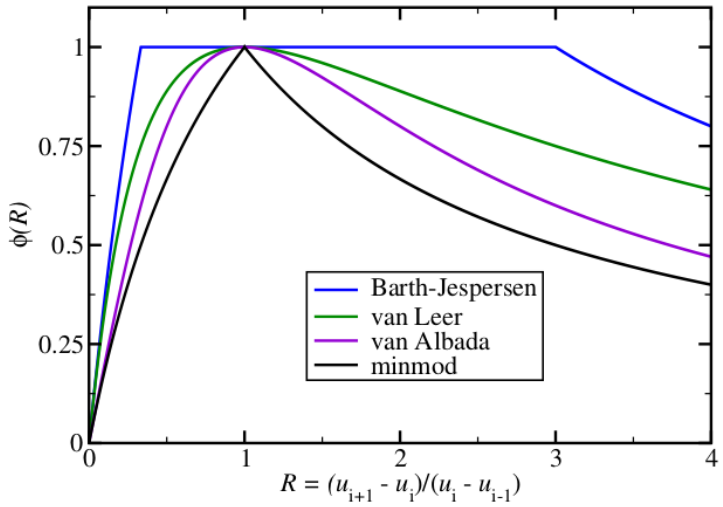

Figure 1.4: Stability regions for commonly used one dimensional slope limiters [1].

developed using geometrical arguments or by direct extension of ideas rigorously developed in one dimension, e.g., requiring solution values at specified points not to exceed solution averages in a chosen neighborhood [21, 13]. More recently, the local maximum principle (LMP) of the solution averages,

$$\min_{k\in\mathcal{N}_i} \overline{U}_k^n \le \overline{U}_i^{n+1} \le \max_{k\in\mathcal{N}_i} \overline{U}_k^n, \tag{1.7}$$

has been employed to develop newer limiters for second-order methods [22, 2, 23]. For scalar problems, the LMP guarantees that solution averages remain bounded for all computational time.

Designing limiters in higher dimensions comes with its own specific challenges. Unlike in one dimension, there is no unique set of directions in which to limit solution gradients. The number of components of the gradient to be limited also increases in higher dimensions. For high-order methods, mixed derivatives appear, which further complicates the limiting process.

One of the first limiters on unstructured meshes in higher dimensions was proposed in [21] for FV methods. The solution gradient is limited by scaling it with a constant coefficient $\alpha \in [0, 1]$. A less diffusive limiter was proposed in [24], where the components of the gradient were scaled by separate multipliers. Limiters from the FV framework have been successfully extended to the DG method. Limiters tailored specifically for the DG method have also been proposed [12, 25, 10, 11, 26, 22, 23, 27]. For example, the WENO reconstruction in [11], hierarchical limiting using a local Taylor series expansion in [28, 29, 13],

and limiting in the directions of the medians [26] have been proposed for the DG method on unstructured triangular and quadrilateral meshes. A high-order hierarchical moment limiter for the DG method on Cartesian grids was proposed in [25]. More recently, a second order moment limiter for the DG method was proposed in [2] for unstructured triangular meshes and in [23] for tetrahedral meshes. They limit the numerical solution by finding the directions in which the linear solution moments decouple and reconstructing the gradient along these directions using a one-dimensional limiter. In three-dimension, a WENO reconstruction [30], and an a posteriori sub-cell finite volume limiter [31] have been proposed for the DG method on tetrahedral meshes. Limiters designed to preserve specific properties of the solution, e.g., positivity preservation [32, 33, 34] and entropy stability [35, 36, 37, 38] for nonlinear system of equations have also been proposed. However, limiters present in the literature for the DG method on unstructured meshes are either computationally expensive, too restrictive or not robust, i.e., they involve problem-dependent tuning parameters. Therefore, developing compact and robust limiting techniques for the higher order DG method on higher dimensional and unstructured meshes remains an open problem.

Traditional limiting techniques [25, 10, 2, 27, 29] were designed for conforming meshes, i.e., meshes where an edge is shared between only two elements. Nonconforming meshes, i.e., meshes where an element shares an edge with more than one neighboring element, often arise in simulations employing run-time adaptive mesh refinement [39, 40, 41, 42, 43]. Adaptive computations allow us to effectively use computational resource where they are needed the most, e.g., to better capture the fine features of the solution. To ensure numerical stability and maintain accuracy of a high-order DG discretization, it is necessary to use limiting techniques compatible with nonconforming meshes. It is known that applying conventional limiters on nonconforming or nonuniform meshes might lead to oscillations. For example, it was shown in [1] that in one dimension applying a second-order TVD limiter developed for uniform grids to non-uniform grids leads to overshoots/undershoots in the solution. A limiter taking into account mesh structure was shown to eliminate this problem. In [44], a direction-aware slope limiter for finite volume (FV) methods on three-dimensional adaptively refined cubic grids was proposed. Extensions of limiters for the DG method to adaptively refined meshes have been proposed in [45, 46, 47]. In order to limit the solution in an element Ω_i, solution values in the neighboring elements are projected onto a ghost element with either the same refinement level or similar cell size as Ω_i. Then, the numerical solution is limited by reconstructing solution gradients using the projected solutions. While such approaches are shown to work well, they are computationally expensive and difficult to implement on unstructured meshes. Before discussing limiters in detail, we provide a brief description of the DG formulation in the next section.

1.2 Discontinuous Galerkin method

Consider a hyperbolic conservation law

$$\mathbf{u}_t + \nabla \cdot \mathbf{F}(\mathbf{u}) = 0, \tag{1.8}$$

where the vector of conserved variables $\mathbf{u}(\mathbf{x}, t)$ is defined on $\Omega \times [0, T]$, Ω is the spatial domain, T is the final time, and $\mathbf{F}(\mathbf{u})$ is the flux function. Additionally, assume that the initial condition $\mathbf{u}(\mathbf{x}, 0) = \mathbf{u}_0(\mathbf{x})$ is provided along with relevant boundary conditions.

The discontinuous Galerkin method is constructed by splitting the domain Ω into a mesh of elements Ω_i, such that $\Omega = \bigcup_i \Omega_i$. The elements can be triangles, quadrilaterals or curvilinear triangles in two-dimensions or tetrahedras in three-dimensions. A weak form of the conservation law is obtained by multiplying (1.8) by a test function $v \in H^1(\Omega_i)$ and integrating on Ω_i. Using the following identity

$$\int_{\Omega_i} v \nabla \cdot \mathbf{F}(\mathbf{u}) d\mathbf{x} = -\int_{\Omega_i} \mathbf{F}(\mathbf{u}) \cdot \nabla v d\mathbf{x} + \int_{\Omega_i} \nabla \cdot (v\mathbf{F}(\mathbf{u}))\, d\mathbf{x}, \tag{1.9}$$

and applying the divergence theorem, we obtain

$$\int_{\Omega_i} \mathbf{u}_t v d\mathbf{x} - \int_{\Omega_i} \mathbf{F}(\mathbf{u}) \cdot \nabla v d\mathbf{x} + \int_{\partial\Omega_i} v\mathbf{F}(\mathbf{u}) \cdot \mathbf{n} dl = \mathbf{0}, \ \ \forall v \in H^1(\Omega_i), \tag{1.10}$$

where $\mathbf{n} = (n_x, n_y)$ is the outward facing unit normal on element Ω_i's boundary $\partial\Omega_i$.

The exact solution on Ω_i is approximated by $\mathbf{U}_i$, a linear combination of the basis functions $\hat{\varphi}_m$ of degree up to p, i.e.,

$$\mathbf{U}_i = \sum_{m=0}^{P} \hat{\mathbf{U}}_{i,m} \hat{\varphi}_m, \tag{1.11}$$

where $\hat{\mathbf{U}}_{i,m}$ are the degrees of freedom (DOFs) and P is the number of the degrees of freedom. The basis functions $\hat{\varphi}_m$ can be defined locally on element Ω_i, for example by using a local Taylor series expansion or a local Lagrange basis. However, to obtain a simple set of semi-discrete equations (shown below) it is more convenient to use orthonormal basis functions defined on a canonical reference element Ω_0.

We give a brief description of the mappings, basis functions and the final set of semi-discrete equations for the mesh elements considered in subsequent chapters. For triangular elements, we map Ω_i to the right unit triangle $\Omega_0 = \{0 \le r, s \le 1, 0 \le r + s \le 1\}$ (Figure 1.5)

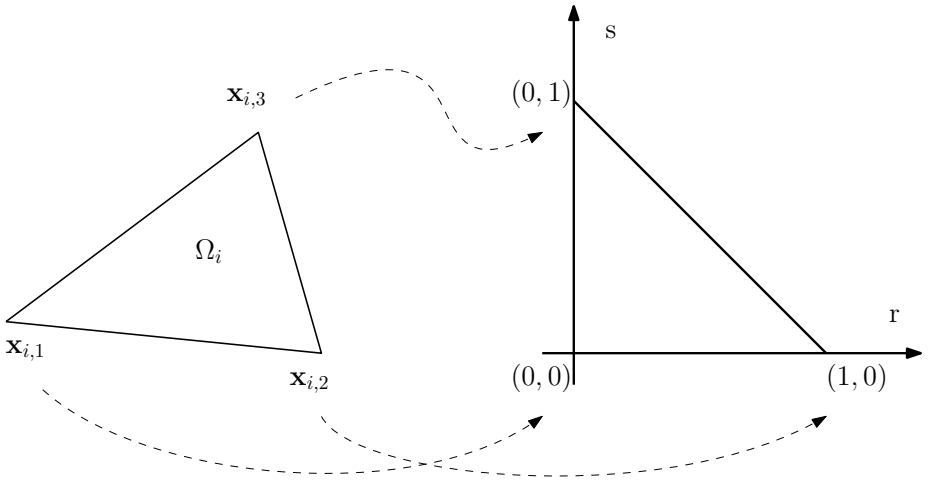

Figure 1.5: Mapping of Ω_i to the canonical triangle Ω_0 by (1.12).

using the transformation

$$\begin{pmatrix} x \\ y \\ 1 \end{pmatrix} = \begin{pmatrix} x_{i,1} & x_{i,2} & x_{i,3} \\ y_{i,1} & y_{i,2} & y_{i,3} \\ 1 & 1 & 1 \end{pmatrix} \begin{pmatrix} 1-r-s \\ r \\ s \end{pmatrix}, \tag{1.12}$$

where $(x_{i,k}, y_{i,k}), k = \{1,2,3\}$, are the vertices of Ω_i. The Jacobian of the transformation is

$$J_i = \begin{pmatrix} x_{i,2} - x_{i,1} & x_{i,3} - x_{i,1} \\ y_{i,2} - y_{i,1} & y_{i,3} - y_{i,1} \end{pmatrix}. \tag{1.13}$$

On Ω_0, the Dubiner basis [48]

$$\varphi_k^l(r,s) = C_k^l 2^k L_k\left(\frac{2s}{1-r} - 1\right)(1-r)^k P_l^{2k+1,0}(2r-1), \;\; 0 \le l+k \le p, \tag{1.14}$$

forms an orthonormal set with respect to the L^2 inner product. Above, C_k^l are normalization constants, $L_k(x)$ is the Legendre polynomial of degree k [49]

$$L_k(x) = \frac{(-1)^k}{2^k k!} \frac{d^k}{dx^k}[(1-x^2)^k], \tag{1.15}$$

and $P_l^{2k+1,0}(x)$ is a Jacobi polynomial of degree l [49]

$$P_l^{2k+1,0}(x) = \frac{(-1)^l}{2^l l!}(1-x)^{-(2k+1)} \frac{d^l}{dx^l}[(1-x^2)^l (1-x)^{2k+1}]. \tag{1.16}$$

With the basis functions (1.14), the numerical solution $\mathbf{U}_i$ is written as

$$\mathbf{U}_i(r,s,t) = \sum_{l+k=0}^{p} \hat{\mathbf{U}}_{i,k}^{l}(t)\varphi_k^l(r,s). \tag{1.17}$$

As continuity of the solution at element interfaces is not imposed, the solution can be multivalued at the boundary between two neighboring cells. Therefore, a numerical flux $\mathbf{F}^*(\mathbf{U}_i, \mathbf{U}_j)$ is introduced to allow communication between the neighboring elements Ω_i and Ω_j. Choosing v to be φ_k^l, equation (1.10) under the map (1.12) becomes

$$\frac{d}{dt}\hat{\mathbf{U}}_{i,k}^{l} = \int_{\Omega_0} \mathbf{F}(\mathbf{U}_i)\cdot(\nabla\varphi_k^l J_i^{-1})\,d\mathbf{r} - \frac{1}{\det J_i}\sum_{j\in N_i^e}\int_{\partial\Omega_{i,j}} \phi_k^l \mathbf{F}^*(\mathbf{U}_i,\mathbf{U}_j)\cdot\mathbf{n}_{i,j}\;dl, \quad 0\le k+l\le p, \tag{1.18}$$

where J_i is the Jacobian given by (1.13), N_i^e is the list of indices of the elements that share an edge with Ω_i, $\partial\Omega_{i,j}$ is the edge shared by Ω_i and Ω_j, and $\phi_k^l(\mathbf{x}) = \varphi_k^l(r,s)$.

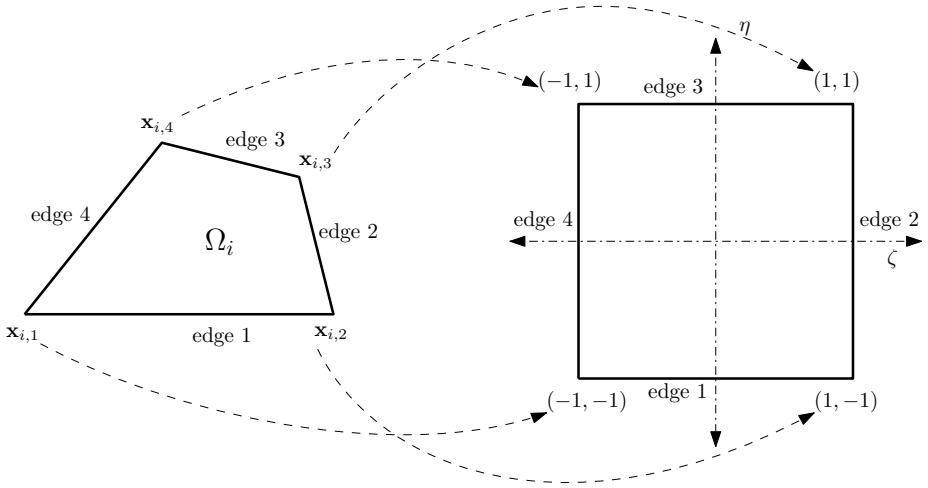

Figure 1.6: Mapping of Ω_i to the canonical square Ω_0 by (1.19).

For quadrilateral elements, we map Ω_i to a unit square $\Omega_0 = \{-1 \le \zeta, \eta \le 1\}$ (Figure 1.6) using the transformation

$$\mathbf{x}_i(\zeta,\eta) = \mathbf{x}_{i,1}\frac{(1-\zeta)(1-\eta)}{4} + \mathbf{x}_{i,2}\frac{(1+\zeta)(1-\eta)}{4} + \mathbf{x}_{i,3}\frac{(1+\zeta)(1+\eta)}{4} + \mathbf{x}_{i,4}\frac{(1-\zeta)(1+\eta)}{4}, \tag{1.19}$$

where $\mathbf{x}_{i,k} = (x_{i,k}, y_{i,k})$, $k = \{1,2,3,4\}$, are the vertices of Ω_i. Regrouping the terms, (1.19)

can be simplified to get

$$\mathbf{x}_i(\zeta,\eta) = C_{i,\mathbf{x}0} + C_{i,\mathbf{x}1}\zeta + C_{i,\mathbf{x}2}\eta + C_{i,\mathbf{x}3}\zeta\eta, \tag{1.20}$$

where the coefficients $C_{i,\mathbf{x}}$ are

$$\begin{aligned} C_{i,\mathbf{x}0} &= \frac{1}{4}\left(\mathbf{x}_{i,1}+\mathbf{x}_{i,2}+\mathbf{x}_{i,3}+\mathbf{x}_{i,4}\right), \quad C_{i,\mathbf{x}1} &= \frac{1}{4}\left(\mathbf{x}_{i,2}+\mathbf{x}_{i,3}-\mathbf{x}_{i,1}-\mathbf{x}_{i,4}\right), \\ C_{i,\mathbf{x}2} &= \frac{1}{4}\left(\mathbf{x}_{i,3}+\mathbf{x}_{i,4}-\mathbf{x}_{i,1}-\mathbf{x}_{i,2}\right), \quad C_{i,\mathbf{x}3} &= \frac{1}{4}\left(\mathbf{x}_{i,1}+\mathbf{x}_{i,3}-\mathbf{x}_{i,2}-\mathbf{x}_{i,4}\right). \end{aligned} \tag{1.21}$$

The Jacobian of the transformation is

$$J_i = \begin{pmatrix} x_\zeta & x_\eta \\ y_\zeta & y_\eta \end{pmatrix} = \begin{pmatrix} C_{i,x1}+C_{i,x3}\eta & C_{i,x2}+C_{i,x3}\zeta \\ C_{i,y1}+C_{i,y3}\eta & C_{i,y2}+C_{i,y3}\zeta \end{pmatrix}, \tag{1.22}$$

and the determinant of the Jacobian is

$$\det J_i = \det J_{i,0} + \det J_{i,1}\zeta + \det J_{i,2}\eta, \tag{1.23}$$

where the coefficients $\det J_{i,j},\ j=\{0,1,2\}$, are

$$\begin{aligned} &\det J_{i,0} = C_{i,x1}C_{i,y2} - C_{i,x2}C_{i,y1}, \quad \det J_{i,1} = C_{i,x1}C_{i,y3} - C_{i,x3}C_{i,y1}, \\ &\det J_{i,2} = C_{i,x3}C_{i,y2} - C_{i,x2}C_{i,y3}. \end{aligned} \tag{1.24}$$

On Ω_0, the tensor product basis

$$\varphi_j^k(\zeta,\eta) = \frac{\sqrt{(2j+1)(2k+1)}}{2} L_j(\zeta)L_k(\eta) \tag{1.25}$$

forms an orthonormal set with respect to the L^2 norm, where $L_j(x)$ is the Legendre polynomial of degree j [49]. With basis functions (1.25), the numerical solution $\mathbf{U}_i$ is written as

$$\mathbf{U}_i(\zeta,\eta) = \sum_{j=0,k=0}^{p} \hat{\mathbf{U}}_{i,j}^k \varphi_j^k(\zeta,\eta). \tag{1.26}$$

Choosing v to be φ_j^k, the equation (1.10) under the map (1.19) becomes

$$\sum_{r=0,s=0}^{p} \mathbf{m}_{i,j,r}^{k,s} \frac{d}{dt}\hat{\mathbf{U}}_{i,r}^s = \int_{\Omega_0} \mathbf{F}(\mathbf{U}_i)\cdot(\nabla\varphi_j^k J_i^{-1}) \det J_i \, d\mathbf{r} - \sum_{v\in N_i^e} \int_{\partial\Omega_{i,v}} \varphi_j^k \mathbf{F}^*(\mathbf{U}_i,\mathbf{U}_v)\cdot\mathbf{n}_{i,v}\, dl, \tag{1.27}$$

where $0 \le j,\ k \le p$, $\det J_i$ is the determinant of the Jacobian (1.23), N_i^e is the list of indices of elements that share an edge with Ω_i, $\partial\Omega_{i,v}$ is the edge shared by Ω_i and Ω_v, and $\mathbf{n}_{i,v}$ is

the outward pointing unit normal on $\partial\Omega_{i,v}$. The mass matrix $\mathbf{M}_i$ on Ω_i, whose entries are given by

$$\mathbf{m}_{i,j,r}^{k,s} = \int_{\Omega_0} \varphi_j^k \varphi_r^s \det J_i \, d\mathbf{r}, \tag{1.28}$$

is computed during the pre-processing stage and stored.

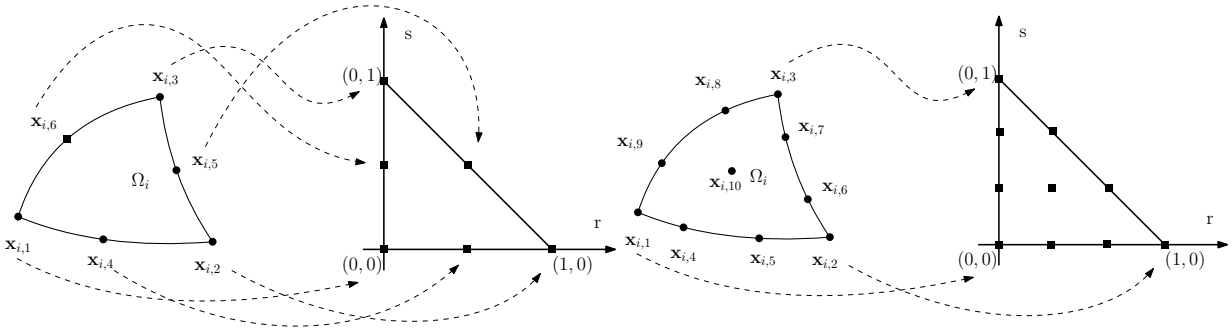

Figure 1.7: Mapping of Ω_i to the canonical Ω_0 by (1.29) (A) for $q = 2$ and (B) for $q = 3$.

For curvilinear triangular elements, we map the element Ω_i to a unit triangle $\Omega_0 = \{0 \le r, s \le 1\}$ (Figure 1.7) using the transformation

$$\mathbf{x}_i(r, s) = \sum_{l+k=0}^{q} \hat{\mathbf{x}}_{i,k}^l \varphi_k^l(r, s). \tag{1.29}$$

The coefficients $\hat{\mathbf{x}}_i$ depend on how the nodes $\mathbf{x}_{i,k} = (x_{i,k}, y_{i,k})$, $1 \le k \le \frac{1}{2}(q+1)(q+2)$, on Ω_i are mapped to nodes on Ω_0 (Figure 1.7). Moreover, the above coefficients can be easily computed in the pre-processing stage by plugging the nodes $\mathbf{x}_{i,k}$ on Ω_i and their corresponding mappings on Ω_0 into (1.29) and solving the resulting linear system of equations. The Jacobian of the transformation (1.29) is

$$J_i = \begin{pmatrix} x_r & x_s \\ y_r & y_s \end{pmatrix}, \tag{1.30}$$

and the determinant of the Jacobian is

$$\det J_i = |x_r y_s - x_s y_r|, \tag{1.31}$$

With the basis functions (1.14), the numerical solution $\mathbf{U}_i$ is written as in (1.17). Choosing

v to be φ_j^k, the equation (1.10) under the map (1.29) becomes

$$\sum_{r=0,s=0}^{p} \mathbf{m}_{i,j,r}^{k,s} \frac{d}{dt} \hat{\mathbf{U}}_{i,r}^{s} = \int_{\Omega_0} \mathbf{F}(\mathbf{U}_i) \cdot (\nabla \varphi_j^k J_i^{-1}) \det J_i \, d\mathbf{r} - \sum_{v \in N_i^e} \int_{\partial \Omega_{i,v}} \varphi_j^k \mathbf{F}^*(\mathbf{U}_i, \mathbf{U}_v) \cdot \mathbf{n}_{i,v} \, dl, \quad (1.32)$$

where $0 \le j,\ k \le p$, $\det J_i$ is the determinant of the Jacobian (1.30), N_i^e is the list of indices of elements that share an edge with Ω_i, $\partial \Omega_{i,v}$ is the edge shared by Ω_i and Ω_v, and $\mathbf{n}_{i,v}$ is the outward pointing unit normal on $\partial \Omega_{i,v}$. The mass matrix $\mathbf{M}_i$ on Ω_i, whose entries are given by

$$\mathbf{m}_{i,j,r}^{k,s} = \int_{\Omega_0} \varphi_j^k \varphi_r^s \det J_i \, d\mathbf{r}, \quad (1.33)$$

is computed during the pre-processing stage.

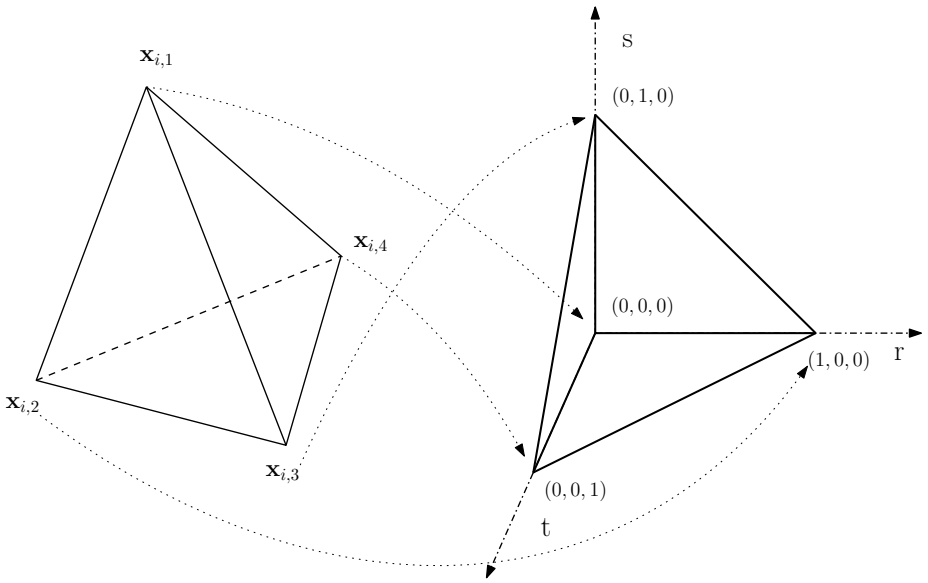

Figure 1.8: Mapping of Ω_i to the canonical tetrahedron Ω_0 by (1.34).

Finally, for tetrahedral elements, we map Ω_i to the reference tetrahedron $\Omega_0 = \{0 \le r, s, t \le 1\}$ (Figure 1.8) using the affine transformation

$$\begin{pmatrix} x \\ y \\ z \\ 1 \end{pmatrix} = \begin{bmatrix} x_{i,1} & x_{i,2} & x_{i,3} & x_{i,4} \\ y_{i,1} & y_{i,2} & y_{i,3} & y_{i,4} \\ z_{i,1} & z_{i,2} & z_{i,3} & z_{i,4} \\ 1 & 1 & 1 & 1 \end{bmatrix} \begin{pmatrix} 1 - r - s - t \\ r \\ s \\ t \end{pmatrix}, \quad (1.34)$$

where $\mathbf{x}_{i,k} = (x_{i,k}, y_{i,k}, z_{i,k})$, $k = \{1, 2, 3, 4\}$, are the vertices of Ω_i. The Jacobian of the

transformation is

$$J_i = \begin{pmatrix} x_{i,2} - x_{i,1} & x_{i,3} - x_{i,1} & x_{i,4} - x_{i,1} \\ y_{i,2} - y_{i,1} & y_{i,3} - y_{i,1} & y_{i,4} - y_{i,1} \\ z_{i,2} - z_{i,1} & z_{i,3} - z_{i,1} & z_{i,4} - z_{i,1} \end{pmatrix}. \tag{1.35}$$

On Ω_0, the Dubiner basis [48]

$$\varphi_k^{l,m}(r,s,t) = C_k^{l,m} 2^{2k+l} L_k\left(\frac{2t+s+r-1}{1-s-r}\right)(1-s-r)^k P_l^{2k+1,0}\left(\frac{2s+r-1}{1-r}\right)(1-r)^l P_m^{2k+2l+2,0}(2r-1), \tag{1.36}$$

where $0 \le k+l+m \le p$, forms an orthonormal set with respect to the L^2 inner product. Above, $C_k^{l,m}$ are normalization constants, $L_k(x)$ is the Legendre polynomial of degree k [49] and $P_l^{2k+1,0}(x)$ is a Jacobi polynomial of degree l [49]. With the basis functions (1.36), the numerical solution $\mathbf{U}_i$ is written as

$$\mathbf{U}_i(\mathbf{r},t) = \sum_{l+k+m=0}^{p} \hat{\mathbf{U}}_{i,k}^{l,m}(t)\varphi_k^{l,m}(\mathbf{r}). \tag{1.37}$$

Choosing v to be $\varphi_k^{l,m}$, equation (1.10) under the map (1.34) becomes

$$\frac{d}{dt}\hat{\mathbf{U}}_{i,k}^{l,m} = \int_{\Omega_0} \mathbf{F}(\mathbf{U}_i)\cdot(\nabla\varphi_k^{l,m} J_i^{-1})\, d\mathbf{r} - \frac{1}{\det J_i}\sum_{j\in N_i^e}\int_{\partial\Omega_{i,j}} \phi_k^{l,m}\mathbf{F}^*(\mathbf{U}_i,\mathbf{U}_j)\cdot\mathbf{n}_{i,j}\, dl, \quad 0 \le k+l+m \le p, \tag{1.38}$$

where J_i is the Jacobian given by (1.35), N_i^e is the list of indices of the elements that share an edge with Ω_i, $\partial\Omega_{i,j}$ is the face shared by Ω_i and Ω_j, and $\phi_k^{l,m}(\mathbf{x}) = \varphi_k^{l,m}(\mathbf{r})$.

The volume and boundary integrals in (1.18), (1.27), (1.32), and (1.38) are evaluated using appropriate numerical quadratures. Finally, we use an explicit Runge-Kutta (RK) method of order $(p+1)$ to solve the above semi-discrete system of equations in time.

1.3 Outline

This thesis is concerned with the design and implementation of compact, robust, and efficient limiting techniques for the DG method on higher dimensional unstructured meshes. In Chapter 2, we describe a second order moment limiter for the DG method on adaptively refined triangular meshes. Further, we also discuss a simple algorithm to update the limiting neighborhood under adaptive mesh refinement. In Chapters 3 and 6, we propose, respectively, an arbitrarily high-order moment limiter for the DG method on unstructured triangular and quadrilateral meshes. Next, we present and analyze the stability of a class of second order slope limiters in Chapter 4 and a second order moment limiter in Chapter

5 for the DG method on quadrilateral meshes. In this process, we propose a new measure of cell size for quadrilateral elements. In Chapters 7 and 9, we discuss how to extend the high-order moment limiter for the DG method on triangles to isoparametric curvilinear triangular meshes and three-dimensional tetrahedral meshes, respectively. Finally, we present and analyze the stability of a class of second order slope limiters for the DG method on tetrahedral meshes in Chapter 8.

Chapter 2

Limiting on adaptively refined nonconforming triangular meshes

In this chapter, we present a second order limiter for DG approximations on adaptively refined nonconforming triangular meshes. The limiter works by decoupling linear solution coefficients along two pre-determined directions in an element and limiting the gradients along these directions using a one-dimensional minmod limiter. The limiter is an extension of the second order moment limiter proposed in [2] for the DG method on unstructured triangular meshes. Limiting the numerical solution in an element Ω_i requires access to solution averages in some neighborhood of Ω_i, for example, a vertex neighborhood (shaded polygon, Figure 2.1b). The vertex neighborhood of an element in a nonconforming mesh usually contains more elements (of varying sizes) compared to a conforming mesh (Figure 2.1a). Further, when the mesh is adaptively refined, with every refinement (and coarsening), the vertex neighborhood can change its composition and the number of elements in it. Therefore, updating the limiting neighborhood of an element in an adaptively refined nonconforming mesh is necessary.

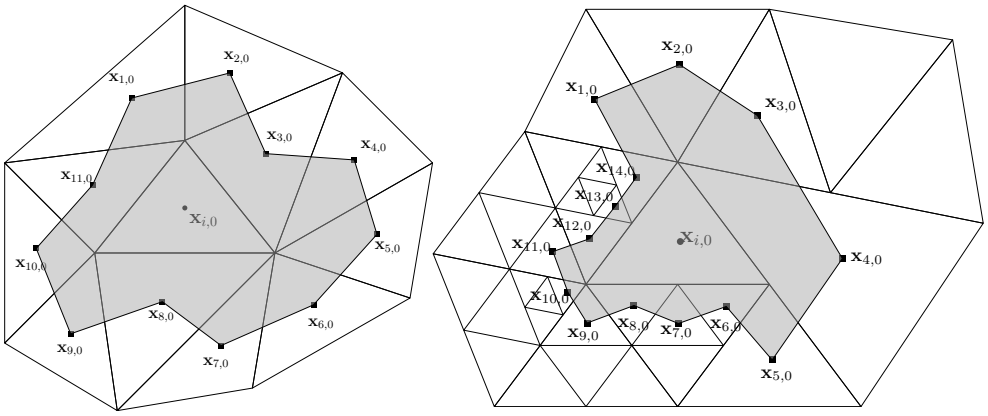

(a) Conforming mesh. (b) Nonconforming mesh.

Figure 2.1: Examples of conforming and nonconforming triangular meshes.

A direct approach to maintaining and updating an element's limiting neighborhood, say LN_i, requires storing a list of IDs of all elements in LN_i. This list is modified whenever the elements in it undergo refinement or coarsening. This process is straightforward in serial computing. However, a parallel implementation on a GPU leads to race conditions, i.e., reading from and writing to the same memory location simultaneously, which can lead to an incorrect neighborhood. Alternatively, we propose an approach that entails maintaining a vertex to element and element to vertex connectivity, i.e., for each element Ω_i, we store the list of IDs of the vertices associated with it, and for each vertex v_i, we store the list of IDs of elements that share vertex v_i and update the corresponding IDs with every refinement (coarsening).

2.1 Limiting algorithm

In this section, we describe the proposed second order moment limiter for the DG method on nonconforming triangular meshes. The limiter works by decoupling linear solution coefficients along two specific directions and limiting the slopes along said directions using a one-dimensional minmod limiter. The choice of the limiting directions and the reconstruction stencil are described below.

2.1.1 Moment limiter

The second order DG approximation on Ω_i can be written in terms of computational variables (r, s) as

$$U_i(r,s) = \hat{U}^0_{i,0}\varphi^0_0(r,s) + \hat{U}^1_{i,0}\varphi^1_0(r,s) + \hat{U}^0_{i,1}\varphi^0_1(r,s). \tag{2.1}$$

The basis functions φ are given by

$$\begin{aligned} \varphi^0_0(r,s) &= \sqrt{2}, \\ \varphi^1_0(r,s) &= -2 + 6r, \\ \varphi^0_1(r,s) &= -2\sqrt{3} + 2\sqrt{3}r + 4\sqrt{3}s. \end{aligned} \tag{2.2}$$

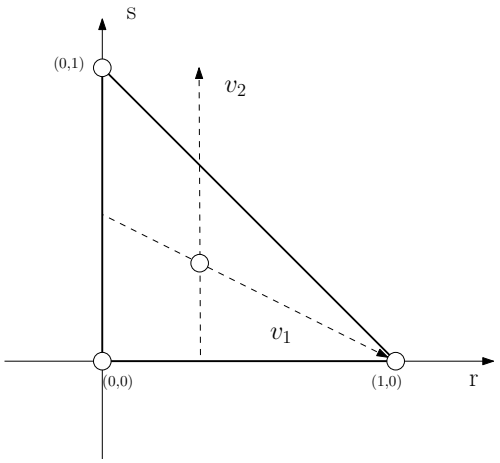

Figure 2.2: Reference triangular element Ω_0.

Consider the vectors $v_1 = \frac{2}{\sqrt{5}}(1, -1/2)$ and $v_2 = (0, 1)$ in the computational space (Figure 2.2). The linear solution coefficients $\hat{U}^1_{i,0}$ and $\hat{U}^0_{i,1}$ can be expressed, respectively, as the directional derivatives along v_1 and v_2 as

$$\hat{U}^1_{i,0} = \frac{\sqrt{5}}{12}\mathbf{D}_{v_1}U_i, \tag{2.3}$$

$$\hat{U}^0_{i,1} = \frac{1}{4\sqrt{3}}\mathbf{D}_{v_2}U_i, \tag{2.4}$$

i.e., the linear solution coefficients decouple along these directions. Using (1.12) for Ω_i, we map the vectors v_1 and v_2 from the computational to the physical space and, after

normalization, obtain the following unit vectors

$$\mathbf{v}_{i,1} = \frac{J_i v_1}{\|J_i v_1\|}, \quad \mathbf{v}_{i,2} = \frac{J_i v_2}{\|J_i v_2\|}, \tag{2.5}$$

where J_i is given by (1.13). Using the mapping (1.12) and the Jacobian (1.13), (2.5) can be simplified to

$$\mathbf{v}_{i,1} = \frac{1}{h_{i,1}} \left(\mathbf{x}_{i,2} - \frac{1}{2}(\mathbf{x}_{i,1} + \mathbf{x}_{i,3}) \right), \quad \mathbf{v}_{i,2} = \frac{1}{h_{i,2}} \left(\mathbf{x}_{i,3} - \mathbf{x}_{i,1} \right), \tag{2.6}$$

where

$$h_{i,1} = \left\| \mathbf{x}_{i,2} - \frac{1}{2}(\mathbf{x}_{i,1} + \mathbf{x}_{i,3}) \right\|, \quad h_{i,2} = \|\mathbf{x}_{i,3} - \mathbf{x}_{i,1}\|. \tag{2.7}$$

Using (1.12), (2.5), and (2.6) in (2.3), the linear solution coefficients can be expressed as directional derivatives along $\mathbf{v}_{i,1}$ and $\mathbf{v}_{i,2}$ as

$$\hat{U}^1_{i,0} = \frac{h_{i,1}}{6} \mathbf{D}_{\mathbf{v}_{i,1}} U_i, \tag{2.8}$$

$$\hat{U}^0_{i,1} = \frac{h_{i,2}}{4\sqrt{3}} \mathbf{D}_{\mathbf{v}_{i,2}} U_i. \tag{2.9}$$

Therefore, we can limit the solution coefficients $\hat{U}^1_{i,0}$ and $\hat{U}^0_{i,1}$ separately by comparing them to the forward and backward differences along $\mathbf{v}_{i,1}$ and $\mathbf{v}_{i,2}$, respectively. The differences are reconstructed using the solution averages on neighboring elements in the reconstruction stencil shown in Figure 2.3 (shaded elements). Computing these differences requires interpolated solution values $U^f_{i,k}$ and $U^b_{i,k}$ at the forward and backward interpolation points $\mathbf{x}^f_{i,k}$ and $\mathbf{x}^b_{i,k}$, $k = \{1, 2\}$ (black squares in Figure 2.3a).

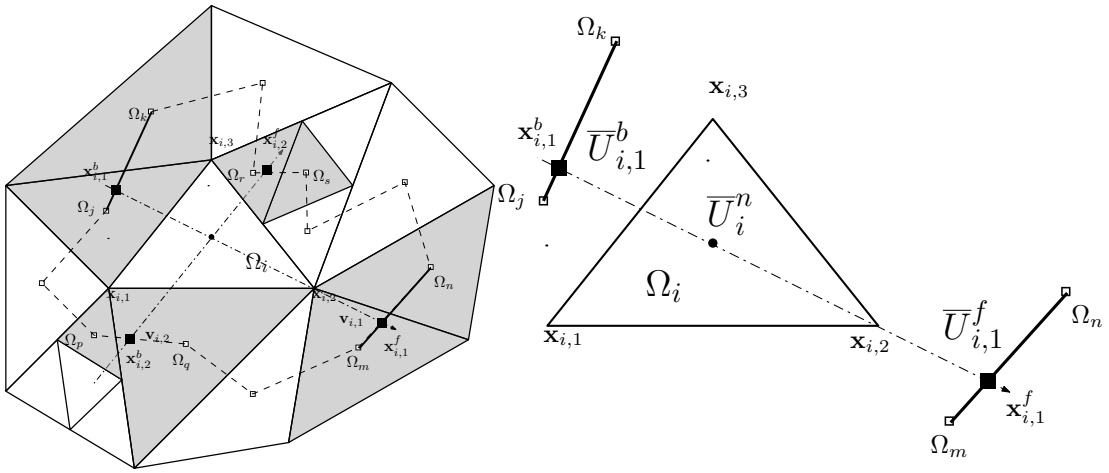

(a) Reconstruction neighborhood.

(b) Reconstruction stencil along $\mathbf{v}_{i,1}$.

Figure 2.3: Reconstruction neighborhood and stencil for Ω_i.

To find the interpolation points, we first form a polygon by joining the cell centroids of elements that share a vertex with Ω_i. Next, we construct two lines passing through the centroid of Ω_i and parallel to $\mathbf{v}_{i,1}$ and $\mathbf{v}_{i,2}$ (Figure 2.3a). The points where these two lines intersect the polygon give the required interpolation points $\mathbf{x}^f_{i,k}$ and $\mathbf{x}^b_{i,k}$. Finally, the solution values at the interpolation points $\mathbf{x}^f_{i,k}$ and $\mathbf{x}^b_{i,k}$ are obtained using linear interpolation of cell averages from the closest neighboring elements. For example, the forward and backward interpolated solution values $U^f_{i,1}$ and $U^b_{i,1}$ along $\mathbf{v}_{i,1}$ are given by (Figure 2.3b)

$$U^f_{i,1} = \beta^f_{i,1}\overline{U}_m + (1-\beta^f_{i,1})\overline{U}_n, \qquad U^b_{i,1} = \beta^b_{i,1}\overline{U}_j + (1-\beta^b_{i,1})\overline{U}_k,$$

where $\beta^f_{i,1}, \beta^b_{i,1} \in [0,1]$ are linear interpolation weights.

After computing the forward and backward differences, we use (2.8) and (2.9) to limit solution coefficients or moments as follows

$$\begin{aligned}
\tilde{U}^1_{i,0} &= \text{minmod}\left(l^f_{i,1}\frac{h_{i,1}}{6}\frac{U^f_{i,1}-\overline{U}_i}{d^f_{i,1}}, \hat{U}^1_{i,0}, l^b_{i,1}\frac{h_{i,1}}{6}\frac{\overline{U}_i - U^b_{i,1}}{d^b_{i,1}}\right),\\
\tilde{U}^0_{i,1} &= \text{minmod}\left(l^f_{i,2}\frac{h_{i,2}}{4\sqrt{3}}\frac{U^f_{i,2}-\overline{U}_i}{d^f_{i,2}}, \hat{U}^0_{i,1}, l^b_{i,2}\frac{h_{i,2}}{4\sqrt{3}}\frac{\overline{U}_i - U^b_{i,2}}{d^b_{i,2}}\right),
\end{aligned} \tag{2.10}$$

where the scaling coefficients $l^f_{i,k}$, $l^b_{i,k}$, $k = \{1,2\}$, are nonnegative, $\overline{U}_i$ is the cell average in Ω_i, and $d^f_{i,k}$ and $d^b_{i,k}$ are, respectively, the distances of the interpolation points $\mathbf{x}^f_{i,k}$ and

$\mathbf{x}_{i,k}^b$, $k = \{1,2\}$, from the cell centroid of Ω_i. The minmod function is given by

$$\text{minmod}(a,b,c) = \begin{cases} \text{sign}(a)\cdot\min(|a|,|b|,|c|), & \text{if } \text{sign}(a) = \text{sign}(b) = \text{sign}(c), \\ 0, & \text{otherwise.} \end{cases} \tag{2.11}$$

In the following sections, we derive admissible range for the scaling coefficients l_i.

2.1.2 Stability constraints for linear advection

The numerical solution in Ω_i satisfies the local maximum principle (LMP) in the means if

$$\min_{k\in\mathcal{N}_i} \overline{U}_k^n \le \overline{U}_i^{n+1} \le \max_{k\in\mathcal{N}_i} \overline{U}_k^n, \tag{2.12}$$

where $\mathcal{N}_i$ is a set containing the indices of Ω_i and its neighbors. Let N_i^+ be the set containing indices of outflow neighbors of Ω_i and N_i^- be the set containing indices of inflow neighbors of Ω_i. Then the following constraints on $l_{i,k}$ need to be satisfied for (2.12) to hold.

1. On each outflow edge of Ω_i, we enforce

$$l_{i,1}\alpha_{i,j,1}^+ + l_{i,2}\alpha_{i,j,2}^+ \le 1, \quad \forall j \in N_i^+. \tag{2.13}$$

2. On each inflow edge of Ω_i, we enforce

$$l_{j,1}\alpha_{j,i,1}^- + l_{j,2}\alpha_{j,i,2}^- \le 1, \quad \forall j \in N_i^-, \tag{2.14}$$

The coefficients $\alpha_{i,j,k}^+$ and $\alpha_{i,j,k}^-$, $k = \{1,2\}$, are defined as

$$\alpha_{i,j,1}^+ = \begin{cases} \dfrac{h_{i,1}}{6}\dfrac{|\phi_0^1(\mathbf{r}_{i,j})|}{d_{i,1}^f}, & \text{if } \phi_0^1(\mathbf{r}_{i,j}) \le 0, \\ \dfrac{h_{i,1}}{6}\dfrac{\phi_0^1(\mathbf{r}_{i,j})}{r_{i,1}d_{i,1}^b}, & \text{otherwise.} \end{cases} \quad \alpha_{i,j,2}^+ = \begin{cases} \dfrac{h_{i,2}}{4\sqrt{3}}\dfrac{|\phi_0^1(\mathbf{r}_{i,j})|}{d_{i,2}^f}, & \text{if } \phi_0^1(\mathbf{r}_{i,j}) \le 0, \\ \dfrac{h_{i,2}}{4\sqrt{3}}\dfrac{\phi_0^1(\mathbf{r}_{i,j})}{r_{i,2}d_{i,2}^b}, & \text{otherwise,} \end{cases},$$

$$\alpha_{j,i,1}^- = \begin{cases} \dfrac{h_{j,1}}{6}\dfrac{|\phi_0^1(\mathbf{r}_{j,i})|}{r_{i,1}d_{j,1}^b}, & \text{if } \phi_0^1(\mathbf{r}_{j,i}) \le 0, \\ \dfrac{h_{j,1}}{6}\dfrac{\phi_0^1(\mathbf{r}_{j,i})}{d_{j,1}^f}, & \text{otherwise,} \end{cases} \quad \alpha_{j,i,2}^- = \begin{cases} \dfrac{h_{i,2}}{4\sqrt{3}}\dfrac{|\phi_0^1(\mathbf{r}_{j,i})|}{r_{j,2}d_{j,2}^b}, & \text{if } \phi_0^1(\mathbf{r}_{j,i}) \le 0, \\ \dfrac{h_{i,2}}{4\sqrt{3}}\dfrac{\phi_0^1(\mathbf{r}_{j,i})}{d_{j,2}^f}, & \text{otherwise.} \end{cases}, \tag{2.15}$$

where $d^f_{i,k}$ and $d^b_{i,k}$ are, respectively, the distances of the interpolation points $\mathbf{x}^f_{i,k}$ and $\mathbf{x}^b_{i,k}$ from the cell centroid $\mathbf{x}_{i,0}$, for $k = \{1, 2\}$, $\mathbf{r}_{i,j}$ is a quadrature point on the edge shared by elements Ω_i and Ω_j, and the ratios $r_{i,1}$ and $r_{i,2}$, are

$$r_{i,1} = \left(\frac{d^f_{i,1}}{d^b_{i,1}}\right)\frac{\overline{U}^n_i - \overline{U}^b_{i,1}}{\overline{U}^f_{i,1} - \overline{U}^n_i}, \quad r_{i,2} = \left(\frac{d^f_{i,2}}{d^b_{i,2}}\right)\frac{\overline{U}^n_i - \overline{U}^b_{i,2}}{\overline{U}^f_{i,2} - \overline{U}^n_i}. \tag{2.16}$$

The constraints (2.13) and (2.14) were derived in [2]. The geometric constants in (2.15) depend on the mapping (1.12) of Ω_i to Ω_0 and can be computed in the preprocessing stage. Consider an outflow edge of Ω_i with edge number b. On this edge, we can enforce

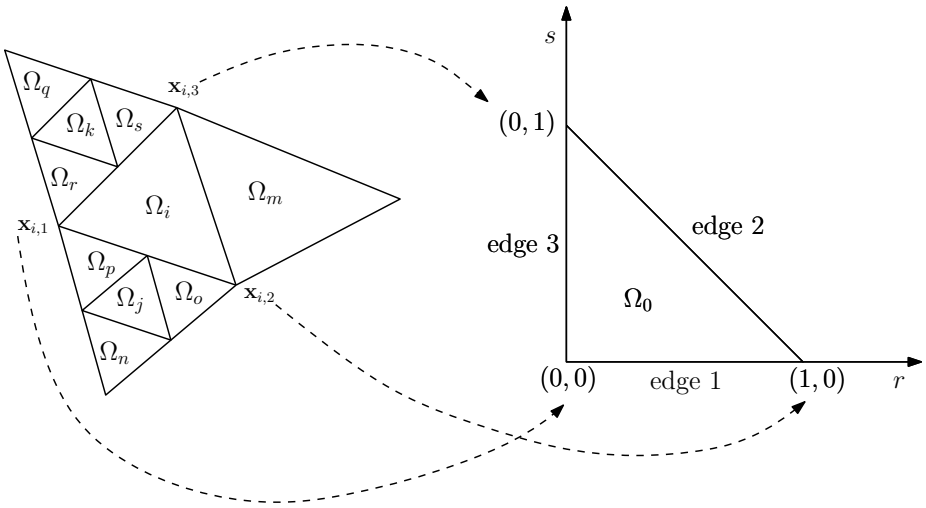

Figure 2.4: Mapping of Ω_i to the canonical triangle Ω_0 by (1.12).

two constraints on the scaling coefficients $l_{i,1}$ and $l_{i,2}$, i.e., the constraint (2.13) on Ω_i and the constraint (2.14) on its inflow neighbor. For a conforming element (Figure 1.5), the basis functions ϕ in the coefficients $\alpha^+_{i,j,k}$ and $\alpha^-_{i,j,k}$ in (2.13) and (2.14) are evaluated at the midpoint of the edges. For nonconforming meshes, we need to consider an extra case. If the

b	ϕ^1_0	ϕ^0_1
1	1	$-\sqrt{3}$
2	1	$\sqrt{3}$
3	-2	0

Table 2.1: Values of the linear basis functions evaluated at the midpoints of the edges of Ω_0.

outflow edge has been refined, the basis functions in (2.13) are evaluated at the midpoint

of the edge with the corresponding values listed in Table 2.1, while the basis functions in (2.14) are evaluated at the midpoints of the two half edges, which are listed in Tables 2.2a and 2.2b. Therefore, if edge b is an outflow edge and hasn't been refined, the constraints (2.14) and (2.13) reduce to

$$\frac{l_{i,1}}{6\gamma^f_{i,1}} + \frac{l_{i,2}}{4\gamma^b_{i,2}r_{i,2}} \le 1 \quad \text{and} \quad \frac{l_{i,1}}{6\gamma^b_{i,1}r_{i,1}} + \frac{l_{i,2}}{4\gamma^f_{i,2}} \le 1 \quad \text{if } b = 1, \tag{2.17}$$

$$\frac{l_{i,1}}{6\gamma^f_{i,1}} + \frac{l_{i,2}}{4\gamma^f_{i,2}} \le 1 \quad \text{and} \quad \frac{l_{i,1}}{6\gamma^b_{i,1}r_{i,1}} + \frac{l_{i,2}}{4\gamma^b_{i,2}r_{i,2}} \le 1 \quad \text{if } b = 2, \tag{2.18}$$

$$\frac{l_{i,1}}{3\gamma^b_{i,1}r_{i,1}} \le 1 \quad \text{and} \quad \frac{l_{i,1}}{3\gamma^f_{i,1}} \le 1 \quad \text{if } b = 3, \tag{2.19}$$

where $\gamma^f_{i,k} = \dfrac{d^f_{i,k}}{h_{i,k}}$ and $\gamma^b_{i,k} = \dfrac{d^b_{i,k}}{h_{i,k}}$ for $k = \{1, 2\}$. However, if the outflow edge b has been refined, the constraints (2.14) and (2.13) reduce to

$$\frac{l_{i,1}}{12r_{i,1}\gamma^b_{i,1}} + \frac{3l_{i,2}}{8\gamma^b_{i,2}r_{i,2}} \le 1 \quad \text{and} \quad \frac{5l_{i,1}}{12\gamma^f_{i,1}} + \frac{l_{i,2}}{8\gamma^b_{i,2}r_{i,2}} \le 1 \quad \text{and} \quad \frac{l_{i,1}}{6\gamma^b_{i,1}r_{i,1}} + \frac{l_{i,2}}{4\gamma^f_{i,2}} \le 1 \quad \text{if } b = 1, \tag{2.20}$$

$$\frac{5l_{i,1}}{12\gamma^f_{i,1}} + \frac{l_{i,2}}{8\gamma^f_{i,2}} \le 1 \quad \text{and} \quad \frac{l_{i,1}}{12r_{i,1}\gamma^b_{i,1}} + \frac{3l_{i,2}}{8\gamma^f_{i,2}} \le 1 \quad \text{and} \quad \frac{l_{i,1}}{6\gamma^b_{i,1}r_{i,1}} + \frac{l_{i,2}}{4\gamma^b_{i,2}r_{i,2}} \le 1 \quad \text{if } b = 2, \tag{2.21}$$

$$\frac{l_{i,1}}{3\gamma^b_{i,1}r_{i,1}} + \frac{l_{i,2}}{4r_{i,2}\gamma^b_{i,2}} \le 1 \quad \text{and} \quad \frac{l_{i,1}}{3\gamma^b_{i,1}r_{i,1}} + \frac{l_{i,2}}{4\gamma^f_{i,2}} \le 1 \quad \text{and} \quad \frac{l_{i,1}}{3\gamma^f_{i,1}} \le 1 \quad \text{if } b = 3. \tag{2.22}$$

b	ϕ^1_0	ϕ^0_1
1	$-\frac{1}{2}$	$-\frac{3}{2}\sqrt{3}$
2	$\frac{5}{2}$	$\frac{1}{2}\sqrt{3}$
3	-2	$\sqrt{3}$

(a)

b	ϕ^1_0	ϕ^0_1
1	$\frac{5}{2}$	$-\frac{1}{2}\sqrt{3}$
2	$-\frac{1}{2}$	$\frac{3}{2}\sqrt{3}$
3	-2	$-\sqrt{3}$

(b)

Table 2.2: Values of the basis functions evaluated at (A) the quarter and (B) three quarter points of the edges of Ω_0.

To find a suitable pair of scaling coefficients $l_{i,1}$ and $l_{i,2}$ during runtime, we need to identify the outflow edges of Ω_i, check if these edges have been refined, identify the edges on Ω_0 to which they are mapped, and finally, select appropriate constraints from (2.17) - (2.19) or (2.20) - (2.22). This is computationally expensive. Instead, if any of the edges of an element has been refined, we can enforce the constraints (2.13) and (2.14) on all edges of Ω_i, i.e., find scaling coefficients that satisfy all inequalities (2.20) - (2.22). Doing so leads to a more diffusive limiter. However, such a limiter is easier to implement. Simplifying (2.20), (2.21), and (2.22) gives

$$\begin{aligned}
&\frac{l_{i,1}}{6\ \min(\gamma^f_{i,1}, r_{i,1}\gamma^b_{i,1})} + \frac{l_{i,2}}{4\ \min(\gamma^f_{i,2}, r_{i,2}\gamma^b_{i,2})} \le 1 \qquad \frac{l_{i,1}}{12\min(\gamma^f_{i,1}, r_{i,1}\gamma^b_{i,1})} + \frac{3l_{i,2}}{8\ \min(\gamma^f_{i,2}, r_{i,2}\gamma^b_{i,2})} \le 1\\
&\frac{5l_{i,1}}{12\ \min(\gamma^f_{i,1}, r_{i,1}\gamma^b_{i,1})} + \frac{l_{i,2}}{8\ \min(\gamma^f_{i,2}, r_{i,2}\gamma^b_{i,2})} \le 1 \qquad \frac{l_{i,1}}{3\ \min(\gamma^f_{i,1}, r_{i,1}\gamma^b_{i,1})} + \frac{l_{i,2}}{4\ \min(\gamma^f_{i,2}, r_{i,2}\gamma^b_{i,2})} \le 1\\
&\qquad\qquad\qquad\qquad\qquad\qquad\qquad\qquad\qquad\qquad \frac{l_{i,1}}{3\ \min(\gamma^f_{i,1}, r_{i,1}\gamma^b_{i,1})} \le 1.
\end{aligned} \tag{2.23}$$

Using notations $\tilde{l}_{i,1} = \dfrac{l_{i,1}}{\min(\gamma^f_{i,1}, r_{i,1}\gamma^b_{i,1})}$ and $\tilde{l}_{i,2} = \dfrac{l_{i,2}}{\min(\gamma^f_{i,2}, r_{i,2}\gamma^b_{i,2})}$, (2.23) can be written as

$$\begin{aligned}
&\frac{\tilde{l}_{i,1}}{6} + \frac{\tilde{l}_{i,2}}{4} \le 1 \qquad \frac{\tilde{l}_{i,1}}{12} + \frac{3\tilde{l}_{i,2}}{8} \le 1\\
&\frac{5\tilde{l}_{i,1}}{12} + \frac{\tilde{l}_{i,2}}{8} \le 1 \qquad \frac{\tilde{l}_{i,1}}{3} + \frac{\tilde{l}_{i,2}}{4} \le 1\\
&\qquad\qquad\qquad\qquad \frac{\tilde{l}_{i,1}}{3} \le 1.
\end{aligned} \tag{2.24}$$

Figure 2.5a shows the region of admissible solutions of (2.24), i.e., choosing any set of scaling coefficients that lies in the shaded region leads to a numerical solution that satisfies the LMP (2.12). To ensure that the scaling coefficients are not too small, i.e., the limiter is not too restrictive, we choose a set of scaling coefficients from the top boundary of the shaded region marked **II** in Figure 2.5b, i.e.,

$$\begin{aligned}
l_{i,1} &= \delta_n\ \min(\gamma^f_{i,1}, r_{i,1}\gamma^b_{i,1}),\\
l_{i,2} &= 4\left(1 - \frac{\delta_n}{3}\right)\ \min(\gamma^f_{i,2}, r_{i,2}\gamma^b_{i,2}), \quad \delta_n \in [\frac{6}{5}, 2].
\end{aligned} \tag{2.25}$$

Moreover, from (2.10), we note that the limited solution coefficients can be written solely

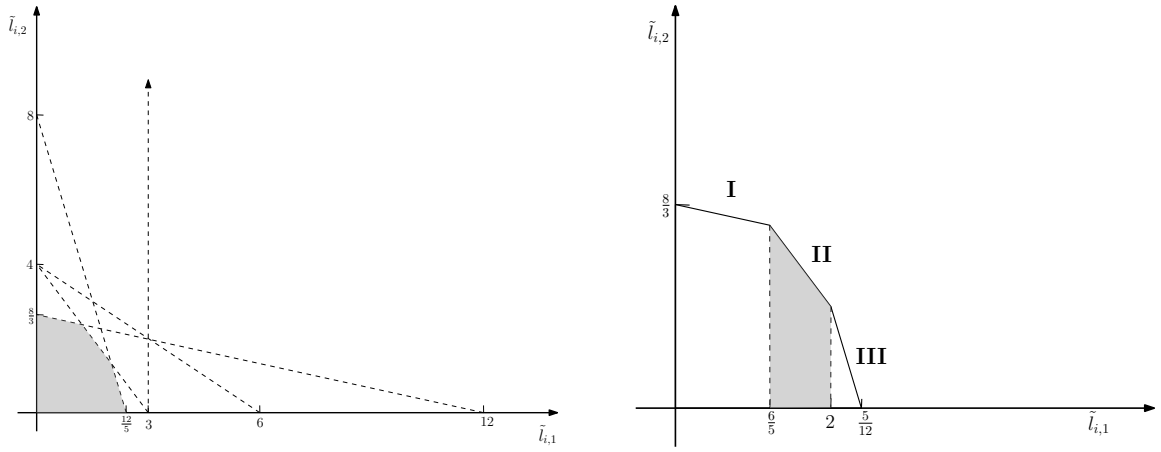

(a) Simplified set of inequalities .

(b) Zoom in near admissible region.

Figure 2.5: Simplified set of inequalities for nonconforming element Ω_i. The shaded region is the the admissible region for scaling factors $\tilde{l}$.

in terms of either the forward differences or the backward differences as

$$\begin{aligned}\tilde{U}^1_{i,0} &= l_{i,1}\frac{h_{i,1}}{6}\frac{U^f_{i,1}-\overline{U}^n_i}{d^f_{i,1}} = l_{i,1}\frac{h_{i,1}}{6}\frac{\overline{U}^n_i-U^b_{i,1}}{r_{i,1}d^b_{i,1}},\\ \tilde{U}^0_{i,1} &= l_{i,2}\frac{h_{i,2}}{4\sqrt{3}}\frac{U^f_{i,2}-\overline{U}^n_i}{d^f_{i,2}} = l_{i,2}\frac{h_{i,2}}{4\sqrt{3}}\frac{\overline{U}^n_i-U^b_{i,2}}{r_{i,2}d^b_{i,2}}.\end{aligned} \tag{2.26}$$

Substituting (2.25) into (2.26) and using (2.16), (2.10) simplifies to

$$\begin{aligned}\tilde{U}_{i,1} &= \text{minmod}\left(\delta_n\frac{U^f_{i,1}-\overline{U}_i}{6}, \hat{U}_{i,1}, \delta_n\frac{\overline{U}_i-U^b_{i,1}}{6}\right),\\ \tilde{U}_{i,2} &= \text{minmod}\left((1-\frac{\delta_n}{3})\frac{U^f_{i,2}-\overline{U}_i}{\sqrt{3}}, \hat{U}_{i,2}, (1-\frac{\delta_n}{3})\frac{\overline{U}_i-U^b_{i,2}}{\sqrt{3}}\right),\end{aligned} \tag{2.27}$$

where $\delta_n \in [\frac{6}{5}, 2]$. To maintain the second order accuracy the linear solution coefficients must not be altered in the case when the exact solution is linear, i.e., $l_{i,1},\ l_{i,2} \geq 1$ and (2.25)

imply

$$\begin{aligned} \delta_n \min(\gamma^f_{i,1}, r_{i,1}\gamma^b_{i,1}) &\geq 1, \\ 4\left(1 - \frac{\delta_n}{3}\right) \min(\gamma^f_{i,2}, r_{i,2}\gamma^b_{i,2}) &\geq 1. \end{aligned} \tag{2.28}$$

Noting that the ratio of the backward and forward differences for a linear solution is one,

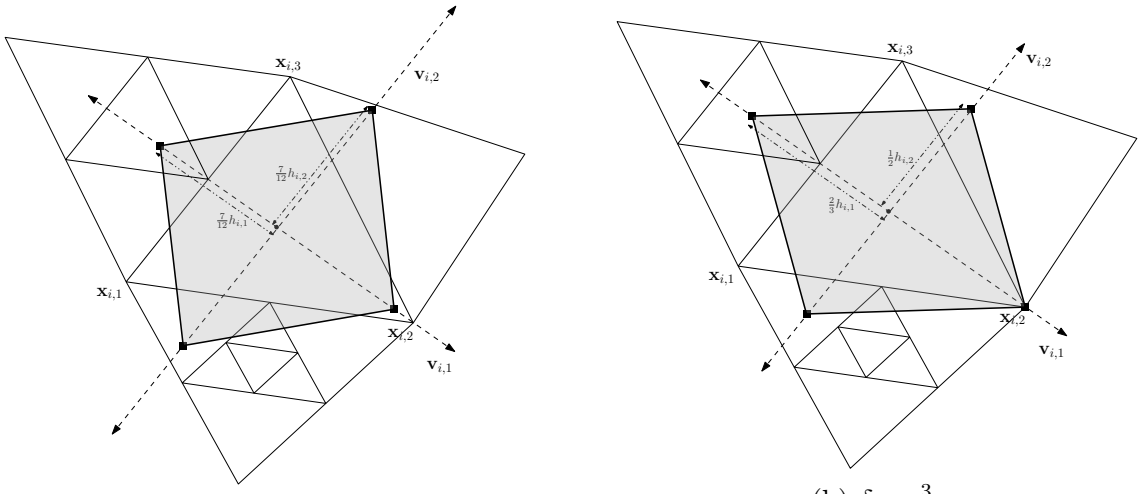

(a) $\delta_n = \frac{12}{7}$. (b) $\delta_n = \frac{3}{2}$.

Figure 2.6: Interpolation points should lie outside the shaded region in order to maintain the second order accuracy.

i.e., $r_{i,1} = r_{i,2} = 1$, and plugging $\gamma^f_{i,k} = \dfrac{d^f_{i,k}}{h_{i,k}}$ and $\gamma^b_{i,k} = \dfrac{d^b_{i,k}}{h_{i,k}}$ for $k = \{1, 2\}$ into (2.28), we get

$$\min(d^f_{i,1}, d^b_{i,1}) \geq \frac{h_{i,1}}{\delta_n}, \qquad \min(d^f_{i,2}, d^b_{i,2}) \geq \frac{3h_{i,2}}{4(3 - \delta_n)}. \tag{2.29}$$

Thus, for the limited solution to retain the second order accuracy, the interpolation points must lie further from the cell centroid of Ω_i than a certain distance. For example, the exclusion regions for two different values of δ are shown in Figure 2.6 as the shaded areas.

2.2 Reconstruction neighborhood

To limit the solution in an element Ω_i using the technique described in Section 2.1, we need access to solutions on elements in the vertex neighborhood of Ω_i. In this section, we

describe our approach to find the vertex neighborhood of elements in an adaptively refined nonconforming triangular mesh using a vertex database (Figure 2.7a).

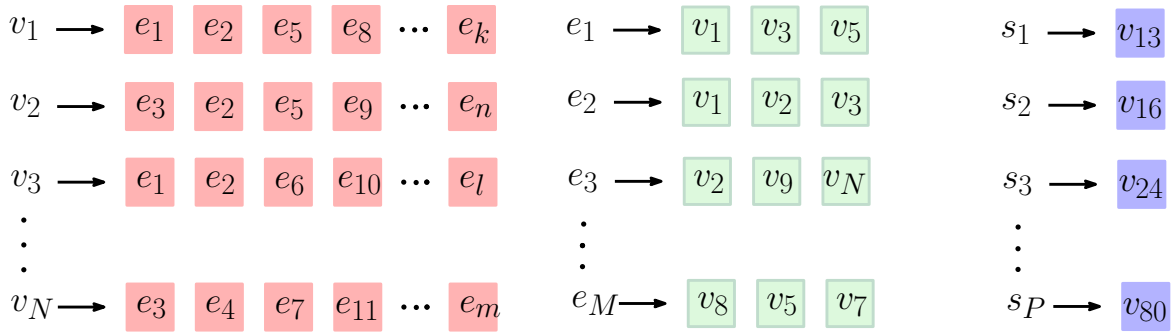

(a) Vertex-Element connectivity. (b) Element-Vertex connectivity.

Figure 2.7: The connectivity and the vertex database for a nonconforming triangular mesh.

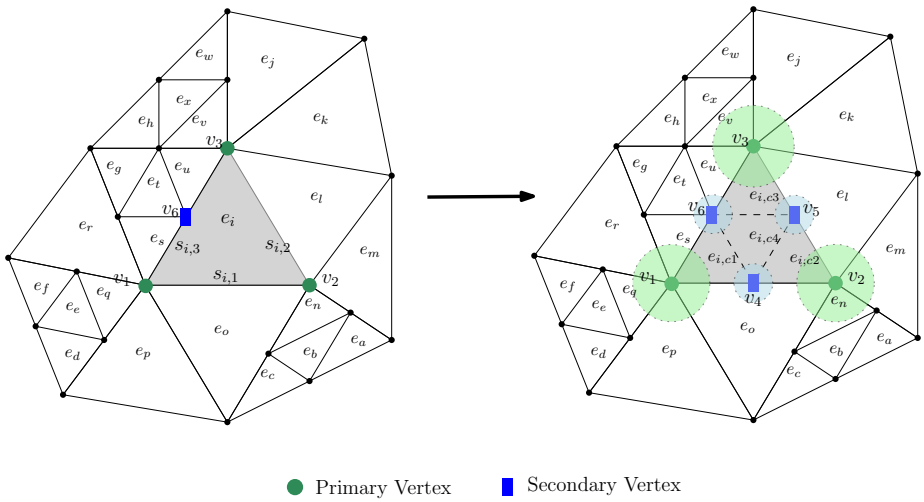

Figure 2.8: Refinement of element Ω_i (shaded).

2.2.1 Vertex database

Consider refinement of element Ω_i with element ID e_i (Figure 2.8). We refer to the vertices of an element as its primary vertices (vertices v_1, v_2, and v_3, marked with green dots) and the midpoints of the edges of an element as the secondary vertices (vertices v_4, v_5, and v_6, marked with blue rectangles). We present a step-by-step algorithm for updating the vertex database when an element is refined (or coarsened).

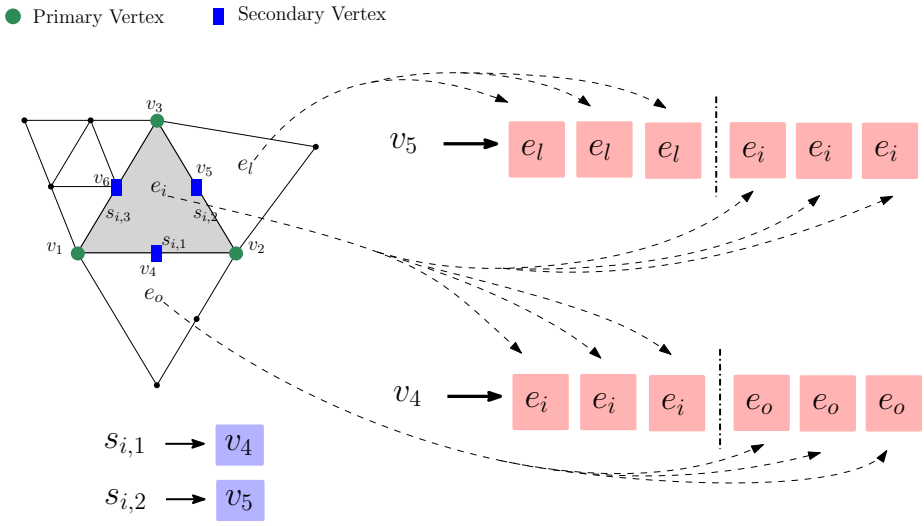

Figure 2.9: Adding newly created vertices and initialising their element ID list.

First, we identify all elements and edges that are to be refined. Next, while refining a edge, we allocate memory in the vertex database for newly created secondary vertices, i.e., the edge midpoints, to store the IDs of the elements sharing the vertex. To ensure mesh regularity, elements sharing an edge differ in their refinement levels by at most one level. Due to this restriction, each secondary vertex is shared by at most six elements. In the example shown in Figure 2.8, edges $s_{i,1}$ and $s_{i,2}$ are being refined. We create two new secondary vertices, v_4 and v_5, and allocate memory for them in the vertex database. Then we initialise the allocated space with IDs of the elements sharing the edge, with the ID of the element on the left occupying the first three positions and the ID of the element on the right occupying the last three. For example, for the secondary vertex v_4, we assign the ID e_i to the first three positions and the ID e_o to the next three positions (Figure 2.9).

Next, we replace the ID of the parent element in the element ID list of a primary vertex with the ID of the corresponding child element. For example, while refining Ω_i, we replace its ID e_i with $e_{i,c1}$ in the element ID list of v_1, $e_{i,c2}$ in the element ID list of v_2, and $e_{i,c3}$ in the element ID list of v_3 (Figure 2.10a to Figure 2.10b). Next, for each of the secondary vertices, we replace the ID of the parent element with the IDs of the three child elements sharing that vertex. For example, for the secondary vertex v_4, we replace e_i with the IDs $e_{i,c1}$, $e_{i,c4}$, and $e_{i,c2}$ (Figure 2.11a to Figure 2.11b). Finally, we add the appropriate vertex IDs to the vertex ID list of each child element. To update the vertex database when elements are coarsened, the steps described above can be applied in reverse. First, for the elements being coarsened, replace the element ID, i.e., ID of the child element, with the ID of the parent element in the element ID lists of all the primary vertices as well as the secondary vertices (if present) (Figure 2.10b to Figure 2.10a).

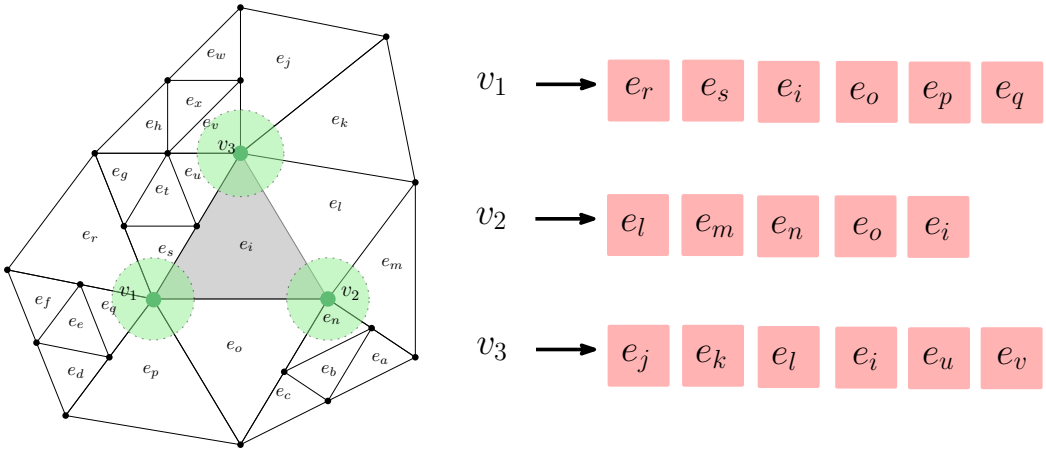

(a) Before refinement.

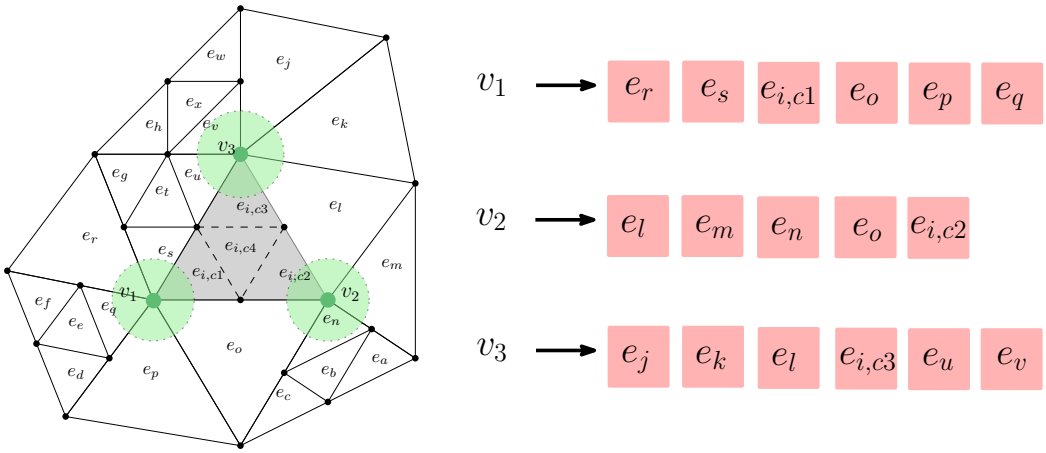

(b) After refinement.

Figure 2.10: Updating the element ID list for primary vertices of element Ω_i.

Finally, if the left and right elements of a edge are coarsened to the same refinement level, i.e., the edge is flagged for coarsening, the associated secondary vertex (the vertex at the edge midpoint) is removed from the vertex database and the allocated memory is freed up to be used later, if needed. Note that, as each element is uniquely identified in the vertex to element connectivity, updating the IDs of the elements with adaptive refinement does not lead to race conditions.

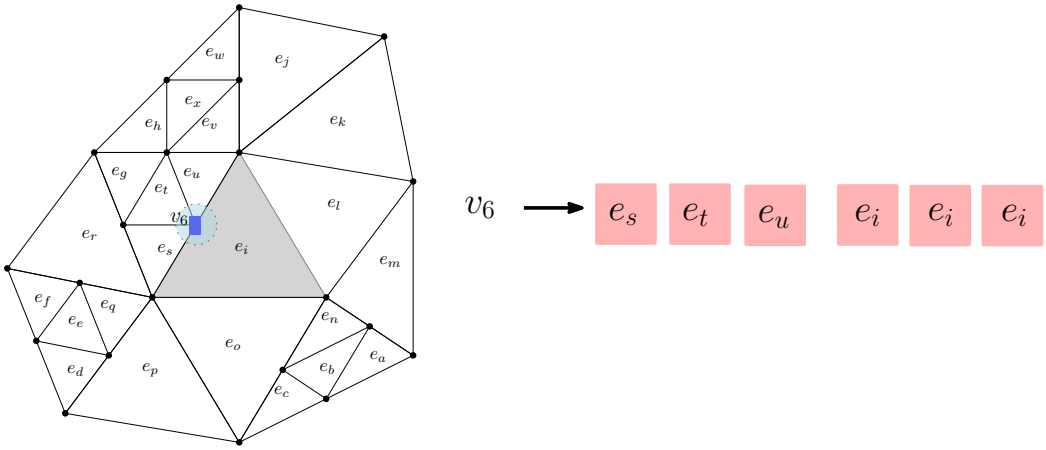

(a) Before refinement.

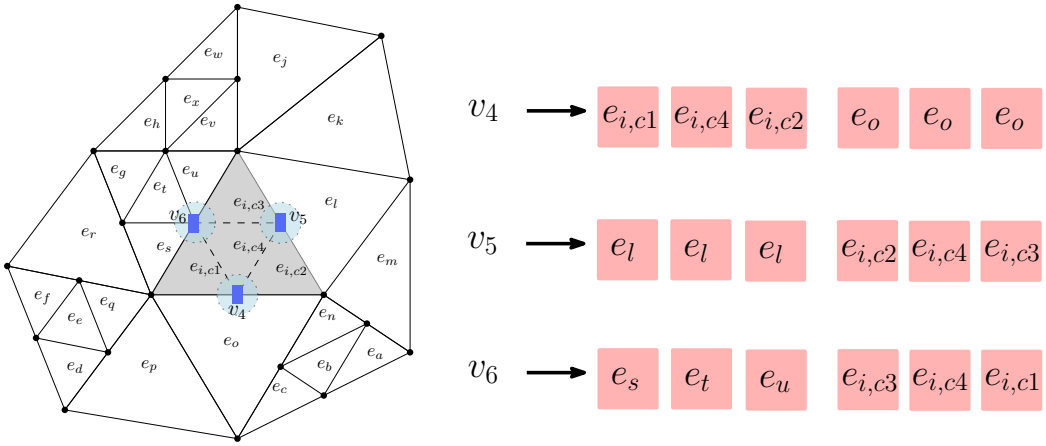

(b) After refinement.

Figure 2.11: Updating the element ID list for secondary vertices of Ω_i.

2.2.2 Updating the vertex neighborhood

Vertex neighborhoods can easily be assembled once the vertex database has been updated. During a refinement cycle, only a small percentage of elements undergo refinement. Therefore, we don't need to update the vertex neighborhood of all elements present in the mesh. So, we flag only those elements whose primary or secondary vertices have an updated element ID list. To update the vertex neighborhood for the flagged elements, we read the element IDs from the element ID list associated with both primary and secondary vertices, assemble the read element IDs, remove duplicate IDs, if any, and finally reorder the IDs if needed.

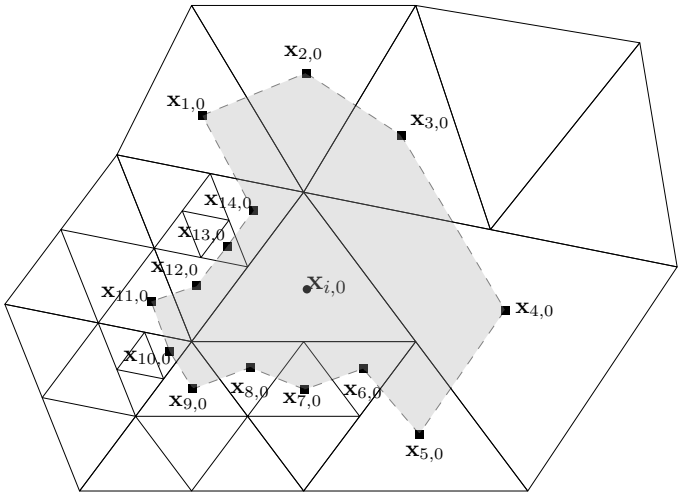

Figure 2.12: Reconstruction neighbourhood for vertex neighbourhood limiter.

2.2.3 Updating the reconstruction stencil

Once the vertex neighborhood for element Ω_i is identified and updated, limiting techniques, e.g., the second order vertex neighborhood limiter [22] and the second order moment limiter described in Section 2.1 can be applied. As the vertex neighborhood limiter requires only the maximum and minimum values of cell averages in the reconstruction neighborhood, the limiter can be directly applied once the vertex neighborhood (Figure 2.12) has been updated. However, for the moment limiter, we need to find interpolation points along the directions $\mathbf{v}_{i,1}$ and $\mathbf{v}_{i,2}$. Moreover, to maintain second order accuracy, we also need to ensure that the interpolation points satisfy the geometric constraints (2.28). To find the interpolation points, we first replace IDs of elements in the vertex neighborhood that are at a refinement level higher than that of Ω_i with the IDs of the middle child element of a parent element at the same refinement level as Ω_i (Figure 2.13c). This is described in Algorithm 1. Next, we compute the convex hull of the enlarged neighborhood (Figure 2.13d) using Algorithm 2. Then, we can find the interpolation points and weights along $\mathbf{v}_{i,1}$ and $\mathbf{v}_{i,2}$ (Figure 2.14) and finally, the moment limiter can be applied as given in (2.27).

2.3 Numerical Results

In this section, we analyze the performance of the proposed moment limiter on adaptively refined nonconforming meshes. We run convergence studies to show that limited solutions exhibit the expected convergence rate. We present numerical experiments to illustrate

Algorithm 1 To update the reconstruction neighborhood to satisfy the geometrical constraints on the interpolation points

$N \leftarrow$ Size of reconstruction neighborhood
$neighbor\_idx[N] \leftarrow$ IDs of elements in the reconstruction neighborhood
$parent[] \leftarrow$ Array of parent IDs
$child4[] \leftarrow$ Array of middle child IDs
$refine\_level[] \leftarrow$ Array of refinement level of elements
$idx \leftarrow$ ID of element Ω_i
$diff\_level \leftarrow 0$
$temp\_idx \leftarrow 0$
for $i : 1 \rightarrow N$ **do**
  $temp\_idx \leftarrow neighbor\_idx[i]$
  $diff\_level \leftarrow refine\_level[temp\_idx] - refine\_level[idx]$
  if $diff\_level > 0$ **then**
    for $k : 1 \rightarrow diff\_level$ **do**
      $temp\_idx \leftarrow parent[temp\_idx]$
    end for
    while $child4[temp\_idx] > -1$ **do**
      $temp\_idx = child4[temp\_idx]$
    end while
    $neighbor\_idx[i] \leftarrow temp\_idx$
  end if
end for

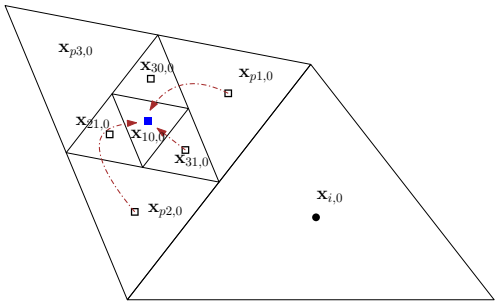

(a) Zoom in on the red inset.

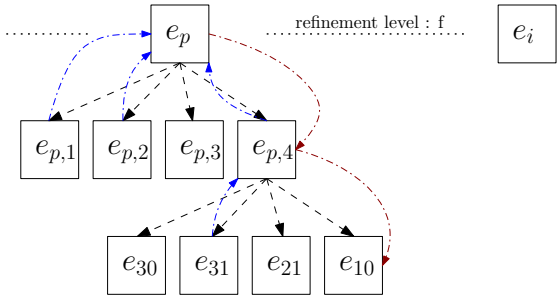

(b) Sample traversal of the element tree.

robustness of the limiter in the presence of discontinuities. In all presented cases, time-stepping was performed using an explicit second order Runge-Kutta integrator with the

Algorithm 2 To compute the convex hull of a given reconstruction neighborhood

$N \leftarrow$ Size of reconstruction neighborhood
$centroid[N] \leftarrow$ Centroids of elements in the neighborhood arranged in anticlockwise direction
$in\_convexhull[N] \leftarrow$ Array of size N initialised to 1
$flag\_change\_in\_hull \leftarrow 1$
$Nb\_iterations \leftarrow 5$
while $flag\_change\_in\_hull = 1$ & $Nb\_iterations > 0$ **do**
  $flag\_change\_in\_hull \leftarrow 0$
  for $i : 1 \rightarrow N$ **do**
    if $in\_convexhull[i] \; != 0$ **then**
      $index\_f \leftarrow$ Index of succeeding element in the convex hull
      $index\_b \leftarrow$ Index of preceding element in the convex hull
      $\theta \leftarrow$ Angle enclosed in the anticlockwise direction by the lines joining centroids of elements with indices $index\_b$, i, $index\_f$
      if $\theta < 180$ **then**
        $flag\_convexhull \leftarrow 0$
      else
        $flag\_convexhull \leftarrow 1$
      end if
      if $flag\_convexhull \; != \; in\_convexhull[i]$ **then**
        $flag\_change\_in\_hull \leftarrow 1$
      end if
      $in\_convexhull[i] \leftarrow flag\_convexhull$
    end if
  end for
  $Nb\_iterations \leftarrow Nb\_iterations - 1$
end while

CFL condition proposed in [50]

$$\Delta t \leq \frac{3}{13} \min_i \frac{h_i}{\|\mathbf{a}\|}, \tag{2.30}$$

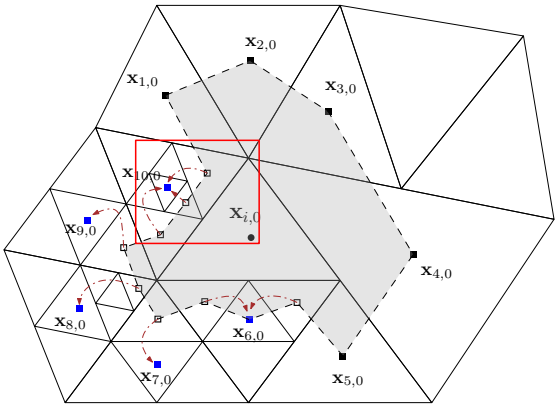

(c) Updating the neighborhood for moment limiter.

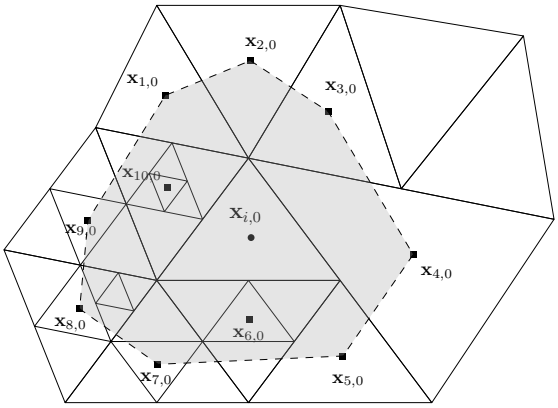

(d) Convex hull of the neighbourhood for moment limiter.

Figure 2.13: Updating the reconstruction neighbourhood for moment limiter on nonconforming mesh.

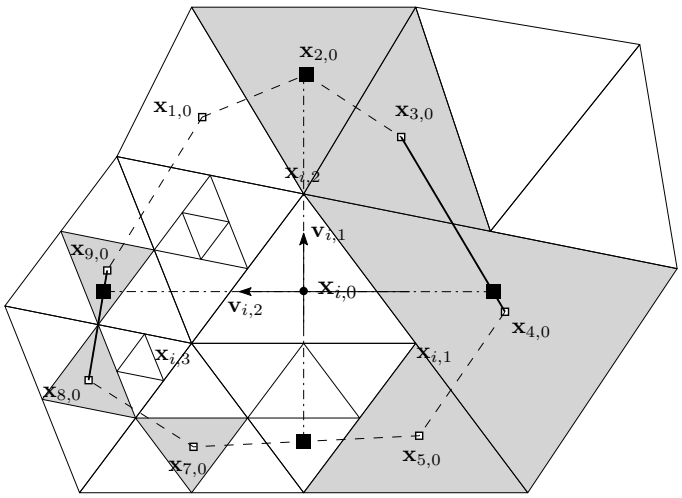

Figure 2.14: Reconstruction neighbourhood for moment limiter.

where h_i is the smallest height of element Ω_i (Figure 2.15). For nonconforming elements, we used the proposed second order limiter (2.27) with $\delta_n = \frac{3}{2}$, i.e.,

$$\tilde{U}_{i,1} = \text{minmod}\left(\frac{U^f_{i,1} - \overline{U}_i}{4}, \hat{U}_{i,1}, \frac{\overline{U}_i - U^b_{i,1}}{4}\right), \qquad \tilde{U}_{i,2} = \text{minmod}\left(\frac{U^f_{i,2} - \overline{U}_i}{2\sqrt{3}}, \hat{U}_{i,2}, \frac{\overline{U}_i - U^b_{i,2}}{2\sqrt{3}}\right). \tag{2.31}$$

For conforming elements, we used the second order limiter proposed in [2]

$$\tilde{U}_{i,1} = \text{minmod}\left(\frac{U^f_{i,1} - \overline{U}_i}{2}, \hat{U}_{i,1}, \frac{\overline{U}_i - U^b_{i,1}}{2}\right), \qquad \tilde{U}_{i,2} = \text{minmod}\left(\frac{U^f_{i,2} - \overline{U}_i}{2\sqrt{3}}, \hat{U}_{i,2}, \frac{\overline{U}_i - U^b_{i,2}}{2\sqrt{3}}\right). \tag{2.32}$$

The mesh is adaptively refined using the refinement strategy proposed in [43]. Finally, we use the local Lax-Friedrichs flux, unless stated otherwise.

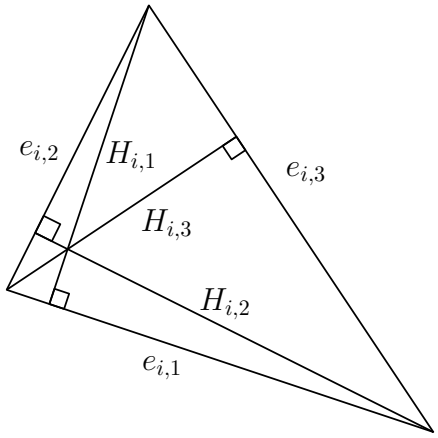

Figure 2.15: Element size $h_i = \min(H_{i,1}, H_{i,2}, H_{i,3})$ [2].

2.3.1 Advecting Pulse.

In this example, we verify the need for using the proposed moment limiter (2.27) over the moment limiter (2.32) developed for conforming meshes. We solve the advecting pulse problem on the domain $\Omega = [-1,1] \times [-1,1]$ with the flux in (1.8) given by $\mathbf{F} = [u, u]$. The initial condition, consisting of a square pulse, is given by

$$u_0(x,y) = \begin{cases} 1, & \text{if } \max(|x - 0.35|, |y|) \leq 0.25, \\ 0, & \text{otherwise.} \end{cases} \tag{2.33}$$

Note that for the given initial condition, the cell averages of the exact solution lie in the interval $[0,1]$. The problem is solved until $t = 0.1$ on a nonconforming mesh of 15,912 triangles (Figure 2.16). Table 2.3 shows the minimum and maximum solution averages at $t = 0.1$ for forward Euler and RK2 time steps. We observe that the cell averages of the solution exceed the global bounds with the moment limiter (2.32) developed for

conforming meshes. However, with the proposed moment limiter (2.27), solution averages remain within the global bounds.

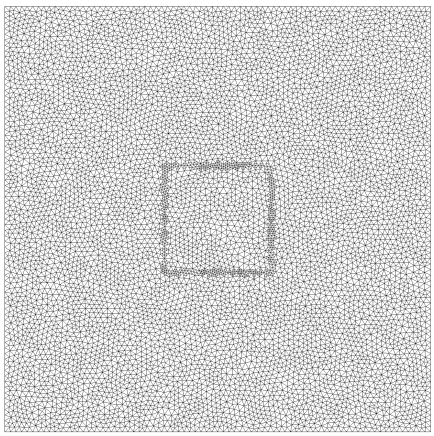

Figure 2.16: Initial nonconforming mesh of 15,912 triangles for the advecting pulse problem.

Limiter	Maximum	Minimum
(2.27)	1	-1.67e-21
(2.32)	1.0021	-1.17e-05

(a) RK2.

Limiter	Maximum	Minimum
(2.27)	1	-2.50e-21
(2.32)	1.0055	-6.27e-06

(b) Forward Euler.

Table 2.3: Global bounds of solution averages at $t = 0.1$ on a nonconforming mesh of 15,912 triangles for the advecting pulse problem with limiter (2.27) developed for nonconforming meshes and limiter (2.32) developed for conforming meshes.

2.3.2 Advecting Hill.

We consider the advecting hill problem on the domain $\Omega = [-1, 1] \times [-1, 1]$, with the flux in (1.8) given by $\mathbf{F} = [u, u]$. The initial condition is $u_0(x, y) = 2.5 \exp\left(\frac{-r^2}{2R^2}\right)$, with $R = 0.15$ and $r = \sqrt{(x + 0.25)^2 + (y + 0.25)^2}$. We solve the problem on a sequence of nonconforming meshes A-D. Mesh A (Figure 2.17b) is a coarse unstructured nonconforming mesh of $4,391$ triangles with the maximum level of refinement set at three, while meshes B-D are obtained by the nested refinement of the preceding mesh. That is, each element in a coarser mesh is divided into four new elements by joining the edge midpoints to form a finer mesh. The L_1 errors and rates of convergence for $p = 1$ DG approximation at $t = 0.5$ are presented in Table 2.4. We observe that limited solutions converge with theoretical rates. We note that

the limiter causes only a moderate increase in the magnitude of numerical errors. Raised solutions for $p = 1$ on meshes A and D are plotted in Figures 2.17a and 2.17c, respectively. Additionally, solution profiles along $y = 0.25$ on meshes A and D are shown in Figure 2.17d. We observe that solutions on all but the coarsest mesh approximate the top of the hill well (Figure 2.17d).

Mesh	Number of elements	L1 error	
		limited	unlimited
A	4,391	3.03e-02 (-)	8.4e-03 (-)
B	17,564	5.3e-03 (2.51)	1.82e-03 (2.2)
C	70,256	1.07e-03 (2.30)	4.04e-04 (2.17)
D	281,024	2.51e-04 (2.09)	9.32e-05 (2.11)

Table 2.4: L_1 errors for the advecting hill problem for limited and unlimited solutions at $t = 0.5$. The convergence rates are given in parentheses.

2.3.3 Rotating shapes.

We solve the rotating shapes problem with the flux in (1.8) given by $\mathbf{F} = [-2\pi yu, 2\pi xu]$. The initial condition, consisting of a square pulse and a hill (Figure 2.18), is given by

$$u_0(x,y) = \begin{cases} \cos^2(2\pi r), & \text{if } r \le 0.25, \\ 1, & \text{if } \max(|x-0.35|, |y|) \le 0.25, \\ 0, & \text{otherwise,} \end{cases} \tag{2.34}$$

where $r = \sqrt{(x+0.5)^2 + y^2}$. The exact solution of the problem is a rotation of the initial condition about the origin. The problem is solved until $t = 1$ on an initial unstructured mesh of $1,540$ triangles. The mesh is refined every 5 time steps with the maximum level of refinement set at six.

Figure 2.19 shows the isolines of the solution obtained with the proposed moment limiter on the final mesh. We observe that the isolines are sharp, the discontinuities are well resolved, and the limiter suppresses oscillations near the discontinuities. This is further demonstrated in the cross-sections in Figure 2.20. We also note that the peak of the hill has been flattened in Figure 2.20a. This well known phenomenon is due to clipping at local extrema by second order limiters.

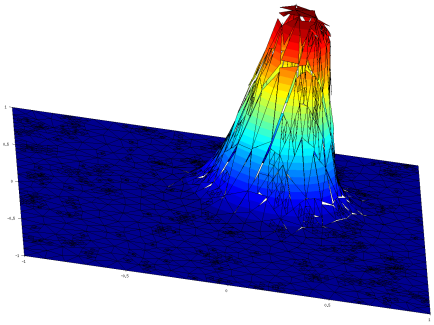

(a) Raised solution on mesh A.

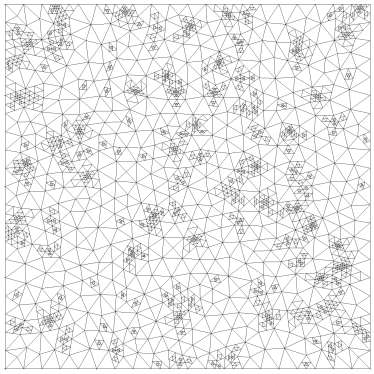

(b) Initial nonconforming mesh A.

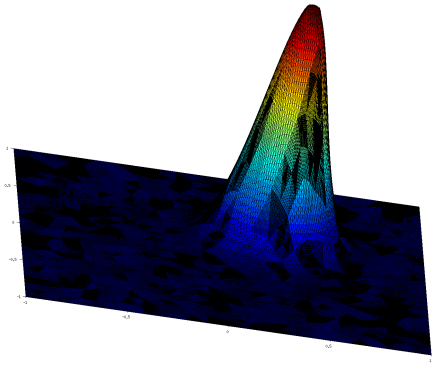

(c) Raised solution on mesh D.

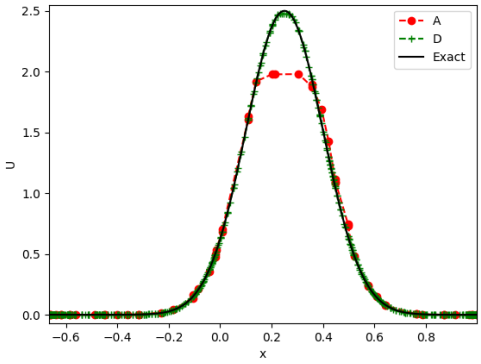

(d) Solution profile along the line $y = 0.25$.

Figure 2.17: Solutions of the advecting hill problem with $p = 1$.

2.3.4 Isentropic vortex.

Next, we test the performance of the limiter when applied to a system of nonlinear equations. We consider the Euler equations

$$\frac{\partial}{\partial t}\begin{pmatrix}\rho\\ \rho u\\ \rho v\\ E\end{pmatrix}+\frac{\partial}{\partial x}\begin{pmatrix}\rho u\\ \rho u^2+p\\ \rho uv\\ (E+p)u\end{pmatrix}+\frac{\partial}{\partial y}\begin{pmatrix}\rho v\\ \rho uv\\ \rho v^2+p\\ (E+p)v\end{pmatrix}=0, \tag{2.35}$$

where ρ is the density, ρu and ρv are the x- and y-direction momenta, E is the energy, and the pressure, p, is given by the equation of state $p = (\gamma-1)\left(E-\frac{\rho}{2}(u^2+v^2)\right)$. We solve the

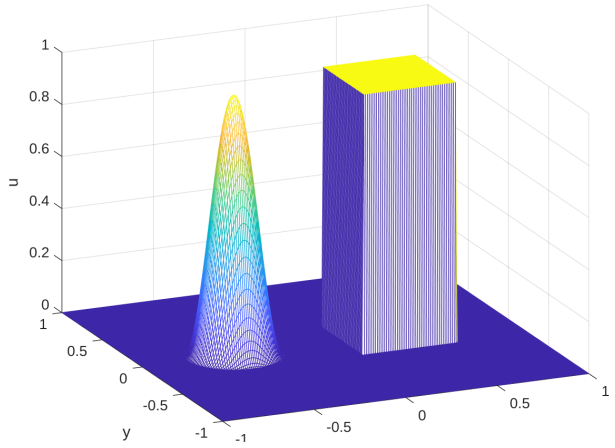

Figure 2.18: Initial set-up for the rotating shapes test case.

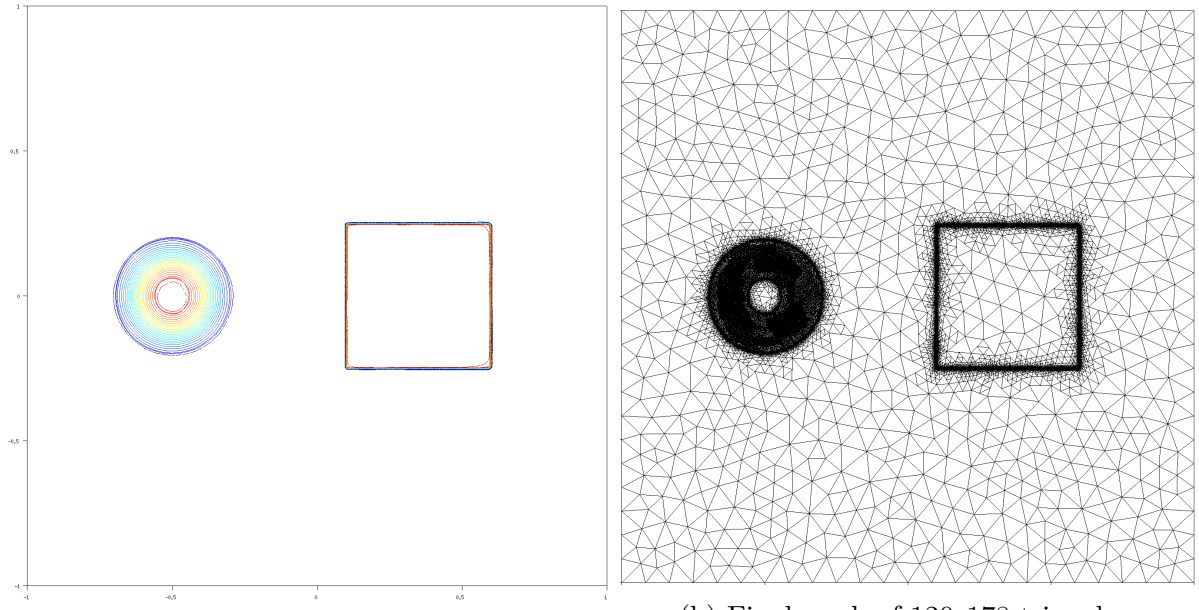

(a) Isolines at $t = 1$.

(b) Final mesh of $120,178$ triangles.

Figure 2.19: Solution of the rotating shapes test case at $t = 1$.

smooth isentropic vortex problem described in [51] with the initial conditions

$$\rho = \left(1 - \frac{(\gamma-1)}{8\pi^2}(M\beta)^2 e^r\right)^{\frac{1}{\gamma-1}}, \quad p = \frac{\rho^\gamma}{\gamma M^2}, \quad u = \frac{\beta}{2\pi R} y e^{\frac{r}{2}}, \quad v = -\frac{\beta}{2\pi R} x e^{\frac{r}{2}}, \tag{2.36}$$

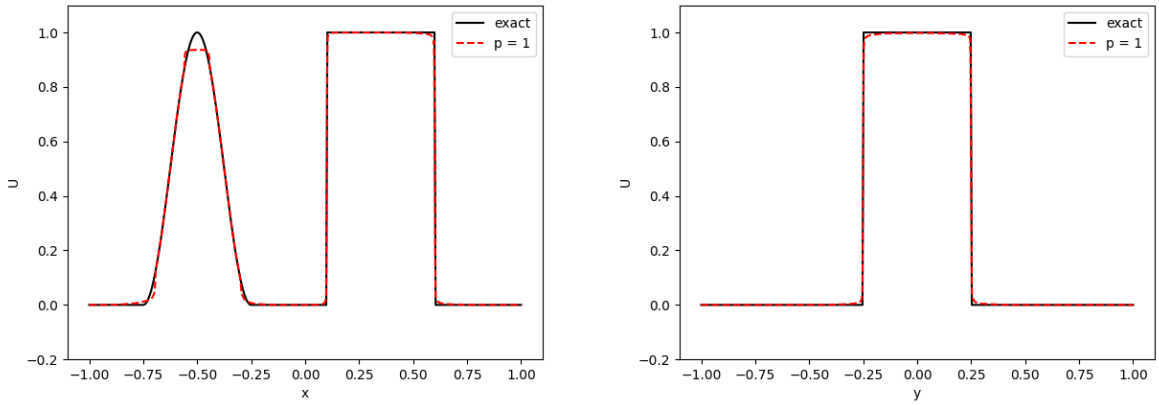

(a) Profile of the solution at $y = 0$.

(b) Profile of the solution at $x = 0.5$.

Figure 2.20: Solution profiles for the rotating shapes test case at $t = 1$.

where $r = \frac{1-(x^2+y^2)}{R^2}$, $R = 1.5$, $\beta = 13.5$, $\gamma = 1.4$, and $M = 0.4$. With these initial conditions, the exact solution is stationary and given by (2.36). The L_1 errors in the density and convergence rates for $p = 1$ at $t = 0.5$ are reported in Table 2.5. Similar to the scalar advection case, we see that the moment limiter does not degrade the expected convergence rate.

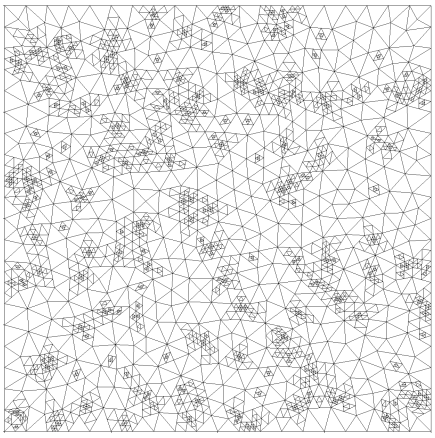

Figure 2.21: Initial nonconforming mesh A for isentropic vortex problem.

Mesh	Number of elements	L1 error	
		limited	unlimited
A	4,781	6.43e-02 (-)	1.07e-02 (-)
B	19,124	1.39e-02 (2.2)	2.56e-03 (2.06)
C	76,496	3.46e-03 (2.00)	6.16e-04 (2.04)
D	305,984	8.70e-04 (1.99)	1.5e-04 (2.04)

Table 2.5: L_1 errors for the isentropic vortex problem for limited and unlimited solutions at $t = 0.5$. The convergence rates are given in parentheses.

2.3.5 Double Mach test case.

We solve the double Mach reflection problem to test the performance of the proposed moment limiter in the presence of strong discontinuities. The initial set-up for the problem is taken from [25] and shown in Figure 2.22. The computational domain $[0, 3.5] \times [0, 1]$ is initially discretized into $1,953$ triangles. The initial condition consists of a Mach 10 shock wave impinging at a 60° angle on a reflecting wall. The states to the left ($\mathbf{U}_l$) and to the right ($\mathbf{U}_r$) of the shock wave are given in Table 2.6. The simulation is run until $t = 0.2$ with the mesh refined every 10 timesteps. The maximum level of refinement is set at seven. Figure 2.23 shows density isolines obtained at $t = 0.2$ on a final mesh of $151,371$ triangles.

	$\mathbf{U}_l$	$\mathbf{U}_r$
ρ	8	1.4
$s = \mathbf{v} \cdot \mathbf{n}$	8.25	0
p	116.5	1

Table 2.6: States to the left and right of the initial shock for the double Mach test case.

We can observe the well-resolved shock structure (Figure 2.23a) as well as the vortices near the slip line (Figure 2.24a).

Next, we perform a wall clock study to compare the performance of the proposed moment limiter and the vertex neighborhood limiter [22] with respect to the computational cost involved. The results of the study are shown in Tables 2.7 and 2.8. We observe that although the cost associated with setting up the reconstruction neighborhood is higher for the moment limiter, the limiting time for the moment limiter is less than 30% of the limiting time for the vertex neighborhood limiter, thereby offsetting the additional set-up costs.

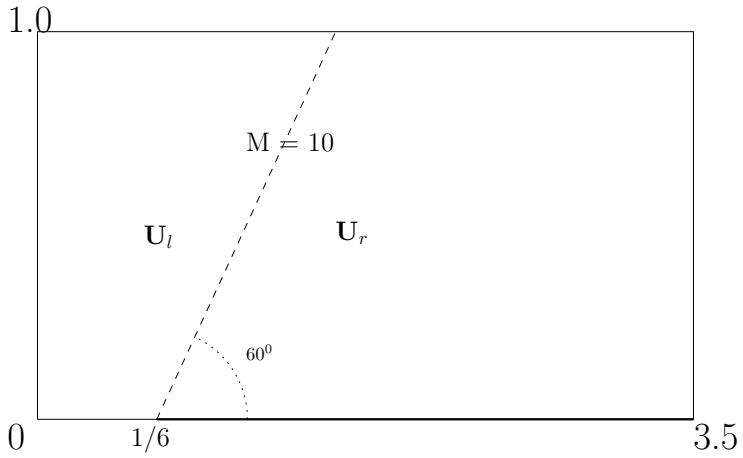

Figure 2.22: The initial set-up for the double Mach reflection test case.

(a) Density isolines.

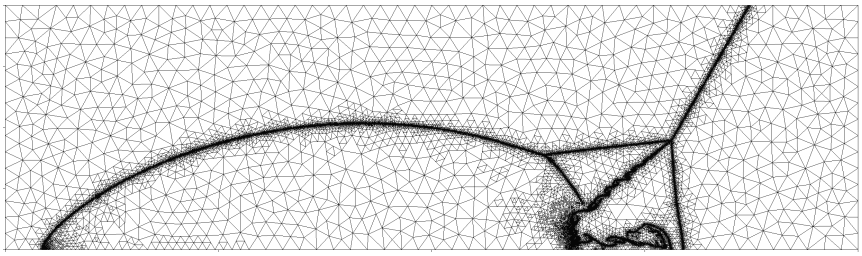

(b) Final adaptively refined mesh.

Figure 2.23: Density isolines at $t = 0.2$ for the double Mach test case obtained using a second order approximation with moment limiter on a final mesh of $156,114$ triangles.

2.3.6 Shock-vortex interaction.

Finally, we solve the shock-vortex interaction test case to analyze the performance of the proposed limiter for problems with smooth flow features as well as discontinuities. The test case involves interaction of two vortices of strength $M_v = 0.9$ with a stationary shock of strength $M_s = 1.5$, as they pass through it. The set-up for the problem (Figure

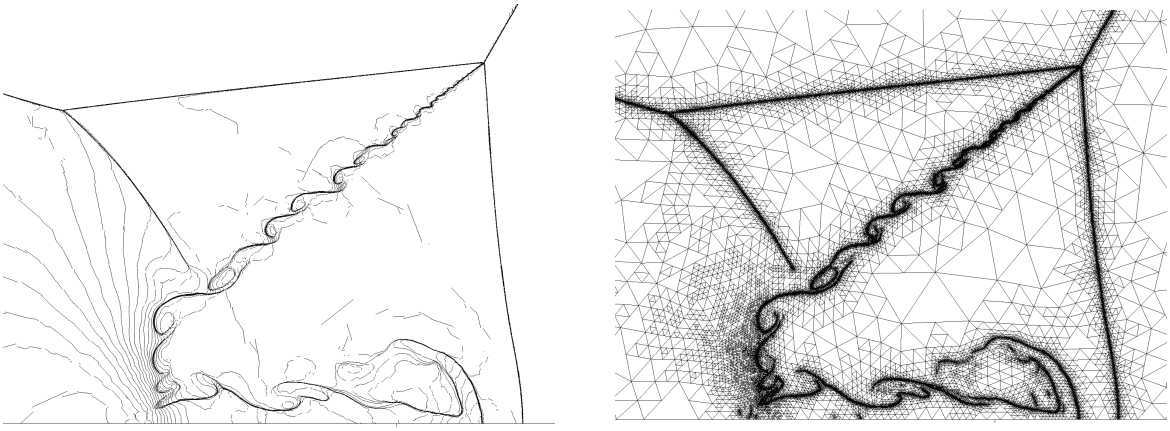

(a) Zoom in near slipline.

(b) Final adaptively refined mesh.

Figure 2.24: Density isolines at $t = 0.2$ for the double Mach test case obtained using a second order approximation with moment limiter, on a final mesh of $156,114$ triangles.

	Moment limiter	Vertex neighborhood limiter
Total run time (s)	733.88	992.15
Limiting time (s)	40.35	174.77
Setting up neighborhood (s)	11.9	4.45
Total limiting time (s)	52.25	179.22

Table 2.7: Wall clock timings (seconds) for the double Mach test case run until $t = 0.2$ using a second order approximation on an initial unstructured mesh of $1,953$ triangles with the mesh refined every 10 timesteps, and the maximum level of refinement set at seven.

	Moment limiter	Vertex neighborhood limiter
Total run time (s)	800.86	1031.84
Limiting time (s)	37.94	157.53
Setting up neighborhood (s)	33.56	13.23
Total limiting time (s)	71.5	170.76

Table 2.8: Wall clock timings (seconds) for the double Mach test case run until $t = 0.2$ using a second order approximation on an initial unstructured mesh of $1,953$ triangles with the mesh refined every 2 timesteps, and the maximum level of refinement set at seven.

2.25) is a modification of the one in [52]. The vortices are initially placed at $(0.25, 0.25)$ and $(0.25, 0.75)$, while the shock is located at $x = 0.5$. The upstream conditions are

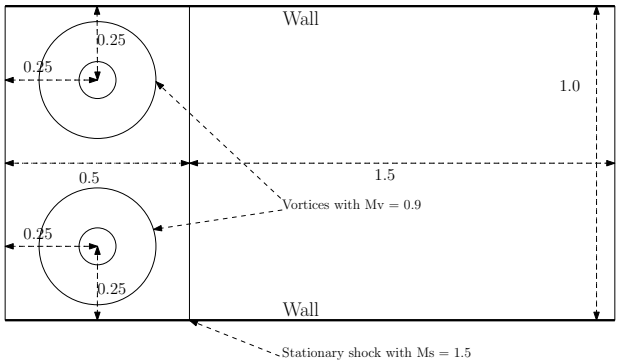

Figure 2.25: Initial set-up for the shock vortex test case.

$(\rho_u, u_u, v_u, p_u) = (1, \sqrt{1.4}M_s, 0, 1)$ and the vortices rotate with an angular velocity

$$\omega = \begin{cases} \omega_m \dfrac{r}{a}, & r \le a, \\ \omega_m \dfrac{a}{a^2 - b^2}\left(r - \dfrac{b^2}{r}\right), & a \le r \le b, \\ 0, & r \ge b, \end{cases} \tag{2.37}$$

where r is the radial distance from the center of the vortex, $\omega_m = \sqrt{1.4}M_v$ is the maximum angular velocity, and $(a, b) = (0.075, 0.175)$. The density and pressure inside the vortices are

$$\rho = \rho_u \left(\frac{T}{T_u}\right)^{2.5}, \quad p = p_u \left(\frac{T}{T_u}\right)^{3.5}, \tag{2.38}$$

where $T_u = 1$ is the upstream temperature and the temperature of the vortices can be obtained by solving

$$\frac{dT}{dr} = \frac{2}{7}\frac{\omega^2}{r}, \tag{2.39}$$

where r is the radial distance from the center of the vortex. The domain is initially discretized into $5,212$ triangles. The simulation is run until $t = 0.7$ with the mesh adaptively refined every 5 timesteps and the maximum level of refinement set at six.

Figure 2.26 shows density isolines at $t = 0.7$ obtained using second order discretization with moment limiter on the final adaptively refined mesh. We observe that the shock structure and compression waves are sharp and well-defined. Further, as the vortex passes through the stationary shock, it splits into two vortices. From Figure 2.26a we see that vortex splitting is captured and the vortices are well resolved.

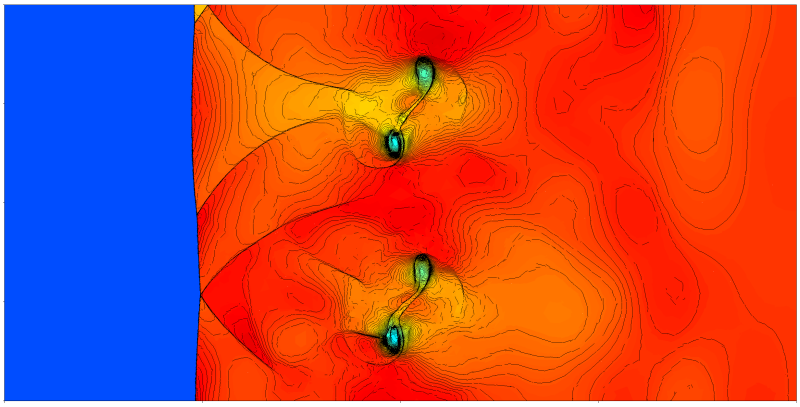

(a) Density isolines.

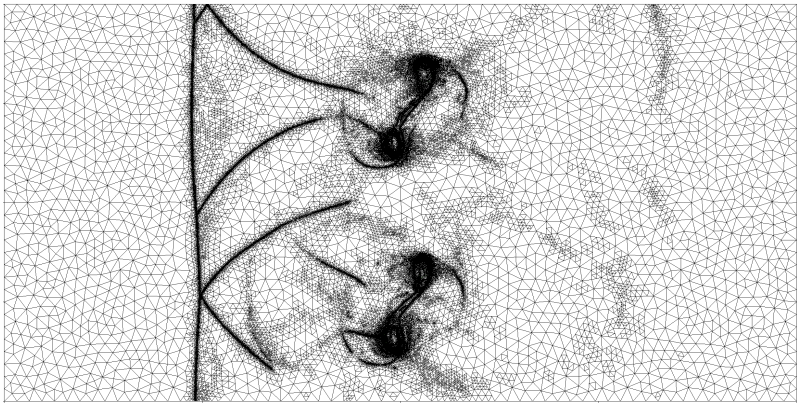

(b) Final adaptivley refined mesh.

Figure 2.26: Density isolines at $t = 0.7$ for the shock vortex test case, obtained using a second order approximation and moment limiter on a final mesh of $181,057$ triangles.

2.4 Summary

In this work, we have described a family of second order moment limiters for the discontinuous Galerkin method on adaptively refined nonconforming triangular meshes. The limiter works by decoupling the linear solution coefficients along two directions and restricting the slopes along said directions using a one-dimensional limiter. The limiter uses solution averages from a compact reconstruction stencil consisting of eight elements. The limiter is an extension of the second order moment limiter proposed in [2] for conforming triangular meshes. Extension of the limiter to nonconforming meshes is not straightforward as a triangular element in the mesh can share an edge with more than one element. We have proposed a simple algorithm, implemented entirely on a GPU, to update the recon-

struction neighborhood of elements in an adaptively refined mesh. The algorithm involves maintaining a database of vertices in the mesh and updating the vertex to element and element to vertex connectivity with every refinement cycle. As every element is uniquely identified in the database, the algorithm avoids race conditions when implemented on a GPU.

The numerical experiments provided in Section 2.3 validate the robustness and accuracy of the proposed limiter. Finally, the performed wall clock timing studies confirm the advantage of using the presented moment limiter over the vertex neighborhood limiter proposed in [22] with respect to the computational cost involved in executing the limiters.

Chapter 3

High-order moment limiter on unstructured triangular meshes

In this chapter, we describe an arbitrarily high-order moment limiter for the DG method on unstructured triangular meshes. The limiter can be viewed as an extension of the second order limiter proposed in [2] to higher order approximations and an extension of the high-order moment limiter on Cartesian grids [25] to triangular meshes. The proposed limiter works by computing directional derivatives of the numerical solution in two specially chosen directions (Figure 3.1). These values are limited by comparing them to approximations computed as forward and backward differences of the directional derivatives of one order less. The limited directional derivatives are then related to the solution coefficients.

The limiter is applied hierarchically, starting with the highest order solution coefficients. That is, the limiter is first applied to the $p+1$ degrees of freedom corresponding to basis functions of degree p. If one or all of these coefficients is modified, the limiter is applied to the coefficients corresponding to the basis functions of degree $p-1$. This process continues until either all non-zero order coefficients are limited or we encounter coefficients that are not altered by the limiter.

The limiter is very simple to implement as it operates on a small, fixed stencil of eight elements for all orders of approximation. This stencil is computed in the pre-processing stage and stored. We also precompute [53] and store geometrical constants involved in the limiting algorithm. For each directional derivative of the solution, the limiter is written as a standard minmod function. The values used by the minmod are given by simple formulas involving solution coefficients and precomputed constants. The limiter is parameter free in the sense that no parameter needs to be fine-tuned. However, there is a range of values for the parameter that describes how we relate a solution derivative to finite differences of lower order derivatives. This is similar to the range of stable slopes in the Sweby region

[6]. We use the value of this parameter used on Cartesian grids in [25].

Since the limiter acts directly on solution coefficients (moments), it does not require costly solution evaluations at limiting points. Choosing to limit in fixed directions in the computational space as opposed to fixed directions in the physical space also leads to computational savings. This is because the solution is defined in the computational space, hence its derivatives have a simple form in there. As a result, the limiter takes only about fifteen percent of total computing time in a parallel implementation [54] for the modal discontinuous Galerkin method.

3.1 Limiting algorithm

We aim to limit directional derivatives of the numerical solution by comparing them to the forward and backward differences of derivatives of one order less. In the following section we derive expressions for directional derivatives of U_i in the physical and computational spaces. The moment limiter is then presented in Section 3.1.2 for an arbitrary order of approximation p. A detailed derivation of the limiter for the $p = 2$ approximation follows in Section 3.1.3.

3.1.1 Directional derivatives

Consider directions given by the vectors

$$v_1 = \frac{2}{\sqrt{5}}(1, -1/2), \quad v_2 = (0, 1), \tag{3.1}$$

on Ω_0 (Figure 3.1). It was shown in [2] that the first order directional derivatives in directions (3.1) uncouple solution coefficients. This lead to development of the second order moment limiter on triangular meshes. While higher order solution coefficients cannot be fully uncoupled, these directions significantly simplify relations between solution coefficients and solution derivatives.

Denote jth directional derivatives along these directions by

$$D^q_{v_1} D^{j-q}_{v_2} U_i(\mathbf{r}) = \frac{\partial^j}{\partial v_1^q \partial v_2^{j-q}} U_i(\mathbf{r}), \quad 0 \le q \le j, \tag{3.2}$$

where $\mathbf{r} = (r, s)$. In order to evaluate (3.2) at the cell centroid of Ω_0, $\mathbf{r}_0 = (\frac{1}{3}, \frac{1}{3})$, we parameterize two lines passing through $\mathbf{r}_0$ and having directions (3.1). We introduce the

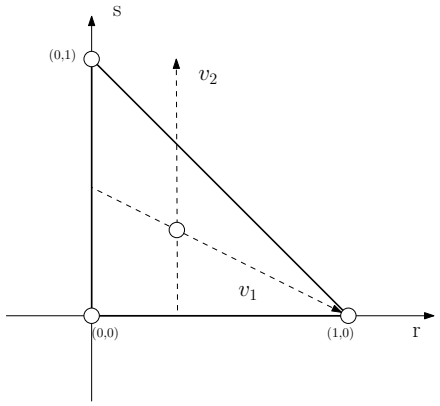

Figure 3.1: Limiting directions v_1 and v_2 on the canonical element Ω_0.

new variables $b = \dfrac{2s}{1-r} - 1$ and $a = r$ and note that $b = 0$ and $a = \frac{1}{3}$ are equations of these two lines (Figure 3.1). Computing directional derivatives (3.2) of the Dubiner polynomials (1.14) results in

$$\begin{aligned}\left(\frac{\sqrt{5}}{2}\right)^q D_{v_1}^q D_{v_2}^{j-q}\varphi_k^l(r,s)\Big|_{(\frac{1}{3},\frac{1}{3})} &= \frac{\partial^q}{\partial a^q}\left(\left(\frac{2}{1-a}\right)^{j-q}\frac{\partial^{j-q}}{\partial b^{j-q}}\varphi_k^l(a,b)\right)\Big|_{(\frac{1}{3},0)} \\ &= C_k^l 2^{k+j-q}\frac{\partial^{j-q}}{\partial b^{j-q}}L_k(b)\frac{\partial^q}{\partial a^q}\left((1-a)^{k-j+q}P_l^{2k+1,0}(2a-1)\right)\Big|_{(\frac{1}{3},0)},\end{aligned} \tag{3.3}$$

where $0 \le q \le j$. Since even degree Legendre polynomials are even polynomials and odd degree Legendre polynomials are odd, odd derivatives of even degree Legendre polynomials and even derivatives of odd degree Legendre polynomials evaluated at zero are zero, i.e.,

$$\frac{d^{2n}}{d\xi^{2n}}L_{2k+1}(\xi)\Big|_0 = 0, \quad \frac{d^{2n+1}}{d\xi^{2n+1}}L_{2k}(\xi)\Big|_0 = 0, \quad k,n = 0,1,2,\cdots. \tag{3.4}$$

Setting $j = p$ in (3.3) and using (3.4), we obtain the pth directional derivatives of $U_i(\mathbf{r})$ along v_1 and v_2 evaluated at the cell centroid $\mathbf{r}_0$

$$\begin{aligned} D_{v_2}^p U_i(\mathbf{r}_0) &= \hat{U}_{i,p}^0\left[C_p^0 2^{2p}\frac{d^p}{db^p}L_p(b)\right]\Big|_{(\frac{1}{3},0)}, \\ \left(\frac{\sqrt{5}}{2}\right)D_{v_2}^{p-1}D_{v_1}^1 U_i(\mathbf{r}_0) &= \hat{U}_{i,p-1}^1\left[C_{p-1}^1 2^{2(p-1)}\frac{d^{p-1}}{db^{p-1}}L_{p-1}(b)\frac{d}{da}P_1^{2p-1,0}(2a-1)\right]\Big|_{(\frac{1}{3},0)}, \end{aligned}$$

$$
\begin{aligned}
&\left(\frac{\sqrt{5}}{2}\right)^2 D_{v_2}^{p-2} D_{v_1}^2 U_i(\mathbf{r}_0) = \hat{U}_{i,p-2}^2 \left[C_{p-2}^2 2^{2(p-2)} \frac{d^{p-2}}{db^{p-2}} L_{p-2}(b) \frac{d^2}{da^2} P_2^{2(p-1)-1,0}(2a-1) \right] \Big|_{(\frac{1}{3},0)} \\
&+ \hat{U}_{i,p}^0 \left[C_p^0 2^{2(p-1)} \frac{d^{p-2}}{db^{p-2}} L_p(b) \frac{d^2}{da^2} \left((1-a)^2 P_0^{2p+1,0}(2a-1) \right) \right] \Big|_{(\frac{1}{3},0)}, \\
&\left(\frac{\sqrt{5}}{2}\right)^3 D_{v_2}^{p-3} D_{v_1}^3 U_i(\mathbf{r}_0) = \hat{U}_{i,p-3}^3 \left[C_{p-3}^3 2^{2(p-3)} \frac{d^{p-3}}{db^{p-3}} L_{p-3}(b) \frac{d^3}{da^3} P_3^{2(p-3)+1,0}(2a-1) \right] \Big|_{(\frac{1}{3},0)} \\
&+ \hat{U}_{i,p-1}^1 \left[C_{p-1}^1 2^{2(p-2)} \frac{d^{p-3}}{db^{p-3}} L_{p-1}(b) \frac{d^3}{da^3} \left((1-a)^2 P_1^{2(p-1)+1,0}(2a-1) \right) \right] \Big|_{(\frac{1}{3},0)}, \\
&\vdots \\
&\left(\frac{\sqrt{5}}{2}\right)^p D_{v_1}^p U_i(\mathbf{r}_0) = \hat{U}_{i,0}^p \left[C_0^p \frac{d^p}{da^p} P_p^{1,0}(2a-1) \right] \Big|_{(\frac{1}{3},0)} \\
&+ \hat{U}_{i,2}^{p-2} \left[C_2^{p-2} 2^2 L_2(b) \frac{d^p}{da^p} \left((1-a)^2 P_{p-2}^{2(2)+1,0}(2a-1) \right) \right] \Big|_{(\frac{1}{3},0)} \\
&+ \hat{U}_{i,4}^{p-4} \left[C_4^{p-4} 2^4 L_4(b) \frac{d^p}{da^p} \left((1-a)^4 P_{p-4}^{2(4)+1,0}(2a-1) \right) \right] \Big|_{(\frac{1}{3},0)} \\
&+ \hat{U}_{i,6}^{p-6} \left[C_6^{p-6} 2^6 L_6(b) \frac{d^p}{da^p} \left((1-a)^6 P_{p-6}^{2(6)+1,0}(2a-1) \right) \right] \Big|_{(\frac{1}{3},0)} + \cdots.
\end{aligned} \tag{3.5}
$$

Expressions in (3.5) can be compactly written as

$$
\begin{aligned}
\left(\frac{\sqrt{5}}{2}\right)^q D_{v_2}^{p-q} D_{v_1}^q U_i(\mathbf{r}_0) = \sum_{\gamma=0}^{\lfloor q/2 \rfloor} \hat{U}_{i,p-q+2\gamma}^{q-2\gamma} \Bigg[& C_{p-q+2\gamma}^{q-2\gamma} 2^{2(p-q-\gamma)} \frac{d^{p-q}}{db^{p-q}} L_{p-q+2\gamma}(b) \\
& \frac{d^q}{da^q} \left((1-a)^{2\gamma} P_{q-2\gamma}^{2(p-q+2\gamma)+1,0}(2a-1) \right) \Bigg] \Big|_{(\frac{1}{3},0)}, \quad 0 \le q \le p,
\end{aligned} \tag{3.6}
$$

where $\lfloor \cdot \rfloor$ is the floor function. Denoting the expression in [] by $\theta_{q,q-2\gamma}$, we write (3.6) in

the matrix form

$$\begin{pmatrix} D_{v_2}^{p} U_i(\mathbf{r}_0) \\ \left(\frac{\sqrt{5}}{2}\right) D_{v_2}^{p-1} D_{v_1}^{1} U_i(\mathbf{r}_0) \\ \left(\frac{\sqrt{5}}{2}\right)^2 D_{v_2}^{p-2} D_{v_1}^{2} U_i(\mathbf{r}_0) \\ \left(\frac{\sqrt{5}}{2}\right)^3 D_{v_2}^{p-3} D_{v_1}^{3} U_i(\mathbf{r}_0) \\ \left(\frac{\sqrt{5}}{2}\right)^4 D_{v_2}^{p-4} D_{v_1}^{4} U_i(\mathbf{r}_0) \\ \vdots \\ \left(\frac{\sqrt{5}}{2}\right)^p D_{v_1}^{p} U_i(\mathbf{r}_0) \end{pmatrix} = \begin{bmatrix} \theta_{0,0} & 0 & 0 & 0 & 0 & 0 & 0 & \cdots \\ 0 & \theta_{1,1} & 0 & 0 & 0 & 0 & 0 & \cdots \\ \theta_{2,0} & 0 & \theta_{2,2} & 0 & 0 & 0 & 0 & \cdots \\ 0 & \theta_{3,1} & 0 & \theta_{3,3} & 0 & 0 & 0 & \cdots \\ \theta_{4,0} & 0 & \theta_{4,2} & 0 & \theta_{4,4} & 0 & 0 & \cdots \\ & & & & \vdots & & & \\ & & & & \cdots & \theta_{p,p-2} & 0 & \theta_{p,p} \end{bmatrix} \begin{pmatrix} \hat{U}_{i,p}^{0} \\ \hat{U}_{i,p-1}^{1} \\ \hat{U}_{i,p-2}^{2} \\ \hat{U}_{i,p-3}^{3} \\ \hat{U}_{i,p-4}^{4} \\ \vdots \\ \hat{U}_{i,0}^{p} \end{pmatrix}. \tag{3.7}$$

Similarly, the jth directional derivatives of $U_i(\mathbf{r})$, $1 \le j \le p$, along v_1 and v_2 evaluated at $\mathbf{r}_0$ are

$$\begin{aligned} \left(\frac{\sqrt{5}}{2}\right)^q D_{v_2}^{j-q} D_{v_1}^{q} U_i(\mathbf{r}_0) = \sum_{k=j}^{p} \sum_{\beta=0}^{\lfloor q/2 \rfloor} \hat{U}_{i,k-q+2\beta}^{q-2\beta} \Bigg[C_{k-q+2\beta}^{q-2\beta} 2^{k+j-2q+2\beta} \frac{d^{j-q}}{db^{j-q}} L_{k-q+2\beta}(b) \\ \frac{d^q}{da^q} \left((1-a)^{k-j+2\beta} P_{q-2\beta}^{2(k-q+2\beta)+1,0}(2a-1) \right) \Bigg] \Bigg|_{(\frac{1}{3},0)}, \quad 0 \le q \le j. \end{aligned} \tag{3.8}$$

Next, we use (1.12) for element Ω_i to map the directions v_1 and v_2 defined in (3.1) from the computational to physical space and obtain the following unit vectors (after normalization)

$$\mathbf{v}_{i,1} = \frac{J_i v_1}{\|J_i v_1\|}, \quad \mathbf{v}_{i,2} = \frac{J_i v_2}{\|J_i v_2\|}, \tag{3.9}$$

where J_i is given by (1.13). Using (1.12), (1.13), and (3.1), (3.9) can be simplified to

$$\mathbf{v}_{i,1} = \frac{1}{h_{i,1}} \left(\mathbf{x}_{i,2} - \frac{1}{2}(\mathbf{x}_{i,1} + \mathbf{x}_{i,3}) \right), \quad \mathbf{v}_{i,2} = \frac{1}{h_{i,2}} \left(\mathbf{x}_{i,3} - \mathbf{x}_{i,1} \right), \tag{3.10}$$

where $\mathbf{x}_{i,k},\ k = \{1,2,3\}$ are the vertices of Ω_i and

$$h_{i,1} = \left\| \mathbf{x}_{i,2} - \frac{1}{2}(\mathbf{x}_{i,1} + \mathbf{x}_{i,3}) \right\|, \quad h_{i,2} = \|\mathbf{x}_{i,3} - \mathbf{x}_{i,1}\|. \tag{3.11}$$

Using (1.12), (1.13), and (3.9), we relate directional derivatives in the physical and computational spaces:

$$D^q_{\mathbf{v}_{i,1}} D^{j-q}_{\mathbf{v}_{i,2}} U_i(\mathbf{x}) = \left(\frac{\sqrt{5}}{2h_{i,1}}\right)^q \left(\frac{1}{h_{i,2}}\right)^{j-q} D^q_{v_1} D^{j-q}_{v_2} U_i(\mathbf{r}), \quad 0 \le q \le j, \quad 1 \le j \le p. \tag{3.12}$$

In the next section, we will derive an algorithm for limiting $D^q_{\mathbf{v}_{i,1}} D^{j-q}_{\mathbf{v}_{i,2}} U_i(\mathbf{x}_0)$.

Remark 1. The process outlined above can be used to compute directional derivatives in any given directions. The advantage of using directions (3.1) is sparsity of the matrix in (3.7).

Remark 2. It can be shown that there are no directions that fully uncouple all directional derivatives, i.e., result in a diagonal matrix in (3.7).

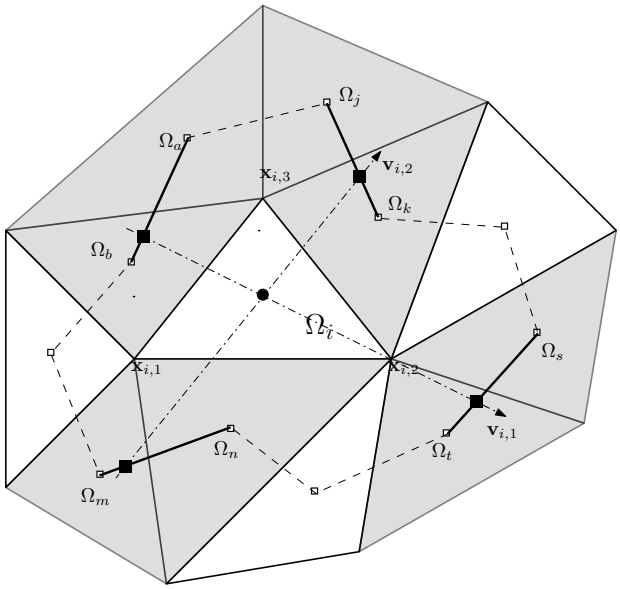

Figure 3.2: Ω_i and the mesh elements sharing a vertex with it. Elements used in limiting are shaded. Limiting directions $\mathbf{v}_{i,1}$ and $\mathbf{v}_{i,2}$ are shown as arrows. Backward and forward interpolation points are shown as solid squares. Linear interpolation of directional derivatives at the interpolation points is performed over the segments shown as thick lines.

3.1.2 Derivation of the moment limiter

We start the limiting process with the highest order solution coefficients $\hat{U}^0_{i,p}, \hat{U}^1_{i,p-1}, ..., \hat{U}^p_{i,0}$ and corresponding directional derivatives. We present the algorithm on an example of limiting on the pth order directional derivative $D^{p-1}_{\mathbf{v}_{i,1}} D^1_{\mathbf{v}_{i,2}} U_i$. We limit $D^{p-1}_{\mathbf{v}_{i,1}} D^1_{\mathbf{v}_{i,2}} U_i$ by comparing its value at the cell centroid of Ω_i to the forward and backward differences of $D^{p-1}_{\mathbf{v}_{i,1}} U$ along $\mathbf{v}_{i,2}$ and $D^{p-2}_{\mathbf{v}_{i,1}} D^1_{\mathbf{v}_{i,2}} U$ along $\mathbf{v}_{i,1}$, i.e., the derivatives of one degree less in $\mathbf{v}_{i,2}$ or $\mathbf{v}_{i,1}$ direction, respectively.

The forward and backward differences are computed from the forward $\mathbf{x}^f_{i,1}$ and $\mathbf{x}^f_{i,2}$, and backward $\mathbf{x}^b_{i,1}$ and $\mathbf{x}^b_{i,2}$ interpolation points (Figure 3.2, solid squares) to the cell centroid (Figure 3.2, solid circle). We find these points by forming a polygon by joining the cell centroids of the neighboring elements that share a vertex with Ω_i. Next, we define two lines parallel to $\mathbf{v}_{i,1}$ and $\mathbf{v}_{i,2}$ that pass through the centroid of Ω_i. The interpolation points $\mathbf{x}^f_{i,k}$, $\mathbf{x}^b_{i,k}$, $k = 1, 2$, are then the points of intersection of these lines and the faces of the polygon.

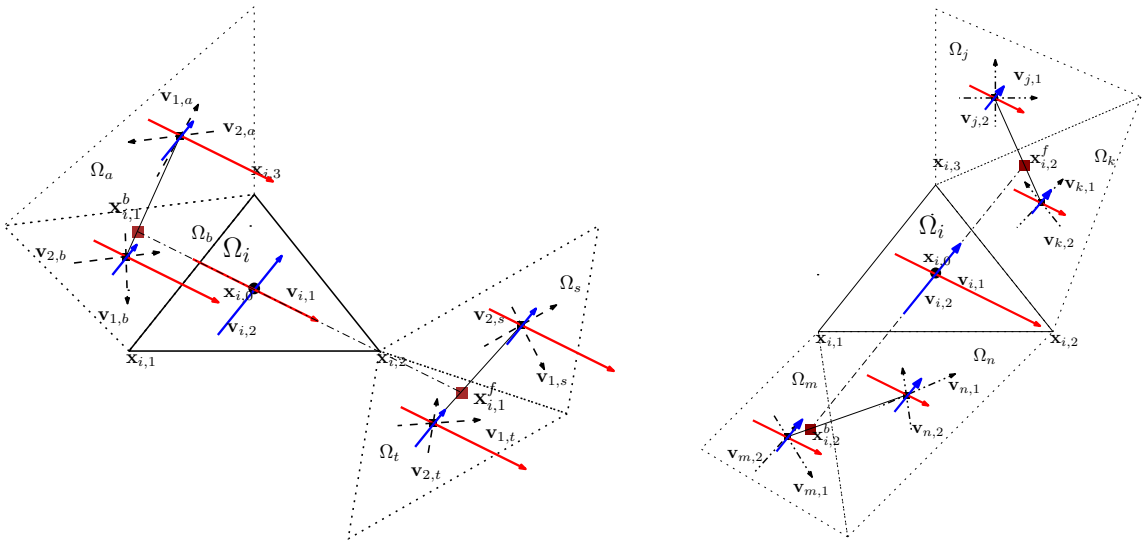

Figure 3.3: (A) Limiting stencil along $\mathbf{v}_{i,1}$, (B) Limiting stencil along $\mathbf{v}_{i,2}$.

Let us consider limiting $D^{p-1}_{\mathbf{v}_{i,1}} D^1_{\mathbf{v}_{i,2}} U_i$ in the direction $\mathbf{v}_{i,2}$. In order to find the values of the $(p-1)$th order derivative $D^{p-1}_{\mathbf{v}_{i,1}} U$ at the interpolation points, we first compute the $(p-1)$th directional derivative $D^{p-1}_{\mathbf{v}_{i,1}} U_f(\mathbf{x}_{f,0}), f = \{j, k, m, n\}$ at the cell centroids of the neighbouring elements Ω_j, Ω_k, Ω_m, and Ω_n (Figure 3.3b). Consider for example element Ω_m. In general, limiting directions $\mathbf{v}_{m,1}$ and $\mathbf{v}_{m,2}$ on Ω_m will not coincide with $\mathbf{v}_{i,1}$ and $\mathbf{v}_{i,2}$

on Ω_i. To obtain directional derivatives in the directions $\mathbf{v}_{i,1}$ and $\mathbf{v}_{i,2}$ on Ω_m, we express directions on Ω_i as linear combinations of directions on Ω_m

$$\mathbf{v}_{i,1} = \alpha^1_{m,1}\mathbf{v}_{m,1} + \alpha^1_{m,2}\mathbf{v}_{m,2}, \quad \mathbf{v}_{i,2} = \alpha^2_{m,1}\mathbf{v}_{m,1} + \alpha^2_{m,2}\mathbf{v}_{m,2}, \tag{3.13}$$

for some coefficients α. Using (3.13) and (3.12), the $(p-1)$th directional derivative $D^{p-1}_{\mathbf{v}_{i,1}}U_m$, evaluated at the cell centroid $\mathbf{x}_{m,0}$ of Ω_m, is

$$\begin{aligned} D^{p-1}_{\mathbf{v}_{i,1}}U_m(\mathbf{x}_{m,0}) &= \left(\alpha^1_{m,1}D_{\mathbf{v}_{m,1}} + \alpha^1_{m,2}D_{\mathbf{v}_{m,2}}\right)^{p-1} U_m(\mathbf{x}_{m,0}) \\ &= \left(\alpha^1_{m,1}\frac{\sqrt{5}}{2h_{m,1}}D_{v_1} + \alpha^1_{m,2}\frac{1}{h_{m,2}}D_{v_2}\right)^{p-1} U_m(\mathbf{r}_0). \end{aligned} \tag{3.14}$$

Similarly, we can compute the $(p-1)$th directional derivatives $D^{p-1}_{\mathbf{v}_{i,1}}U_j(\mathbf{x}_{j,0})$, $D^{p-1}_{\mathbf{v}_{i,1}}U_k(\mathbf{x}_{k,0})$, and $D^{p-1}_{\mathbf{v}_{i,1}}U_n(\mathbf{x}_{n,0})$ at the centroids of Ω_j, Ω_k, and Ω_n (Figure 3.3b). We use these values to linearly interpolate the forward and backward reconstructions of the $(p-1)$th directional derivatives $D^{p-1}_{\mathbf{v}_{i,1}}U^b_{i,2}$ and $D^{p-1}_{\mathbf{v}_{i,1}}U^f_{i,2}$ at the backward and forward interpolation points $\mathbf{x}^b_{i,2}$ and $\mathbf{x}^f_{i,2}$ as

$$\begin{aligned} D^{p-1}_{\mathbf{v}_{i,1}}U^f_{i,2} &= \beta^f_{i,2}D^{p-1}_{\mathbf{v}_{i,1}}U_j(\mathbf{x}_{j,0}) + (1-\beta^f_{i,2})D^{p-1}_{\mathbf{v}_{i,1}}U_k(\mathbf{x}_{k,0}), \\ D^{p-1}_{\mathbf{v}_{i,1}}U^b_{i,2} &= \beta^b_{i,2}D^{p-1}_{\mathbf{v}_{i,1}}U_m(\mathbf{x}_{m,0}) + (1-\beta^b_{i,2})D^{p-1}_{\mathbf{v}_{i,1}}U_n(\mathbf{x}_{n,0}), \end{aligned} \tag{3.15}$$

where $0 \le \beta^b_{i,2} \le 1$ and $0 \le \beta^f_{i,2} \le 1$ are the backward and forward interpolation weights for the limiting stencil in Figure 3.3b. That is, $D^{p-1}_{\mathbf{v}_{i,1}}U^f_{i,2}$ is the weighted average of $D^{p-1}_{\mathbf{v}_{i,1}}U_j(\mathbf{x}_{j,0})$ and $D^{p-1}_{\mathbf{v}_{i,1}}U_k(\mathbf{x}_{k,0})$, where $\beta^f_{i,2}$ is

$$\beta^f_{i,2} = \frac{\left\|\mathbf{x}_{k,0} - \mathbf{x}^f_{i,2}\right\|}{\left\|\mathbf{x}_{j,0} - \mathbf{x}_{k,0}\right\|}. \tag{3.16}$$

Finally, the limited pth order directional derivative $D^{p-1}_{\mathbf{v}_{i,1}}D^1_{\mathbf{v}_{i,2}}U_i$ is obtained by comparing its value to the forward and backward differences in the $(p-1)$th directional derivatives multiplied by the scaling parameters $l^f_{i,2}$ and $l^b_{i,2}$

$$\begin{aligned} D^{p-1}_{\mathbf{v}_{i,1}}D^1_{\mathbf{v}_{i,2}}U_i(\mathbf{x}_{i,0}) \leftarrow \operatorname{minmod}\Bigg(& D^{p-1}_{\mathbf{v}_{i,1}}D^1_{\mathbf{v}_{i,2}}U_i(\mathbf{x}_{i,0}), l^f_{i,2}\frac{D^{p-1}_{\mathbf{v}_{i,1}}U^f_{i,2} - D^{p-1}_{\mathbf{v}_{i,1}}U_i(\mathbf{x}_{i,0})}{\left\|\mathbf{x}^f_{i,2} - \mathbf{x}_{i,0}\right\|}, \\ & l^b_{i,2}\frac{D^{p-1}_{\mathbf{v}_{i,1}}U_i(\mathbf{x}_{i,0}) - D^{p-1}_{\mathbf{v}_{i,1}}U^b_{i,2}}{\left\|\mathbf{x}^b_{i,2} - \mathbf{x}_{i,0}\right\|}\Bigg), \end{aligned} \tag{3.17}$$

where the minmod function is

$$\text{minmod}(a,b,c) = \begin{cases} sign(a)\cdot min(|a|,|b|,|c|), & \text{if } sign(a) = sign(b) = sign(c), \\ 0, & \text{otherwise.} \end{cases} \tag{3.18}$$

Next, we limit $D^{p-1}_{\mathbf{v}_{i,1}} D^1_{\mathbf{v}_{i,2}} U_i$ along $\mathbf{v}_{i,1}$. We compute the $(p-1)$th directional derivative $D^{p-2}_{\mathbf{v}_{i,1}} D^1_{\mathbf{v}_{i,2}} U$ at the cell centroids of Ω_a, Ω_b, Ω_s, and Ω_t (Figure 3.3a), e.g. $D^{p-2}_{\mathbf{v}_{i,1}} D^1_{\mathbf{v}_{i,2}} U_s$, evaluated at $\mathbf{x}_{s,0}$, is

$$\begin{aligned} D^{p-2}_{\mathbf{v}_{i,1}} D^1_{\mathbf{v}_{i,2}} U_s(\mathbf{x}_{s,0}) &= \left(\alpha^1_{s,1} D_{\mathbf{v}_{s,1}} + \alpha^1_{s,2} D_{\mathbf{v}_{s,2}}\right)^{p-2} \left(\alpha^2_{s,1} D_{\mathbf{v}_{s,1}} + \alpha^2_{s,2} D_{\mathbf{v}_{s,2}}\right) U_s(\mathbf{x}_{s,0}) \\ &= \left(\alpha^1_{s,1} \frac{\sqrt{5}}{2h_{s,1}} D_{v_1} + \alpha^1_{s,2} \frac{1}{h_{s,2}} D_{v_2}\right)^{p-2} \left(\alpha^2_{s,1} \frac{\sqrt{5}}{2h_{s,1}} D_{v_1} + \alpha^2_{s,2} \frac{1}{h_{s,2}} D_{v_2}\right) U_s(\mathbf{r}_0). \end{aligned} \tag{3.19}$$

Then, we linearly interpolate $D^{p-2}_{\mathbf{v}_{i,1}} D^1_{\mathbf{v}_{i,2}} U$ at the forward and backward interpolation points $\mathbf{x}^f_{i,1}$ and $\mathbf{x}^b_{i,1}$ using the values at the cell centroids

$$\begin{aligned} D^{p-2}_{\mathbf{v}_{i,1}} D^1_{\mathbf{v}_{i,2}} U^f_{i,1} &= \beta^f_{i,1} D^{p-2}_{\mathbf{v}_{i,1}} D^1_{\mathbf{v}_{i,2}} U_s(\mathbf{x}_{s,0}) + (1-\beta^f_{i,1}) D^{p-2}_{\mathbf{v}_{i,1}} D^1_{\mathbf{v}_{i,2}} U_t(\mathbf{x}_{t,0}), \\ D^{p-2}_{\mathbf{v}_{i,1}} D^1_{\mathbf{v}_{i,2}} U^b_{i,1} &= \beta^b_{i,1} D^{p-2}_{\mathbf{v}_{i,1}} D^1_{\mathbf{v}_{i,2}} U_a(\mathbf{x}_{a,0}) + (1-\beta^b_{i,1}) D^{p-2}_{\mathbf{v}_{i,1}} D^1_{\mathbf{v}_{i,2}} U_b(\mathbf{x}_{b,0}), \end{aligned} \tag{3.20}$$

where $0 \le \beta^b_{i,1} \le 1$ and $0 \le \beta^f_{i,1} \le 1$. Finally, we limit $D^{p-1}_{\mathbf{v}_{i,1}} D^1_{\mathbf{v}_{i,2}} U_i$ by comparing it to the forward and backward differences of $D^{p-2}_{\mathbf{v}_{i,1}} D^1_{\mathbf{v}_{i,2}} U$ scaled by the parameters $l^f_{i,1}$ and $l^b_{i,1}$

$$\begin{aligned} D^{p-1}_{\mathbf{v}_{i,1}} D^1_{\mathbf{v}_{i,2}} U_i(\mathbf{x}_{i,0}) \leftarrow \text{minmod}\Bigg(& D^{p-1}_{\mathbf{v}_{i,1}} D^1_{\mathbf{v}_{i,2}} U_i(\mathbf{x}_{i,0}), l^f_{i,1} \frac{D^{p-2}_{\mathbf{v}_{i,1}} D^1_{\mathbf{v}_{i,2}} U^f_{i,1} - D^{p-2}_{\mathbf{v}_{i,1}} D^1_{\mathbf{v}_{i,2}} U_i(\mathbf{x}_{i,0})}{\left\|\mathbf{x}^f_{i,1} - \mathbf{x}_{i,0}\right\|}, \\ & l^b_{i,1} \frac{D^{p-2}_{\mathbf{v}_{i,1}} D^1_{\mathbf{v}_{i,2}} U_i(\mathbf{x}_{i,0}) - D^{p-2}_{\mathbf{v}_{i,1}} D^1_{\mathbf{v}_{i,2}} U^b_{i,1}}{\left\|\mathbf{x}^b_{i,1} - \mathbf{x}_{i,0}\right\|} \Bigg). \end{aligned} \tag{3.21}$$

The scaling parameters $l^f_{i,k}$ and $l^b_{i,k}$, $k = \{1,2\}$, depend on the order of the derivative being limited. For pth order derivatives, the admissible range is

$$\begin{aligned} 1 \le l^f_{i,2} \le \gamma^f_{i,2}(2p-1), \quad 1 \le l^b_{i,2} \le \gamma^b_{i,2}(2p-1), \\ 1 \le l^f_{i,1} \le \gamma^f_{i,1}(2p-1), \quad 1 \le l^b_{i,1} \le \gamma^b_{i,1}(2p-1), \end{aligned} \tag{3.22}$$

which is equivalent to the range for the scaling parameters used on Cartesian grids in [25].

The geometric parameters γ_i in (3.22) are

$$\begin{aligned} \gamma_{i,1}^f &= \frac{\left\|\mathbf{x}_{i,1}^f - \mathbf{x}_{i,0}\right\|}{h_{i,1}}, \quad \gamma_{i,1}^b = \frac{\left\|\mathbf{x}_{i,1}^b - \mathbf{x}_{i,0}\right\|}{h_{i,1}}, \\ \gamma_{i,2}^f &= \frac{\left\|\mathbf{x}_{i,2}^f - \mathbf{x}_{i,0}\right\|}{h_{i,2}}, \quad \gamma_{i,2}^b = \frac{\left\|\mathbf{x}_{i,2}^b - \mathbf{x}_{i,0}\right\|}{h_{i,2}}, \end{aligned} \tag{3.23}$$

where $h_{i,1}$ and $h_{i,2}$ are given in (3.11). To minimize loss in accuracy of the solution, in all experiments in Section 3.2 we choose the least restrictive limiter, i.e., the right hand side of the intervals in (3.22).

Remark 3. Directional derivatives $D^j_{\mathbf{v}_{i,1}}U$ and $D^j_{\mathbf{v}_{i,2}}U$, $1 \le j \le p$, are limited only in directions $\mathbf{v}_{i,1}$ and $\mathbf{v}_{i,2}$, respectively. Mixed derivatives are limited in both directions with the smallest of the two limited values taken.

In a similar way, we limit every pth order directional derivative along $\mathbf{v}_{i,1}$ and $\mathbf{v}_{i,2}$. Substituting these limited directional derivatives into (3.7), we obtain the limited pth order moments. If all pth order directional derivatives are modified by the limiter, we repeat the process for the $(p-1)$th order moments $\hat{U}^0_{i,p-1}, \hat{U}^1_{i,p-2}, \cdots, \hat{U}^{p-1}_{i,0}$. We limit the $(p-1)$th directional derivatives along $\mathbf{v}_{i,1}$ and $\mathbf{v}_{i,2}$ by comparing them to the forward and backward differences in $(p-2)$th directional derivatives. We find modified values of $(p-1)$th order moments by substituting the limited $(p-1)$th directional derivatives into a system of equations similar to (3.7), obtained by ignoring the contribution of pth order moments in (3.8). The process is continued until we reach either a set of kth order directional derivatives that are not modified or the zeroth order moment.

3.1.3 Third order limiter

To illustrate implementation of the high-order moment limiter, we give a detailed description for the case $p = 2$ in this section and $p = 3$ in the Appedix A. The third order DG approximation on element Ω_i, written as a linear combination of the Dubiner basis, is

$$U_i(r,s) = \sum_{l+k=0}^{2} \hat{U}^l_{i,k}\varphi^l_k(r,s). \tag{3.24}$$

The quadratic basis functions are given by

$$\begin{aligned}
\varphi_2^0(r,s) &= \frac{3\sqrt{30}}{2}(2s+r-1)^2 - \frac{\sqrt{30}}{2}(1-r)^2,\\
\varphi_1^1(r,s) &= 3\sqrt{2}(2s+r-1)(5r-1),\\
\varphi_0^2(r,s) &= 3\sqrt{6} + 12\sqrt{6}(r-1) + 10\sqrt{6}(r-1)^2,
\end{aligned} \tag{3.25}$$

and the linear and constant basis functions are given by

$$\begin{aligned}
\varphi_0^0(r,s) &= \sqrt{2},\\
\varphi_0^1(r,s) &= -2 + 6r,\\
\varphi_1^0(r,s) &= -2\sqrt{3} + 2\sqrt{3}r + 4\sqrt{3}s.
\end{aligned} \tag{3.26}$$

Using (3.5) and (3.7), the second order moments of U_i can be expressed in terms of the second order directional derivatives along $\mathbf{v}_{i,1}$ and $\mathbf{v}_{i,2}$ as

$$\begin{pmatrix} h_{i,2}^2 D_{\mathbf{v}_{i,2}}^2 U_i(\mathbf{x}_{i,0}) \\ h_{i,2}h_{i,1} D_{\mathbf{v}_{i,2}} D_{\mathbf{v}_{i,1}} U_i(\mathbf{x}_{i,0}) \\ h_{i,1}^2 D_{\mathbf{v}_{i,1}}^2 U_i(\mathbf{x}_{i,0}) \end{pmatrix} = \begin{pmatrix} D_{v_2}^2 U_i(\mathbf{r}_0) \\ \left(\frac{\sqrt{5}}{2}\right) D_{v_2}^1 D_{v_1}^1 U_i(\mathbf{r}_0) \\ \left(\frac{\sqrt{5}}{2}\right)^2 D_{v_1}^2 U_i(\mathbf{r}_0) \end{pmatrix} = \begin{bmatrix} 12\sqrt{30} & 0 & 0 \\ 0 & 30\sqrt{2} & 0 \\ -\sqrt{30} & 0 & 20\sqrt{6} \end{bmatrix} \begin{pmatrix} \hat{U}_{i,2}^0 \\ \hat{U}_{i,1}^1 \\ \hat{U}_{i,0}^2 \end{pmatrix}. \tag{3.27}$$

We start by computing the first order directional derivatives along $\mathbf{v}_{i,1}$ and $\mathbf{v}_{i,2}$ at the cell centroids of the elements involved in the limiting stencil (Figures 3.2 and 3.3). For example, to limit $D_{\mathbf{v}_{i,2}}^2 U_i$ and $D_{\mathbf{v}_{i,2}} D_{\mathbf{v}_{i,1}} U_i$, we need to compute directional derivatives along $\mathbf{v}_{i,1}$ and $\mathbf{v}_{i,2}$ at the cell centroids of Ω_j, Ω_k, Ω_m, and Ω_n (Figure 3.3b). Consider element Ω_n. Using (3.8), the first order directional derivatives along $\mathbf{v}_{n,1}$ and $\mathbf{v}_{n,2}$ at the cell centroid $\mathbf{x}_{n,0}$ are

$$\begin{aligned}
h_{n,1} D_{\mathbf{v}_{n,1}}^1 U_n(\mathbf{x}_{n,0}) &= \left(\frac{\sqrt{5}}{2}\right) D_{v_1}^1 U_n(\mathbf{r}_0) = 6\left(\hat{U}_{n,0}^1 + \frac{\sqrt{30}}{9}\hat{U}_{n,2}^0 - \frac{2\sqrt{6}}{9}\hat{U}_{n,0}^2\right),\\
h_{n,2} D_{\mathbf{v}_{n,2}}^1 U_n(\mathbf{x}_{n,0}) &= D_{v_2}^1 U_n(\mathbf{r}_0) = 4\sqrt{3}\left(\hat{U}_{n,1}^0 + \sqrt{\frac{2}{3}}\hat{U}_{n,1}^1\right).
\end{aligned} \tag{3.28}$$

Then, the directional derivatives along $\mathbf{v}_{i,1}$ and $\mathbf{v}_{i,2}$ at $\mathbf{x}_{n,0}$ are computed as

$$\begin{aligned}
D_{\mathbf{v}_{i,1}}^1 U_n &= \alpha_{n,1}^1 D_{\mathbf{v}_{n,1}} U_n + \alpha_{n,2}^1 D_{\mathbf{v}_{n,2}} U_n,\\
D_{\mathbf{v}_{i,2}}^1 U_n &= \alpha_{n,1}^2 D_{\mathbf{v}_{n,1}} U_n + \alpha_{n,2}^2 D_{\mathbf{v}_{n,2}} U_n,
\end{aligned} \tag{3.29}$$

where the coefficients α are obtained from

$$\mathbf{v}_{i,1} = \alpha^1_{n,1}\mathbf{v}_{n,1} + \alpha^1_{n,2}\mathbf{v}_{n,2}, \quad \mathbf{v}_{i,2} = \alpha^2_{n,1}\mathbf{v}_{n,1} + \alpha^2_{n,2}\mathbf{v}_{n,2}. \tag{3.30}$$

In a similar way, the first order directional derivatives along $\mathbf{v}_{i,1}$ and $\mathbf{v}_{i,2}$ are computed at the cell centroids of Ω_j, Ω_k, and Ω_m. The computed values at the cell centroids are used to linearly interpolate the values at the forward and backward interpolation points $\mathbf{x}^f_{i,2}$ and $\mathbf{x}^b_{i,2}$ as

$$\begin{aligned}
D_{\mathbf{v}_{i,1}}U^f_{i,2} &= \beta^f_{i,2}D_{\mathbf{v}_{i,1}}U_j(\mathbf{x}_{j,0}) + (1-\beta^f_{i,2})D_{\mathbf{v}_{i,1}}U_k(\mathbf{x}_{k,0}),\\
D_{\mathbf{v}_{i,1}}U^b_{i,2} &= \beta^b_{i,2}D_{\mathbf{v}_{i,1}}U_m(\mathbf{x}_{m,0}) + (1-\beta^b_{i,2})D_{\mathbf{v}_{i,1}}U_n(\mathbf{x}_{n,0}),\\
D_{\mathbf{v}_{i,2}}U^f_{i,2} &= \beta^f_{i,2}D_{\mathbf{v}_{i,2}}U_j(\mathbf{x}_{j,0}) + (1-\beta^f_{i,2})D_{\mathbf{v}_{i,2}}U_k(\mathbf{x}_{k,0}),\\
D_{\mathbf{v}_{i,2}}U^b_{i,2} &= \beta^b_{i,2}D_{\mathbf{v}_{i,2}}U_m(\mathbf{x}_{m,0}) + (1-\beta^b_{i,2})D_{\mathbf{v}_{i,2}}U_n(\mathbf{x}_{n,0}).
\end{aligned} \tag{3.31}$$

Finally, the directional derivatives $D^2_{\mathbf{v}_{i,2}}U_i$ and $D_{\mathbf{v}_{i,2}}D_{\mathbf{v}_{i,1}}U_i$ are limited by comparing them to the forward and backward differences along $\mathbf{v}_{i,2}$ as

$$\begin{aligned}
D^2_{\mathbf{v}_{i,2}}U_i(\mathbf{x}_{i,0}) \leftarrow \text{minmod}\Bigg(&D^2_{\mathbf{v}_{i,2}}U_i(\mathbf{x}_{i,0}), l^f_{i,2}\frac{D_{\mathbf{v}_{i,2}}U^f_{i,2} - D_{\mathbf{v}_{i,2}}U_i(\mathbf{x}_{i,0})}{\left\|\mathbf{x}^f_{i,2} - \mathbf{x}_{i,0}\right\|},\\
&l^b_{i,2}\frac{D_{\mathbf{v}_{i,2}}U_i(\mathbf{x}_{i,0}) - D_{\mathbf{v}_{i,2}}U^b_{i,2}}{\left\|\mathbf{x}^b_{i,2} - \mathbf{x}_{i,0}\right\|}\Bigg),\\
D_{\mathbf{v}_{i,2}}D_{\mathbf{v}_{i,1}}U_i(\mathbf{x}_{i,0}) \leftarrow \text{minmod}\Bigg(&D_{\mathbf{v}_{i,2}}D_{\mathbf{v}_{i,1}}U_i(\mathbf{x}_{i,0}), l^f_{i,2}\frac{D_{\mathbf{v}_{i,1}}U^f_{i,2} - D_{\mathbf{v}_{i,1}}U_i(\mathbf{x}_{i,0})}{\left\|\mathbf{x}^f_{i,2} - \mathbf{x}_{i,0}\right\|},\\
&l^b_{i,2}\frac{D_{\mathbf{v}_{i,1}}U_i(\mathbf{x}_{i,0}) - D_{\mathbf{v}_{i,1}}U^b_{i,2}}{\left\|\mathbf{x}^b_{i,2} - \mathbf{x}_{i,0}\right\|}\Bigg).
\end{aligned} \tag{3.32}$$

The range for the scaling parameters $l^f_{i,k}$ and $l^b_{i,k}$, $k = \{1,2\}$, is given in (3.22). Similarly, the first order directional derivatives along $\mathbf{v}_{i,1}$ and $\mathbf{v}_{i,2}$ are computed at the cell centroids of Ω_s, Ω_t, Ω_a, and Ω_b (Figure 3.3a), and are used to linearly interpolate the values of the first order directional derivatives at the forward and backward interpolation points $\mathbf{x}^f_{i,1}$ and

$\mathbf{x}^b_{i,1}$ as

$$\begin{aligned}
D_{\mathbf{v}_{i,1}} U^f_{i,1} &= \beta^f_{i,1} D_{\mathbf{v}_{i,1}} U_s(\mathbf{x}_{s,0}) + (1-\beta^f_{i,1}) D_{\mathbf{v}_{i,1}} U_t(\mathbf{x}_{t,0}),\\
D_{\mathbf{v}_{i,1}} U^b_{i,1} &= \beta^b_{i,1} D_{\mathbf{v}_{i,1}} U_a(\mathbf{x}_{a,0}) + (1-\beta^b_{i,1}) D_{\mathbf{v}_{i,1}} U_b(\mathbf{x}_{b,0}),\\
D_{\mathbf{v}_{i,2}} U^f_{i,1} &= \beta^f_{i,1} D_{\mathbf{v}_{i,2}} U_s(\mathbf{x}_{s,0}) + (1-\beta^f_{i,1}) D_{\mathbf{v}_{i,2}} U_t(\mathbf{x}_{t,0}),\\
D_{\mathbf{v}_{i,2}} U^b_{i,1} &= \beta^b_{i,1} D_{\mathbf{v}_{i,2}} U_a(\mathbf{x}_{a,0}) + (1-\beta^b_{i,1}) D_{\mathbf{v}_{i,2}} U_b(\mathbf{x}_{b,0}).
\end{aligned} \tag{3.33}$$

The directional derivatives $D^2_{\mathbf{v}_{i,1}} U_i$ and $D_{\mathbf{v}_{i,1}} D_{\mathbf{v}_{i,2}} U_i$ are limited by comparing them to the forward and backward difference along $\mathbf{v}_{i,1}$ as

$$\begin{aligned}
D^2_{\mathbf{v}_{i,1}} U_i(\mathbf{x}_{i,0}) \leftarrow \operatorname{minmod}\Bigg(& D^2_{\mathbf{v}_{i,1}} U_i(\mathbf{x}_{i,0}), l^f_{i,1} \frac{D_{\mathbf{v}_{i,1}} U^f_{i,1} - D_{\mathbf{v}_{i,1}} U_i(\mathbf{x}_{i,0})}{\left\|\mathbf{x}^f_{i,1} - \mathbf{x}_{i,0}\right\|},\\
& l^b_{i,1} \frac{D_{\mathbf{v}_{i,1}} U_i(\mathbf{x}_{i,0}) - D_{\mathbf{v}_{i,1}} U^b_{i,1}}{\left\|\mathbf{x}^b_{i,1} - \mathbf{x}_{i,0}\right\|} \Bigg),\\
D_{\mathbf{v}_{i,1}} D_{\mathbf{v}_{i,2}} U_i(\mathbf{x}_{i,0}) \leftarrow \operatorname{minmod}\Bigg(& D_{\mathbf{v}_{i,1}} D_{\mathbf{v}_{i,2}} U_i(\mathbf{x}_{i,0}), l^f_{i,1} \frac{D_{\mathbf{v}_{i,2}} U^f_{i,1} - D_{\mathbf{v}_{i,2}} U_i(\mathbf{x}_{i,0})}{\left\|\mathbf{x}^f_{i,1} - \mathbf{x}_{i,0}\right\|},\\
& l^b_{i,1} \frac{D_{\mathbf{v}_{i,2}} U_i(\mathbf{x}_{i,0}) - D_{\mathbf{v}_{i,2}} U^b_{i,1}}{\left\|\mathbf{x}^b_{i,1} - \mathbf{x}_{i,0}\right\|} \Bigg).
\end{aligned} \tag{3.34}$$

Finally, the modified second order moments $\hat{U}^2_{i,0}$, $\hat{U}^1_{i,1}$, and $\hat{U}^0_{i,2}$ are computed by substituting the limited second order directional derivatives $D^2_{\mathbf{v}_{i,1}} U_i$, $D^2_{\mathbf{v}_{i,2}} U_i$, and $D_{\mathbf{v}_{i,1}} D_{\mathbf{v}_{i,2}} U_i$ into (3.27)

$$\begin{aligned}
\hat{U}^0_{i,2} &= \frac{h^2_{i,2}}{12\sqrt{30}} D^2_{\mathbf{v}_{i,2}} U_i,\\
\hat{U}^1_{i,1} &= \frac{h_{i,2} h_{i,1}}{30\sqrt{2}} D_{\mathbf{v}_{i,2}} D_{\mathbf{v}_{i,1}} U_i,\\
\hat{U}^2_{i,0} &= \frac{h^2_{i,1}}{20\sqrt{6}} D^2_{\mathbf{v}_{i,1}} U_i + \frac{h^2_{i,2}}{240\sqrt{6}} D^2_{\mathbf{v}_{i,2}} U_i.
\end{aligned} \tag{3.35}$$

If all second order directional derivatives have been modified by the limiter, then the linear

moments are limited using the second order moment limiter [2]

$$\begin{aligned}\hat{U}^0_{i,1} &\leftarrow \text{minmod}\left(\frac{U^f_{i,1}-\overline{U}_i}{2}, \hat{U}^0_{i,1}, \frac{\overline{U}_i - U^b_{i,1}}{2}\right),\\ \hat{U}^0_{i,2} &\leftarrow \text{minmod}\left(\frac{U^f_{i,2}-\overline{U}_i}{2\sqrt{3}}, \hat{U}^0_{i,2}, \frac{\overline{U}_i - U^b_{i,2}}{2\sqrt{3}}\right),\end{aligned} \tag{3.36}$$

where $\overline{U}^n_i$ is the cell average in Ω_i. The forward and backward interpolation values $U^f_{i,q}$ and $U^b_{i,q}$, $q = \{1,2\}$, are linearly interpolated using the cell averages from respective neighboring elements (Figure 3.2). For example, the forward and backward interpolation values along $\mathbf{v}_{i,2}$ are given by

$$\begin{aligned}U^f_{i,2} &= \beta^f_{i,2}\overline{U}_j + (1-\beta^f_{i,2})\overline{U}_k,\\ U^b_{i,2} &= \beta^b_{i,2}\overline{U}_m + (1-\beta^b_{i,2})\overline{U}_n,\end{aligned} \tag{3.37}$$

with $0 \le \beta^f_{i,2}, \beta^b_{i,2} \le 1$.

3.1.4 Implementation of the moment limiter

The limiter is easy to implement and fast in execution. We pre-compute [53] the limiting stencil for each mesh element (Figures 3.2 and 3.3), i.e., for each Ω_i, we store pointers to the eight mesh elements involved in the limiting stencil. We compute and store the constants α in (3.30) and interpolation weights β in (3.31) and (3.33). For example, with $p = 2$, we

1. Compute higher order derivatives using (3.27).
2. Compute lower order derivatives using (3.28).
3. Compute the directional derivatives along the required direction on neighboring elements using (3.29).
4. Interpolate lower order derivatives at the interpolation points using (3.31) and (3.33).
5. Apply the minmod function.

Each step in the above Algorithm is a set of simple algebraic operations involving the solution coefficients and the pre-computed constants. Consequently, the limiter takes only 15% of the total runtime (Example 3.2.5) in this implementation of the modal discontinuous Galerkin method.

3.2 Numerical Results

We perform numerical experiments to analyze the performance of the proposed high-order moment limiter. We run convergence studies to show that limited solutions exhibit the expected convergence rates. We also present numerical experiments to show robustness of the limiter in the presence of discontinuities. In all presented cases, time-stepping was performed using an explicit Runge-Kutta integrator of order $(p+1)$ with the CFL condition proposed in [50]

$$\begin{aligned} \Delta t &\leq CFL \ \min_i \frac{h_i}{\|\mathbf{a}\|}, \\ CFL &= \frac{1}{(2p+1)\left(1+\frac{4}{(p+2)^2}\right)}, \end{aligned} \tag{3.38}$$

where h_i is the smallest height of element Ω_i (Figure 3.4). Finally, unless stated otherwise, the local Lax-Friedrichs flux was used.

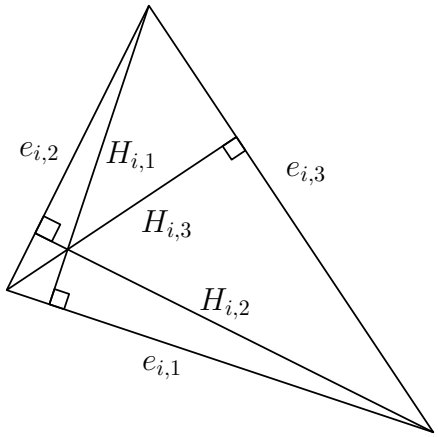

Figure 3.4: Element size $h_i = \min(H_{i,1}, H_{i,2}, H_{i,3})$ [2].

3.2.1 Advecting hill.

We consider the advecting hill problem on the domain $\Omega = [-1,1]\times[-1,1]$, with the flux in (1.8) given by $\mathbf{F} = [u,u]$. The initial condition is $u_0(x,y) = 2.5\exp\left(\frac{-r^2}{2R^2}\right)$, where $R = 0.15$ and $r = \sqrt{(x+0.25)^2+(y+0.25)^2}$. We solve the problem on a sequence of meshes A-E. Mesh A is a coarse unstructured triangular mesh. Meshes B-E are obtained by nested refinement, i.e., each element in a coarser mesh is divided into four new triangles by

connecting the edge midpoints with the centroid to obtain a finer mesh. The L_1 errors and rates of convergence for $p = 2$ and $p = 3$ at $t = 0.5$ are presented in Table 3.1. We observe that limited solutions converge with the theoretical rates. It is expected that a limiter will increase the magnitude of the numerical error. We note that such an increase in the error is modest. Raised solutions for $p = 2$ on meshes A and C are plotted in Figures 3.5a and 3.5b. Additionally, solution profiles along $y = 0.25$ on meshes A-C are shown in Figure 3.5c. We observe that solutions on all but the coarsest mesh approximate the top of the hill well.

Mesh	Nb. elems	L1 error			
		p = 2	p = 2 (unlimited)	p = 3	p = 3 (unlimited)
A	1,046	4.82e-03 (-)	7.86e-04 (-)	4.98e-04 (-)	6.49e-05 (-)
B	4,184	3.70e-04 (3.70)	9.09e-05 (3.11)	1.85e-05 (4.75)	3.81e-06 (4.09)
C	16,736	4.08e-05 (3.18)	1.07e-05 (3.08)	1.06e-06 (4.13)	2.24e-07 (4.09)
D	66,944	4.63e-06 (3.14)	1.29e-06 (3.05)	6.37e-08 (4.06)	1.35e-08 (4.05)
E	267,776	5.72e-07 (3.02)	1.56e-07 (3.047)	3.91e-09 (4.03)	8.23e-10 (4.035)

Table 3.1: L_1 errors for the advecting hill problem for limited and unlimited solutions at $t = 0.5$. Convergence rates are given in parentheses.

3.2.2 Limiting directions.

In this section we investigate how ordering of vertices influences performance of the limiter. Triangle Ω_i is described by its vertices $\mathbf{x}_{i,1}, \mathbf{x}_{i,2}$, and $\mathbf{x}_{i,3}$. Assuming that the vertices are arranged in the counter-clockwise direction, there are three ways to describe Ω_i, i.e., $(\mathbf{x}_{i,1}, \mathbf{x}_{i,2}, \mathbf{x}_{i,3})$, $(\mathbf{x}_{i,2}, \mathbf{x}_{i,3}, \mathbf{x}_{i,1})$, and $(\mathbf{x}_{i,3}, \mathbf{x}_{i,1}, \mathbf{x}_{i,2})$ (Figure 3.6). With mapping (1.12), this results in three possible limiting directions. We analyse the effect of vertex ordering and, hence, limiting directions, on the accuracy of limited solutions. One way to do so is to compare the distances of the points used in reconstructing the forward and backward approximations of solution derivatives from the cell's centroid. For each vertex ordering of Ω_i, we compute the maximum ($\gamma_{i,M}$) and the minimum ($\gamma_{i,m}$) of the geometric parameter γ_i (3.23). Next, we name the vertex ordering with the smallest $\gamma_{i,M}$ on Ω_i Configuration 1, the mesh generator's vertex ordering Configuration 2, and the vertex ordering with the largest $\gamma_{i,m}$ on Ω_i Configuration 3. Tables 3.2 and 3.3 show the solution errors obtained with three configurations for $p = 2$ and $p = 3$ approximations. We note that the stencils with the interpolation points closest to the cell centroid have the smallest errors. However, variation in the errors for the three configurations is not significant. Thus, mesh-generated vertex ordering can be directly used, without any additional pre-processing.

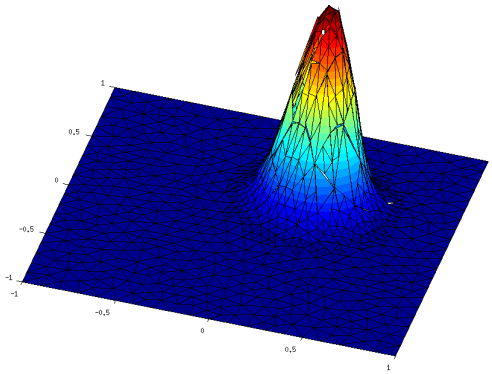

(a) Raised solution on mesh A.

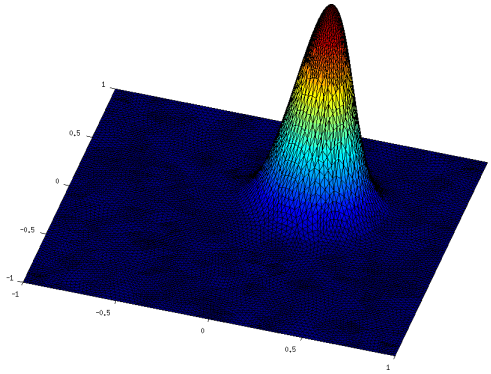

(b) Raised solution on mesh C.

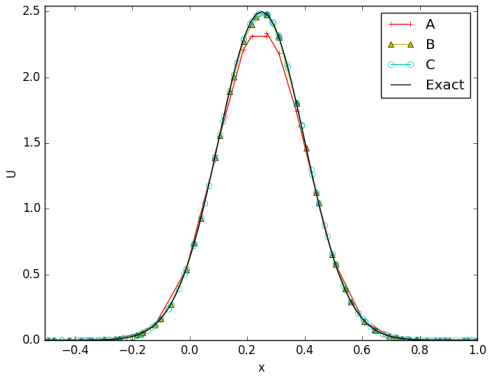

(c) Solution profile along the line $y = 0.25$.

Figure 3.5: Solutions of the advecting hill problem with $p = 2$.

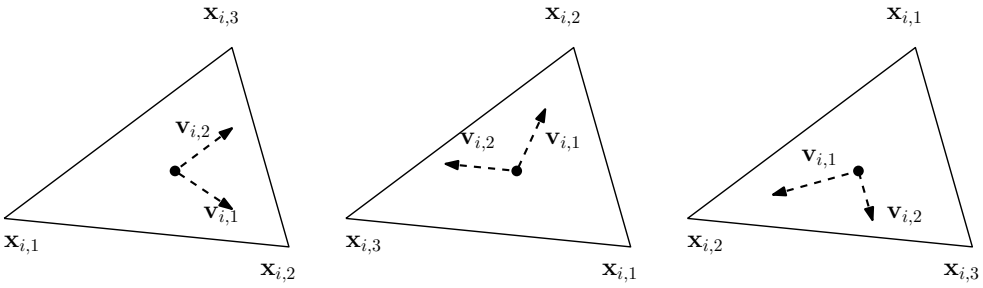

Figure 3.6: Limiting directions on Ω_i.

3.2.3 Rotating shapes.

We solve the rotating shape problem with the flux in (1.8) given by $\mathbf{F} = [-2\pi yu, 2\pi xu]$. The initial condition consists of a hill and a square pulse (Figure 3.7) and is given by

Mesh	Configuration 1	Configuration 2	Configuration 3
A	4.43e-03	4.82e-03	4.14e-03
B	3.54e-04	3.70e-04	3.68e-04
C	3.96e-05	4.08e-05	3.96e-05
D	4.39e-06	4.63e-06	4.45e-06
E	5.37e-07	5.71e-07	5.41e-07

Table 3.2: L_1 errors for the advecting hill problem at $t = 0.5$ with three different vertex ordering, $p = 2$.

Mesh	Configuration 1	Configuration 2	Configuration 3
A	5.08e-04	4.98e-04	4.00e-04
B	1.72e-05	1.85e-05	1.87e-05
C	9.81e-07	1.06e-06	1.05e-06
D	5.78e-08	6.37e-08	6.06e-08
E	3.57e-09	3.91e-09	3.66e-09

Table 3.3: L_1 errors for the advecting hill problem at $t = 0.5$ with three different vertex ordering, $p = 3$.

$$u_0(x, y) = \begin{cases} \cos^2(2\pi r), & \text{if } r \leq 0.25, \\ 1, & \text{if } \max(|x - 0.35|, |y|) \leq 0.25, \\ 0, & \text{otherwise,} \end{cases} \tag{3.39}$$

where $r = \sqrt{(x + 0.5)^2 + y^2}$. The exact solution is a rotation of the initial condition about the origin. The problem is solved until $t = 1$ on an unstructured mesh of $12,792$ triangles.

Figure 3.8 shows the isolines of the solutions and solution profiles along $y = 0$, $x = 0.5$, and $x = 0.55$ obtained using the $p = 1$, $p = 2$, and $p = 3$ approximations with the moment limiter. The quality of the solutions is comparable to solutions on Cartesian meshes with an equivalent number of elements [25]. We observe that the peak of the hill is captured well only by the third and fourth order schemes (Figure 3.8c). This is due to a well known phenomenon of clipping at local extremas by second order limiters. Due to the hierarchical nature of the moment limiter, the second and higher order moments are not limited with the $p = 2$ and $p = 3$ approximations and the accuracy at the peak is preserved. We see that all three limiters suppress oscillations near solution discontinuities. Comparing solution isolines in Figures 3.8a and 3.8b, we note that the higher order approximation of the square pulse is less diffused and more symmetrical. This is further demonstrated in the

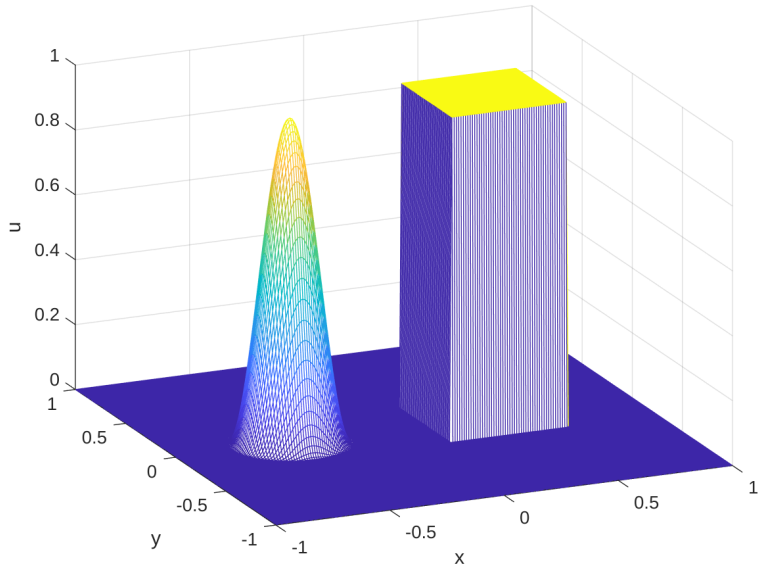

Figure 3.7: Initial condition for the rotating shapes problem.

cross-sections in Figure 3.8e.

Finally, Figure 3.9 shows the isolines of the solutions and solution profiles along $y = 0$, $x = 0.5$, and $x = 0.55$ obtained using the $p = 1$ and $p = 2$ approximations without limiting. We can clearly observe oscillations near the discontinuities for both $p = 1$ and $p = 2$, which are severely affecting the quality of the solution.

3.2.4 Isentropic vortex.

Next, we test the performance of the high-order limiter when applied to a system of nonlinear equations. For this example, we consider the Euler equations, the system of nonlinear hyperbolic conservation law governing inviscid fluid flows, given by

$$\frac{\partial}{\partial t}\begin{pmatrix}\rho\\ \rho u\\ \rho v\\ E\end{pmatrix}+\frac{\partial}{\partial x}\begin{pmatrix}\rho u\\ \rho u^2+p\\ \rho uv\\ (E+p)u\end{pmatrix}+\frac{\partial}{\partial y}\begin{pmatrix}\rho v\\ \rho uv\\ \rho v^2+p\\ (E+p)v\end{pmatrix}=0, \tag{3.40}$$

where ρ is the density, ρu and ρv are the x- and y-direction momenta, E is the energy, and the pressure, p, is given by the equation of state $p = (\gamma-1)\left(E - \frac{\rho}{2}(u^2+v^2)\right)$. We solve the

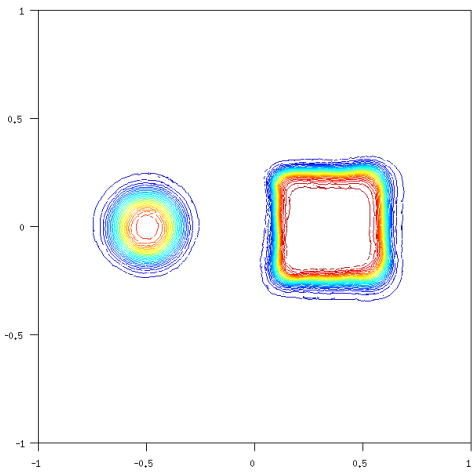

(a) Isolines with second order moment limiter [2].

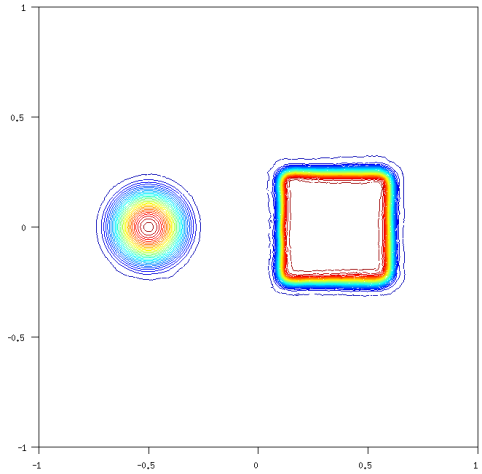

(b) Isolines with third order moment limiter.

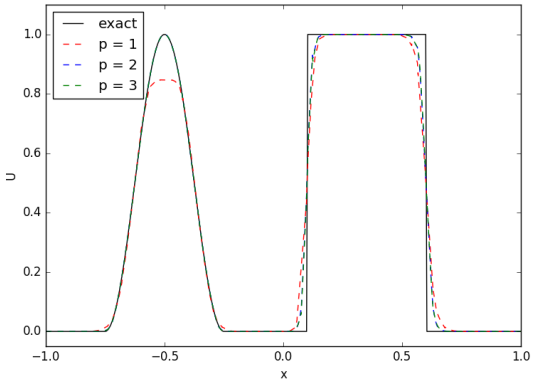

(c) Profile of the solution along $y = 0$.

smooth isentropic vortex problem described in [51] with the initial conditions

$$\rho = \left(1 - \frac{(\gamma-1)}{8\pi^2}(M\beta)^2 e^r\right)^{\frac{1}{\gamma-1}}, \quad p = \frac{\rho^\gamma}{\gamma M^2}, \quad u = \frac{\beta}{2\pi R} y e^{\frac{r}{2}}, \quad v = -\frac{\beta}{2\pi R} x e^{\frac{r}{2}}, \tag{3.41}$$

where $r = \frac{1-(x^2+y^2)}{R^2}$, $R = 1.5$, $\beta = 13.5$, $\gamma = 1.4$, and $M = 0.4$. With these initial conditions, the exact solution is stationary and given by (3.41). The L_1 errors in the density and convergence rates at $t = 0.5$ are reported in Table 3.4 for the $p = 2$ and $p = 3$ discretizations. Similar to the scalar advection case, we see that the high-order moment limiter does not degrade the expected convergence rates.

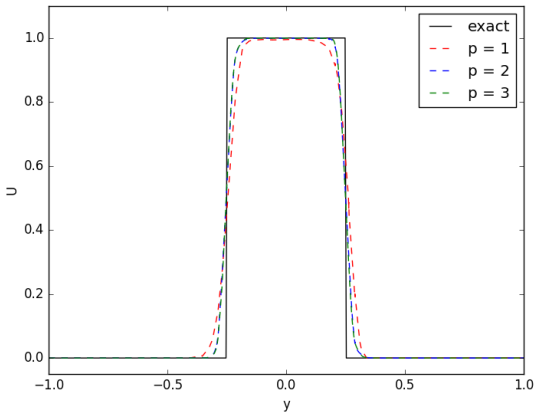

(d) Profile of the solution along $x = 0.5$.

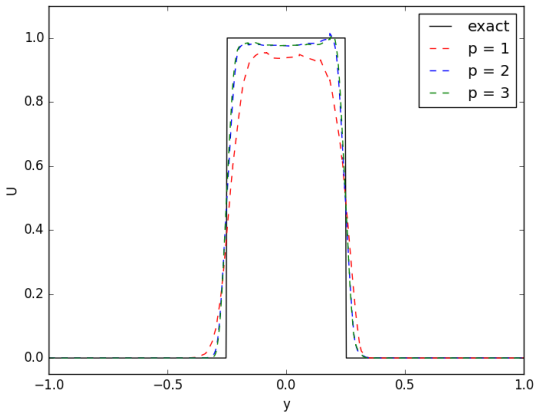

(e) Profile of the solution along $x = 0.55$.

Figure 3.8: Rotating shapes at $t = 1$ on an unstructured mesh of $12,792$ triangles.

Nb. elems	L1 error			
	p = 2	p = 2 (unlimited)	p = 3	p = 3 (unlimited)
1,560	3.37e-03 (-)	3.36e-04 (-)	8.25e-05 (-)	7.36e-06 (-)
6,240	2.44e-04 (3.79)	4.57e-05 (2.89)	5.96e-06 (3.79)	4.24e-07 (4.12)
24,960	3.25e-05 (2.91)	6.11e-06 (2.90)	3.55e-07 (4.07)	2.51e-08 (4.08)
99,840	4.1e-06 (2.99)	8.10e-07 (2.92)	2.24e-08 (3.99)	1.51e-09 (4.06)

Table 3.4: L_1 errors in the density for the isentropic vortex example at $t = 0.5$. Convergence rates are shown in parentheses.

3.2.5 Shock shock interactions.

In this example we test performance of the limiter in the presence of shock-shock interactions. The initial condition is a modification of a test case from the two-dimensional Riemann test suite proposed in [55] (Figure 3.10). The simulation is run until $t = 0.8$ on a mesh of $320,000$ triangles. Figure 3.11 presents density isolines obtained using the $p = 1$, $p = 2$, and $p = 3$ approximations with the moment limiter. We see that the high-order DG method equipped with the moment limiter is able to capture finer flow structures, as well as the shocks.

Finally, we check the computational cost of the limiter. The limiter takes about fifteen percent of the total run time (Table 3.5) of a parallel GPU implementation of the modal discontinuous Galerkin method [54] and this number is about the same for both orders of approximation.

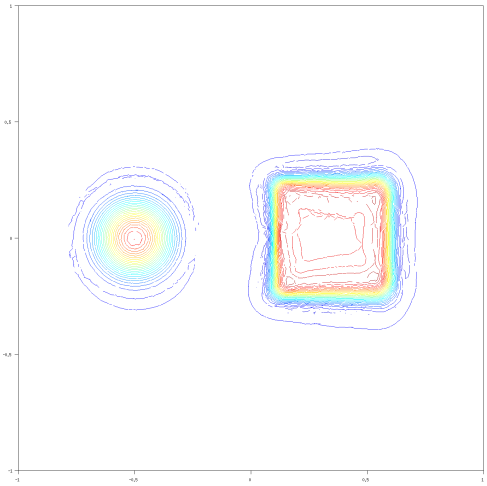

(a) Isolines with $p = 1$.

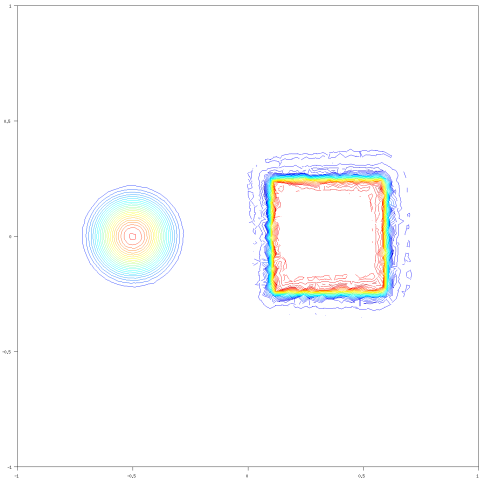

(b) Isolines with $p = 2$.

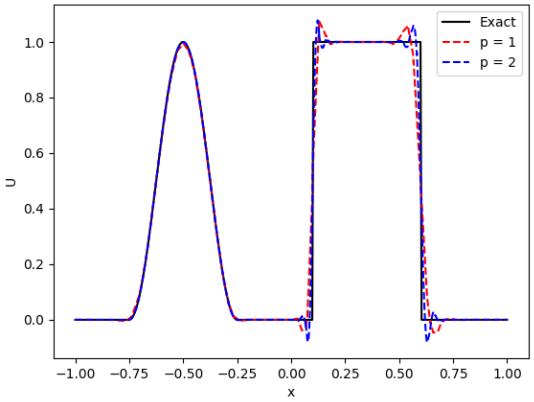

(c) Profile of the solution along $y = 0$.

3.2.6 Double Mach test case.

We solve the double Mach reflection problem to test the performance of the proposed moment limiter in the presence of strong shocks. The initial set-up for the problem is taken from [25] and shown in Figure 3.12. The initial condition consists of a Mach 10 shock wave impinging on a reflecting wall at an angle of 60°. The states to the left ($\mathbf{U}_l$) and to the right ($\mathbf{U}_r$) of the shock wave are given in Table 3.6. The computational domain $[0, 3.5] \times [0, 1]$ is initially discretized into $1,953$ triangles (Figure 3.12a). The simulation is run until $t = 0.2$ with the mesh refined every 10 timesteps. The maximum level of refinement is set as seven. The reconstruction stencil is updated after every refinement using the strategy proposed in [56] and discussed in the previous chapter. Figures 3.13,

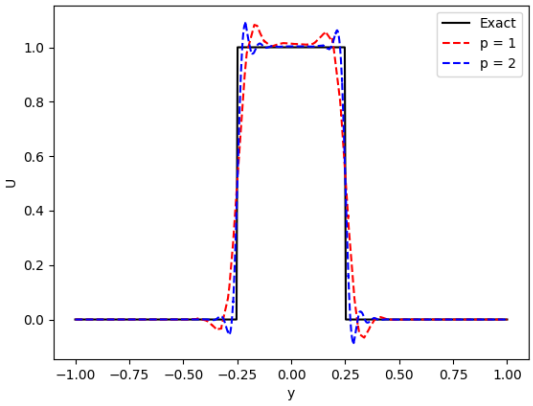

(d) Profile of the solution along $x = 0.5$.

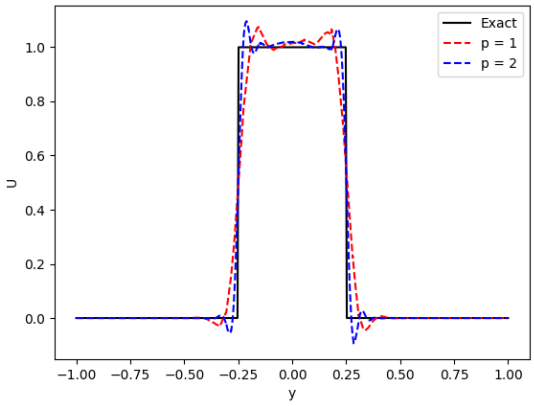

(e) Profile of the solution along $x = 0.55$.

Figure 3.9: Solution of the rotating shapes problem at $t = 1$ without limiting on an unstructured mesh of $12,792$ triangles.

p	Run time (s)	Limiting time (s)	Time steps
2	749.16	115.8(15.5%)	9,751
3	2947.9	427.22(14.5%)	12,876

Table 3.5: Limiting time for the shock-shock interaction example. The limiting time as a percentage of the total run time is given in parenthesis under "Limiting time".

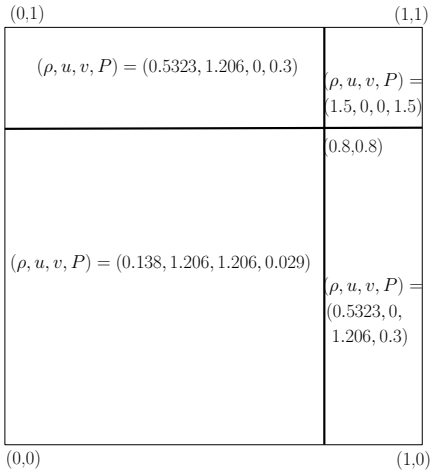

Figure 3.10: Initial condition for the 2D Riemann problem.

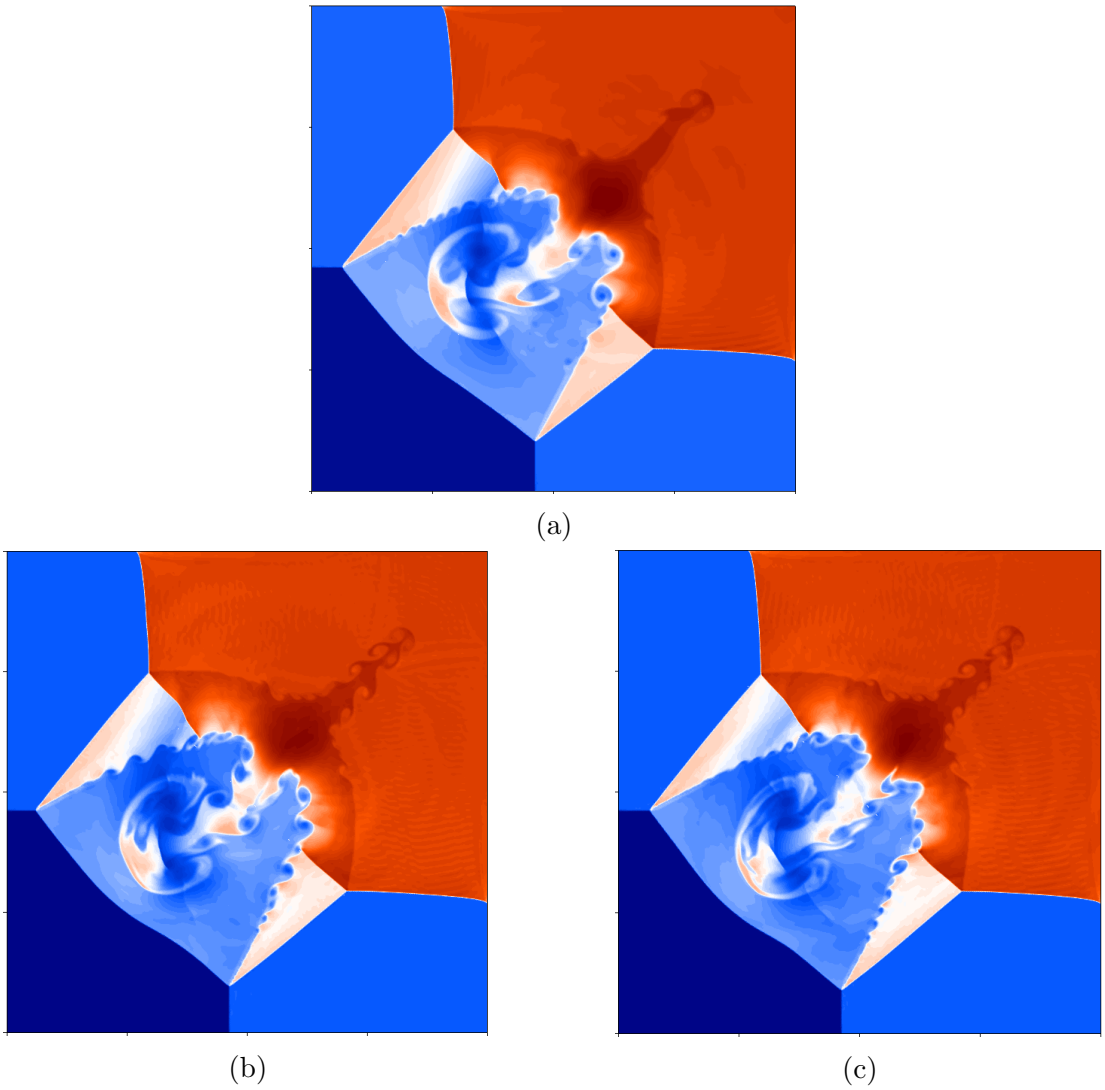

(a)

(b)

(c)

Figure 3.11: Density isolines at $t = 0.8$ for the shock-shock interaction example with (A) $p = 1$, (B) $p = 2$, and (C) $p = 3$, on a mesh of $320,000$ triangles.

3.14, and 3.15 show the density isolines at $t = 0.2$ obtained using second, third, and fourth order DG approximations with the moment limiter.We observe that all DG approximations resolve the shock structures well. We also note that the slip line near the primary triple point is tighter as well as the finer vortical structures are better resolved for the higher order approximation (Figure 3.16).

	$\mathbf{U}_l$	$\mathbf{U}_r$
ρ	8	1.4
$s = \mathbf{v} \cdot \mathbf{n}$	8.25	0
p	116.5	1

Table 3.6: States to the left and right of the initial shock for the double Mach test case.

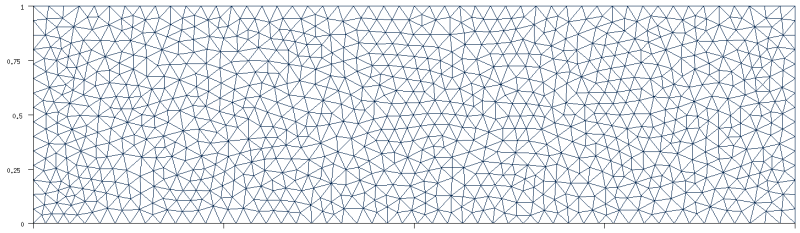

(a) Initial mesh of $1,953$ triangles.

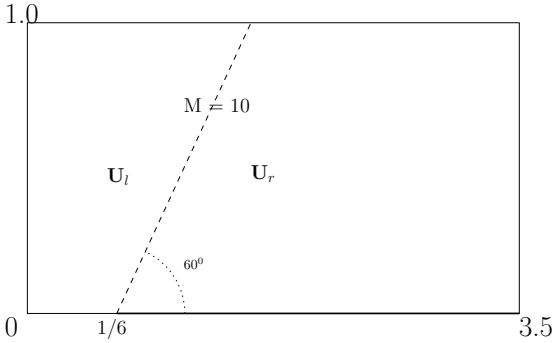

(b) Initial condition.

Figure 3.12: The initial set-up for the double mach reflection test case.

3.3 Summary

In this chapter, we have presented a high-order moment limiter for the DG method on triangular meshes. It limits numerical solution by hierarchically limiting solution coefficients (moments) starting with the highest. The limiter stops when it encounters solution coefficients or corresponding directional derivatives that are left unchanged by the minmod function. This avoids overlimiting, especially at solution extrema where second order methods and second order limiters visibly damage solutions even on reasonably fine meshes.

Numerical experiments presented in Section 3.2 demonstrate that the DG method equipped with the proposed limiter retains the $p + 1$ convergence rate for smooth solutions and eliminates spurious oscillations in the presence of discontinuities.

(a) Density isolines.

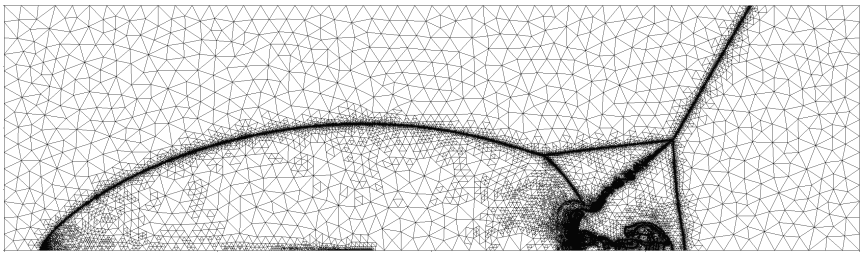

(b) Final adaptively refined mesh of $236,310$ triangles.

Figure 3.13: Density isolines at $t = 0.2$ for the double Mach test case obtained using second order approximation with moment limiter.

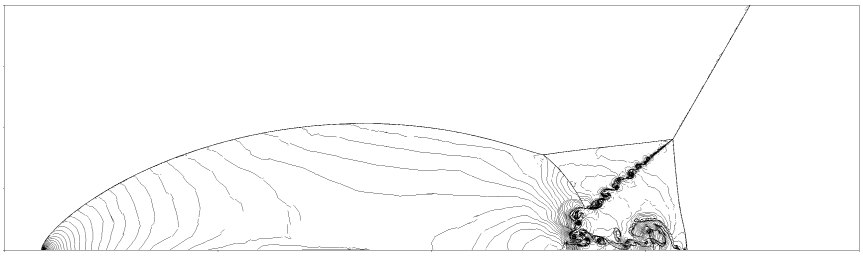

(a) Density isolines.

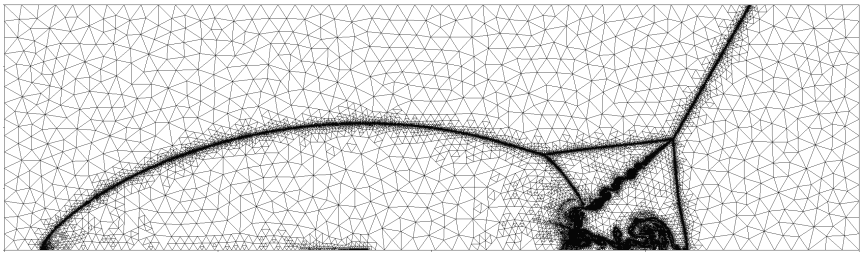

(b) Final adaptively refined mesh of $237,924$ triangles.

Figure 3.14: Density isolines at $t = 0.2$ for the double Mach test case obtained using third order approximation with moment limiter.

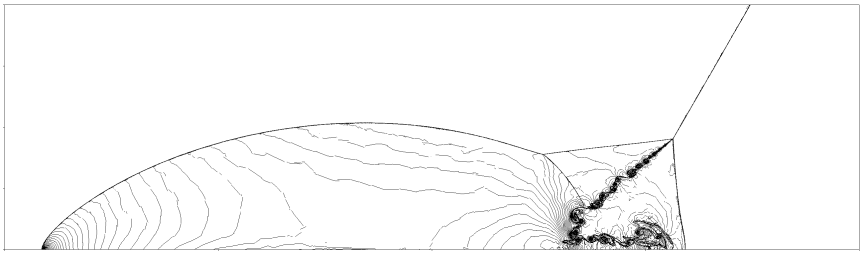

(a) Density isolines.

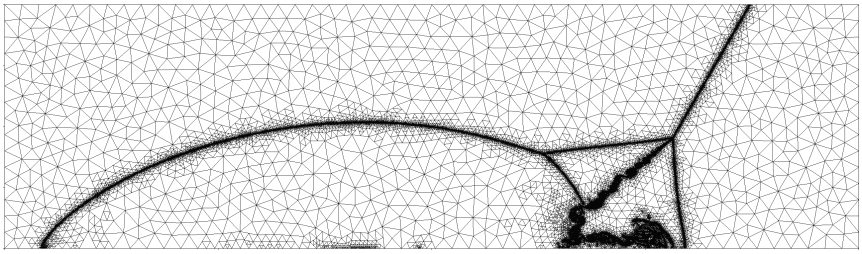

(b) Final adaptively refined mesh of 222,969 triangles.

Figure 3.15: Density isolines at $t = 0.2$ for the double Mach test case obtained using fourth order approximation with moment limiter.

The key component of the limiter is the choice of the directions in which the solution is limited. The proposed limiting directions nearly uncouple solution coefficients, which allows us a fast transition between solution coefficients and directional derivatives of the solution. This also allows us to limit only the moments that exhibit excessive growth and retain the accuracy of the solution.

The proposed limiter has a simple and fixed reconstruction stencil, which is computed [53] during the preprocessing stage. Despite a complex derivation, the limiter itself consists of a set of algebraic operations on solution coefficients and precomputed constants. As a result, it takes only about fifteen percent of the total computing time in a parallel implementation of the modal discontinuous Galerkin method for solution of Euler equations, which is very modest.

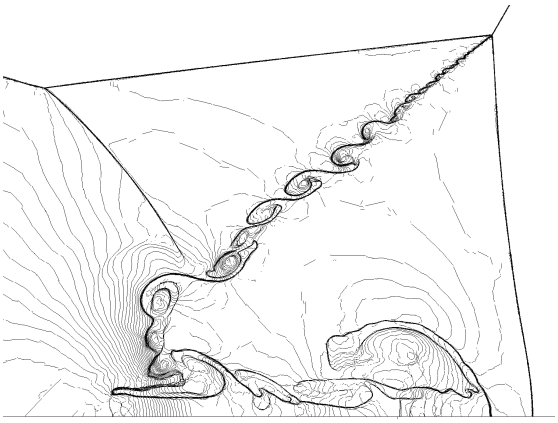

(a) Zoom in near slipline for $p = 1$.

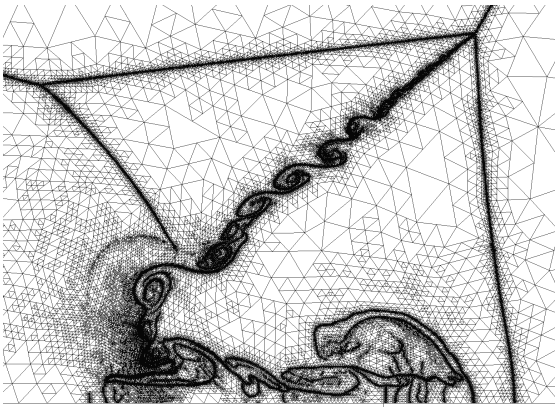

(b) Final adaptively refined mesh.

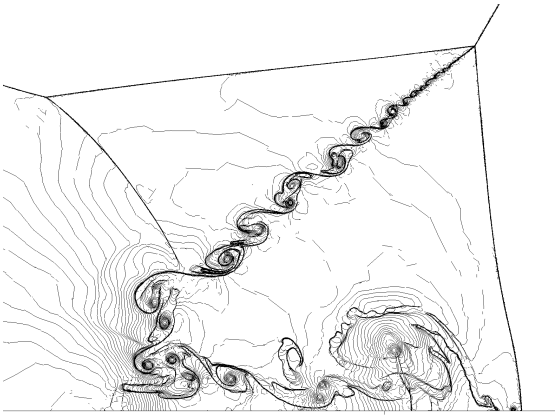

(c) Zoom in near slipline for $p = 2$.

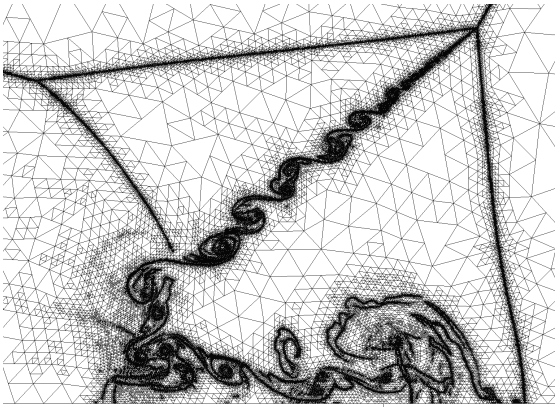

(d) Final adaptively refined mesh.

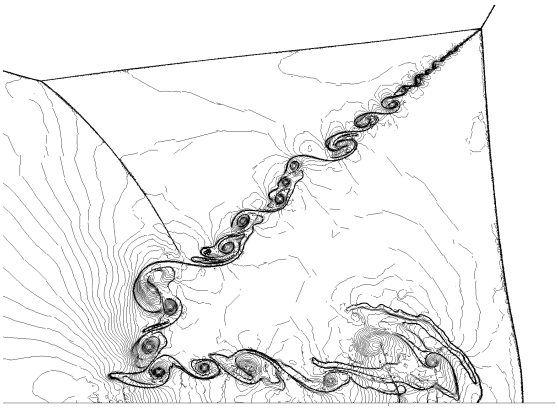

(e) Zoom in near slipline for $p = 3$.

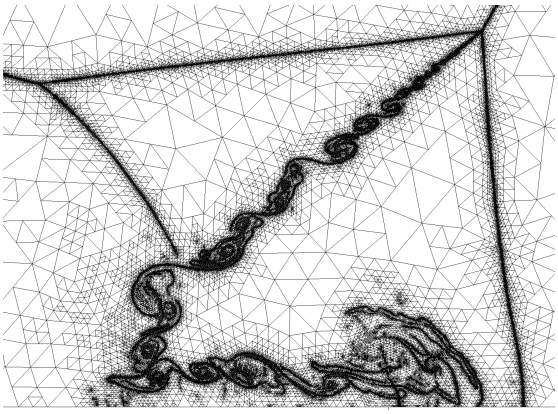

(f) Final adaptively refined mesh.

Figure 3.16: Density isolines at $t = 0.2$ for the double Mach test case obtained using second (top), third (middle), and fourth order (bottom) approximations with moment limiter.

Chapter 4

Slope limiter on quadrilateral meshes

In this chapter, we present and analyze a family of scalar slope limiters for the second order DG method on unstructured quadrilateral meshes. The limiter works by multiplying linear solution coefficients by a scaling factor γ_i that lies in the interval $[0, 1]$ so that the numerical solution at chosen limiting points along the element boundary remains bounded by solution averages from a neighborhood of the element. Moreover, we prove that with appropriate timestep size, applying the above limiter ensures that the numerical solution satisfies local maximum principle (LMP) (4.16) in the means. The choice of limiting

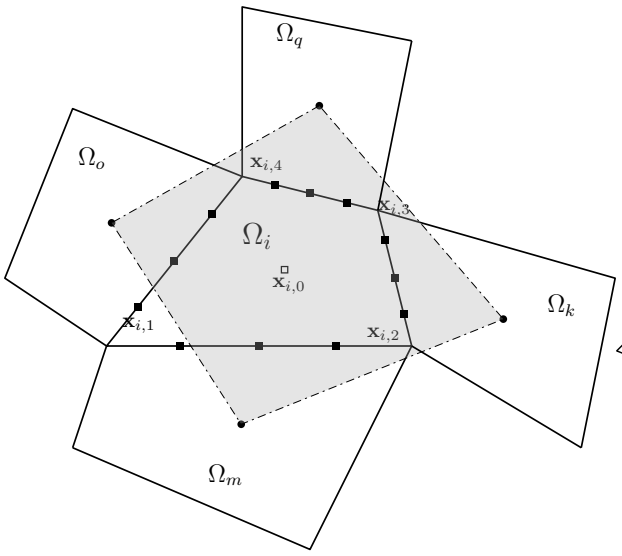

(a) Edge neighborhood.

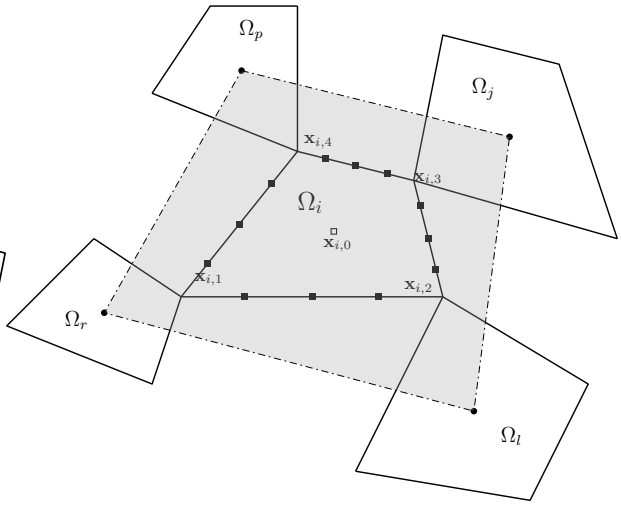

(b) Reduced neighborhood.

points and the limiting neighborhood is crucial to the performance of the limiter. Figure 4.1 shows a few possible choices for the limiting neighborhood. For the limited solution to

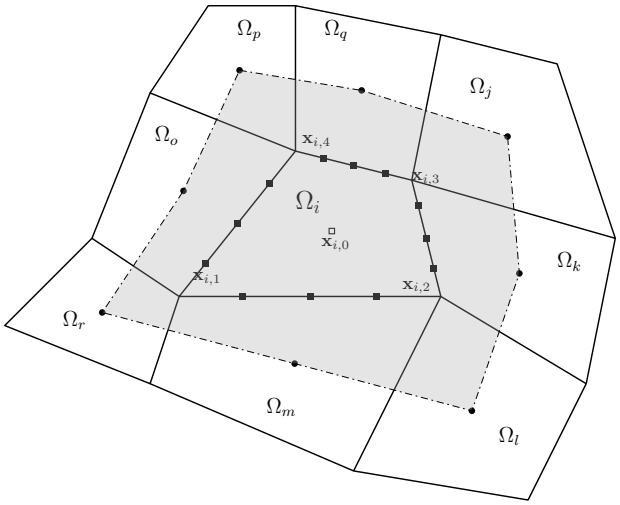

(c) Vertex neighborhood.

Figure 4.1: Possible limiting neighborhoods for a quadrilateral element. The filled disks denote the center of masses of the elements while the filled squares represent the limiting points.

retain its second order accuracy on a triangular mesh, it was shown in [22] that the limiting points must lie within the convex hull formed by the center of masses of the elements in the limiting neighborhood. The same proof and conclusion follows for a quadrilateral mesh as well. A simple choice for a neighborhood that always satisfies the above condition is the vertex neighborhood (Figure 4.1c), i.e., the neighborhood consisting of elements sharing a vertex with the element. Therefore, in the present work, we have chosen the vertex neighborhood as the limiting neighborhood.

We give a short description of the second order slope limiter in Section 4.1. We analyze the stability of the limited solution for scalar linear conservation laws in Section 4.1.1 and scalar nonlinear conservation laws in Section 4.1.2. Finally, we present numerical experiments in Section 4.2 to verify the performance of the proposed limiter.

4.1 Limiting algorithm

The second order DG approximation on Ω_i can be written as a linear combination of the Legendre tensor product basis (1.25)

$$U_i^n(\zeta,\eta) = \hat{U}_{i,0}^{n,0}\varphi_0^0(\zeta,\eta) + \hat{U}_{i,1}^{n,0}\varphi_1^0(\zeta,\eta) + \hat{U}_{i,0}^{n,1}\varphi_0^1(\zeta,\eta) + \hat{U}_{i,1}^{n,1}\varphi_1^1(\zeta,\eta), \tag{4.1}$$

where the constant and linear basis functions are

$$\varphi_0^0 = \frac{1}{2}, \quad \varphi_1^0 = \frac{\sqrt{3}}{2}\zeta, \quad \varphi_0^1 = \frac{\sqrt{3}}{2}\eta, \quad \varphi_1^1 = \frac{3}{2}\zeta\eta. \tag{4.2}$$

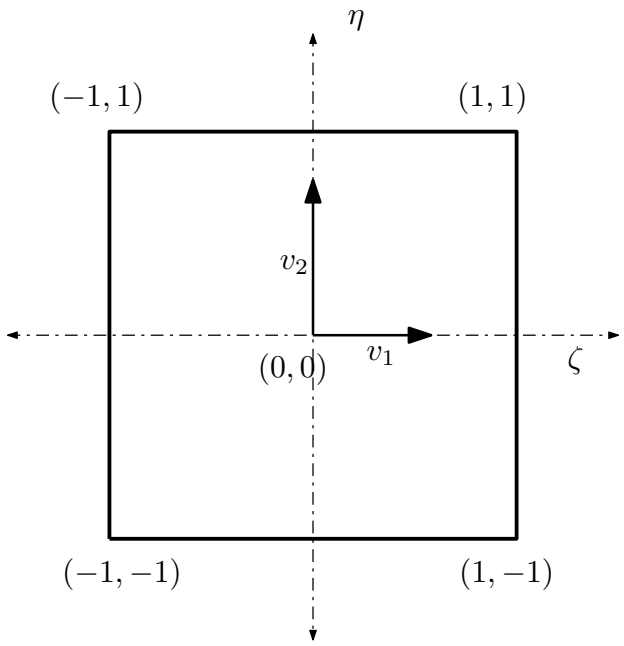

Figure 4.2: Reference square element Ω_0.

The limited numerical solution is given by

$$\tilde{U}_i^n = \overline{U}_i^n + \gamma_i \left(U_i^n - \overline{U}_i^n \right), \tag{4.3}$$

where $\overline{U}_i^n$ is the cell average of the solution in Ω_i and γ_i is a scalar multiplier that lies in the interval $[0, 1]$ and is computed using the following algorithm

1. Compute the minimum and maximum cell averages in a neighborhood of Ω_i, i.e.,

$$m_i = \min_{j \in N_i} \overline{U}_j \text{ and } M_i = \max_{j \in N_i} \overline{U}_j, \tag{4.4}$$

   where N_i is a set containing the indices of Ω_i and elements in the neighborhood of Ω_i, e.g., vertex neighborhood.

2. Compute the coefficient $y_i(\mathbf{x}_k)$ at each limiting point $\mathbf{x}_k$, e.g., edge midpoints, Gauss

quadrature points, etc., as

$$y_i(\mathbf{x}_k) = \begin{cases} \dfrac{M_i - \overline{U}_i}{U_i(\mathbf{x}_k) - \overline{U}_i}, & \text{if } U_i(\mathbf{x}_k) - \overline{U}_i > 0, \\ \dfrac{m_i - \overline{U}_i}{U_i(\mathbf{x}_k) - \overline{U}_i}, & \text{if } U_i(\mathbf{x}_k) - \overline{U}_i < 0, \\ 1 \qquad \text{otherwise.} \end{cases} \tag{4.5}$$

3. Finally, compute the scalar multiplier γ_i as

$$\gamma_i = \min(1, \min_k y_i(\mathbf{x}_k)). \tag{4.6}$$

Remark 1. We note that limiting the solution U_i^n using (4.3) doesn't change the cell average $\overline{U}_i^n$ in Ω_i and thus, does not affect conservation.

4.1.1 Stability analysis for linear advection

Consider the case where (1.8) is a scalar linear advection equation, i.e.,

$$u_t + \nabla \cdot (\mathbf{a}u) = 0. \tag{4.7}$$

Setting $k = l = 0$ in (1.27), we get

$$\frac{d\overline{U}_i}{dt} = -\frac{1}{|\Omega_i|} \sum_{j \in N_i^e} \int_{\delta\Omega_{i,j}} \mathbf{F}^*(U_i, U_j) \cdot \mathbf{n}_{i,j} dl. \tag{4.8}$$

After one Euler time step, the cell average in Ω_i is given by

$$\overline{U}_i^{n+1} = \overline{U}_i^n - \frac{\Delta t}{|\Omega_i|} \sum_{j \in N_i^e} \int_{\delta\Omega_{i,j}} \mathbf{F}^*(U_i, U_j) \cdot \mathbf{n}_{i,j} dl. \tag{4.9}$$

For linear advection, the flux in (1.8) is given by $\mathbf{F}(u) = u\mathbf{a}$, where $\mathbf{a}$ is the flow direction. Choosing the upwind flux as the numerical flux gives us

$$\mathbf{F}^*(U_i, U_j) \cdot \mathbf{n}_{i,j} = \begin{cases} (\mathbf{a} \cdot \mathbf{n}_{i,j}) U_i, & \text{if } j \in N_i^+, \\ (\mathbf{a} \cdot \mathbf{n}_{i,j}) U_j, & \text{if } j \in N_i^-, \end{cases} \tag{4.10}$$

where N_i^+ and N_i^- are, respectively, the indices of the outflow and inflow neighbors of Ω_i, i.e., $N_i^{\pm} = \{j \in N_i^e \Big| \pm (\mathbf{a}\cdot\mathbf{n}_{i,j}) > 0\}$. Further, from the divergence theorem we have

$$\sum_{j\in N_i^e} \int_{\delta\Omega_{i,j}} U_i^n(\mathbf{x}_{i,0})\mathbf{a}\cdot\mathbf{n}_{i,j}dl = \sum_{j\in N_i^+} U_i^n(\mathbf{x}_{i,0})|\mathbf{a}\cdot\mathbf{n}_{i,j}||\delta\Omega_{i,j}| - \sum_{j\in N_i^-} U_i^n(\mathbf{x}_{i,0})|\mathbf{a}\cdot\mathbf{n}_{i,j}||\delta\Omega_{i,j}| = 0. \quad (4.11)$$

Substituting (4.10) and (4.11) in (4.9), we get

$$\begin{aligned}\overline{U}_i^{n+1} = \overline{U}_i^n + \frac{\Delta t}{|\Omega_i|}\Bigg[&\sum_{j\in N_i^-}\left(U_j^n(\mathbf{x}_{i,j}) - U_i^n(\mathbf{x}_{i,0})\right)|\mathbf{a}\cdot\mathbf{n}_{j,i}||\delta\Omega_{i,j}| \\ &- \sum_{j\in N_i^+}\left(U_i^n(\mathbf{x}_{i,j}) - U_i^n(\mathbf{x}_{i,0})\right)|\mathbf{a}\cdot\mathbf{n}_{i,j}||\delta\Omega_{i,j}|\Bigg],\end{aligned} \quad (4.12)$$

where we chose the edge midpoint as the quadrature point $\mathbf{x}_{i,j}$. If the solution is limited at time t_n, then (4.12) becomes

$$\begin{aligned}\overline{U}_i^{n+1} = \overline{U}_i^n + \frac{\Delta t}{|\Omega_i|}\Bigg[&\sum_{j\in N_i^-}\left(\tilde{U}_j^n(\mathbf{x}_{i,j}) - \tilde{U}_i^n(\mathbf{x}_{i,0})\right)|\mathbf{a}\cdot\mathbf{n}_{j,i}||\delta\Omega_{i,j}| \\ &- \sum_{j\in N_i^+}\left(\tilde{U}_i^n(\mathbf{x}_{i,j}) - \tilde{U}_i^n(\mathbf{x}_{i,0})\right)|\mathbf{a}\cdot\mathbf{n}_{i,j}||\delta\Omega_{i,j}|\Bigg],\end{aligned} \quad (4.13)$$

where $\tilde{U}^n$ is the limited solution. We aim to rewrite (4.13) in the form

$$\overline{U}_i^{n+1} = \delta_0\overline{U}_i^n + \sum_k \delta_k U_k, \quad (4.14)$$

where U_k is either the cell average or a convex combination of cell averages in some neighborhood of Ω_i. If the scaling coefficients δ_k satisfy

$$\delta_k \geq 0, \quad \delta_0 \geq 0, \quad \text{and} \quad \delta_0 + \sum_k \delta_k = 1, \quad (4.15)$$

then the right hand side of (4.14) is a convex combination of cell averages in some neighborhood of Ω_i, and thus, the numerical solution in Ω_i satisfies the local maximum principle (LMP) in the means, i.e.,

$$\min_{k\in\mathcal{N}_i}\overline{U}_k^n \leq \overline{U}_i^{n+1} \leq \max_{k\in\mathcal{N}_i}\overline{U}_k^n, \quad (4.16)$$

where $\mathcal{N}_i$ is a set containing the indices of Ω_i and its neighbors.

For a scalar linear conservation law, we choose the edge midpoints as limiting points while computing the scalar multiplier γ_i in (4.3). Therefore, using (4.5) and (4.6) in (4.3), we note that the limited solution at the quadrature point (edge midpoint) $\mathbf{x}_{i,j}$ satisfies

$$\begin{aligned}\tilde{U}_i^n(\mathbf{x}_{i,j}) &= \overline{U}_i^n + \gamma_i \left(U_i^n(\mathbf{x}_{i,j}) - \overline{U}_i^n\right) \\ &= \overline{U}_i^n + \tau_i \left(\overline{U}_m - \overline{U}_i^n\right),\end{aligned} \tag{4.17}$$

where $\tau_i \in [0,1]$ and $\overline{U}_m = \{m_i, M_i\}$, i.e., $\tilde{U}_i^n(\mathbf{x}_{i,j})$ can be written as a convex combination of solution averages in some neighborhood of Ω_i. Moreover, since the bilinear map (1.19) reduces to a linear transformation along $\eta = 0$ and $\zeta = 0$ in the canonical space, we have

$$2\tilde{U}_i^n(\mathbf{x}_{i,0}) = \tilde{U}_i^n(\mathbf{x}_{i,j}) + \tilde{U}_i^n(\tilde{\mathbf{x}}_{i,j}), \tag{4.18}$$

where $\mathbf{x}_{i,0}$ is the cell center of Ω_i while $\mathbf{x}_{i,j}$ and $\tilde{\mathbf{x}}_{i,j}$ are midpoints of opposite edges. Further, using its definition, the cell average $\overline{U}_i^n$ can be written in terms of solution coefficients as

$$\overline{U}_i^n = \frac{1}{2}\tilde{U}_{i,0}^{n,0} + \frac{\sqrt{3}}{2}\frac{\alpha_i}{3}\tilde{U}_{i,1}^{n,0} + \frac{\sqrt{3}}{2}\frac{\beta_i}{3}\tilde{U}_{i,0}^{n,1}, \tag{4.19}$$

where α_i and β_i are geometric parameters given by

$$\alpha_i = \frac{\det J_{i,1}}{\det J_{i,0}}, \quad \beta_i = \frac{\det J_{i,2}}{\det J_{i,0}}, \tag{4.20}$$

that satisfy the constraint

$$|\alpha_i| + |\beta_i| < 1. \tag{4.21}$$

The constraint (4.21) follows from the condition that the determinant of the Jacobian (1.22) has to be non-negative at all points in the element.

Now, consider the bilinear equation in the canonical space

$$\frac{1}{2}\tilde{U}_{i,0}^{n,0} + \frac{\sqrt{3}}{2}\tilde{U}_{i,1}^{n,0}\zeta + \frac{\sqrt{3}}{2}\tilde{U}_{i,0}^{n,1}\eta + \frac{3}{2}\tilde{U}_{i,1}^{n,1}\zeta\eta = \overline{U}_i^n. \tag{4.22}$$

Plugging (4.19) in (4.22), we get

$$\frac{\sqrt{3}}{2}\tilde{U}_{i,1}^{n,0}\zeta + \frac{\sqrt{3}}{2}\tilde{U}_{i,0}^{n,1}\eta + \frac{3}{2}\tilde{U}_{i,1}^{n,1}\zeta\eta = \frac{\sqrt{3}}{2}\frac{\alpha_i}{3}\tilde{U}_{i,1}^{n,0} + \frac{\sqrt{3}}{2}\frac{\beta_i}{3}\tilde{U}_{i,0}^{n,1}. \tag{4.23}$$

The intercepts of (4.23) on the (ζ, η)-axes in the canonical space satisfy

$$\tilde{U}_{i,1}^{n,0}\zeta_{i,int} = \tilde{U}_{i,0}^{n,1}\eta_{i,int} = \frac{\alpha_i}{3}\tilde{U}_{i,1}^{n,0} + \frac{\beta_i}{3}\tilde{U}_{i,0}^{n,1}. \tag{4.24}$$

Without loss of generality, let's assume $|\tilde{U}_{i,1}^{n,0}| \geq |\tilde{U}_{i,0}^{n,1}|$. Therefore, using (4.21) and (4.24), the ζ intercept, $\zeta_{i,int}$, satisfies

$$\begin{aligned} \|\mathbf{r}_{i,int}\| = r = |\zeta_{i,int}| &= |\frac{\alpha_i}{3}\frac{\tilde{U}_{i,1}^{n,0}}{|\tilde{U}_{i,1}^{n,0}|} + \frac{\beta_i}{3}\frac{\tilde{U}_{i,0}^{n,1}}{|\tilde{U}_{i,1}^{n,0}|}| \\ &\leq \frac{|\alpha_i|}{3} + \frac{|\beta_i|}{3} < \frac{1}{3}. \end{aligned} \tag{4.25}$$

Further, let's assume that the intercept $\mathbf{r}_{i,int}$ maps to the point $\mathbf{x}_{i,c}$ on Ω_i (hollow disk, Figure 4.3). Therefore, we can express $\overline{U}_i^n$ as

$$\overline{U}_i^n = r\tilde{U}_i^n(\mathbf{x}_{i,4e}) + (1-r)\,\tilde{U}_i^n(\mathbf{x}_{i,0}). \tag{4.26}$$

Using the results in (4.11), (4.17), (4.18), and (4.26), the expression on the right hand side of (4.13) can be rewritten as

$$\begin{aligned} \overline{U}_i^{n+1} &= \overline{U}_i^n + \frac{\Delta t}{|\Omega_i|}\Bigg[\sum_{j\in N_i^-}\left(\tilde{U}_j^n(\mathbf{x}_{i,j}) - \tilde{U}_i^n(\mathbf{x}_{i,0})\right)|\mathbf{a}\cdot\mathbf{n}_{j,i}||\delta\Omega_{i,j}| \\ &\quad - \sum_{j\in N_i^+}\left(\tilde{U}_i^n(\mathbf{x}_{i,j}) - \tilde{U}_i^n(\mathbf{x}_{i,0})\right)|\mathbf{a}\cdot\mathbf{n}_{i,j}||\delta\Omega_{i,j}|\Bigg], \\ &= \overline{U}_i^n + \frac{\Delta t}{|\Omega_i|}\Bigg[\sum_{j\in N_i^-}\tilde{U}_j^n(\mathbf{x}_{i,j})|\mathbf{a}\cdot\mathbf{n}_{j,i}||\delta\Omega_{i,j}| + \sum_{j\in N_i^+}\tilde{U}_i^n(\tilde{\mathbf{x}}_{i,j})|\mathbf{a}\cdot\mathbf{n}_{i,j}||\delta\Omega_{i,j}| \\ &\quad -2\sum_{j\in N_i^-}\tilde{U}_i^n(\mathbf{x}_{i,0})|\mathbf{a}\cdot\mathbf{n}_{j,i}||\delta\Omega_{i,j}|\Bigg], \\ &= \left[1 - \frac{2}{1-r}\frac{\Delta t}{|\Omega_i|}\sum_{j\in N_i^-}|\mathbf{a}\cdot\mathbf{n}_{j,i}||\delta\Omega_{i,j}|\right]\overline{U}_i^n + \frac{\Delta t}{|\Omega_i|}\Bigg[\sum_{j\in N_i^-}\tilde{U}_j^n(\mathbf{x}_{i,j})|\mathbf{a}\cdot\mathbf{n}_{j,i}||\delta\Omega_{i,j}| \\ &\quad + \sum_{j\in N_i^+}\tilde{U}_i^n(\tilde{\mathbf{x}}_{i,j})|\mathbf{a}\cdot\mathbf{n}_{i,j}||\delta\Omega_{i,j}| + \frac{2r}{1-r}\sum_{j\in N_i^-}\tilde{U}_i^n(\mathbf{x}_{i,4e})|\mathbf{a}\cdot\mathbf{n}_{j,i}||\delta\Omega_{i,j}|\Bigg], \end{aligned} \tag{4.27}$$

which is of the form (4.14). We note that all of the scaling coefficients on the right hand side of (4.27) add up to one. Further, the scaling coefficients of the values of the limited solution at edge midpoints are non negative by construction. Therefore, to satisfy (4.15),

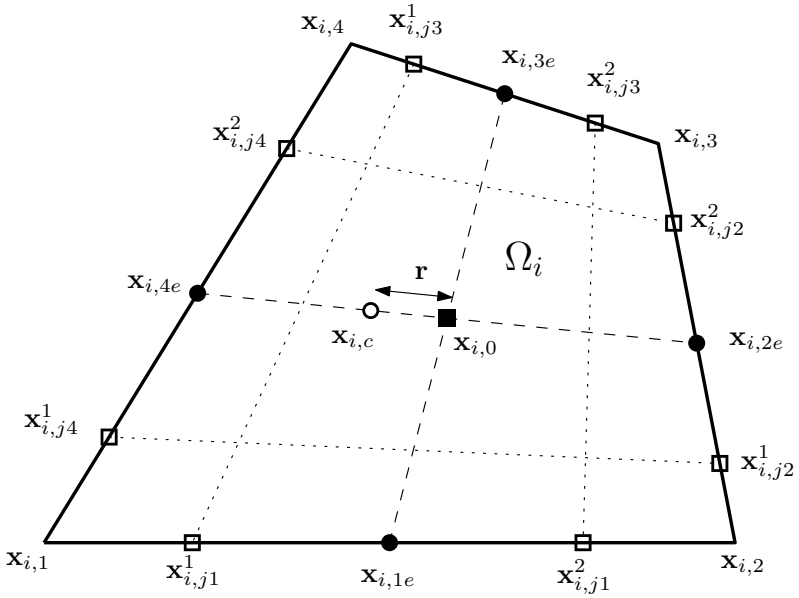

Figure 4.3: Quadrature or limiting points on the edges of element Ω_i.

the scaling coefficient of $\overline{U}_i^n$ should satisfy

$$\begin{aligned} \frac{2}{1-r}\frac{\Delta t}{|\Omega_i|}\sum_{j\in N_i^-}|\mathbf{a}\cdot\mathbf{n}_{j,i}||\delta\Omega_{i,j}| &\le 1 \\ \Delta t &\le \frac{1-r}{2}\frac{|\Omega_i|}{\sum_{j\in N_i^-}|\mathbf{a}\cdot\mathbf{n}_{j,i}||\delta\Omega_{i,j}|}. \end{aligned} \tag{4.28}$$

Using (4.25) in (4.28), we obtain a restrictive condition on an admissible time step

$$\Delta t \le \frac{1}{3}\frac{|\Omega_i|}{\sum_{j\in N_i^-}|\mathbf{a}\cdot\mathbf{n}_{j,i}||\delta\Omega_{i,j}|}. \tag{4.29}$$

Timestep restriction

For a given flow direction $\mathbf{a}$, the quadrilateral element Ω_i can have one, two (Figure 4.4a), or three (Figure 4.4b) inflow (outflow) edges. The case of one inflow edge is the same as three outflow edges and is not considered here.

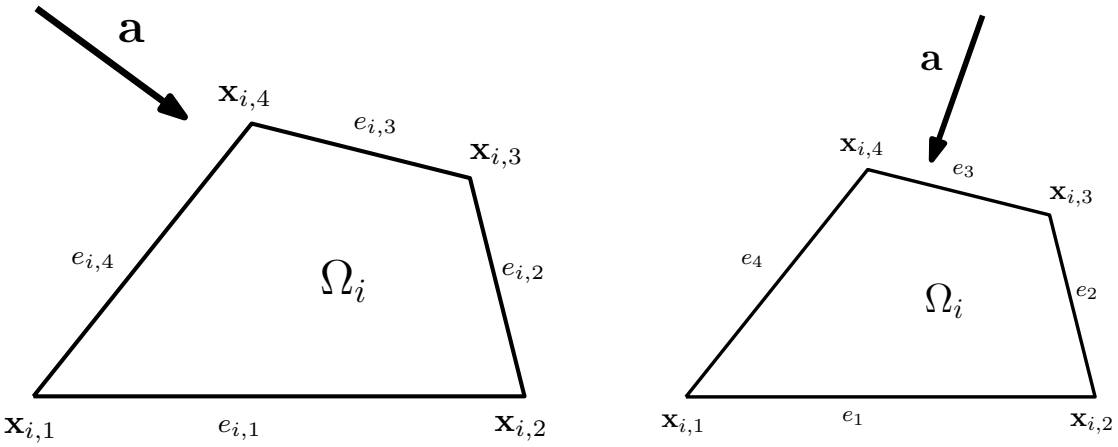

(a) **I** : Two inflow edges.

(b) **II** : Three inflow edge.

Figure 4.4: Inflow configurations.

First, let's consider the scenario in Figures 4.4a and 4.5, where Ω_i has two inflow edges. Using the divergence theorem, we can rewrite $\sum_{j\in N_i^-} |\mathbf{a}\cdot\mathbf{n}_{j,i}||\delta\Omega_{i,j}|$ as

$$\sum_{j\in N_i^-} |\mathbf{a}\cdot\mathbf{n}_{j,i}||\delta\Omega_{i,j}| = |\mathbf{a}\cdot\mathbf{n}_{d_1}|d_1, \tag{4.30}$$

where d_1 is the length of the diagonal opposing the two inflow edges (Figure 4.5). Further, note that the area of Ω_i can be expressed as

$$|\Omega_i| = \frac{1}{2}\left(h_4 + h_2\right) d_1, \tag{4.31}$$

where h_1 and h_2 are the heights of the two triangles created by the diagonal. Using (4.30) and (4.31), the time step restriction (4.29) can be rewritten as

$$\Delta t \leq \frac{1}{6}\frac{h_4 + h_2}{|\mathbf{a}\cdot\mathbf{n}_{d_1}|}. \tag{4.32}$$

From Figure 4.5b, we observe that

$$\max\{H_{i,41}, H_{i,42}\} \leq a_4, \quad H_4 \leq h_4 + h_2, \quad |\mathbf{a}\cdot\mathbf{n}_{d_1}| = |\mathbf{a}|\frac{H_4}{a_4}. \tag{4.33}$$

Plugging (4.33) into (4.32), we arrive at a slightly restrictive estimate for the time step

$$\Delta t \leq \frac{1}{6}\frac{a_4}{|\mathbf{a}|}. \tag{4.34}$$

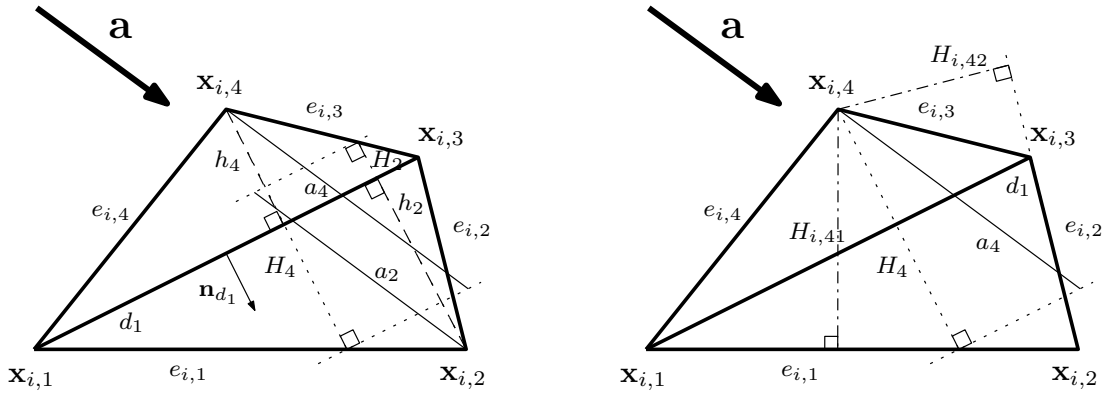

(a) **I** . (b) **I**.

Figure 4.5: Configuration with two inflow and two outflow edges.

Next, let's consider the scenario in Figures 4.4b and 4.6, where Ω_i has one outflow edge. We can write $\sum_{j\in N_i^+} |\mathbf{a}\cdot\mathbf{n}_{j,i}||\delta\Omega_{i,j}|$ as

$$\sum_{j\in N_i^+} |\mathbf{a}\cdot\mathbf{n}_{j,i}||\delta\Omega_{i,j}| = |\mathbf{a}\cdot\mathbf{n}_{e_{i,1}}|e_{i,1}, \tag{4.35}$$

where $e_{i,1}$ is the length of the outflow edge. Further, the area of Ω_i satisfies the inequalities

$$|\Omega_i| \geq \frac{1}{2}H_{i,41}e_{i,1}, \qquad |\Omega_i| \geq \frac{1}{2}H_{i,31}e_{i,1}. \tag{4.36}$$

From Figure 4.6, we observe that

$$H_{i,41} \leq a_4, \quad |\mathbf{a}\cdot\mathbf{n}_{e_1}| = |\mathbf{a}|\frac{H_{i,41}}{a_4}. \tag{4.37}$$

Plugging (4.37) and (4.36) into (4.29), we arrive at a similar, slightly more restrictive estimate for the time step

$$\Delta t \leq \frac{1}{6}\frac{a_4}{|\mathbf{a}|}. \tag{4.38}$$

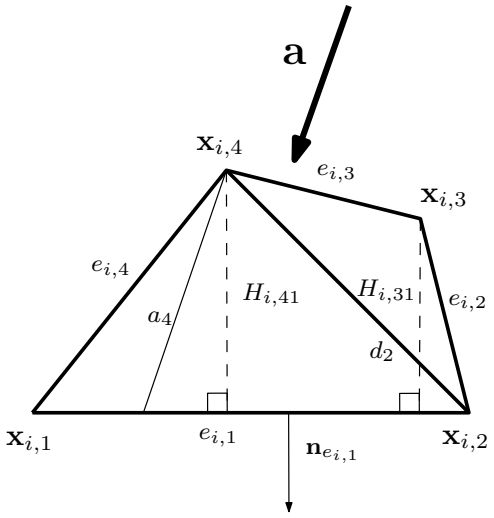

(a) **II** .

Figure 4.6: Configuration with one outflow edge.

Note that the height $H_{i,41}$ was used in (4.36) and (4.38) because $H_{i,41} > H_{i,31}$, i.e., the restriction (4.38) is valid or required only when vertex $\mathbf{x}_{i,4}$ lies further away from edge 1 than vertex $\mathbf{x}_{i,3}$. Finally, as the flow can be in any arbitrary direction, we apply (4.34) and (4.38) at each vertex to arrive at the following time step restriction

$$\Delta t \leq \frac{1}{6} \min_i \frac{h_i}{\|\mathbf{a}\|}, \tag{4.39}$$

where h_i, the smallest height of element Ω_i (Figure 4.7), is given by

$$\begin{aligned} h_i &= \min(h_1, h_2), \\ h_1 &= \min(\max(\min(H_{i,12}, H_{i,13}), \min(H_{i,34}, H_{i,31})), \max(\min(H_{i,24}, H_{i,23}), \\ &\quad \min(H_{i,41}, H_{i,42}))), \\ h_2 &= \min(\max(H_{i,41}, H_{i,31}), \max(H_{i,12}, H_{i,42}), \max(H_{i,13}, H_{i,23}), \max(H_{i,24}, H_{i,34})). \end{aligned} \tag{4.40}$$

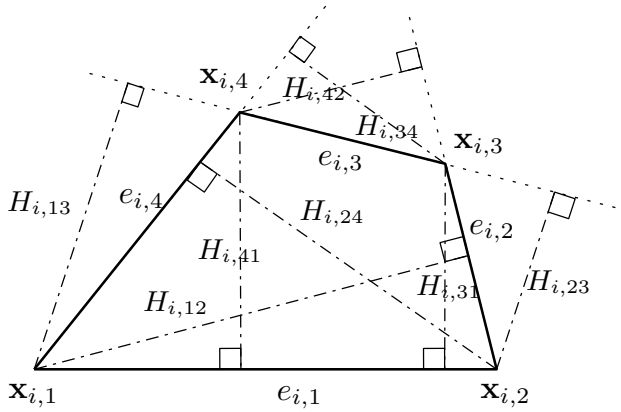

Figure 4.7: Element size h_i.

4.1.2 Stability analysis for scalar nonlinear conservation laws

Consider the case where (1.8) is a scalar nonlinear hyperbolic equation, i.e.,

$$u_t + \nabla \cdot (\mathbf{F}(u)) = 0. \tag{4.41}$$

Setting $k = l = 0$ in (1.27), we get

$$\frac{d\overline{U}_i}{dt} = -\frac{1}{|\Omega_i|} \sum_{j \in N_i^e} \int_{\delta\Omega_{i,j}} \mathbf{F}^*(U_i, U_j) \cdot \mathbf{n}_{i,j} dl. \tag{4.42}$$

After one Euler time step, the cell average in Ω_i is given by

$$\overline{U}_i^{n+1} = \overline{U}_i^n - \frac{\Delta t}{|\Omega_i|} \sum_{j \in N_i^e} \int_{\delta\Omega_{i,j}} \mathbf{F}^*(U_i, U_j) \cdot \mathbf{n}_{i,j} dl. \tag{4.43}$$

As the cell average $\overline{U}_i^n$ is a constant, from the divergence theorem we have

$$\sum_{j \in N_i^e} \int_{\delta\Omega_{i,j}} \mathbf{F}^*(\overline{U}_i^n, \overline{U}_i^n) \cdot \mathbf{n}_{i,j} dl = 0. \tag{4.44}$$

Using (4.44), a two point quadrature rule to compute the nonlinear flux at boundary $\delta\Omega_{i,j}$, and denoting the normal flux at a quadrature point $\mathbf{x}_{i,j}^q$ on $\delta\Omega_{i,j}$ as

$$\hat{\mathbf{F}}_q(U_i, U_j) = \mathbf{F}_q^*(U_i, U_j) \cdot \mathbf{n}_{i,j}, \tag{4.45}$$

we get

$$\overline{U}_i^{n+1} = \overline{U}_i^n - \frac{\Delta t}{2|\Omega_i|} \sum_{j \in N_i^e} \sum_{q=1}^{2} \left(\hat{\mathbf{F}}_q(U_i^n, U_j^n) - \hat{\mathbf{F}}_q(\overline{U}_i^n, \overline{U}_i^n) \right) |\delta\Omega_{i,j}|. \tag{4.46}$$

If the solution is limited at time t_n, then (4.46) becomes

$$\overline{U}_i^{n+1} = \overline{U}_i^n - \frac{\Delta t}{2|\Omega_i|} \sum_{j \in N_i^e} \sum_{q=1}^{2} \left(\hat{\mathbf{F}}_q(\tilde{U}_i^n, \tilde{U}_j^n) - \hat{\mathbf{F}}_q(\overline{U}_i^n, \overline{U}_i^n) \right) |\delta\Omega_{i,j}|, \tag{4.47}$$

where $\tilde{U}^n$ is the limited solution. Further, adding and subtracting $\hat{\mathbf{F}}_q(\overline{U}_i^n, \tilde{U}_j^n)$ at each quadrature point in (4.47), we get

$$\begin{aligned}
\overline{U}_i^{n+1} &= \overline{U}_i^n - \frac{\Delta t}{2|\Omega_i|} \sum_{j \in N_i^e} \sum_{q=1}^{2} \left(\hat{\mathbf{F}}_q(\tilde{U}_i^n, \tilde{U}_j^n) \pm \hat{\mathbf{F}}_q(\overline{U}_i^n, \tilde{U}_j^n) - \hat{\mathbf{F}}_q(\overline{U}_i^n, \overline{U}_i^n) \right) |\delta\Omega_{i,j}|, \\
&= \overline{U}_i^n + \frac{\Delta t}{2|\Omega_i|} \sum_{j \in N_i^e} \sum_{q=1}^{2} \frac{\partial \hat{\mathbf{F}}_q}{\partial U_1}(\theta_{i,1q}, \tilde{U}_j^n) \left(\overline{U}_i^n - \tilde{U}_i^n(\mathbf{x}_{i,j}^q) \right) |\delta\Omega_{i,j}| \\
&\quad - \frac{\Delta t}{2|\Omega_i|} \sum_{j \in N_i^e} \sum_{q=1}^{2} \frac{\partial \hat{\mathbf{F}}_q}{\partial U_2}(\tilde{U}_i^n, \theta_{j,1q}) \left(\tilde{U}_j^n(\mathbf{x}_{i,j}^q) - \overline{U}_i^n \right) |\delta\Omega_{i,j}|,
\end{aligned} \tag{4.48}$$

where $\theta_{i,1q}$ lies between $\tilde{U}_i^n(\mathbf{x}_{i,j}^q)$ and $\overline{U}_i^n$, $\theta_{j,1q}$ lies between $\tilde{U}_j^n(\mathbf{x}_{i,j}^q)$ and $\overline{U}_i^n$, and by the monotonicity property of the numerical flux, the partial derivatives satisfy

$$\hat{\mathbf{F}}_{U_1,q} = \frac{\partial \hat{\mathbf{F}}_q}{\partial U_1} \geq 0, \quad \hat{\mathbf{F}}_{U_2,q} = -\frac{\partial \hat{\mathbf{F}}_q}{\partial U_2} \geq 0. \tag{4.49}$$

We aim to rewrite (4.48) in the form

$$\overline{U}_i^{n+1} = \overline{U}_i^n + \sum_k \omega_k \left(U_k - \overline{U}_i^n \right), \tag{4.50}$$

where U_k is either the cell average or a convex combination of cell averages in some neighborhood of Ω_i. If the scaling coefficients ω_k satisfy

$$\omega_k \geq 0, \quad \text{and} \quad \sum_k \omega_k \leq 1, \tag{4.51}$$

then the right hand side of (4.14) is a convex combination of cell averages in some neighborhood of Ω_i, and thus, the numerical solution in Ω_i satisfies the local maximum principle (LMP) (4.16) in the means.

Consider the difference $\overline{U}_i^n - \tilde{U}_i^n(\mathbf{x}_{i,j}^q)$. We note that the solution is linear on each edge of Ω_i. Therefore, on an edge with edge number s (Figure 4.3), we have

$$\tilde{U}_i^n(\mathbf{x}_{i,js}^1) + \tilde{U}_i^n(\mathbf{x}_{i,js}^2) = 2\tilde{U}_i^n(\mathbf{x}_{i,se}), \tag{4.52}$$

where $\mathbf{x}_{i,se}$ is the midpoint of edge s. Using the results in (4.52), (4.11), (4.17), (4.18), and (4.26), the difference $\overline{U}_i^n - \tilde{U}_i^n(\mathbf{x}_{i,js}^q)$ can be written as

$$\begin{aligned}
\overline{U}_i^n - \tilde{U}_i^n(\mathbf{x}_{i,js}^q) &= \overline{U}_i^n + \tilde{U}_i^n(\mathbf{x}_{i,js}^{q'}) - 2\tilde{U}_i^n(\mathbf{x}_{i,se}) \\
&= \left(\tilde{U}_i^n(\mathbf{x}_{i,js}^{q'}) - \overline{U}_i^n\right) + 2\overline{U}_i^n - 2\left(2\tilde{U}_i^n(\mathbf{x}_{i,0}) - \tilde{U}_i^n(\mathbf{x}_{i,\tilde{s}e})\right) \\
&= \left(\tilde{U}_i^n(\mathbf{x}_{i,js}^{q'}) - \overline{U}_i^n\right) + 2\left(\tilde{U}_i^n(\mathbf{x}_{i,\tilde{s}e}) - \overline{U}_i^n\right) + 4\overline{U}_i^n + \frac{4}{1-r}\left(r\tilde{U}_i^n(\mathbf{x}_{i,4e}) - \overline{U}_i^n\right) \\
&= \left(\tilde{U}_i^n(\mathbf{x}_{i,js}^{q'}) - \overline{U}_i^n\right) + 2\left(\tilde{U}_i^n(\mathbf{x}_{i,\tilde{s}e}) - \overline{U}_i^n\right) + \frac{4r}{1-r}\left(r\tilde{U}_i^n(\mathbf{x}_{i,4e}) - \overline{U}_i^n\right).
\end{aligned} \tag{4.53}$$

Plugging (4.53) and (4.49) into (4.48), we get

$$\begin{aligned}
\overline{U}_i^{n+1} = \overline{U}_i + \frac{\Delta t}{2|\Omega_i|}\sum_{j\in N_i^e}\sum_{q=1}^{2}\hat{\mathbf{F}}_{U_1,q}\Bigg[&\left(\tilde{U}_i^n(\mathbf{x}_{i,js}^{q'}) - \overline{U}_i^n\right) + 2\left(\tilde{U}_i^n(\mathbf{x}_{i,\tilde{s}e}) - \overline{U}_i^n\right) \\
&+ \frac{4r}{1-r}\left(r\tilde{U}_i^n(\mathbf{x}_{i,4e}) - \overline{U}_i^n\right)\Bigg]|\delta\Omega_{i,j}| + \frac{\Delta t}{2|\Omega_i|}\sum_{j\in N_i^e}\sum_{q=1}^{2}\hat{\mathbf{F}}_{U_2,q}\left(\tilde{U}_j^n(\mathbf{x}_{i,j}^q) - \overline{U}_i^n\right)|\delta\Omega_{i,j}|,
\end{aligned} \tag{4.54}$$

which is of the form (4.50). Moreover, we require the scaling coefficients to satisfy (4.51). To do so, we need to impose the following restriction on the time step size

$$\begin{aligned}
\frac{\Delta t}{2|\Omega_i|}\sum_{j\in N_i^e}\left[\sum_{q=1}^{2}\hat{\mathbf{F}}_{U_1,q}\left(3 + \frac{4r}{1-r}\right) + \hat{\mathbf{F}}_{U_2,q}\right]|\delta\Omega_{i,j}| &\le 1 \\
\frac{\Delta t}{2|\Omega_i|}\lambda_i\sum_{j\in N_i^e}2\left(\frac{3+r}{1-r} + 1\right)|\delta\Omega_{i,j}| &\le 1 \\
\Delta t \le \frac{1-r}{4}\frac{|\Omega_i|}{\lambda_i\sum_{j\in N_i^e}|\delta\Omega_{i,j}|},&
\end{aligned} \tag{4.55}$$

where λ_i is the maximum wavespeed in the element. Finally, using (4.25), we arrive at the following time step restriction

$$\Delta t \le \frac{1}{6}\frac{h_{i,c}}{\lambda_i}, \tag{4.56}$$

where $h_{i,c} = \dfrac{|\Omega_i|}{\sum_{j \in N_i^e} |\delta\Omega_{i,j}|}$.

4.2 Numerical Results

In this section, we present numerical experiments to analyze the performance of the proposed scalar limiter. We perform convergence studies to show that the limited solution retains the second order rate of convergence for smooth problems. We also run tests to show the robustness of the proposed limiter in the presence of discontinuities. In all presented cases, time-stepping was performed using an explicit second order Runge-Kutta method with the CFL condition (4.29). Finally, unless stated otherwise, the local Lax-Friedrichs flux was used.

4.2.1 Sinusoidal Wave.

We solve the linear advection equation on the domain $\Omega = [-1, 1] \times [-1, 1]$, with the flux in (1.8) given by $\mathbf{F} = [u, u]$. The initial condition consists of a sinusoidal wave $u_0(x, y) = \sin(2\pi(x + y))$ advected with speed $a = \sqrt{2}$ along the direction $(1, 1)$. The problem is solved until $t = 0.5$ on a series of quadrilateral meshes $A - D$. Mesh A is the coarsest with 509 quadrilaterals. The finer meshes are obtained by remeshing the preceding mesh such that the area of the element is reduced by a factor of four. Table 4.1 shows the L_1 errors and the observed convergence rates for the second order DG approximation with and without limiting. We observe that the second order limiter retains the theoretical rate of convergence. Employing a limiter is expected to reduce accuracy of the solution. However, we note that such reductions are relatively modest.

Mesh	Number of elements	L1 error	
		limited	unlimited
A	509	4.14e-01 (-)	1.0e-01 (-)
B	2035	1.11e-01 (1.89)	2.11e-02 (2.24)
C	8363	2.34e-02 (2.24)	4.83e-03 (2.13)
D	33000	5.15e-03 (2.18)	1.23e-03 (1.97)

Table 4.1: L_1 errors for the advecting sinusoidal wave problem at $t = 0.5$ with and without limiting. The numbers in parentheses are the observed rates of convergence.

4.2.2 Rotating Shapes.

Next, we solve the rotating shapes problem with the flux in (1.8) given by $\mathbf{F} = [-2\pi yu, 2\pi xu]$. The initial condition consists of a hill and a square pulse as shown in Figure 4.8 and given by

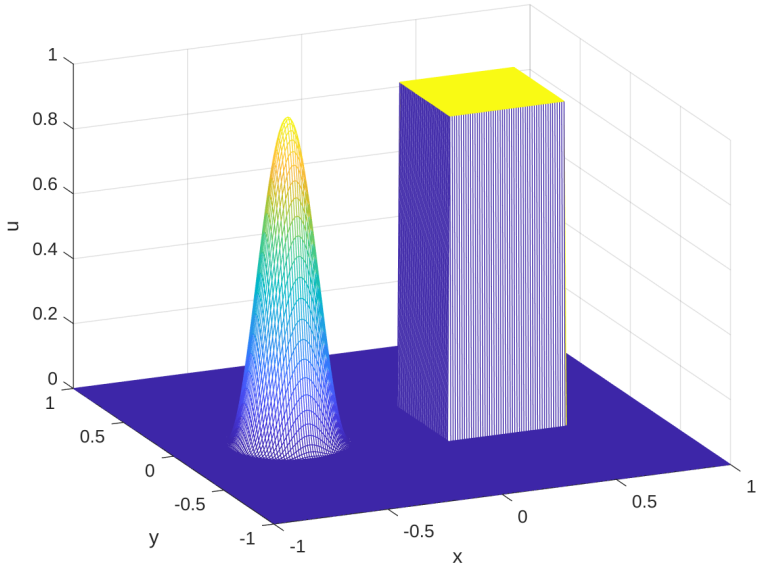

Figure 4.8: Initial condition for the rotating shapes problem.

$$u_0(x,y) = \begin{cases} \cos^2(2\pi r), & \text{if } r \le 0.25, \\ 1, & \text{if } \max(|x-0.35|, |y|) \le 0.25, \\ 0, & \text{otherwise}, \end{cases} \tag{4.57}$$

where $r = \sqrt{(x+0.5)^2 + y^2}$. The exact solution is a rotation of the initial condition about the origin. The problem is solved until $t = 1$ on an unstructured mesh of 6472 quadrilateral elements. Figure 4.9 shows the isolines and the solution profiles at $y = 0$, $x = 0.5$, and $x = 0.55$, obtained using second order DG approximation with and without limiting. The quality of the solution is comparable to the results obtained using the moment limiter described in [25] on a 80×80 Cartesian mesh. From Figure 4.9b, we note that the limiter is successful in reducing the oscillations near the discontinuities, which is corroborated by the solution profiles in Figures 4.9c and 4.9e. We also note that the accuracy near the peak of the hill has reduced. This occurs due to the well known phenomenon of clipping at the local extrema by a second order slope limiter.

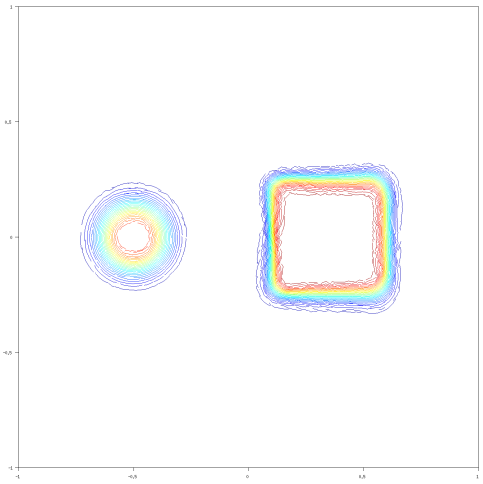

(a) Isolines with second order limiter.

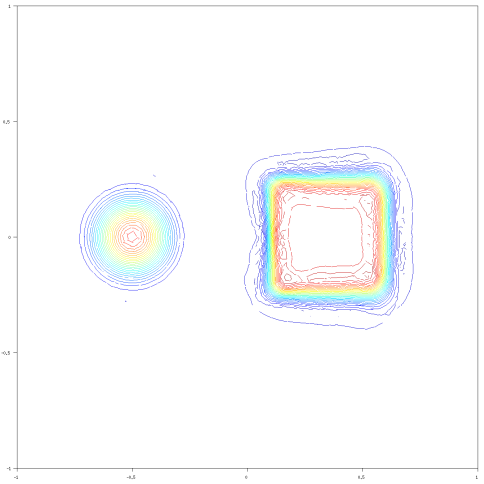

(b) Isolines without limiting.

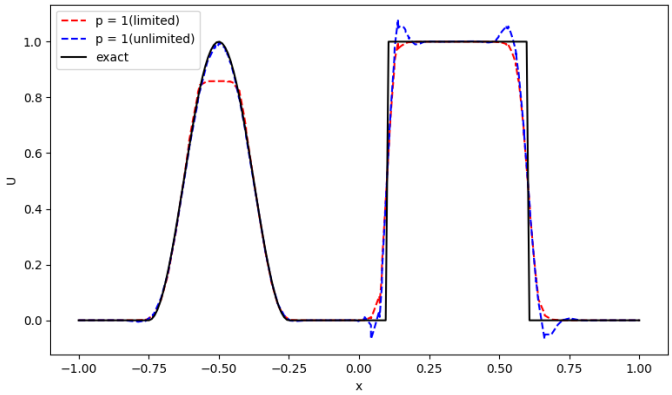

(c) Profile of the solution at $y = 0$.

4.2.3 Isentropic vortex.

Next, we test the performance of the second order limiter when applied to a system of nonlinear equations, for example, the Euler equations given by

$$\frac{\partial}{\partial t}\begin{pmatrix}\rho\\ \rho u\\ \rho v\\ E\end{pmatrix}+\frac{\partial}{\partial x}\begin{pmatrix}\rho u\\ \rho u^2+p\\ \rho uv\\ (E+p)u\end{pmatrix}+\frac{\partial}{\partial y}\begin{pmatrix}\rho v\\ \rho uv\\ \rho v^2+p\\ (E+p)v\end{pmatrix}=0, \tag{4.58}$$

where ρ is the density, ρu and ρv are the x- and y-direction momenta, E is the energy, and the pressure, p, is given by the equation of state $p = (\gamma-1)\left(E-\frac{\rho}{2}(u^2+v^2)\right)$. We solve the

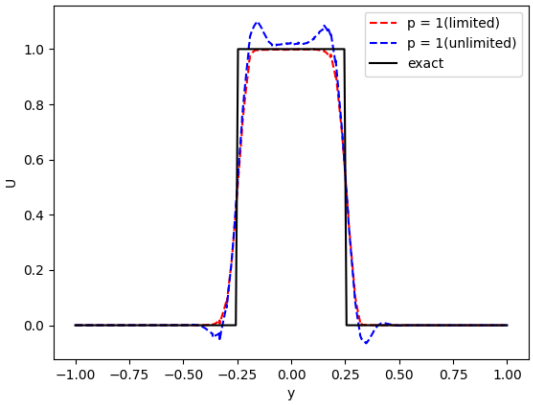

(d) Profile of the solution at $x = 0.5$.

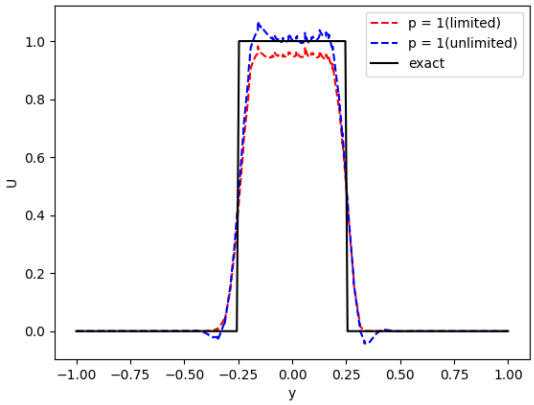

(e) Profile of the solution at $x = 0.55$.

Figure 4.9: Isolines and profiles of the solution for the rotating shapes problem at $t = 1$ on an unstructured mesh of 6472 quadrilaterals.

smooth isentropic vortex problem described in [51] on the domain $[-3, 3] \times [-3, 3]$ with the initial conditions

$$\rho = \left(1 - \frac{(\gamma - 1)}{8\pi^2}(M\beta)^2 e^r\right)^{\frac{1}{\gamma - 1}}, \quad p = \frac{\rho^\gamma}{\gamma M^2}, \quad u = \frac{\beta}{2\pi R} y e^{\frac{r}{2}}, \quad v = -\frac{\beta}{2\pi R} x e^{\frac{r}{2}}, \tag{4.59}$$

where $r = \frac{1-(x^2+y^2)}{R^2}$, $R = 1.5$, $\beta = 13.5$, $\gamma = 1.4$, and $M = 0.4$. With the given initial conditions, the exact solution is stationary and given by (4.59). The L_1 errors in energy and the observed convergence rates for the second order DG approximation at $t = 0.5$ are reported in Table 4.2. Similar to the advecting sinusoidal wave problem, we see that the proposed limiter maintains the theoretical convergence rate and introduces only modest errors.

Mesh	Number of elements	L1 error	
		p = 1 limited	p = 1 (unlimited)
A	515	4.06e-01 (-)	2.85e-01 (-)
B	2047	8.93e-02 (2.18)	6.86e-02 (2.05)
C	8372	2.05e-02 (2.12)	1.7e-02 (2.01)
D	33532	5.19e-03 (1.98)	4.29e-03 (1.99)

Table 4.2: L_1 errors in energy for the stationary isentropic vortex test case at $t = 0.5$ on unstructured quadrilateral mesh. The numbers in parentheses are the observed rates of convergence.

4.2.4 Shock shock interactions.

Next, we test the performance of the limiter in the presence of shock-shock interactions. The initial condition for the test problem is taken from the two-dimensional Riemann test suite proposed in [55] (Figure 4.10). The simulation is run until $t = 0.8$ on a mesh of $160,660$ quadrilaterals. Figure 4.11 shows the density isolines at $t = 0.8$ obtained using the second order DG approximation. We note that the method is able to resolve the vortical structures along contact discontinuities well.

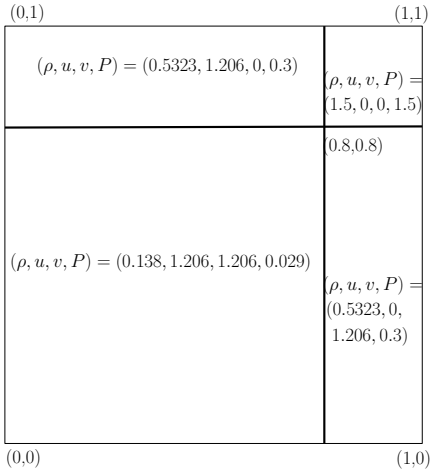

Figure 4.10: Initial condition for the 2D Riemann problem.

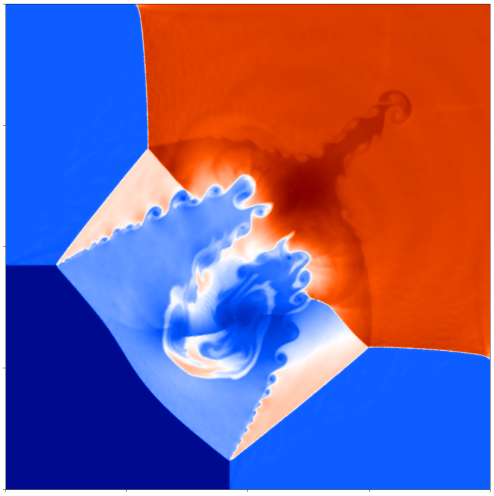

(a)

Figure 4.11: Density isolines at $t = 0.8$ for the shock-shock interaction example for $p = 1$ on a mesh of $160,660$ quadrilaterals.

4.2.5 Double Mach reflection.

Finally, we solve the double Mach reflection problem to test the performance of the proposed limiter in the presence of strong discontinuities. The initial set-up for the problem is taken from [25] and shown in Figure 4.12. The initial condition consists of a Mach 10 shock wave impinging on a reflecting wall at an angle of 60°. The states to the left ($\mathbf{U}_l$) and to the right ($\mathbf{U}_r$) of the shock wave are given in Table 4.3. The computational domain $[0, 3.5] \times [0, 1]$ is discretized into $230,266$ quadrilaterals. The simulation is run until $t = 0.2$. Figure 4.13 shows the density isolines obtained at $t = 0.2$ using the second order DG ap-

	$\mathbf{U}_l$	$\mathbf{U}_r$
ρ	8	1.4
$s = \mathbf{v} \cdot \mathbf{n}$	8.25	0
p	116.5	1

Table 4.3: States to the left and right of the initial shock for the double Mach test case.

proximation. We can observe the well-resolved shock structure as well as the vortices near the slip line (Figure 4.14).

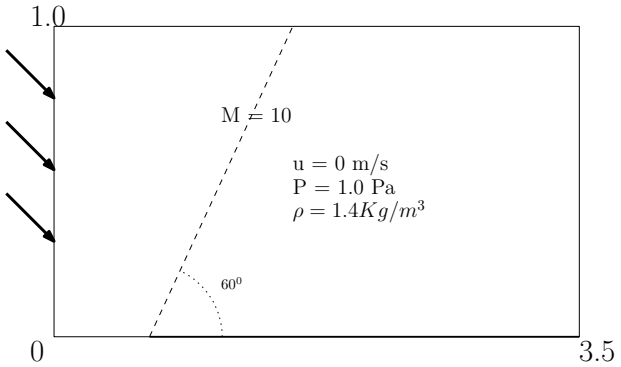

Figure 4.12: The initial set-up for the double Mach reflection test case.

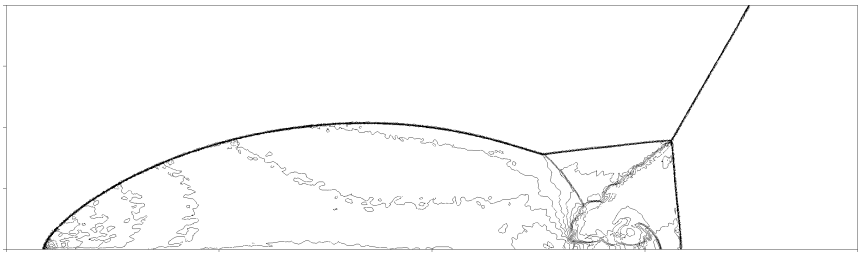

Figure 4.13: Density isolines at $t = 0.2$ for the double Mach test case for $p = 1$ with limiter on a final mesh of $230,266$ quadrilaterals.

Figure 4.14: Density isolines at $t = 0.2$ for the double Mach test case for $p = 1$ with limiter on a final mesh of $230,266$ quadrilaterals.

4.3 Summary

We have presented a stability analysis for a family of second order scalar slope limiters for the DG method on unstructured quadrilateral meshes. The limiter works by scaling the linear solution coefficients by a constant scaling factor $\gamma_i \in [0, 1]$. Further, we derive conditions on the limiter as well as the time step which ensure the solution satisfies the local maximum principle in the means. In this process, we also arrived at a new estimate for the cell size for a quadrilateral element.

Numerical experiments presented in Section 4.2 confirm that the DG method with the proposed limiter eliminates spurious oscillations and is robust in the presence of discontinuities. Further, the experiments also demonstrate that the limited solution retains the second order convergence rate for smooth solutions.

Chapter 5

Moment limiter on quadrilateral meshes

In this chapter, we propose a second order moment limiter for the DG method on unstructured quadrilateral meshes. The limiter can be viewed as an extension of the high-order moment limiter on Cartesian grids [25] and the second order moment limiter on triangular grids [2] to quadrilateral meshes. The proposed limiter works by decoupling solution coefficients as the directional derivatives of the numerical solution along two specially chosen directions (Figure 5.1) and then limiting by comparing them to forward and backward differences of the derivatives of one order less. The proposed limiter requires access to the solution from a compact and fixed stencil consisting of at most twelve neighboring elements. The parameters associated with the reconstruction stencil, e.g., geometric distances, element size etc, are computed in the preprocessing stage and stored. Further, we provide a range of values for scaling coefficients that relates the computed differences to the solution coefficient, which is similar to the range of stable slopes in the Sweby region [6]. With the prescribed range of values, the numerical solution in an element Ω_i satisfies a local maximum principle (LMP) (5.37) in its means which ensures stability of the numerical solution in the infinity norm.

We give a detailed description of the proposed limiter in Section 5.1. We provide a stability anaylsis of the second order DG method with the moment limiter for scalar linear conservation laws in Section 5.1.1 and derive a range of values for the scaling parameters of the solution coefficients in Section 5.1.2. Finally, we present numerical experiments in Section 5.2 to verify the performance of the proposed limiter.

5.1 Limiting algorithm

Consider the second order DG approximation on Ω_i, written as a linear combination of Legendre tensor product basis

$$U_i^n = \hat{U}_{i,0}^{n,0}\varphi_0^0(\zeta,\eta) + \hat{U}_{i,1}^{n,0}\varphi_1^0(\zeta,\eta) + \hat{U}_{i,0}^{n,1}\varphi_0^1(\zeta,\eta) + \hat{U}_{i,1}^{n,1}\varphi_1^1(\zeta,\eta), \tag{5.1}$$

where the constant and linear basis functions are

$$\varphi_0^0 = \frac{1}{2}, \quad \varphi_1^0 = \frac{\sqrt{3}}{2}\zeta, \quad \varphi_0^1 = \frac{\sqrt{3}}{2}\eta, \quad \varphi_1^1 = \frac{3}{2}\zeta\eta. \tag{5.2}$$

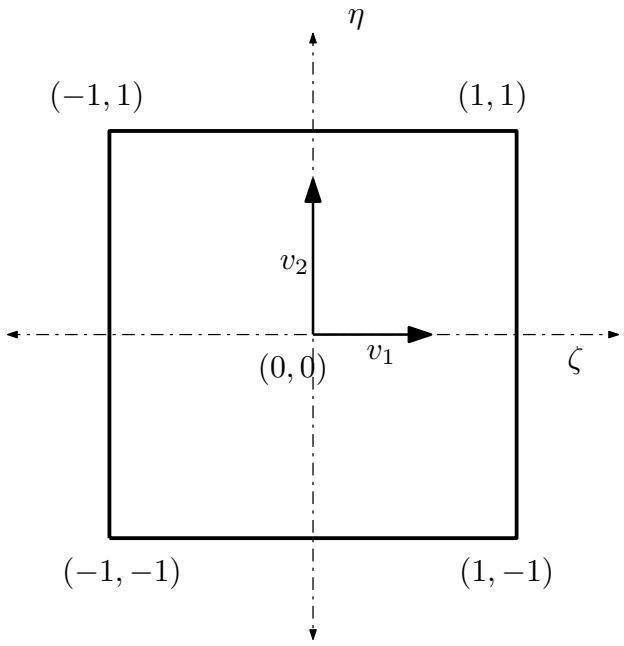

Figure 5.1: The canonical rectangle Ω_0.

The derivatives of U_i^n along the vectors $v_1 = (1,0)$ and $v_2 = (0,1)$ in the canonical space are

$$U_{i,\zeta}^n = \frac{\sqrt{3}}{2}\hat{U}_{i,1}^{n,0} + \frac{3}{2}\hat{U}_{i,1}^{n,1}\eta, \quad U_{i,\eta}^n = \frac{\sqrt{3}}{2}\hat{U}_{i,0}^{n,1} + \frac{3}{2}\hat{U}_{i,1}^{1}\zeta, \quad U_{i,\zeta\eta}^n = \frac{3}{2}\hat{U}_{i,1}^{n,1}. \tag{5.3}$$

Using (1.19), (1.20), (1.22), and the chain rule, the derivatives in (5.3) can be expressed

in terms of the derivatives of U_i^n in the physical space as

$$\begin{aligned} U_{i,\zeta}^n &= U_{i,x}^n x_\zeta + U_{i,y}^n y_\zeta, \quad U_{i,\eta}^n = U_{i,x}^n x_\eta + U_{i,y}^n y_\eta, \\ U_{i,\zeta\eta}^n &= U_{i,xx}^n x_\zeta x_\eta + U_{i,yy}^n y_\zeta y_\eta + U_{i,xy}^n (x_\eta y_\zeta + x_\zeta y_\eta) + U_{i,x}^n C_{i,x3} + U_{i,y}^n C_{i,y3}., \end{aligned} \tag{5.4}$$

where the coefficients $C_{i,\mathbf{x}}$ are defined in (1.21). Denote the kth directional derivative of U_i along v_1 and v_2 as

$$D_{v_1}^s D_{v_2}^{k-s} U_i = \frac{\partial^q}{\partial \zeta^s \partial \eta^{k-s}} U_i, \quad 0 \le s \le k, \quad k \le p. \tag{5.5}$$

Consider the directional derivatives $D_{v_1} U_i^n$ and $D_{v_2} U_i^n$. Using (5.3), the derivatives can be written as

$$D_{v_1} U_i^n = \frac{\sqrt{3}}{2} \hat{U}_{i,1}^{n,0} + \frac{3}{2} \hat{U}_{i,1}^{n,1} \eta, \quad D_{v_2} U_i^n = \frac{\sqrt{3}}{2} \hat{U}_{i,0}^{n,1} + \frac{3}{2} \hat{U}_{i,1}^{1} \zeta, \tag{5.6}$$

i.e., $D_{v_1} U_i^n$ and $D_{v_2} U_i^n$ are, respectively, linear in ζ and η. Now, under the transformation (1.19), the vectors v_1 and v_2 respectively map to the directions $\mathbf{v}_{i,1}$ and $\mathbf{v}_{i,2}$ in the physical space, given by

$$\mathbf{v}_{i,1} = (C_{i,x1}, C_{i,y1}), \quad \mathbf{v}_{i,2} = (C_{i,x2}, C_{i,y2}), \tag{5.7}$$

and passing through the cell centroid $\mathbf{x}_{i,0}$ of Ω_i. Further, the bilinear map (1.19) reduces to a linear transformation along $\zeta = 0$ and $\eta = 0$. Therefore, we can approximate $U_{i,1}^{n,1}$ by relating it to the forward and backward differences of $D_{v_1} U_i^n$ along $\mathbf{v}_{i,2}$ and $D_{v_2} U_i^n$ along $\mathbf{v}_{i,1}$.

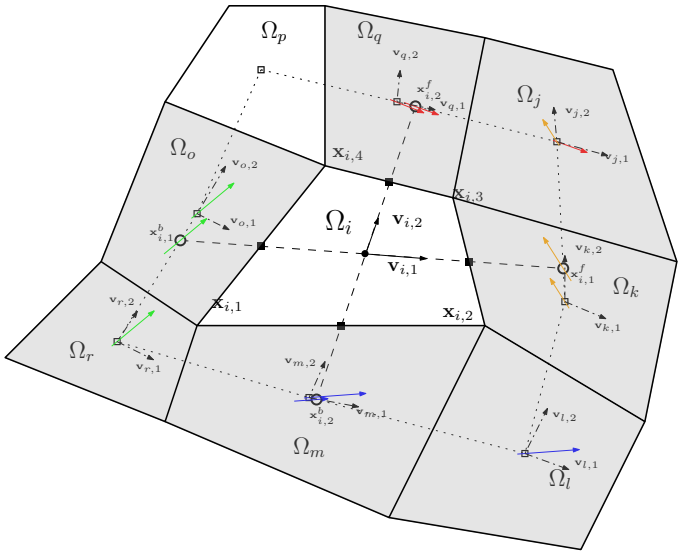

(a) Reconstruction stencil for $\hat{U}_{i,1}^{n,1}$.

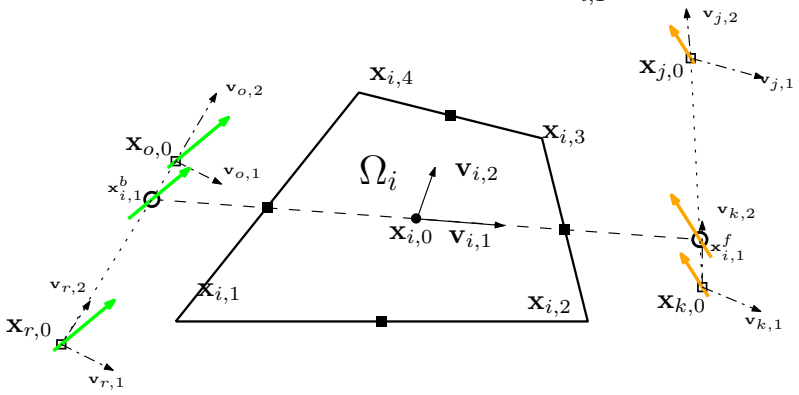

(b) Reconstruction stencil for $\hat{U}_{i,1}^{n,1}$ along $\mathbf{v}_{i,1}$.

Figure 5.2: Reconstruction stencil for the second order moment limiter.

To compute the forward and backward differences, we need to find the forward ($\mathbf{x}_{i,1}^f$ and $\mathbf{x}_{i,2}^f$), and backward ($\mathbf{x}_{i,1}^b$ and $\mathbf{x}_{i,2}^b$) interpolation points (Figure 5.2, hollow disks), evaluate the value of the directional derivatives at these points, and finally, compute their difference from the value at the cell centroid (Figure 5.2, solid circle). To find the interpolation points, we form a polygon by joining the cell centroids of the neighboring elements that share a vertex with Ω_i. Next, we define two lines parallel to $\mathbf{v}_{i,1}$ and $\mathbf{v}_{i,2}$ that pass through the centroid of Ω_i. The interpolation points $\mathbf{x}_{i,k}^f$, $\mathbf{x}_{i,k}^b$, $k = 1, 2$, are then the points of intersection of these lines and the sides of the polygon.

First, let's consider $D_{v_2} U_i^n$. From (5.3), we see that $\hat{U}_{i,1}^{n,1}$ is proportional to the derivative

of $D_{v_2}U_i^n$ along $\eta = 0$, i.e., we need to compute the forward and backward difference of $D_{v_2}U_i$ along $\mathbf{v}_{i,1}$ to limit $U_{i,1}^{n,1}$. To do so, we find the values of $D_{v_2}U_i^n$ at the forward and backward interpolation points $\mathbf{x}_{i,1}^f$ and $\mathbf{x}_{i,1}^b$ (Figure 5.2b).Let's consider the forward interpolation point $\mathbf{x}_{i,1}^f$. Under (1.19), $\mathbf{x}_{i,1}^f$ maps to the point $\zeta_1^f = (\dfrac{x_{i,1}^f - C_{i,x0}}{C_{i,x1}}, 0)$ in the canonical space. Now, consider the following vectors at $\mathbf{x}_{i,1}^f$

$$\mathbf{v}_{i,\zeta}^{1,f} = \left(C_{i,x1}, C_{i,y1}\right), \quad \mathbf{v}_{i,\eta}^{1,f} = \left(C_{i,x2} + C_{i,x3}\zeta_1^f, C_{i,y2} + C_{i,y3}\zeta_1^f\right). \tag{5.8}$$

Under the map (1.19) and by applying chain rule, the value of $D_{v_2}U_i^n$ at $\mathbf{x}_{i,1}^f$ can be written as

$$D_{v_2}U_i^n(\mathbf{x}_{i,1}^f) = D_{\mathbf{v}_{i,\eta}^{1,f}}U_i^n. \tag{5.9}$$

To find the approximate value of $D_{v_2}U_i^n$ at $\mathbf{x}_{i,1}^f$, we first compute the directional derivative $D_{\mathbf{v}_{i,\eta}^{1,f}}U$ at the cell centroids of the neighboring elements Ω_j and Ω_k. The computed values are then used to linearly interpolate the value of the directional derivative at $\mathbf{x}_{i,1}^f$. For example, consider the neighboring element Ω_k. Using (5.3), we compute the directional derivative $D_{\mathbf{v}_{i,\eta}^{1,f}}U$ at the cell centroid of Ω_k as

$$D_{\mathbf{v}_{i,\eta}^{1,f}}U_k^n = \alpha_{k,\eta}^{1,f}U_{k,\zeta}^n\Big|_{(0,0)} + \theta_{k,\eta}^{1,f}U_{k,\eta}^n\Big|_{(0,0)}. \tag{5.10}$$

Similarly, we compute the directional derivative $D_{\mathbf{v}_{i,\eta}^{1,f}}U$ at the cell centroid of the neighboring element Ω_j

$$D_{\mathbf{v}_{i,\eta}^{1,f}}U_j^n = \alpha_{j,\eta}^{1,f}U_{j,\zeta}^n\Big|_{(0,0)} + \theta_{j,\eta}^{1,f}U_{j,\eta}^n\Big|_{(0,0)}. \tag{5.11}$$

Finally, we linearly interpolate $D_{v_2}U_i^n(\mathbf{x}_{i,1}^f)$ using the directional derivatives computed in (5.10) and (5.11)

$$D_{v_2}U_i^n(\mathbf{x}_{i,1}^f) = D_{\mathbf{v}_{i,\eta}^{1,f}}U_i^n = \beta_{i,1}^f D_{\mathbf{v}_{i,\eta}^{1,f}}U_k^n + (1 - \beta_{i,1}^f)D_{\mathbf{v}_{i,\eta}^{1,f}}U_j^n, \tag{5.12}$$

where the interpolation weight $\beta_{i,1}^f$ is given by

$$\beta_{i,1}^f = \frac{\left\|\mathbf{x}_{j,0} - \mathbf{x}_{i,1}^f\right\|}{\left\|\mathbf{x}_{j,0} - \mathbf{x}_{k,0}\right\|}, \tag{5.13}$$

with $0 \le \beta_{i,1}^f \le 1$. In a similar fashion, we can estimate the value of $D_{v_2}U_i^n$ at the backward

interpolation point $\mathbf{x}_{i,1}^b$ as

$$D_{v_2}U_i^n(\mathbf{x}_{i,1}^b) = \beta_{i,1}^b D_{\mathbf{v}_{i,\eta}^{1,b}}U_r^n + (1-\beta_{i,1}^b)D_{\mathbf{v}_{i,\eta}^{1,b}}U_o^n. \tag{5.14}$$

Finally, we compute the limited solution coefficient $\tilde{U}_{i,1}^{n,1}$ by plugging the forward and backward differences into a one-dimensional slope limiter as

$$\tilde{U}_{i,1}^{n,1} \leftarrow \text{minmod}\left(\hat{U}_{i,1}^{n,1}, \frac{l_{i,1}^f}{|\zeta_1^{1,f}|}\left(\frac{2D_{v_2}U_i^n(\mathbf{x}_{i,1}^f)}{3} - \frac{1}{\sqrt{3}}\hat{U}_{i,0}^{n,1}\right), \frac{l_{i,1}^b}{|\zeta_1^{1,b}|}\left(\frac{1}{\sqrt{3}}\hat{U}_{i,0}^{n,1} - \frac{2D_{v_2}U_i^n(\mathbf{x}_{i,1}^b)}{3}\right)\right), \tag{5.15}$$

where minmod() is the minmod limiter given by

$$\text{minmod}(a,b,c) = \begin{cases} sign(a)\cdot min(|a|,|b|,|c|), & \text{if } sign(a) = sign(b) = sign(c), \\ 0, & \text{otherwise.} \end{cases} \tag{5.16}$$

Similarly, we compute the forward and backward differences of $D_{v_1}U_i^n$ along $\mathbf{v}_{i,2}$ and plug them into a one-dimensional slope limiter to find the limited solution coefficient $\tilde{U}_{i,1}^{n,1}$

$$\tilde{U}_{i,1}^{n,1} \leftarrow \text{minmod}\left(\tilde{U}_{i,1}^{n,1}, \frac{l_{i,2}^f}{|\eta_1^{1,f}|}\left(\frac{2D_{v_1}U_i^n(\mathbf{x}_{i,2}^f)}{3} - \frac{1}{\sqrt{3}}\hat{U}_{i,1}^{n,0}\right), \frac{l_{i,2}^b}{|\eta_1^{1,b}|}\left(\frac{1}{\sqrt{3}}\hat{U}_{i,1}^{n,0} - \frac{2D_{v_1}U_i^n(\mathbf{x}_{i,2}^b)}{3}\right)\right). \tag{5.17}$$

Next, we limit the linear solution coefficients $U_{i,1}^{n,0}$ and $U_{i,0}^{n,1}$. Substituting the basis functions (5.2) into (5.1), the solution U_i^n in Ω_i can be written as

$$U_i^n = \frac{1}{2}\hat{U}_{i,0}^{n,0} + \frac{\sqrt{3}}{2}\hat{U}_{i,1}^{n,0}\zeta + \frac{\sqrt{3}}{2}\hat{U}_{i,0}^{n,1}\eta + \frac{3}{2}\hat{U}_{i,1}^{n,1}\zeta\eta. \tag{5.18}$$

From (5.18), we note that U_i^n can be written as

$$U_i^n = \frac{1}{2}\hat{U}_{i,0}^{n,0} + \frac{\sqrt{3}}{2}\hat{U}_{i,1}^{n,0}\zeta, \tag{5.19}$$

along $\eta = 0$ and

$$U_i^n = \frac{1}{2}\hat{U}_{i,0}^{n,0} + \frac{\sqrt{3}}{2}\hat{U}_{i,0}^{n,1}\eta, \tag{5.20}$$

along $\zeta = 0$, i.e., we can find approximations for $\hat{U}_{i,1}^{n,0}$ and $\hat{U}_{i,0}^{n,1}$ by computing the forward and backward differences of the numerical solution along $\mathbf{v}_{i,1}$ and $\mathbf{v}_{i,2}$, respectively. Moreover, to ensure that the solution U_i^{n+1} satisfies (5.37), we would like to express the forward and backward differences in terms of solution averages. We aim to find a reconstruction stencil

with forward ($\mathbf{x}^f_{i,1c}$, $\mathbf{x}^f_{i,2c}$) and backward ($\mathbf{x}^b_{i,1c}$, $\mathbf{x}^b_{i,2c}$) interpolation points that enable us to do so. For this, we note that if the solution U^n_i were linear on Ω_i, the cell average $\overline{U}^n_i$ would be located at the center of mass of Ω_i, $\mathbf{x}_{i,c}$ (Figure 5.3a).

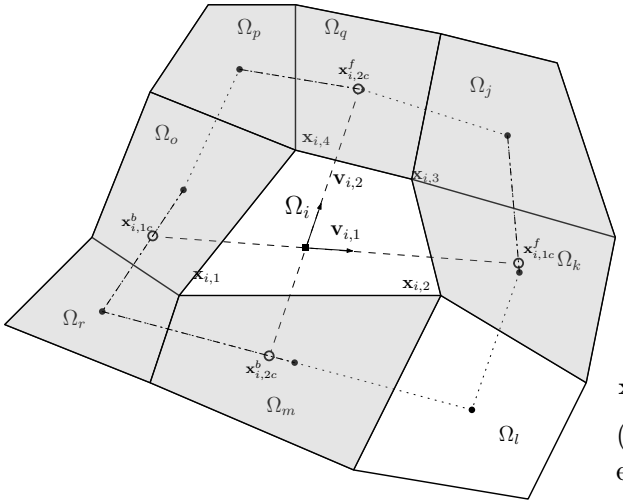

(a) Reconstruction stencil for linear solution coefficients $\hat{U}^{n,0}_{i,1}$ and $\hat{U}^{n,1}_{i,0}$.

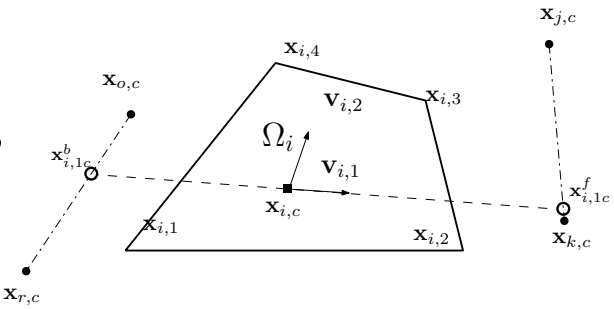

(b) Reconstruction stencil for linear solution coefficients $\hat{U}^{n,1}_{i,1}$ and $\hat{U}^{n,1}_{i,0}$ along $\mathbf{v}_{i,1}$.

Figure 5.3: Reconstruction stencil for the second order moment limiter.

To find the interpolation points, we form a polygon by joining the centers of mass of all neighboring elements that share a vertex with Ω_i. Next, we draw two lines parallel to $\mathbf{v}_{i,1}$ and $\mathbf{v}_{i,2}$ and passing through $\mathbf{x}_{i,c}$. The interpolation points are then given by the points of intersection of the two lines with the polygon (hollow points, Figure 5.3a). Finally, the values at the interpolation points are linearly interpolated using the cell averages from the closest neighboring elements, e.g., the value at the forward interpolation point $\mathbf{x}^f_{i,1c}$ is

$$U^f_{i,1c} = \beta^f_{i,1c}\overline{U}_k + \left(1 - \beta^f_{i,1c}\right)\overline{U}_j, \tag{5.21}$$

where the linear interpolation weight is given by

$$\beta^f_{i,1c} = \frac{\left\|\mathbf{x}_{j,c} - \mathbf{x}^f_{i,1c}\right\|}{\left\|\mathbf{x}_{j,c} - \mathbf{x}_{k,c}\right\|}, \tag{5.22}$$

with $0 \le \beta^f_{i,1c} \le 1$. Therefore, the limited linear coefficients $\tilde{U}^{n,0}_{i,1}$ and $\tilde{U}^{n,1}_{i,0}$ are given by

$$\begin{aligned}
\tilde{U}^{n,0}_{i,1} &= \text{minmod}\left(\hat{U}^{n,0}_{i,1}, \frac{2}{\sqrt{3}} l_{i,1} \frac{h_{i,1}}{d^f_{i,1c}} (U^f_{i,1c} - \overline{U}^n_i), \frac{2}{\sqrt{3}} \tilde{l}_{i,1} \frac{h_{i,1}}{d^b_{i,1c}} (\overline{U}_i - U^b_{i,1c})\right), \\
\tilde{U}^{n,1}_{i,0} &= \text{minmod}\left(\hat{U}^{n,1}_{i,0}, \frac{2}{\sqrt{3}} l_{i,2} \frac{h_{i,2}}{d^f_{i,2c}} (U^f_{i,2c} - \overline{U}^n_i), \frac{2}{\sqrt{3}} \tilde{l}_{i,2} \frac{h_{i,2}}{d^b_{i,2c}} (\overline{U}_i - U^b_{i,2c})\right),
\end{aligned} \tag{5.23}$$

where $\overline{U}^n_i$ is the solution average in Ω_i, the element lengths $h_{i,1}$ and $h_{i,2}$ are given by

$$h_{i,1} = \|\mathbf{v}_{i,1}\| = \sqrt{C^2_{i,x1} + C^2_{i,y1}}, \quad h_{i,2} = \|\mathbf{v}_{i,2}\| = \sqrt{C^2_{i,x2} + C^2_{i,y2}}, \tag{5.24}$$

where the coefficients $C_{i,\mathbf{x}}$ are defined in (1.21). Denoting the ratio of the backward and forward differences as

$$r_{i,1} = \left(\frac{d^f_{i,1c}}{d^b_{i,1c}}\right) \frac{\overline{U}^n_i - \overline{U}^b_{i,1c}}{\overline{U}^f_{i,1c} - \overline{U}^n_i}, \quad r_{i,2} = \left(\frac{d^f_{i,2c}}{d^b_{i,2c}}\right) \frac{\overline{U}^n_i - \overline{U}^b_{i,2c}}{\overline{U}^f_{i,2c} - \overline{U}^n_i}, \tag{5.25}$$

the limited linear solution coefficients in (5.23) can be written solely in terms of either the forward differences or the backward differences as

$$\begin{aligned}
\tilde{U}^{n,0}_{i,1} &= l_{i,1} \frac{2h_{i,1}}{\sqrt{3}} \frac{U^f_{i,1c} - \overline{U}^n_i}{d^f_{i,1c}} = l_{i,1} \frac{2h_{i,1}}{\sqrt{3}} \frac{\overline{U}^n_i - U^b_{i,1c}}{r_{i,1} d^b_{i,1c}} \\
\tilde{U}^{n,1}_{i,0} &= l_{i,2} \frac{2h_{i,2}}{\sqrt{3}} \frac{U^f_{i,2c} - \overline{U}^n_i}{d^f_{i,2c}} = l_{i,2} \frac{2h_{i,2}}{\sqrt{3}} \frac{\overline{U}^n_i - U^b_{i,2c}}{r_{i,2} d^b_{i,2c}}.
\end{aligned} \tag{5.26}$$

Finally, if the linear solution coefficients $\hat{U}^{n,1}_{i,0}$, and $\hat{U}^{n,0}_{i,1}$ are modified, we update the zeroth order solution coefficient $\hat{U}^{n,0}_{i,0}$ as

$$\hat{U}^{n,0}_{i,0} \leftarrow \hat{U}^{n,0}_{i,0} + \frac{\det J_{i,1}}{\sqrt{3} \det J_{i,0}} \left(\hat{U}^{n,0}_{i,1} - \tilde{U}^{n,0}_{i,1}\right) + \frac{\det J_{i,2}}{\sqrt{3} \det J_{i,0}} \left(\hat{U}^{n,1}_{i,0} - \tilde{U}^{n,1}_{i,0}\right), \tag{5.27}$$

to ensure that the cell average $\overline{U}^n_i$ remains unchanged.

In the next section, we establish the range of values of the scaling coefficients for which the numerical solution satisfies the LMP in means for linear advection.

5.1.1 Stability analysis for linear advection

The following analysis can be viewed as an extension of the stability analysis presented in [2] for triangular meshes to quadrilateral meshes. Consider the case where (1.8) is a scalar linear advection equation, i.e.,

$$u_t + \nabla \cdot (\mathbf{a}u) = 0. \tag{5.28}$$

Setting $k = l = 0$ in (1.19), we get

$$\frac{d\overline{U}_i}{dt} = -\frac{1}{|\Omega_i|} \sum_{j \in N_i^e} \int_{\delta\Omega_{i,j}} \mathbf{F}^*(U_i, U_j) \cdot \mathbf{n}_{i,j} dl. \tag{5.29}$$

After one Euler time step, the cell average in Ω_i is given by

$$\overline{U}_i^{n+1} = \overline{U}_i^n - \frac{\Delta t}{|\Omega_i|} \sum_{j \in N_i^e} \int_{\delta\Omega_{i,j}} \mathbf{F}^*(U_i, U_j) \cdot \mathbf{n}_{i,j} dl. \tag{5.30}$$

For linear advection, the flux in (1.8) is $\mathbf{F}(u) = u\mathbf{a}$, $\mathbf{a}$ being the flow direction. Choosing the upwind flux as the numerical flux gives us

$$\mathbf{F}^*(U_i, U_j) \cdot \mathbf{n}_{i,j} = \begin{cases} (\mathbf{a} \cdot \mathbf{n}_{i,j}) U_i, & \text{if } j \in N_i^+, \\ (\mathbf{a} \cdot \mathbf{n}_{i,j}) U_j, & \text{if } j \in N_i^-, \end{cases} \tag{5.31}$$

where N_i^+ and N_i^- are respectively the indices of the outflow and inflow neighbors of Ω_i, i.e., $N_i^\pm = \{ j \in N_i^e \,\big|\, \pm(\mathbf{a} \cdot \mathbf{n}_{i,j}) > 0 \}$. As the cell average $\overline{U}_i^n$ is a constant, from the divergence theorem we have

$$\sum_{j \in N_i^e} \int_{\delta\Omega_{i,j}} \overline{U}_i^n \mathbf{a} \cdot \mathbf{n}_{i,j} dl = \sum_{j \in N_i^+} \overline{U}_i^n |\mathbf{a} \cdot \mathbf{n}_{i,j}| |\delta\Omega_{i,j}| - \sum_{j \in N_i^-} \overline{U}_i^n |\mathbf{a} \cdot \mathbf{n}_{i,j}| |\delta\Omega_{i,j}| = 0. \tag{5.32}$$

Therefore, substituting (5.31) and (5.32) in (5.30) we get

$$\overline{U}_i^{n+1} = \overline{U}_i + \frac{\Delta t}{|\Omega_i|} \left[\sum_{j \in N_i^-} \left(U_j^n(\mathbf{x}_{i,j}) - \overline{U}_i \right) |\mathbf{a} \cdot \mathbf{n}_{j,i}| |\delta\Omega_{i,j}| - \sum_{j \in N_i^+} \left(U_i^n(\mathbf{x}_{i,j}) - \overline{U}_i \right) |\mathbf{a} \cdot \mathbf{n}_{i,j}| |\delta\Omega_{i,j}| \right] \tag{5.33}$$

If the solution is limited at time t_n, then (5.33) becomes

$$\overline{U}_i^{n+1} = \overline{U}_i + \frac{\Delta t}{|\Omega_i|}\left[\sum_{j\in N_i^-}\left(\tilde{U}_j^n(\mathbf{x}_{i,j}) - \overline{U}_i\right)|\mathbf{a}\cdot\mathbf{n}_{j,i}||\delta\Omega_{i,j}| - \sum_{j\in N_i^+}\left(\tilde{U}_i^n(\mathbf{x}_{i,j}) - \overline{U}_i\right)|\mathbf{a}\cdot\mathbf{n}_{i,j}||\delta\Omega_{i,j}|\right], \tag{5.34}$$

where $\tilde{U}^n$ is the limited solution.

We aim to rewrite (5.34) in the form

$$\overline{U}_i^{n+1} = \overline{U}_i^n + \sum_k \omega_k\left(U_k - \overline{U}_i^n\right), \tag{5.35}$$

where U_k is either the cell average or a convex combination of cell averages in some neighborhood of Ω_i. If the scaling coefficients ω_k satisfy

$$\omega_k \geq 0, \quad \text{and} \quad \sum_k \omega_k \leq 1, \tag{5.36}$$

then the right hand side of (5.35) is a convex combination of cell averages in some neighborhood of Ω_i, and thus, the numerical solution in Ω_i satisfies the local maximum principle (LMP) in the means, i.e.,

$$\min_{k\in\mathcal{N}_i}\overline{U}_k^n \leq \overline{U}_i^{n+1} \leq \max_{k\in\mathcal{N}_i}\overline{U}_k^n, \tag{5.37}$$

where $\mathcal{N}_i$ is a set containing the indices of Ω_i and its neighbors. We note that the cell average $\overline{U}_i^n$ can be written in terms of the solution coefficients as

$$\overline{U}_i^n = \frac{1}{2}\hat{U}_{i,0}^{n,0} + \frac{\sqrt{3}}{2}\frac{\alpha_i}{3}\hat{U}_{i,1}^{n,0} + \frac{\sqrt{3}}{2}\frac{\beta_i}{3}\hat{U}_{i,0}^{n,1}, \tag{5.38}$$

where α_i and β_i are geometric parameters given by

$$\alpha_i = \frac{\det J_{i,1}}{\det J_{i,0}}, \quad \beta_i = \frac{\det J_{i,2}}{\det J_{i,0}}, \tag{5.39}$$

that satisfy the following constraint

$$|\alpha_i| + |\beta_i| < 1. \tag{5.40}$$

Outflow

Consider the limited numerical solution $\tilde{U}_i^n$ on Ω_i evaluated at $\mathbf{x}_{i,j}$

$$\tilde{U}_i^n(\mathbf{x}_{i,j}) = \tilde{U}_{i,0}^{n,0}\varphi_0^0(\mathbf{r}_{i,j}) + \tilde{U}_{i,1}^{n,0}\varphi_1^0(\mathbf{r}_{i,j}) + \tilde{U}_{i,0}^{n,1}\phi_0^1(\mathbf{r}_{i,j}) + \tilde{U}_{i,1}^{n,1}\varphi_1^1(\mathbf{r}_{i,j}), \tag{5.41}$$

where $\mathbf{r}_{i,j}$ is a quadrature point on Ω_0. For the second order DG approximation of equations of the form (5.28), the quadrature points are the midpoints of the edges, i.e., one of the coordinates of $\mathbf{r}_{i,j}$ will be zero. Therefore, at the chosen quadrature points, $\varphi_1^1(\mathbf{r}_{i,j}) = 0$ and (5.41) reduces to

$$\tilde{U}_i^n(\mathbf{x}_{i,j}) = \tilde{U}_{i,0}^{n,0}\varphi_0^0(\mathbf{r}_{i,j}) + \tilde{U}_{i,1}^{n,0}\varphi_1^0(\mathbf{r}_{i,j}) + \tilde{U}_{i,0}^{n,1}\phi_0^1(\mathbf{r}_{i,j}). \tag{5.42}$$

Using (5.38) and (5.27), (5.42) can be rewritten as

$$\tilde{U}_i^n(\mathbf{x}_{i,j}) = \overline{U}_i^n + \tilde{U}_{i,1}^{n,0}\left(\varphi_1^0(\mathbf{r}_{i,j}) - \frac{1}{2\sqrt{3}}\alpha_i\right) + \tilde{U}_{i,0}^{n,1}\left(\phi_0^1(\mathbf{r}_{i,j}) - \frac{1}{2\sqrt{3}}\beta_i\right). \tag{5.43}$$

Replacing the limited linear solution coefficients with the expressions in (5.26) and using (5.25), (5.43) can be written as

$$\begin{aligned}\tilde{U}_i^n(\mathbf{x}_{i,j}) = \overline{U}_i^n &+ l_{i,1}\frac{2h_{i,1}}{\sqrt{3}d_{i,1c}^f}\left(\varphi_1^0(\mathbf{r}_{i,j}) - \frac{1}{2\sqrt{3}}\alpha_i\right)\left(U_{i,1c}^f - \overline{U}_i^n\right) \\ &+ l_{i,2}\frac{2h_{i,2}}{\sqrt{3}d_{i,2c}^f}\left(\varphi_0^1(\mathbf{r}_{i,j}) - \frac{1}{2\sqrt{3}}\beta_i\right)\left(U_{i,2c}^f - \overline{U}_i^n\right).\end{aligned} \tag{5.44}$$

To satisfy (5.36), we require the coefficients in front of the differences on the right hand side of (5.44) to be non-negative. If $\varphi_1^0(\mathbf{r}_{i,j}) \geq \frac{1}{2\sqrt{3}}\alpha_i$ and $\varphi_0^1(\mathbf{r}_{i,j}) \geq \frac{1}{2\sqrt{3}}\beta_i$, then this is satisfied. If not, using (5.25), we replace the forward difference in (5.44) with the corresponding backward difference

$$\begin{aligned}\frac{2h_{i,1}}{\sqrt{3}d_{i,1c}^f}\left(\varphi_1^0(\mathbf{r}_{i,j}) - \frac{1}{2\sqrt{3}}\alpha_i\right)\left(U_{i,1c}^f - \overline{U}_i^n\right) &= \frac{2h_{i,1}}{\sqrt{3}r_{i,1}d_{i,1c}^b}|\varphi_1^0(\mathbf{r}_{i,j}) - \frac{1}{2\sqrt{3}}\alpha_i|\left(\overline{U}_i^n - U_{i,1c}^b\right), \\ \frac{2h_{i,2}}{\sqrt{3}d_{i,2c}^f}\left(\varphi_0^1(\mathbf{r}_{i,j}) - \frac{1}{2\sqrt{3}}\beta_i\right)\left(U_{i,2c}^f - \overline{U}_i^n\right) &= \frac{2h_{i,2}}{\sqrt{3}r_{i,2}d_{i,2c}^b}|\varphi_0^1(\mathbf{r}_{i,j}) - \frac{1}{2\sqrt{3}}\beta_i|\left(\overline{U}_i^n - U_{i,2c}^b\right),\end{aligned} \tag{5.45}$$

to get non-negative multipliers. To serve this purpose, we define non-negative coefficients $\gamma^+_{i,j,1}$ and $\gamma^+_{i,j,2}$

$$\gamma^+_{i,j,1} = \begin{cases} \dfrac{2h_{i,1}}{\sqrt{3}d^f_{i,1c}}|\varphi^0_1(\mathbf{r}_{i,j}) - \dfrac{1}{2\sqrt{3}}\alpha_i|, & \text{if } \varphi^0_1(\mathbf{r}_{i,j}) \le \dfrac{1}{2\sqrt{3}}\alpha_i, \\ \dfrac{2h_{i,1}}{\sqrt{3}r_{i,1}d^b_{i,1c}}|\varphi^0_1(\mathbf{r}_{i,j}) - \dfrac{1}{2\sqrt{3}}\alpha_i|, & \text{otherwise.} \end{cases}, \\ \gamma^+_{i,j,2} = \begin{cases} \dfrac{2h_{i,2}}{\sqrt{3}d^f_{i,2c}}|\varphi^1_0(\mathbf{r}_{i,j}) - \dfrac{1}{2\sqrt{3}}\beta_i|, & \text{if } \varphi^1_0(\mathbf{r}_{i,j}) \le \dfrac{1}{2\sqrt{3}}\beta_i, \\ \dfrac{2h_{i,2}}{\sqrt{3}r_{i,2}d^b_{i,2c}}|\varphi^1_0(\mathbf{r}_{i,j}) - \dfrac{1}{2\sqrt{3}}\beta_i|, & \text{otherwise.} \end{cases}, \tag{5.46}$$

where $d^f_{i,k}$ and $d^b_{i,k}$ are respectively the distances of the interpolation points $\mathbf{x}^f_{i,k}$ and $\mathbf{x}^b_{i,k}$ from the center of mass $\mathbf{x}_{i,c}$, for $k = \{1c, 2c\}$ and the ratios $r_{i,1}$ and $r_{i,2}$ are given in (5.25). Plugging (5.46) into (5.44), we can write the difference $\tilde{U}^n_i(\mathbf{x}_{i,j}) - \overline{U}^n_i$ in the outflow term in (5.34) as

$$\begin{aligned} \tilde{U}^n_i(\mathbf{x}_{i,j}) - \overline{U}^n_i &= -l_{i,1}\gamma^+_{i,j,1}\left(U_{i,j,1} - \overline{U}^n_i\right) - l_{i,2}\gamma^+_{i,j,2}\left(U_{i,j,2} - \overline{U}^n_i\right) \\ &= -\theta_{i,j,1}\left(U_{i,j,1} - \overline{U}^n_i\right) - \theta_{i,j,2}\left(U_{i,j,2} - \overline{U}^n_i\right), \end{aligned} \tag{5.47}$$

where the values $U_{i,j,1}$ and $U_{i,j,2}$ are

$$U_{i,j,1} = \begin{cases} U^f_{i,1c}, & \text{if } \varphi^0_1(\mathbf{r}_{i,j}) \le \dfrac{1}{2\sqrt{3}}\alpha_i, \\ U^b_{i,1c}, & \text{otherwise.} \end{cases} \qquad U_{i,j,2} = \begin{cases} U^f_{i,2c}, & \text{if } \varphi^1_0(\mathbf{r}_{i,j}) \le \dfrac{1}{2\sqrt{3}}\beta_i, \\ U^b_{i,2c}, & \text{otherwise.} \end{cases} . \tag{5.48}$$

Inflow

Consider the limited numerical solution $\tilde{U}^n_j$ on an inflow neighbor of Ω_i, Ω_j, $j \in N^-_i$, evaluated at $\mathbf{x}_{i,j}$

$$\tilde{U}^n_j(\mathbf{x}_{i,j}) = \tilde{U}^{n,0}_{j,0}\varphi^0_0(\mathbf{r}_{j,i}) + \tilde{U}^{n,0}_{j,1}\varphi^0_1(\mathbf{r}_{j,i}) + \tilde{U}^{n,1}_{j,0}\phi^1_0(\mathbf{r}_{j,i}) + \tilde{U}^{n,1}_{j,1}\varphi^1_1(\mathbf{r}_{j,i}), \tag{5.49}$$

where $\mathbf{r}_{j,i}$ is a quadrature point on Ω_0. Again, as a result of the choice of the quadrature points and the arguments made in Section 5.1.1, (5.49) can be rewritten as

$$\tilde{U}^n_j(\mathbf{x}_{i,j}) = \overline{U}^n_j + \tilde{U}^{n,0}_{j,i}\left(\varphi^0_1(\mathbf{r}_{j,i}) - \frac{1}{2\sqrt{3}}\alpha_j\right) + \tilde{U}^{n,1}_{j,0}\left(\phi^1_0(\mathbf{r}_{j,i}) - \frac{1}{2\sqrt{3}}\beta_j\right). \tag{5.50}$$

Replacing the limited linear solution coefficients with the expressions in (5.26) and using (5.25), (5.50) can be written as

$$\begin{aligned}\tilde{U}_j^n(\mathbf{x}_{i,j}) = \overline{U}_j^n &+ l_{j,1}\frac{2h_{j,1}}{\sqrt{3}d_{j,1c}^f}\left(\varphi_1^0(\mathbf{r}_{j,i}) - \frac{1}{2\sqrt{3}}\alpha_j\right)\left(U_{j,1c}^f - \overline{U}_j^n\right)\\ &+ l_{j,2}\frac{2h_{j,2}}{\sqrt{3}d_{j,2c}^f}\left(\varphi_0^1(\mathbf{r}_{j,i}) - \frac{1}{2\sqrt{3}}\beta_j\right)\left(U_{j,2c}^f - \overline{U}_j^n\right).\end{aligned} \tag{5.51}$$

Proceeding as in Section 5.1.1 for outflow terms, we define two non negative coefficients $\gamma_{j,i,1}^-$ and $\gamma_{j,i,2}^-$

$$\gamma_{j,i,1}^- = \begin{cases}\dfrac{2h_{j,1}}{\sqrt{3}d_{j,1c}^f}\left|\varphi_1^0(\mathbf{r}_{j,i}) - \dfrac{1}{2\sqrt{3}}\alpha_j\right|, & \text{if } \varphi_1^0(\mathbf{r}_{j,i}) \geq \dfrac{1}{2\sqrt{3}}\alpha_j,\\ \dfrac{2h_{j,1}}{\sqrt{3}r_{j,1}d_{j,1c}^b}\left|\varphi_1^0(\mathbf{r}_{j,i}) - \dfrac{1}{2\sqrt{3}}\alpha_j\right|, & \text{otherwise.}\end{cases},$$

$$\gamma_{j,i,2}^- = \begin{cases}\dfrac{2h_{j,2}}{\sqrt{3}d_{j,2c}^f}\left|\varphi_0^1(\mathbf{r}_{j,i}) - \dfrac{1}{2\sqrt{3}}\beta_j\right|, & \text{if } \varphi_0^1(\mathbf{r}_{j,i}) \leq \dfrac{1}{2\sqrt{3}}\beta_j,\\ \dfrac{2h_{j,2}}{\sqrt{3}r_{j,2}d_{j,2c}^b}\left|\varphi_0^1(\mathbf{r}_{j,i}) - \dfrac{1}{2\sqrt{3}}\beta_j\right|, & \text{otherwise.}\end{cases}, \tag{5.52}$$

where $d_{j,k}^f$ and $d_{j,k}^b$ are, respectively, the distances of the interpolation points $\mathbf{x}_{j,k}^f$ and $\mathbf{x}_{j,k}^b$ from the center of mass $\mathbf{x}_{j,c}$, for $k = \{1c, 2c\}$, and the ratios $r_{j,1}$ and $r_{j,2}$ are given in (5.25). Therefore, plugging (5.52) into (5.51), the difference $\tilde{U}_j^n(\mathbf{x}_{i,j}) - \overline{U}_i^n$ in the inflow term in (5.34) can be written as

$$\begin{aligned}\tilde{U}_j^n(\mathbf{x}_{i,j}) - \overline{U}_i^n &= \overline{U}_j^n - \overline{U}_i^n + l_{j,1}\gamma_{j,i,1}^-\left(U_{j,i,1} - \overline{U}_j^n \pm \overline{U}_i^n\right) + l_{j,2}\gamma_{j,i,2}^-\left(U_{j,i,2} - \overline{U}_j^n \pm \overline{U}_i^n\right)\\ &= \left(1 - l_{j,1}\gamma_{j,i,1}^- - l_{j,2}\gamma_{j,i,2}^-\right)\left(\overline{U}_j^n - \overline{U}_i^n\right) + l_{j,1}\gamma_{j,i,1}^-\left(U_{j,i,1} - \overline{U}_i^n\right) + l_{j,2}\gamma_{j,i,2}^-\left(U_{j,i,2} - \overline{U}_i^n\right)\\ &= \theta_{j,i,0}(\overline{U}_j^n - \overline{U}_i^n) + \theta_{j,i,1}\left(U_{j,i,1} - \overline{U}_i^n\right) + \theta_{j,i,2}\left(U_{j,i,2} - \overline{U}_i^n\right),\end{aligned} \tag{5.53}$$

where the values $U_{j,i,1}$ and $U_{j,i,2}$ are

$$U_{j,i,1} = \begin{cases}U_{j,1c}^f, & \text{if } \varphi_1^0(\mathbf{r}_{j,i}) \geq \dfrac{1}{2\sqrt{3}}\alpha_j,\\ U_{j,1c}^b, & \text{otherwise.}\end{cases} \qquad U_{j,i,2} = \begin{cases}U_{j,2c}^f, & \text{if } \varphi_0^1(\mathbf{r}_{j,i}) \geq \dfrac{1}{2\sqrt{3}}\beta_j,\\ U_{j,2c}^b, & \text{otherwise.}\end{cases}. \tag{5.54}$$

For the multipliers on the right hand side of (5.53) to be non negative, we need to impose

$$l_{j,1}\gamma^{-}_{j,i,1} + l_{j,2}\gamma^{-}_{j,i,2} \leq 1, \quad \forall j \in N_i^{-}. \tag{5.55}$$

Putting it together

Denoting $\lambda^{-}_{j,i} = \dfrac{|\mathbf{a}\cdot\mathbf{n}_{j,i}||\delta\Omega_{i,j}|}{|\Omega_i|}$, $\lambda^{+}_{i,j} = \dfrac{|\mathbf{a}\cdot\mathbf{n}_{i,j}||\delta\Omega_{i,j}|}{|\Omega_i|}$ and plugging (5.53) and (5.47) into (5.34), we get

$$\begin{aligned}\overline{U}_i^{n+1} = \overline{U}_i^n + \Delta t \sum_{j\in N_i^-} \lambda^{-}_{j,i}[\theta_{j,i,0}(\overline{U}_j^n - \overline{U}_i^n) + \theta_{j,i,1}\left(U_{j,i,1} - \overline{U}_i^n\right) + \theta_{j,i,2}\left(U_{j,i,2} - \overline{U}_i^n\right)] \\ +\Delta t \sum_{j\in N_i^+} \lambda^{+}_{i,j}[\theta_{i,j,1}\left(U_{i,j,1} - \overline{U}_i^n\right) + \theta_{i,j,2}\left(U_{i,j,2} - \overline{U}_i^n\right)],\end{aligned} \tag{5.56}$$

which is of the form (5.35). Moreover, we require the sum of the multipliers to be less than one, i.e.,

$$\begin{aligned}\Delta t \sum_{j\in N_i^-} \lambda^{-}_{j,i}[\theta_{j,i,0} + \theta_{j,i,1} + \theta_{j,i,2}] + \Delta t \sum_{j\in N_i^+} \lambda^{+}_{i,j}[\theta_{i,j,1} + \theta_{i,j,2}] \leq 1 \\ \Delta t \sum_{j\in N_i^-} \lambda^{-}_{j,i}[\left(1 - l_{j,1}\gamma^{-}_{j,i,1} - l_{j,2}\gamma^{-}_{j,i,2}\right) + l_{j,1}\gamma^{-}_{j,i,1} + l_{j,2}\gamma^{-}_{j,i,2}] + \Delta t \sum_{j\in N_i^+} \lambda^{+}_{i,j}[l_{i,1}\gamma^{+}_{i,j,1} + l_{i,2}\gamma^{+}_{i,j,2}] \leq 1 \\ \Delta t \sum_{j\in N_i^-} \lambda^{-}_{j,i} + \Delta t \sum_{j\in N_i^+} \lambda^{+}_{i,j}[l_{i,1}\gamma^{+}_{i,j,1} + l_{i,2}\gamma^{+}_{i,j,2}] \leq 1.\end{aligned} \tag{5.57}$$

Inequalities (5.57) are satisfied if we enforce an additional condition

$$l_{i,1}\gamma^{+}_{i,j,1} + l_{i,2}\gamma^{+}_{i,j,2} \leq 1, \quad \forall j \in N_i^{+}, \tag{5.58}$$

on all outflow edges of Ω_i, and the following restriction on the time step size Δt

$$\begin{aligned}\Delta t[\sum_{j\in N_j^-} \lambda^{-}_{j,i} + \sum_{j\in N_i^+} \lambda^{+}_{i,j}] \leq 1 \\ \Delta t\left[\sum_{j\in N_j^-} \frac{|\mathbf{a}\cdot\mathbf{n}_{j,i}||\delta\Omega_{i,j}|}{|\Omega_i|} + \sum_{j\in N_i^+} \frac{|\mathbf{a}\cdot\mathbf{n}_{i,j}||\delta\Omega_{i,j}|}{|\Omega_i|}\right] \leq 1.\end{aligned} \tag{5.59}$$

Using the divergence theorem, we get

$$\sum_{j \in N_i^-} |\mathbf{a} \cdot \mathbf{n}_{j,i}| \|\delta\Omega_{i,j}| = \sum_{j \in N_i^+} |\mathbf{a} \cdot \mathbf{n}_{j,i}| \|\delta\Omega_{i,j}|. \tag{5.60}$$

Plugging (5.60) into (5.59), the restriction on the time step reduces to

$$\Delta t \leq \frac{1}{2} \frac{|\Omega_i|}{\sum_{j \in N_i^+} |\mathbf{a} \cdot \mathbf{n}_{i,j}| \|\delta\Omega_{i,j}|}. \tag{5.61}$$

Following the steps presented in Section 4.1.1 from Chapter 4 to find an estimate for the cell size h_i, we arrive at the following time step restriction

$$\Delta t \leq \frac{1}{4} \min_i \frac{h_i}{\|\mathbf{a}\|}, \tag{5.62}$$

where h_i, the smallest height of element Ω_i (Figure 5.4), is given by

$$\begin{aligned} h_i &= \min(h_1, h_2), \\ h_1 &= \min(\max(\min(H_{i,12}, H_{i,13}), \min(H_{i,34}, H_{i,31})), \max(\min(H_{i,24}, H_{i,23}), \\ &\quad \min(H_{i,41}, H_{i,42}))), \\ h_2 &= \min(\max(H_{i,41}, H_{i,31}), \max(H_{i,12}, H_{i,42}), \max(H_{i,13}, H_{i,23}), \max(H_{i,24}, H_{i,34})). \end{aligned} \tag{5.63}$$

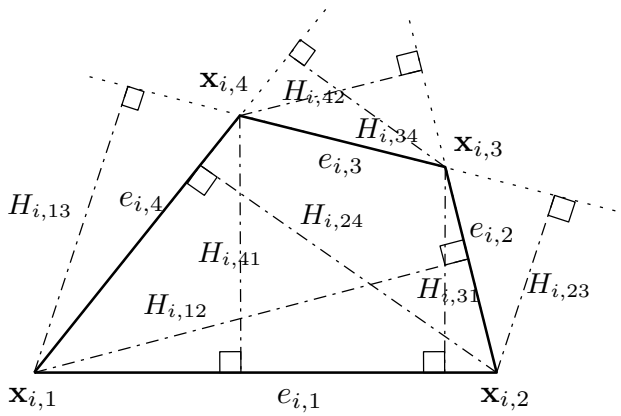

Figure 5.4: Element size h_i.

5.1.2 Scaling Coefficients

For the numerical solution U_i^{n+1} in the element Ω_i to satisfy the LMP (5.37) in means, the scaling coefficients for the limited linear solution coefficients must satisfy the following conditions

1.
$$l_{i,1}\gamma^+_{i,j,1} + l_{i,2}\gamma^+_{i,j,2} \leq 1, \quad \forall j \in N_i^+, \tag{5.64}$$
on each outflow edge of Ω_i and

2.
$$l_{j,1}\gamma^-_{j,i,1} + l_{j,2}\gamma^-_{j,i,2} \leq 1, \quad \forall j \in N_i^-, \tag{5.65}$$
on each inflow edge of Ω_i,

where the non negative coefficients γ are defined in (5.52) and (5.46). Consider an outflow edge of Ω_i with edge number s. We can enforce two constraints on the scaling coefficients $l_{i,1}$ and $l_{i,2}$, i.e., (5.64) on the outflow edge of Ω_i and (5.65) on the inflow edge of a neighboring element Ω_j. As we have already noted, the basis functions in (5.52) and (5.46) are evaluated at the edge midpoints, with the corresponding values reported in Table 5.1. Moreover, the geometric parameters in (5.52) and (5.46) depend on the mapping of Ω_i to Ω_0 and are evaluated in the pre-processing stage.

s	ϕ_1^0	ϕ_0^1
1	0	$-\sqrt{3}/2$
2	$\sqrt{3}/2$	0
3	0	$\sqrt{3}/2$
4	$-\sqrt{3}/2$	0

Table 5.1: Values of the basis functions evaluated at the midpoints of the edges of canonical element Ω_0.

Consider the edge $s = 1$. Further, assume it's an outflow edge. Depending on whether the inequalities
$$\alpha_i \geq 0, \quad \beta_i \geq -3, \tag{5.66}$$

hold true or not, (5.52) and (5.46) reduce to one of the following constraints

$$\begin{aligned} l_{i,1}\frac{1}{3\lambda^f_{i,1c}}|\alpha_i| + l_{i,2}\frac{1}{3\lambda^f_{i,2c}}|3+\beta_i| \le 1, \quad l_{i,1}\frac{1}{3r_{i,1}\lambda^b_{i,1c}}|\alpha_i| + l_{i,2}\frac{1}{3\lambda^f_{i,2c}}|3+\beta_i| \le 1, \\ l_{i,1}\frac{1}{3\lambda^f_{i,1c}}|\alpha_i| + l_{i,2}\frac{1}{3r_{i,2}\lambda^b_{i,2c}}|3+\beta_i| \le 1, \quad l_{i,1}\frac{1}{3r_{i,1}\lambda^b_{i,1c}}|\alpha_i| + l_{i,2}\frac{1}{3r_{i,2}\lambda^b_{i,2c}}|3+\beta_i| \le 1, \end{aligned} \tag{5.67}$$

where $\lambda^f_{i,kc} = \dfrac{d^f_{i,kc}}{h_{i,k}}$ and $\lambda^b_{i,kc} = \dfrac{d^b_{i,kc}}{h_{i,k}}$, $k = \{1,2\}$. The geometric constants α_i and β_i given by (5.39) depend on how Ω_i maps to Ω_0 and thus varies from element to element. Therefore, the reduced form of (5.52) and (5.46) depend on the mapping of an element and can be cumbersome to code. Thus, it is convenient to consider the simplified and more restrictive constraint

$$l_{i,1}\frac{1}{3\min\{r_{i,1}\lambda^b_{i,1c}, \lambda^f_{i,1c}\}}|\alpha_i| + l_{i,2}\frac{1}{3\min\{r_{i,2}\lambda^b_{i,2c}, \lambda^f_{i,2c}\}}|3+\beta_i| \le 1. \tag{5.68}$$

Following a similar procedure for the other edges, if the edge s is an outflow edge, then (5.52) and (5.46) reduce to

$$l_{i,1}\frac{1}{3\min\{r_{i,1}\lambda^b_{i,1c}, \lambda^f_{i,1c}\}}|\alpha_i| + l_{i,2}\frac{1}{3\min\{r_{i,2}\lambda^b_{i,2c}, \lambda^f_{i,2c}\}}|3+\beta_i| \le 1 \quad \text{if } s=1 \tag{5.69}$$

$$l_{i,1}\frac{1}{3\min\{r_{i,1}\lambda^b_{i,1c}, \lambda^f_{i,1c}\}}|3-\alpha_i| + l_{i,2}\frac{1}{3\min\{r_{i,2}\lambda^b_{i,2c}, \lambda^f_{i,2c}\}}|\beta_i| \le 1 \quad \text{if } s=2 \tag{5.70}$$

$$l_{i,1}\frac{1}{3\min\{r_{i,1}\lambda^b_{i,1c}, \lambda^f_{i,1c}\}}|\alpha_i| + l_{i,2}\frac{1}{3\min\{r_{i,2}\lambda^b_{i,2c}, \lambda^f_{i,2c}\}}|3-\beta_i| \le 1 \quad \text{if } s=3 \tag{5.71}$$

$$l_{i,1}\frac{1}{3\min\{r_{i,1}\lambda^b_{i,1c}, \lambda^f_{i,1c}\}}|3+\alpha_i| + l_{i,2}\frac{1}{3\min\{r_{i,2}\lambda^b_{i,2c}, \lambda^f_{i,2c}\}}|\beta_i| \le 1 \quad \text{if } s=4. \tag{5.72}$$

To find suitable scaling coefficients $l_{i,1}$ and $l_{i,2}$ during runtime, we need to identify the outflow edges of Ω_i, identify the edges on the canonical element Ω_0 to which they are mapped, and finally, select appropriate constraints from (5.69) - (5.72). This is computationally expensive. Instead, using the triangle inequalities

$$|3+f| \le 3+|f|, \quad |3-f| \le 3+|f|, \quad f = \{\alpha_i, \beta_i\}, \tag{5.73}$$

we can reduce (5.69) - (5.72) to a slightly more restrictive set of constraints

$$\begin{aligned} l_{i,1}\frac{1}{\min\{r_{i,1}\lambda^b_{i,1c},\lambda^f_{i,1c}\}}\frac{1}{3}|\alpha_i| + l_{i,2}\frac{1}{\min\{r_{i,2}\lambda^b_{i,2c},\lambda^f_{i,2c}\}}\left(1+\frac{1}{3}|\beta_i|\right) \le 1 \\ l_{i,1}\frac{1}{\min\{r_{i,1}\lambda^b_{i,1c},\lambda^f_{i,1c}\}}\left(\frac{1}{3}|\alpha_i|+1\right) + l_{i,2}\frac{1}{\min\{r_{i,2}\lambda^b_{i,2c},\lambda^f_{i,2c}\}}\frac{1}{3}|\beta_i| \le 1. \end{aligned} \tag{5.74}$$

Using the notations $\tilde{l}_{i,1} = \dfrac{l_{i,1}}{\min\{r_{i,1}\lambda^b_{i,1c},\lambda^f_{i,1c}\}}$ and $\tilde{l}_{i,2} = \dfrac{l_{i,2}}{\min\{r_{i,2}\lambda^b_{i,2c},\lambda^f_{i,2c}\}}$, (5.74) can be written as

$$\frac{1}{3}|\alpha_i|\tilde{l}_{i,1} + \left(1+\frac{1}{3}|\beta_i|\right)\tilde{l}_{i,2} \le 1, \quad \left(1+\frac{1}{3}|\alpha_i|\right)\tilde{l}_{i,1} + \frac{1}{3}|\beta_i|\tilde{l}_{i,2} \le 1. \tag{5.75}$$

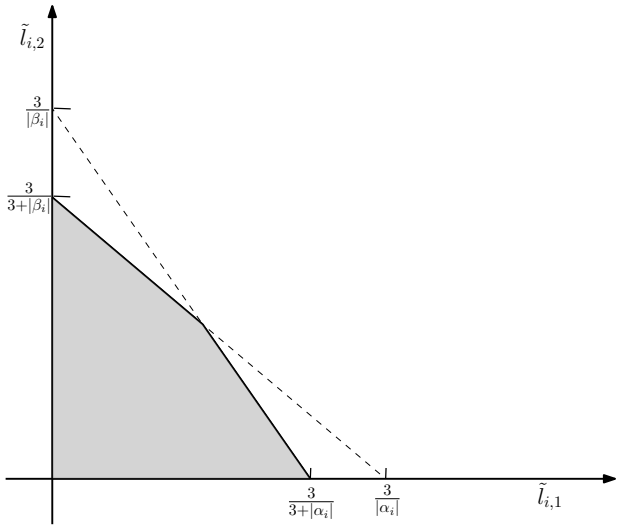

Figure 5.5: Simplified set of inequalities for element Ω_i. The shaded region is the region of admissible scaling coefficients $\tilde{l}_i$.

Figure 5.5 shows the region of admissible solutions of (5.75), i.e., choosing any set of scaling coefficients that lies in the shaded region leads to a limited numerical solution that satisfies LMP (5.37) in the means. To ensure that the scaling coefficients are not too small,

we choose the set of scaling coefficients from the top boundary of the shaded region, i.e.,

$$
\begin{aligned}
l_{i,1} &= \delta \ \min(\lambda^f_{i,1}, r_{i,1}\lambda^b_{i,1}), \\
l_{i,2} &= \begin{cases} \dfrac{3}{3+|\beta_i|}(1-\delta\dfrac{|\alpha_i|}{3}) \ \min(\lambda^f_{i,2}, r_{i,2}\lambda^b_{i,2}), & \text{if } \delta \in [\dfrac{3(1-|\beta_i|)}{4|\alpha_i|}), \dfrac{3}{3+|\alpha_i|+|\beta_i|}], \\ \dfrac{3}{|\beta_i|}(1-\delta\dfrac{|3+\alpha_i|}{3}) \ \min(\lambda^f_{i,2}, r_{i,2}\lambda^b_{i,2}), & \text{if } \delta \in [\dfrac{3}{3+|\alpha_i|+|\beta_i|}, \dfrac{3}{4}]. \end{cases}
\end{aligned} \tag{5.76}
$$

For the numerical experiments presented in Section 5.2, we choose the following set of scaling coefficients

$$
\tilde{l}_{1,i} = \tilde{l}_{2,i} = \frac{1}{1+\dfrac{|\alpha_i|+|\beta_i|}{3}}. \tag{5.77}
$$

5.1.3 Geometric constraints

For a linear solution, the solution coefficients must not be altered to maintain second order accuracy, i.e., $l_{i,1},\ l_{i,2} \geq 1$ which implies

$$
\begin{aligned}
\delta \min(\lambda^f_{i,1}, r_{i,1}\lambda^b_{i,1}) &\geq 1, \\
\frac{3}{3+|\beta_i|}(1-\delta\frac{|\alpha_i|}{3}) \ \min(\lambda^f_{i,2}, r_{i,2}\lambda^b_{i,2}) &\geq 1, \ \text{if } \delta \in [\frac{3(1-|\beta_i|)}{4|\alpha_i|}), \frac{3}{3+|\alpha_i|+|\beta_i|}], \\
\frac{3}{|\beta_i|}(1-\delta\frac{3+|\alpha_i|}{3}) \ \min(\lambda^f_{i,2}, r_{i,2}\lambda^b_{i,2}) &\geq 1, \ \text{if } \delta \in [\frac{3}{3+|\alpha_i|+|\beta_i|}, \frac{3}{4}].
\end{aligned} \tag{5.78}
$$

Noting that the ratio of the backward and forward differences for a linear solution is one, i.e., $r_{i,1} = r_{i,2} = 1$ and plugging $\lambda^f_{i,k} = \dfrac{d^f_{i,kc}}{h_{i,k}}$ and $\lambda^b_{i,k} = \dfrac{d^b_{i,kc}}{h_{i,k}}$, $k = \{1,2\}$, into (5.78), we get

$$
\begin{aligned}
\min(d^f_{i,1c}, d^b_{i,1c}) &\geq \frac{h_{i,1}}{\delta} \\
\min(d^f_{i,2}, d^b_{i,2}) &\geq \frac{3+|\beta_i|}{3-|\alpha_i|\delta} h_{i,2}, \ \delta \in [\frac{3(1-|\beta_i|)}{4|\alpha_i|}), \frac{3}{3+|\alpha_i|+|\beta_i|}], \\
\min(d^f_{i,2}, d^b_{i,2}) &\geq \frac{|\beta_i|}{3(1-\delta)-|\alpha_i|\delta} h_{i,2}, \ \delta \in [\frac{3}{3+|\alpha_i|+|\beta_i|}, \frac{3}{4}].
\end{aligned} \tag{5.79}
$$

Thus, for the limited solution to retain the second order accuracy, depending on the choice of δ, the interpolation points must lie at a certain distance from the center of mass of an element (Figure 5.6).

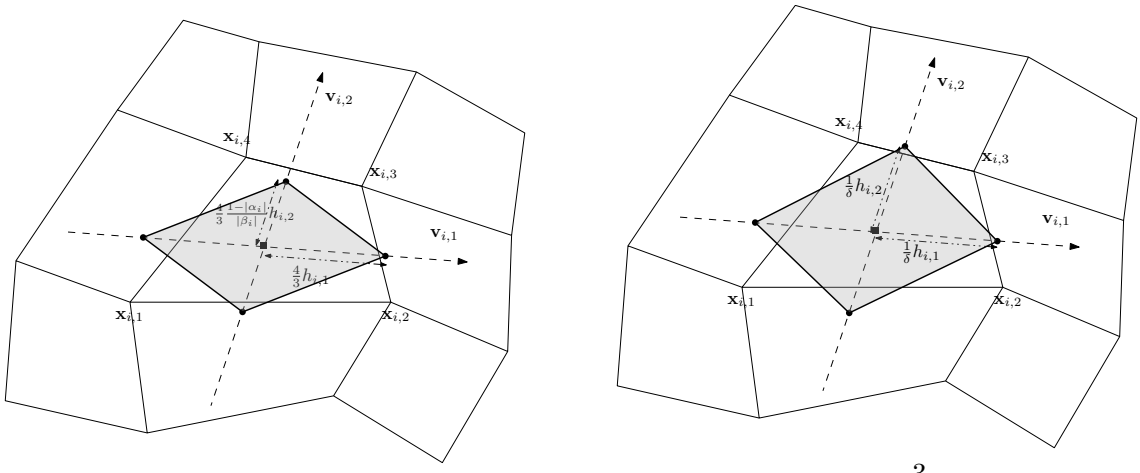

(a) $\delta = \frac{3}{4}$. (b) $\delta = \dfrac{3}{3 + |\alpha_i| + |\beta_i|}$.

Figure 5.6: The interpolation points should lie outside the shaded region for second order accuracy.

For a system of conservation laws, the proposed limiter can be applied sequentially to the conserved variables. For nonlinear scalar conservation laws, we can derive a moment limiter with a modified reconstruction stencil and prove stability of the numerical solution in the sense of satisfying LMP (5.37) in the means. However, due to the involved nature of the reconstruction stencil and severe restrictions on the time step, we proceed with applying the moment limiter proposed in Section 5.1 to nonlinear conservation laws as well, and from the numerical experiments in Section 5.2 we note that this leads to reasonably good results.

5.2 Numerical Results

In this section, we present numerical experiments to analyze the performance of the proposed moment limiter. We perform convergence studies to show that the limited solution maintains the theoretical second order convergence rate for smooth problems. We also run tests to show the robustness of the proposed limiter in the presence of discontinuities. In all presented cases, time-stepping was performed using an explicit second order Runge-Kutta method with the CFL condition given in (5.62). Finally, unless stated otherwise, the local Lax-Friedrichs flux was used.

5.2.1 Sinusoidal Wave.

We solve the linear advection equation on the domain $\Omega = [-1,1] \times [-1,1]$, with the flux in (1.8) given by $\mathbf{F} = [u,u]$. The initial condition consists of a sinusoidal wave $u_0(x,y) = \sin(2\pi(x+y))$ advected with speed $a = \sqrt{2}$ along the direction $(1,1)$. The problem is solved until $t = 0.5$ on a series of quadrilateral meshes $A - D$. A is the coarsest mesh with 509 elements. The finer meshes are obtained by remeshing the preceding mesh such that the area of an element is reduced by a factor of four. Table 5.2 shows the L_1 errors and the observed convergence rates for $p = 1$ DG approximation with and without limiting. We observe that the second order limiter retains the theoretical rate of convergence. We also note that limiting introduces only relatively modest errors in the solution.

Mesh	Number of elements	L1 error	
		p = 1	p = 1 (unlimited)
A	509	3.79e-01 (-)	1.0e-01 (-)
B	2035	1.09e-01 (1.79)	2.13e-02 (2.24)
C	8363	2.35e-02 (2.21)	4.86e-03 (2.13)
D	33469	4.48e-03 (2.37)	1.17e-03 (2.07)

Table 5.2: L_1 errors for the linear advection of a sinusoidal wave at $t = 0.5$ on an unstructured quadrilateral mesh. The numbers in parentheses are the observed rates of convergence.

5.2.2 Rotating shapes.

Next, we solve the rotating shapes problem with the flux in (1.8) given by $\mathbf{F} = [-2\pi yu, 2\pi xu]$. The initial condition consists of a hill and a square pulse as shown in Figure 5.7 and given by

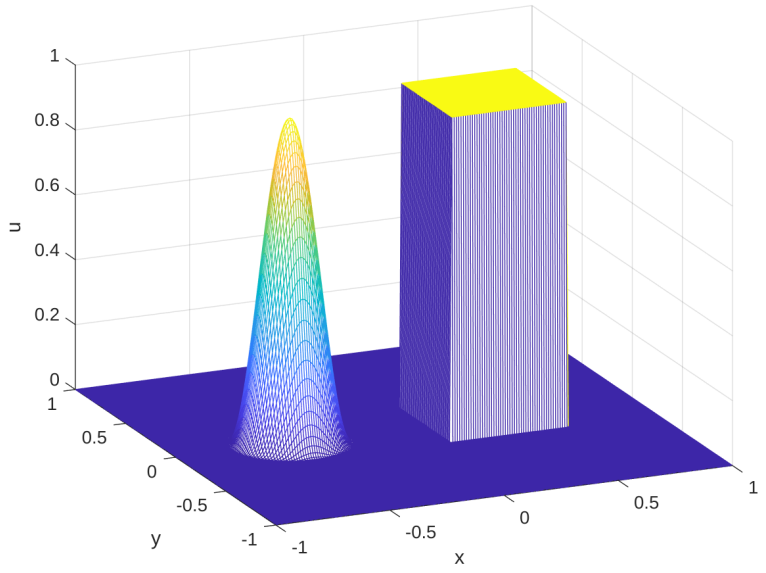

Figure 5.7: Initial condition for the rotating shapes problem.

$$u_0(x,y) = \begin{cases} \cos^2(2\pi r), & \text{if } r \le 0.25, \\ 1, & \text{if } \max\left(|x-0.35|, |y|\right) \le 0.25, \\ 0, & \text{otherwise}, \end{cases} \tag{5.80}$$

where $r = \sqrt{(x+0.5)^2 + y^2}$. The exact solution is a rotation of the initial condition about the origin. The problem is solved until $t = 1$ on an unstructured mesh of 6472 quadrilateral elements. Figure 5.8 shows the isolines and the solution profiles at $y = 0$, $x = 0.5, 0.55$, obtained using second order DG approximation with and without the moment limiter. The quality of the solution is comparable to the results obtained on a 80×80 Cartesian mesh using the moment limiter described in [25] and the results obtained on a quadrilateral mesh using the slope limiter described in chapter 4. From Figure 5.8b, we note that the limiter is successful in reducing the oscillations near the discontinuities, which is corroborated by the solution profiles in Figures 5.8c and 5.8e. We also note that the well known phenomenon of clipping at the local extremas by a second order limiter has reduced the accuracy near the peak of the hill.

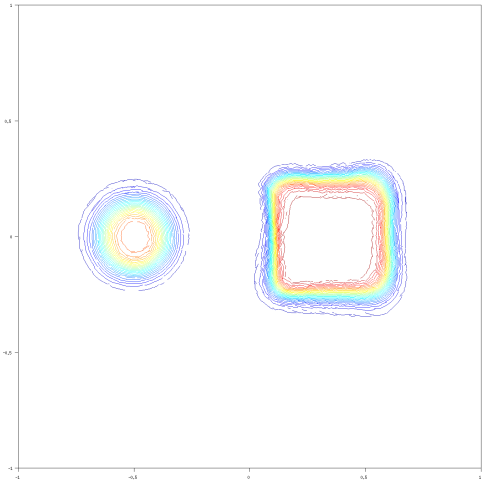

(a) Isolines with second order moment limiter.

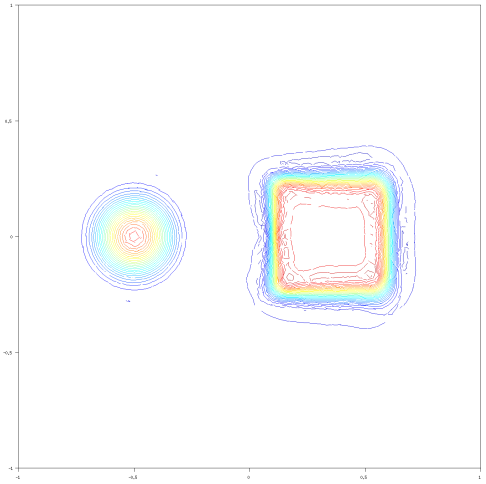

(b) Isolines without limiting.

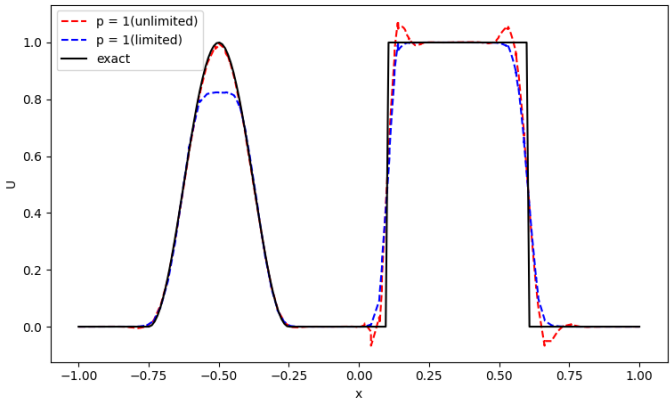

(c) Profile of the solution along $y = 0$.

5.2.3 Isentropic vortex.

Next, we test the performance of the second order limiter when applied to a system of nonlinear equations, for example, the Euler equations given by

$$\frac{\partial}{\partial t}\begin{pmatrix}\rho\\ \rho u\\ \rho v\\ E\end{pmatrix}+\frac{\partial}{\partial x}\begin{pmatrix}\rho u\\ \rho u^2+p\\ \rho uv\\ (E+p)u\end{pmatrix}+\frac{\partial}{\partial y}\begin{pmatrix}\rho v\\ \rho uv\\ \rho v^2+p\\ (E+p)v\end{pmatrix}=0, \tag{5.81}$$

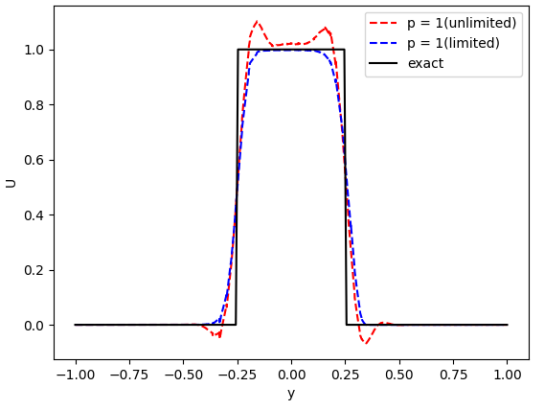

(d) Profile of the solution along $x = 0.5$.

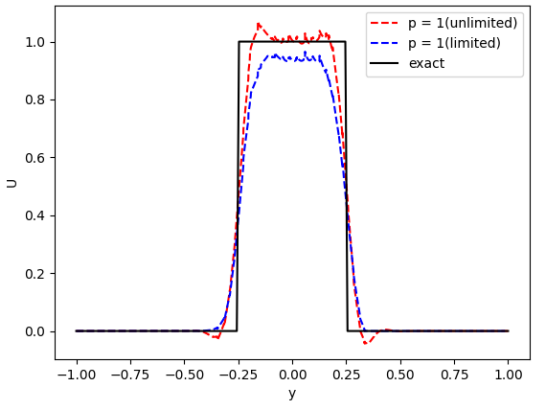

(e) Profile of the solution along $x = 0.55$.

Figure 5.8: Rotating shapes at $t = 1$, on a quadrilateral mesh with 6472 elements.

where ρ is the density, ρu and ρv are the x- and y-direction momenta, E is the energy, and the pressure, p, is given by the equation of state $p = (\gamma - 1)\left(E - \frac{\rho}{2}(u^2 + v^2)\right)$. We solve the smooth isentropic vortex problem described in [51] on the domain $[-3, 3] \times [-3, 3]$ with the initial conditions

$$\rho = \left(1 - \frac{(\gamma - 1)}{8\pi^2}(M\beta)^2 e^r\right)^{\frac{1}{\gamma - 1}}, \quad p = \frac{\rho^\gamma}{\gamma M^2}, \quad u = \frac{\beta}{2\pi R} y e^{\frac{r}{2}}, \quad v = -\frac{\beta}{2\pi R} x e^{\frac{r}{2}}, \tag{5.82}$$

where $r = \frac{1-(x^2+y^2)}{R^2}$, $R = 1.5$, $\beta = 13.5$, $\gamma = 1.4$, and $M = 0.4$. With the given initial conditions, the exact solution is stationary and given by (5.82). The L_1 errors in density and the observed convergence rates are reported in Table 5.3. Similar to the linear advection test case, we see that the proposed limiter maintains the theoretical convergence rates and introduces only modest errors.

5.2.4 Shock shock interactions.

Next, we test the performance of the limiter in the presence of shock-shock interactions. The initial conditions for the test problem were taken from the two-dimensional Riemann test suite proposed in [55] and shown in Figure 5.9. The simulation was run until $t = 0.8$ on a mesh with $160,103$ quads. Figure 5.10 shows the density isolines at $t = 0.8$ obtained using the second order DG approximation. We note that the method is able to resolve the vortical structures along the contact discontinuities well.

Mesh	Number of elements	L1 error	
		p = 1 limited	p = 1 (unlimited)
A	515	6.87e-02 (-)	1.70e-02 (-)
B	2047	1.42e-02 (2.19)	4.06e-03 (2.07)
C	8372	3.61e-03 (2.02)	1.00e-03 (2.02)
D	33532	7.42e-04 (2.27)	2.54e-04 (1.98)

Table 5.3: L_1 errors in density for the stationary isentropic vortex example at $t = 0.5$ on unstructured quadrilateral mesh. The numbers in parentheses are the observed rates of convergence.

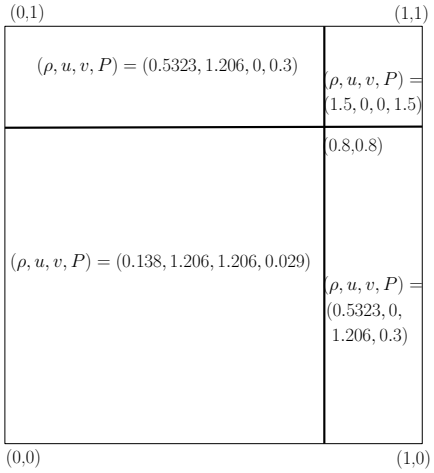

Figure 5.9: Modified initial condition for 2D Riemann problem.

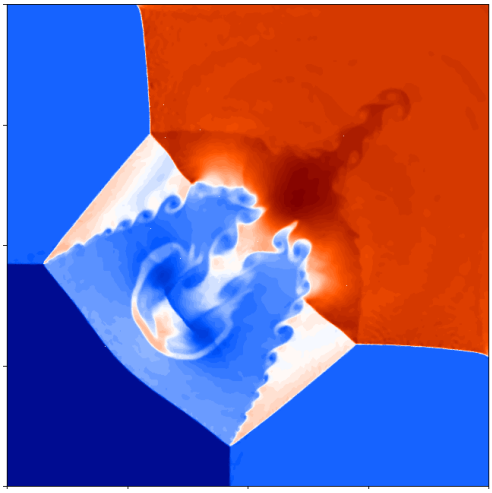

(a)

Figure 5.10: Density isolines at $t = 0.8$ for the shock-shock interaction example for $p = 1$ with moment limiter on a mesh of $160,103$ quads.

5.2.5 Double Mach reflection.

Finally, we solve the double Mach reflection problem to test the performance of the proposed moment limiter in the presence of strong discontinuities. The initial set-up for the problem is taken from [25] and shown in Figure 5.11. The initial condition consists of a Mach 10 shock wave impinging on a reflecting wall at an angle of 60°. The states to the left ($\mathbf{U}_l$) and to the right ($\mathbf{U}_r$) of the shock wave are given in Table 5.4. The computational domain $[0, 3.5] \times [0, 1]$ is discretized into $230,266$ quadrilaterals. The simulation is run until $t = 0.2$. Figure 5.12 shows the density isolines obtained at $t = 0.2$ using the second

	$\mathbf{U}_l$	$\mathbf{U}_r$
ρ	8	1.4
$s = \mathbf{v} \cdot \mathbf{n}$	8.25	0
p	116.5	1

Table 5.4: States to the left and right of the initial shock for the double Mach test case.

order DG approximation with the moment limiter. We can observe the well-resolved shock structure as well as the vortices near the slip line (Figure 5.13).

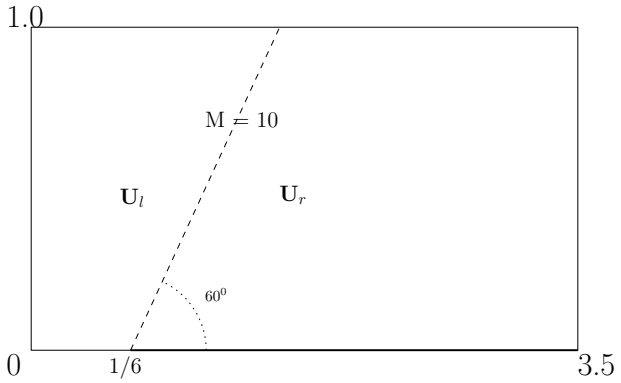

Figure 5.11: The initial set-up for the double mach reflection test case.

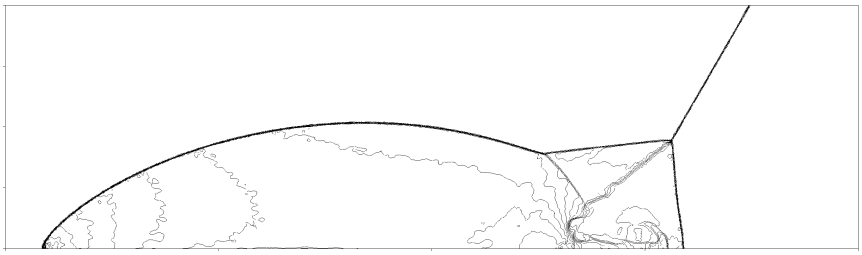

Figure 5.12: Density isolines at $t = 0.2$ for the double Mach test case for $p = 1$ with moment limiter on a final mesh of $230,266$ quads.

Figure 5.13: Density isolines at $t = 0.2$ for the double Mach test case for $p = 1$ with moment limiter on a final mesh of $230,266$ quads.

5.3 Summary

We have presented a family of second order moment limiters for the DG method on unstructured quadrilateral meshes. The limiter works by decoupling the solution coefficents as derivatives along two specific directions and restricting the gradients along said directions using a one-dimensional minmod function. With the proposed limiting directions, the solutions coefficients are fully uncoupled which allows us to selectively limit moments that show excessive growth while retaining the solution accuracy.

We provide a range of values for the scaling parameters of the solution coefficients and a suitable time step which ensure stability of the numerical solution in the sense of satisfying LMP (5.37) in the solution averages. Numerical experiments presented in Section 5.2 illustrate that the DG method with the proposed limiter eliminates spurious oscillations and is robust in the presence of discontinuities. Further, the experiments also demonstrate that the limited solution retains the theoretical second order convergence rate for smooth solutions.

Chapter 6

High-order moment limiter on quadrilateral meshes

In this chapter, we describe a high-order moment limiter for the DG method on quadrilateral meshes. The limiter works by decoupling the solution coefficients (moments) as directional derivatives along two specific directions (Figure 6.1). Starting with the highest moment, we hierarchically limit the moments by reconstructing the associated directional derivatives using a compact stencil and restricting their values using a one-dimensional minmod limiter. The choice of limiting directions and the compact reconstruction stencil are described in 6.1.1, while the formulae for the generalized moment limiter is described in 6.1.2 . Finally, we describe of the hierarchical implementation of the limiter in 6.1.3.

6.1 Limiting algorithm

6.1.1 Directional derivatives

Consider the $(p+1)$th DG approximation of a scalar conserved variable on the element Ω_i

$$U_i(\zeta,\eta) = \sum_{j=0,k=0}^{p} \hat{U}_{i,j}^k \varphi_j^k(\zeta,\eta), \tag{6.1}$$

where the tensor product basis $\{\varphi_j^k\}$ is given by (1.25). Using the bilinear transformation (1.19), Ω_i can be mapped to the canonical element Ω_0. Consider the vectors $v_1 = (1,0)$ and $v_2 = (0,1)$ passing through the cell centroid $\mathbf{r}_0 = (0,0)$ of Ω_0 in the canonical space.

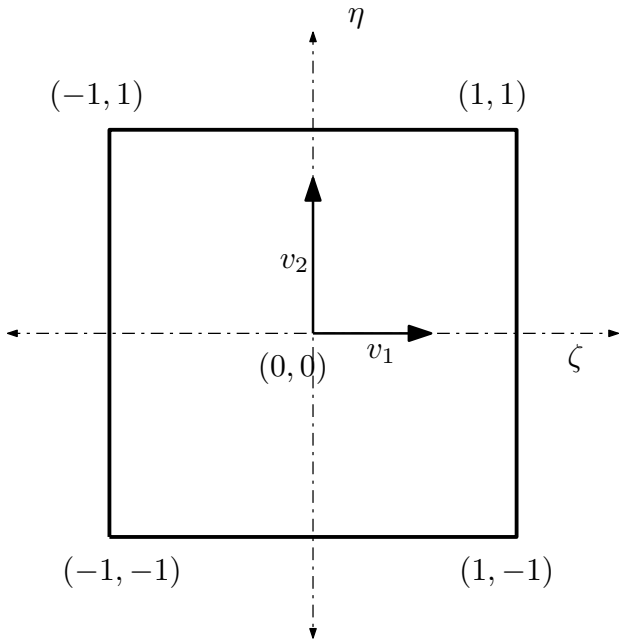

Figure 6.1: The canonical rectangle Ω_0.

Denote the qth directional derivative of U_i along v_1 and v_2 as

$$D^s_{v_1} D^{q-s}_{v_2} U_i = \frac{\partial^q}{\partial \zeta^s \partial \eta^{q-s}} U_i, \quad 0 \le s \le q, \quad q \le p. \tag{6.2}$$

Plugging in the expression for U_i from (6.1) in (6.2), we get

$$\begin{aligned}
D^s_{v_1} D^{q-s}_{v_2} U_i &= \sum_{j=0,k=0}^{p} \hat{U}^k_{i,j} D^s_{v_1} D^{q-s}_{v_2} \varphi^k_j(\zeta,\eta) \\
&= \frac{\sqrt{(2s+1)(2(q-s)+1)}}{2} (2s-1)!(2(q-s)-1)! \hat{U}^{q-s}_{i,s} \\
&+ \frac{\sqrt{(2s+3)(2(q-s)+1)}}{2} (2s+1)!(2(q-s)-1)! \hat{U}^{q-s}_{i,s+1} \zeta \\
&+ \frac{\sqrt{(2s+1)(2(q-s)+3)}}{2} (2s-1)!(2(q-s)+1)! \hat{U}^{q+1-s}_{i,s} \eta \\
&+ \sum_{k>q+1-s}^{p} \hat{U}^k_{i,s} D^s_{v_1} D^{q-s}_{v_2} \varphi^k_s(\zeta,\eta) + \sum_{j>s+1}^{p} \hat{U}^{q-s}_{i,j} D^s_{v_1} D^{q-s}_{v_2} \varphi^{q-s}_s(\zeta,\eta) \\
&+ \sum_{j>s+1,k>q+1-s}^{p} \hat{U}^k_{i,j} D^s_{v_1} D^{q-s}_{v_2} \varphi^k_j(\zeta,\eta).
\end{aligned} \tag{6.3}$$

Ignoring the contribution from the higher order terms, we can approximate the qth directional derivative $D^s_{v_1} D^{q-s}_{v_2} U_i$ as

$$\begin{aligned} D^s_{v_1} D^{q-s}_{v_2} U_i \approx & \frac{\sqrt{(2s+1)(2(q-s)+1)}}{2} (2s-1)!(2(q-s)-1)! \hat{U}^{q-s}_{i,s} \\ & + \frac{\sqrt{(2s+3)(2(q-s)+1)}}{2} (2s+1)!(2(q-s)-1)! \hat{U}^{q-s}_{i,s+1} \zeta \\ & + \frac{\sqrt{(2s+1)(2(q-s)+3)}}{2} (2s-1)!(2(q-s)+1)! \hat{U}^{q+1-s}_{i,s} \eta. \end{aligned} \tag{6.4}$$

Under the transformation (1.19), the vectors v_1 and v_2, respectively, map to the directions $\mathbf{v}_{i,1}$ and $\mathbf{v}_{i,2}$ in the physical space

$$\mathbf{v}_{i,1} = (C_{i,x1}, C_{i,y1}), \quad \mathbf{v}_{i,2} = (C_{i,x2}, C_{i,y2}), \tag{6.5}$$

where the coefficients $C_{i\mathbf{x}}$ are defined in (1.21). Noting that the transformation (1.19) is a bilinear map, (1.19) reduces to a linear transformation along $\zeta = 0$ and along $\eta = 0$. Therefore, we can find approximate values of the solution coefficients $\hat{U}^{q-s}_{i,s+1}$ and $\hat{U}^{q+1-s}_{i,s}$ by computing the forward and backward differences of $D^s_{v_1} D^{q-s}_{v_2} U_i$ along $\mathbf{v}_{i,1}$ and $\mathbf{v}_{i,2}$, respectively.

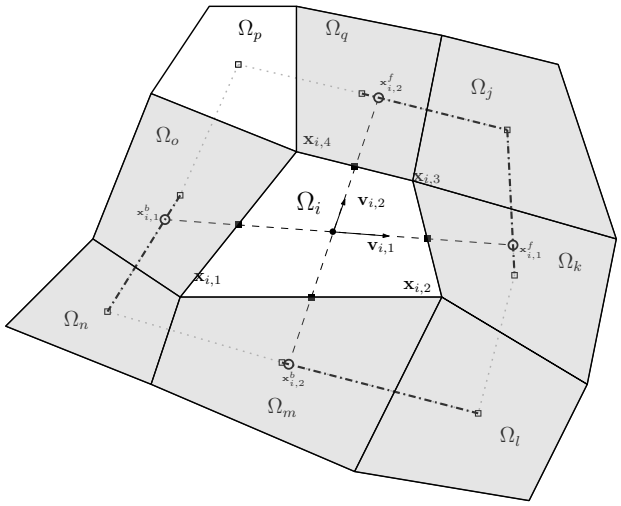

Figure 6.2: Reconstruction neighborhood for Ω_i. Elements used in limiting are shaded. Limiting directions $\mathbf{v}_{i,1}$ and $\mathbf{v}_{i,2}$ are shown as arrows. Backward and forward interpolation points are shown as hollow disks.

To compute the forward and backward differences, we need to find the forward ($\mathbf{x}^f_{i,1}$ and

$\mathbf{x}^f_{i,2}$), and backward ($\mathbf{x}^b_{i,1}$ and $\mathbf{x}^b_{i,2}$) interpolation points (Figure 6.2, hollow disks), evaluate the value of the directional derivatives at these points and finally, compute their difference from the value at the cell centroid (Figure 6.2, solid circle). To find the interpolation points, first, we form a polygon by joining the cell centroids of the neighboring elements that share a vertex with Ω_i. Next, we define two lines parallel to $\mathbf{v}_{i,1}$ and $\mathbf{v}_{i,2}$ that pass through the centroid of Ω_i. The interpolation points $\mathbf{x}^f_{i,k}$, $\mathbf{x}^b_{i,k}$, $k = 1, 2$, are then the points of intersection of these lines and the faces of the polygon.

6.1.2 Generalized moment limiter

Let's consider limiting the solution coefficient $\hat{U}^{q-s}_{i,s+1}$. Along $\eta = 0$, (6.4) reduces to

$$\begin{aligned} D^s_{v_1} D^{q-s}_{v_2} U_i = &\frac{\sqrt{(2s+1)(2(q-s)+1)}}{2}(2s-1)!(2(q-s)-1)!\hat{U}^{q-s}_{i,s} \\ &+ \frac{\sqrt{(2s+3)(2(q-s)+1)}}{2}(2s+1)!(2(q-s)-1)!\hat{U}^{q-s}_{i,s+1}\zeta, \end{aligned} \tag{6.6}$$

i.e., $\hat{U}^{q-s}_{i,s+1}$ is proportional to the gradient of $D^s_{v_1} D^{q-s}_{v_2} U_i$ along v_1. Since the map (1.19) reduces to a linear transformation when $\eta = 0$, we can obtain an approximate value of $\hat{U}^{q-s}_{i,s+1}$ by computing the forward and backward differences of $D^s_{v_1} D^{q-s}_{v_2} U_i$ along $\mathbf{v}_{i,1}$. To do so, first, we need to compute the values of $D^s_{v_1} D^{q-s}_{v_2} U_i$ at the forward and backward interpolation points $\mathbf{x}^f_{i,1}$ and $\mathbf{x}^b_{i,1}$ (Figure 6.2). Consider the forward interpolation point $\mathbf{x}^f_{i,1}$. Under (1.19), $\mathbf{x}^f_{i,1}$ maps to the point $\zeta^f_{i,1} = (\frac{x^f_{i,1} - C_{i,x0}}{C_{i,x1}}, 0)$ in the canonical space. Consider the following vectors at $\mathbf{x}^f_{i,1}$

$$\mathbf{v}^{1,f}_{i,\zeta} = (C_{i,x1}, C_{i,y1}), \quad \mathbf{v}^{1,f}_{i,\eta} = \left(C_{i,x2} + C_{i,x3}\zeta^f_1, C_{i,y2} + C_{i,y3}\zeta^f_1\right), \quad \mathbf{v}_{i,3} = (C_{i,x3}, C_{i,y3}), \tag{6.7}$$

where the coefficients $C_{i,x}$ are defined in (1.21). Using the map (1.19) and the chain rule, the value of $D^s_{v_1} D^{q-s}_{v_2} U_i$ at $\mathbf{x}^f_{i,1}$ can be written as a linear combination of the directional derivatives along the vectors in (6.7)

$$D^s_{v_1} D^{q-s}_{v_2} U_i(\mathbf{x}^f_{i,1}) = \alpha_0 D^s_{\mathbf{v}^{1,f}_{i,\zeta}} D^{q-s}_{\mathbf{v}^{1,f}_{i,\eta}} U_i + \alpha_1 D_{\mathbf{v}_{i,3}} D^{s-1}_{\mathbf{v}^{1,f}_{i,\zeta}} D^{q-1-s}_{\mathbf{v}^{1,f}_{i,\eta}} U_i + \cdots + \alpha_n D^a_{\mathbf{v}_{i,3}} D^b_{\mathbf{v}^{1,f}_{i,\zeta}} D^{n-a-b}_{\mathbf{v}^{1,f}_{i,\eta}} U_i, \tag{6.8}$$

where α_i are constant coefficients and n is the order of approximation corresponding to $\hat{U}^{q-s}_{i,s+1}$. To find the approximate value of $D^s_{v_1} D^{q-s}_{v_2} U_i$ at $\mathbf{x}^f_{i,1}$, we compute $D^s_{v_1} D^{q-s}_{v_2} U_i$ at the cell centroids of the neighboring elements Ω_j and Ω_k by evaluating the expression on the right hand side of (6.8). The computed values are then used to linearly interpolate

the value of $D^s_{v_1} D^{q-s}_{v_2} U_i$ at $\mathbf{x}^f_{i,1}$. For example, consider the computation of the directional derivative $D^a_{\mathbf{v}_{i,3}} D^b_{\mathbf{v}^{1,f}_{i,\zeta}} D^c_{\mathbf{v}^{1,f}_{i,\eta}} U$ at the cell centroid $\mathbf{x}_{k,0}$ of the neighboring element Ω_k. Note that the vectors in (6.7) can be written as a linear combination of the vectors $\mathbf{v}_{k,1}$ and $\mathbf{v}_{k,2}$, which respectively map to v_1 and v_2 under (1.19) for Ω_k, as

$$\mathbf{v}^{1,f}_{i,\zeta} = \alpha^{1,f}_{k,\zeta} \mathbf{v}_{k,1} + \beta^{1,f}_{k,\zeta} \mathbf{v}_{k,2}, \quad \mathbf{v}^{1,f}_{i,\eta} = \alpha^{1,f}_{k,\eta} \mathbf{v}_{k,1} + \beta^{1,f}_{k,\eta} \mathbf{v}_{k,2}, \quad \mathbf{v}_{i,3} = \alpha^{1,f}_{k,3} \mathbf{v}_{k,1} + \beta^{1,f}_{k,3} \mathbf{v}_{k,2}. \tag{6.9}$$

Therefore, the value of $D^a_{\mathbf{v}_{i,3}} D^b_{\mathbf{v}^{1,f}_{i,\zeta}} D^c_{\mathbf{v}^{1,f}_{i,\eta}} U$ at the cell centroid $\mathbf{x}_{k,0}$ can be computed as

$$\begin{aligned} D^a_{\mathbf{v}_{i,3}} D^b_{\mathbf{v}^{1,f}_{i,\zeta}} D^c_{\mathbf{v}^{1,f}_{i,\eta}} U_k = \left(\alpha^{1,f}_{k,3} D_{\mathbf{v}_{k,1}} + \beta^{1,f}_{k,3} D_{\mathbf{v}_{k,2}}\right)^a \left(\alpha^{1,f}_{k,\zeta} D_{\mathbf{v}_{k,1}} + \beta^{1,f}_{k,\zeta} D_{\mathbf{v}_{k,2}}\right)^b \left(\alpha^{1,f}_{k,\eta} D_{\mathbf{v}_{k,1}} \right. \\ \left. + \beta^{1,f}_{k,\eta} D_{\mathbf{v}_{k,2}}\right)^c U_i, \end{aligned} \tag{6.10}$$

i.e., a linear combination of directional derivatives along $\mathbf{v}_{k,1}$ and $\mathbf{v}_{k,2}$. Note that the chain rule gives

$$D_{\mathbf{v}_{k,1}} U_k = U_{k,\zeta}\Big|_{(0,0)}, \quad D_{\mathbf{v}_{k,2}} U_k = U_{k,\eta}\Big|_{(0,0)}. \tag{6.11}$$

By applying the chain rule, $U_{k,\zeta^l \eta^m}$ evaluated at $\mathbf{r}_0 = (0,0)$ can be written in terms of directional derivatives along $\mathbf{v}_{k,1}$ and $\mathbf{v}_{k,2}$

$$U_{k,\zeta^l \eta^m}\Big|_{(0,0)} = \sum_{r=1,s=1}^{l,m} \omega_{r,s} D^r_{\mathbf{v}_{k,1}} D^s_{\mathbf{v}_{k,2}} U_k. \tag{6.12}$$

Therefore, using (6.11), (6.12) and (6.3), the directional derivatives along $\mathbf{v}_{k,1}$ and $\mathbf{v}_{k,2}$ can be expressed as a linear combination of the solution coefficients in Ω_k, which can then be plugged into (6.10) to compute $D^a_{\mathbf{v}_{i,3}} D^b_{\mathbf{v}^{1,f}_{i,\zeta}} D^c_{\mathbf{v}^{1,f}_{i,\eta}} U_k$. In a similar fashion, we can compute the value of $D^a_{\mathbf{v}_{i,3}} D^b_{\mathbf{v}^{1,f}_{i,\zeta}} D^c_{\mathbf{v}^{1,f}_{i,\eta}} U$ at the cell centroid of the neighboring element Ω_j. Finally, the computed values at the cell centroids of Ω_k and Ω_j are used to linearly interpolate $D^a_{\mathbf{v}_{i,3}} D^b_{\mathbf{v}^{1,f}_{i,\zeta}} D^c_{\mathbf{v}^{1,f}_{i,\eta}} U$ at $\mathbf{x}^f_{i,1}$

$$D^a_{\mathbf{v}_{i,3}} D^b_{\mathbf{v}^{1,f}_{i,\zeta}} D^c_{\mathbf{v}^{1,f}_{i,\eta}} U_i\Big|_{\mathbf{x}^f_{i,1}} = \beta^f_{i,1} D^a_{\mathbf{v}_{i,3}} D^b_{\mathbf{v}^{1,f}_{i,\zeta}} D^c_{\mathbf{v}^{1,f}_{i,\eta}} U_k + \left(1 - \beta^f_{i,1}\right) D^a_{\mathbf{v}_{i,3}} D^b_{\mathbf{v}^{1,f}_{i,\zeta}} D^c_{\mathbf{v}^{1,f}_{i,\eta}} U_j, \tag{6.13}$$

where $0 \le \beta_{i,1}^f \le 1$, i.e., a weighted average of $D^a_{\mathbf{v}_{i,3}} D^b_{\mathbf{v}^{1,f}_{i,\zeta}} D^c_{\mathbf{v}^{1,f}_{i,\eta}} U_k$ and $D^a_{\mathbf{v}_{i,3}} D^b_{\mathbf{v}^{1,f}_{i,\zeta}} D^c_{\mathbf{v}^{1,f}_{i,\eta}} U_j$ with the interpolation weight given by

$$\beta_{i,1}^f = \frac{\left\| \mathbf{x}_{j,0} - \mathbf{x}_{i,1}^f \right\|}{\left\| \mathbf{x}_{j,0} - \mathbf{x}_{k,0} \right\|}. \tag{6.14}$$

Similarly, all of the directional derivatives on the right hand side of (6.8) can be computed to obtain the value of $D^s_{v_1} D^{q-s}_{v_2} U_i(\mathbf{x}_{i,1}^f)$.

Finally, the limited solution coefficient $\tilde{U}^{q-s}_{i,s+1}$ is obtained by comparing $\hat{U}^{q-s}_{i,s+1}$ to the forward and backward differences of $D^s_{v_1} D^{q-s}_{v_2} U_i$ multiplied by the scaling parameters $l^f_{i,1}$ and $l^b_{i,1}$

$$\begin{aligned}
\tilde{U}^{q-s}_{i,s+1} &\leftarrow \text{minmod}\left(\hat{U}^{q-s}_{i,s+1}, l^f_{i,1} D_1^+, l^b_{i,1} D_1^-\right), \\
D_1^+ &= \frac{1}{|\zeta^f_{i,1}|}\left(\frac{2 D^s_{v_1} D^{q-s}_{v_2} U_i(\mathbf{x}^f_{i,1})}{\sqrt{(2s+3)(2(q-s)+1)}(2s+1)!(2(q-s)-1)!} - \sqrt{\frac{2s+1}{2s+3}}\frac{(2s-1)!}{(2s+1)!}\hat{U}^{q-s}_{i,s}\right), \\
D_1^- &= \frac{1}{|\zeta^b_{i,1}|}\left(\sqrt{\frac{2s+1}{2s+3}}\frac{(2s-1)!}{(2s+1)!}\hat{U}^{q-s}_{i,s} - \frac{2 D^s_{v_1} D^{q-s}_{v_2} U_i(\mathbf{x}^b_{i,1})}{\sqrt{(2s+3)(2(q-s)+1)}(2s+1)!(2(q-s)-1)!}\right),
\end{aligned} \tag{6.15}$$

where the minmod function is

$$\text{minmod}(a,b,c) = \begin{cases} sign(a)\cdot min(|a|,|b|,|c|), & \text{if } sign(a) = sign(b) = sign(c), \\ 0, & \text{otherwise.} \end{cases} \tag{6.16}$$

Now, consider the qth directional derivative $D^{s+1}_{v_1} D^{q-s-1}_{v_2} U_i$. Similarly to (6.3) and (6.4), it can be approximated as

$$\begin{aligned}
D^{s+1}_{v_1} D^{q-s-1}_{v_2} U_i \approx{}& \frac{\sqrt{(2s+3)(2(q-s)-1)}}{2}(2s+1)!(2(q-s)-3)!\hat{U}^{q-s-1}_{i,s+1} \\
&+ \frac{\sqrt{(2s+5)(2(q-s)-1)}}{2}(2s+3)!(2(q-s)-3)!\hat{U}^{q-s-1}_{i,s+2}\zeta \\
&+ \frac{\sqrt{(2s+3)(2(q-s)+1)}}{2}(2s+1)!(2(q-s)-1)!\hat{U}^{q-s}_{i,s+1}\eta,
\end{aligned} \tag{6.17}$$

Along $\zeta = 0$, (6.17) reduces to

$$
\begin{aligned}
D_{v_1}^{s+1} D_{v_2}^{q-s-1} U_i = & \frac{\sqrt{(2s+3)(2(q-s)-1)}}{2} (2s+1)!(2(q-s)-3)! \hat{U}_{i,s+1}^{q-s-1} \\
& + \frac{\sqrt{(2s+3)(2(q-s)+1)}}{2} (2s+1)!(2(q-s)-1)! \hat{U}_{i,s+1}^{q-s} \eta,
\end{aligned}
\tag{6.18}
$$

i.e., $\hat{U}_{i,s+1}^{q-s}$ is proportional to the gradient of $D_{v_1}^{s+1} D_{v_2}^{q-s-1} U_i$ along v_2. Following steps similar to the ones outlined for $D_{v_1}^{s} D_{v_2}^{q-s} U_i$, the limited solution coefficient $\tilde{U}_{i,s+1}^{q-s}$ is obtained by comparing $U_{i,s+1}^{q-s}$ to the forward and backward differences of $D_{v_1}^{s+1} D_{v_2}^{q-s-1} U_i$ multiplied by the scaling parameters $l_{i,2}^f$ and $l_{i,2}^b$

$$
\begin{aligned}
\tilde{U}_{i,s+1}^{q-s} & \leftarrow \text{minmod}\left(\tilde{U}_{i,s+1}^{q-s}, l_{i,2}^f D_2^+, l_{i,2}^b D_2^-\right), \\
D_2^+ & = \frac{1}{|\eta_{i,2}^f|} \left(\frac{2 D_{v_1}^{s+1} D_{v_2}^{q-s-1} U_i(\mathbf{x}_{i,2}^f)}{\sqrt{(2s+3)(2(q-s)+1)}(2s+1)!(2(q-s)-1)!} \right. \\
& \quad \left. - \sqrt{\frac{2(q-s)-1}{2(q-s)+1}} \frac{(2(q-s)-3)!}{(2(q-s)-1)!} \hat{U}_{i,s+1}^{q-s-1} \right), \\
D_2^- & = \frac{1}{|\eta_{i,2}^b|} \left(\sqrt{\frac{2(q-s)-1}{2(q-s)+1}} \frac{(2(q-s)-3)!}{(2(q-s)-1)!} \hat{U}_{i,s+1}^{q-s-1} \right. \\
& \quad \left. - \frac{2 D_{v_1}^{s+1} D_{v_2}^{q-s-1} U_i(\mathbf{x}_{i,2}^b)}{\sqrt{(2s+3)(2(q-s)+1)}(2s+1)!(2(q-s)-1)!} \right).
\end{aligned}
\tag{6.19}
$$

The admissible range for the scaling parameters $l_{i,k}^f$ and $l_{i,k}^b$, $k = \{1, 2\}$, is

$$
\begin{aligned}
1 \le l_{i,2}^f \le |\eta_{i,2}^f|, \quad 1 \le l_{i,2}^b \le |\eta_{i,2}^b|, \\
1 \le l_{i,1}^f \le |\zeta_{i,1}^f|, \quad 1 \le l_{i,1}^b \le |\zeta_{i,1}^b|,
\end{aligned}
\tag{6.20}
$$

which is equivalent to the range for the scaling parameters used on unstructured two-dimensional mesh in [57]. In all experiments in Section 6.2 we choose the least restrictive limiter, i.e., the right hand side of the intervals in (6.20).

6.1.3 Implementation strategy

The limiter is applied hierarchically starting with the highest solution coefficient. For the $(p+1)$th DG approximation, we find the limited coefficient $\tilde{U}^p_{i,p}$. If $\hat{U}^p_{i,p} \neq \tilde{U}^p_{i,p}$, then we limit the solution coefficients $(\hat{U}^p_{i,p-1},\ \hat{U}^{p-1}_{i,p})$. If both these solution coefficients are modified, then we move on to the next set of lower order solution coefficients until we reach either a set of coefficients that are not modified or $(\hat{U}^p_{i,0},\ \hat{U}^0_{i,p})$. If $(\hat{U}^p_{i,0},\ \hat{U}^0_{i,p})$ are limited, we compute the limited coefficient $\tilde{U}^{p-1}_{i,p-1}$ and the process continues until we reach a set of coefficients that are not limited or $\hat{U}^0_{i,0}$. We provide the order of hierarchical limiting of the solution coefficients in (6.21).

$$\begin{aligned}
&\hat{U}^p_{i,p},\ (\hat{U}^p_{i,p-1},\ \hat{U}^{p-1}_{i,p}),\ (\hat{U}^p_{i,p-2},\ \hat{U}^{p-2}_{i,p}),\ \cdots (\hat{U}^p_{i,0},\ \hat{U}^0_{i,p}),\\
&\hat{U}^{p-1}_{i,p-1},\ (\hat{U}^{p-1}_{i,p-2},\ \hat{U}^{p-2}_{i,p-1}),\ (\hat{U}^{p-1}_{i,p-3},\ \hat{U}^{p-3}_{i,p-1}),\ \cdots (\hat{U}^{p-1}_{i,0},\ \hat{U}^0_{i,p-1}),\\
&\hat{U}^{p-2}_{i,p-2},\ (\hat{U}^{p-2}_{i,p-3},\ \hat{U}^{p-3}_{i,p-2}),\ (\hat{U}^{p-2}_{i,p-4},\ \hat{U}^{p-4}_{i,p-2}),\ \cdots (\hat{U}^{p-2}_{i,0},\ \hat{U}^0_{i,p-2}),\\
&\qquad\qquad\qquad\qquad\qquad\qquad\qquad\qquad\qquad\qquad\qquad\qquad\vdots\\
&\qquad\qquad\qquad\qquad\qquad\qquad\qquad\qquad\qquad\qquad\qquad\qquad\hat{U}^1_{i,1},\ (\hat{U}^1_{i,0},\ \hat{U}^0_{i,1}).
\end{aligned} \tag{6.21}$$

Remark 1. If the linear solution coefficients $(\hat{U}^1_{i,0},\ \hat{U}^0_{i,1})$ are limited, then we update the zeroth order solution coefficient $\hat{U}^0_{i,0}$ using (6.22) to ensure that the cell average of U_i in Ω_i, $\overline{U}_i$, remains unchanged.

$$\hat{U}^0_{i,0} \leftarrow \hat{U}^0_{i,0} + \frac{\det J_{i,1}}{\sqrt{3}\det J_{i,0}}\left(\hat{U}^0_{i,1} - \tilde{U}^0_{i,1}\right) + \frac{\det J_{i,2}}{\sqrt{3}\det J_{i,0}}\left(\hat{U}^1_{i,0} - \tilde{U}^1_{i,0}\right). \tag{6.22}$$

To further elaborate the limiting technique discussed above, we give a brief description of the implementation of the second order limiter in the next section and the third order moment limiter in the Appendix B.

6.1.4 Second order limiter

The $p = 1$ DG approximation on Ω_i, written as a linear combination of Legendre tensor product basis, is

$$U_i = \hat{U}^0_{i,0}\varphi^0_0(\zeta,\eta) + \hat{U}^0_{i,1}\varphi^0_1(\zeta,\eta) + \hat{U}^1_{i,0}\varphi^1_0(\zeta,\eta) + \hat{U}^1_{i,1}\varphi^1_1(\zeta,\eta), \tag{6.23}$$

where the constant and linear basis functions are

$$\varphi_0^0 = \frac{1}{2}, \quad \varphi_1^0 = \frac{\sqrt{3}}{2}\zeta, \quad \varphi_0^1 = \frac{\sqrt{3}}{2}\eta, \quad \varphi_1^1 = \frac{3}{2}\zeta\eta. \tag{6.24}$$

The derivatives of U_i along the vectors $v_1 = (1,0)$ and $v_2 = (0,1)$ in the canonical space are

$$U_{i,\zeta} = \frac{\sqrt{3}}{2}\hat{U}_{i,1}^0 + \frac{3}{2}\hat{U}_{i,1}^1\eta, \quad U_{i,\eta} = \frac{\sqrt{3}}{2}\hat{U}_{i,0}^1 + \frac{3}{2}\hat{U}_{i,1}^1\zeta, \quad U_{i,\zeta\eta} = \frac{3}{2}\hat{U}_{i,1}^1. \tag{6.25}$$

Using (1.19), (1.20), (1.22), and the chain rule, the derivatives in (6.25) can be expressed in terms of the derivatives of U_i in the physical space as

$$\begin{aligned} &U_{i,\zeta} = U_{i,x}x_\zeta + U_{i,y}y_\zeta, \quad U_{i,\eta} = U_{i,x}x_\eta + U_{i,y}y_\eta, \\ &U_{i,\zeta\eta} = U_{i,xx}x_\zeta x_\eta + U_{i,yy}y_\zeta y_\eta + U_{i,xy}(x_\eta y_\zeta + x_\zeta y_\eta) + U_{i,x}C_{i,x3} + U_{i,y}C_{i,y3}. \end{aligned} \tag{6.26}$$

We start limiting at the highest solution coefficient, i.e., $\hat{U}_{i,1}^1$. From (6.25), we see that $\hat{U}_{i,1}^1$ is proportional to the gradient of $D_{v_2}U_i$ along $\eta = 0$, i.e., we can find the limited solution coefficient $\tilde{U}_{i,1}^1$ by computing the forward and backward difference of $D_{v_2}U_i$ along $\mathbf{v}_{i,1}$. For this, we need to find the values of $D_{v_2}U_i$ at the forward and backward interpolation points $\mathbf{x}_{i,1}^f$ and $\mathbf{x}_{i,1}^b$ (Figure 6.2). From (6.26), (6.8), and the chain rule, the value of $D_{v_2}U_i$ at $\mathbf{x}_{i,1}^f$ is

$$D_{v_2}U_i(\mathbf{x}_{i,1}^f) = D_{\mathbf{v}_{i,\eta}^{1,f}}U_i. \tag{6.27}$$

Now, using (6.9), (6.10), and (6.25), we compute the directional derivative $D_{\mathbf{v}_{i,\eta}^{1,f}}U$ at the cell centroid of the neighboring element Ω_k

$$D_{\mathbf{v}_{i,\eta}^{1,f}}U_k = \alpha_{k,\eta}^{1,f}U_{k,\zeta}\Big|_{(0,0)} + \theta_{k,\eta}^{1,f}U_{k,\eta}\Big|_{(0,0)}. \tag{6.28}$$

Similarly, we compute the directional derivative $D_{\mathbf{v}_{i,\eta}^{1,f}}U$ at the cell centroid of the neighboring element Ω_j

$$D_{\mathbf{v}_{i,\eta}^{1,f}}U_j = \alpha_{j,\eta}^{1,f}U_{j,\zeta}\Big|_{(0,0)} + \theta_{j,\eta}^{1,f}U_{j,\eta}\Big|_{(0,0)}. \tag{6.29}$$

Finally, we linearly interpolate the value of $D_{v_2}U_i(\mathbf{x}_{i,1}^f)$ using the directional derivatives computed in (6.28) and (6.29)

$$D_{v_2}U_i(\mathbf{x}_{i,1}^f) = D_{\mathbf{v}_{i,\eta}^{1,f}}U_i = \beta_{i,1}^f D_{\mathbf{v}_{i,\eta}^{1,f}}U_k + (1-\beta_{i,1}^f)D_{\mathbf{v}_{i,\eta}^{1,f}}U_j. \tag{6.30}$$

In a similar fashion, we estimate the value of $D_{v_2}U_i$ at the backward interpolation point

$\mathbf{x}^b_{i,1}$ as

$$D_{v_2}U_i(\mathbf{x}^b_{i,1}) = \beta^b_{i,1} D_{\mathbf{v}^{1,b}_{i,\eta}} U_n + (1-\beta^b_{i,1}) D_{\mathbf{v}^{1,b}_{i,\eta}} U_o. \tag{6.31}$$

Finally, we compute the limited solution coefficient $\tilde{U}^1_{i,1}$ by plugging the forward and backward differences into (6.15) as

$$\tilde{U}^1_{i,1} \leftarrow \text{minmod}\left(\hat{U}^1_{i,1}, l^f_{i,1}\frac{1}{|\zeta^f_{i,1}|}\left(\frac{2D_{v_2}U_i(\mathbf{x}^f_{i,1})}{3} - \frac{1}{\sqrt{3}}\hat{U}^1_{i,0}\right), l^b_{i,1}\frac{1}{|\zeta^b_{i,1}|}\left(\frac{1}{\sqrt{3}}\hat{U}^1_{i,0} - \frac{2D_{v_2}U_i(\mathbf{x}^b_{i,1})}{3}\right)\right). \tag{6.32}$$

Similarly, we compute the forward and backward differences of $D_{v_1}U_i$ along $\mathbf{v}_{i,2}$ and plug them into (6.19) to find the limited solution coefficient $\tilde{U}^1_{i,1}$

$$\tilde{U}^1_{i,1} \leftarrow \text{minmod}\left(\tilde{U}^1_{i,1}, l^f_{i,2}\frac{1}{|\eta^f_{i,2}|}\left(\frac{2D_{v_1}U_i(\mathbf{x}^f_{i,2})}{3} - \frac{1}{\sqrt{3}}\hat{U}^0_{i,1}\right), l^b_{i,2}\frac{1}{|\eta^b_{i,2}|}\left(\frac{1}{\sqrt{3}}\hat{U}^0_{i,1} - \frac{2D_{v_1}U_i(\mathbf{x}^b_{i,2})}{3}\right)\right). \tag{6.33}$$

If $\hat{U}^1_{i,1}$ is modified, then we find the limited linear solution coefficients $\tilde{U}^0_{i,1}$ and $\tilde{U}^1_{i,0}$. Consider $\hat{U}^0_{i,1}$. Along $\eta = 0$, from (6.23) we see that

$$U_i = \frac{1}{2}\hat{U}^0_{i,0} + \frac{\sqrt{3}}{2}\hat{U}^0_{i,1}\zeta, \tag{6.34}$$

i.e., $\hat{U}^0_{i,1}$ is proportional to the gradient of U_i along $\eta = 0$. Similar to the steps outlined above for $\hat{U}^1_{i,1}$, we can linearly interpolate values of U_i at the forward and backward interpolation points $\mathbf{x}^f_{i,1}$ and $\mathbf{x}^b_{i,1}$ along $\mathbf{v}_{i,1}$ using the solution values at the cell centroids of the closest neighboring elements, i.e.,

$$U(\mathbf{x}^f_{i,1}) = \beta^f_{i,1}\frac{\hat{U}^0_{k,0}}{2} + (1-\beta^f_{i,1})\frac{\hat{U}^0_{j,0}}{2}, \quad U(\mathbf{x}^b_{i,1}) = \beta^b_{i,1}\frac{\hat{U}^0_{n,0}}{2} + (1-\beta^b_{i,1})\frac{\hat{U}^0_{o,0}}{2}. \tag{6.35}$$

Thus, the limited linear solution coefficient $\tilde{U}^0_{i,1}$ is given by

$$\tilde{U}^0_{i,1} \leftarrow \text{minmod}\left(\hat{U}^0_{i,1}, l^f_{i,1}\frac{1}{|\zeta^f_{i,1}|}\left(\frac{2U(\mathbf{x}^f_{i,1})}{\sqrt{3}} - \frac{1}{\sqrt{3}\hat{U}^0_{i,0}}\right), l^b_{i,1}\frac{1}{|\zeta^b_{i,1}|}\left(\frac{1}{\sqrt{3}\hat{U}^0_{i,0}} - \frac{2U(\mathbf{x}^b_{i,1})}{\sqrt{3}}\right)\right). \tag{6.36}$$

Similarly, the limited linear solution coefficient $\tilde{U}^1_{i,0}$ is given by

$$\tilde{U}^1_{i,0} \leftarrow \text{minmod}\left(\hat{U}^1_{i,0}, l^f_{i,2}\frac{1}{|\eta^f_{i,2}|}\left(\frac{2U(\mathbf{x}^f_{i,2})}{\sqrt{3}} - \frac{1}{\sqrt{3}\hat{U}^0_{i,0}}\right), l^b_{i,2}\frac{1}{|\eta^b_{i,2}|}\left(\frac{1}{\sqrt{3}\hat{U}^0_{i,0}} - \frac{2U(\mathbf{x}^b_{i,2})}{\sqrt{3}}\right)\right). \tag{6.37}$$

Finally, if the linear solution coefficients are modified, we update the value of the zeroth solution coefficient as shown in (6.22).

6.2 Numerical Results

In this section, we present numerical experiments to analyze the performance of the proposed high-order moment limiter. We perform convergence studies to show that the limited solution maintains the theoretical rate of convergence for smooth problems. We also run tests to show the robustness of the proposed limiter in the presence of discontinuities. In all presented cases, time-stepping was performed using an explicit Runge-Kutta method of order $p+1$ with the CFL condition

$$\begin{aligned} \Delta t &\leq CFL \ \min_i \frac{h_i}{\|\mathbf{a}\|}, \\ CFL &= \frac{1}{(2p+1)}, \end{aligned} \tag{6.38}$$

where h_i, the smallest height of element Ω_i (Figure 6.3), is given by

$$\begin{aligned} h_i &= \min(h_1, h_2), \\ h_1 &= \min(\max(\min(H_{i,12}, H_{i,13}), \min(H_{i,34}, H_{i,31})), \max(\min(H_{i,24}, H_{i,23}), \\ &\quad \min(H_{i,41}, H_{i,42}))), \\ h_2 &= \min(\max(H_{i,41}, H_{i,31}), \max(H_{i,12}, H_{i,42}), \max(H_{i,13}, H_{i,23}), \max(H_{i,24}, H_{i,34})). \end{aligned} \tag{6.39}$$

Finally, unless stated otherwise, the local Lax-Friedrichs flux was used.

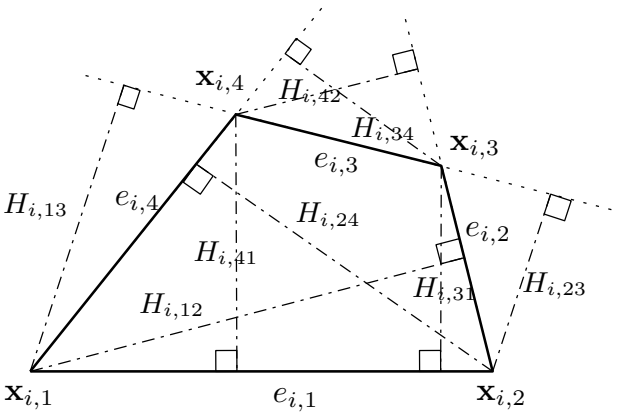

Figure 6.3: Element size h_i.

6.2.1 Sinusoidal Wave.

We solve the linear advection equation on the domain $\Omega = [-1,1] \times [-1,1]$, with the flux in (1.8) given by $\mathbf{F} = [u,u]$. The initial condition consists of a sinusoidal wave $u_0(x,y) = sin(2\pi(x+y))$ advected with speed $a = \sqrt{2}$ along the direction $(1,1)$. The problem is solved until $t = 0.5$ on a series of quadrilateral meshes $A - D$, A being the coarsest mesh with 509 elements. The finer mesh is obtained by remeshing the preceding mesh such that the element size is reduced by a factor of two. Table 6.1 shows the L_1 errors and the observed convergence rates for $p = 1, 2$, and 3 DG approximations with and without limiting. We observe that the limited solution retains the theoretical rate of convergence. We also note that the errors introduced by limiting are relatively modest.

Mesh	Nb	L1 error					
		p = 1	p = 1 (unlimited)	p = 2	p = 2 (unlimited)	p = 3	p = 3 (unlimited)
A	509	3.51e-01 (-)	1.0e-01 (-)	5.87e-02 (-)	4.28e-03 (-)	1.83e-02 (-)	2.05e-04 (-)
B	2035	9.92e-02 (1.82)	2.13e-02 (2.24)	4.04e-03 (3.6)	5.01e-04 (3.09)	1.08e-04 (7.4)	1.22e-05 (4.07)
C	8363	2.17e-02 (2.20)	4.86e-03 (2.13)	4.3e-04 (3.22)	6.08e-05 (3.04)	5.24e-06 (4.37)	7.51e-07 (4.02)
D	33469	4.24e-03 (2.35)	1.17e-03 (2.07)	4.220e-05 (3.36)	7.57e-06 (3.00)	2.54e-07 (4.37)	4.73e-08 (3.99)

Table 6.1: L_1 errors for the linear advection of a sinusoidal wave at $t = 0.5$ on an unstructured quadrilateral mesh. The numbers in parentheses are the observed rates of convergence.

6.2.2 Rotating shapes.

Next, we solve the rotating shapes problem with the flux in (1.8) given by $\mathbf{F} = [-2\pi yu, 2\pi xu]$. The initial condition consists of a hill and a square pulse as shown in Figure 6.4 and given by

$$u_0(x,y) = \begin{cases} \cos^2(2\pi r), & \text{if } r \le 0.25, \\ 1, & \text{if } \max(|x-0.35|, |y|) \le 0.25, \\ 0, & \text{otherwise,} \end{cases} \tag{6.40}$$

where $r = \sqrt{(x+0.5)^2 + y^2}$. The exact solution is a rotation of the initial condition about the origin. The problem is solved until $t = 1$ on an unstructured mesh of 6389 quadrilateral elements. Figure 6.5 shows the isolines and the solution profiles at $y = 0$, $x = 0.5, 0.55$, obtained using second, third, and fourth order DG approximations and the respective moment limiters. The quality of the solution is comparable to the results obtained on a 80×80 Cartesian mesh using the moment limiter described in [25]. We note that while the discontinuities are sufficiently resolved by all three limiters, the peak of the hill is captured

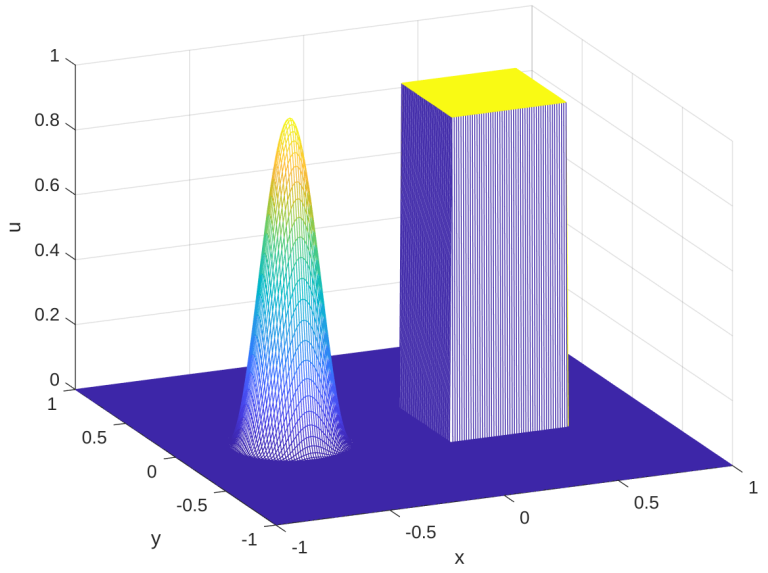

Figure 6.4: Initial condition for the rotating shapes problem.

well only by the third and fourth order moment limiters. This occurs due to the well known phenomenon of 'clipping' by a second order slope limiter at local extrema. Moreover, while all three limiters are successful in reducing the spurious oscillations near discontinuities, from Figure 6.5b we see that discontinuities are sharper with high-order limiters, which is further supported by the solution profiles shown in Figures 6.5d and 6.5e.

6.2.3 Isentropic vortex.

Next, we test the performance of the high-order limiter when applied to a system of non-linear equations, for example, the Euler equations given by

$$\frac{\partial}{\partial t}\begin{pmatrix}\rho\\ \rho u\\ \rho v\\ E\end{pmatrix}+\frac{\partial}{\partial x}\begin{pmatrix}\rho u\\ \rho u^2+p\\ \rho uv\\ (E+p)u\end{pmatrix}+\frac{\partial}{\partial y}\begin{pmatrix}\rho v\\ \rho uv\\ \rho v^2+p\\ (E+p)v\end{pmatrix}=0, \tag{6.41}$$

where ρ is the density, ρu and ρv are the x- and y-direction momenta, E is the energy, and the pressure, p, is given by the equation of state $p=(\gamma-1)\left(E-\frac{\rho}{2}(u^2+v^2)\right)$.

We solve the smooth isentropic vortex problem described in [51] on the domain $[-3,3]\times$

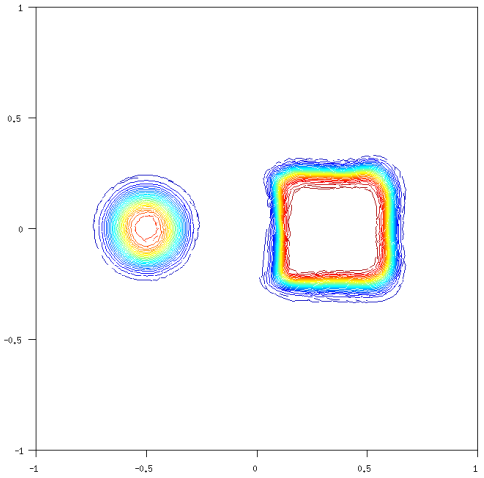

(a) Isolines with second order moment limiter.

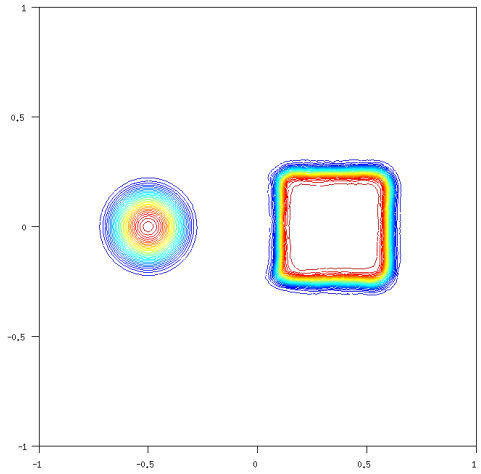

(b) Isolines with third order moment limiter.

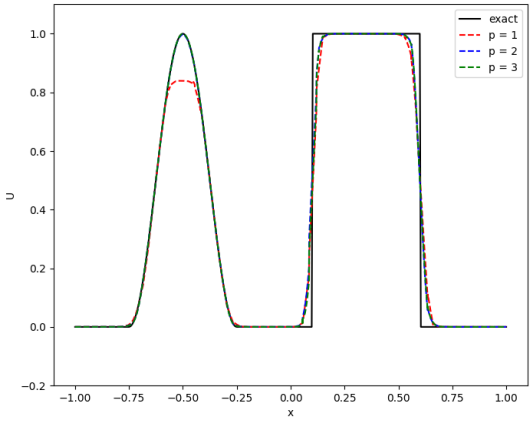

(c) Profile of the solution along $y = 0$.

$[-3, 3]$ with the initial conditions

$$\rho = \left(1 - \frac{(\gamma-1)}{8\pi^2}(M\beta)^2 e^r\right)^{\frac{1}{\gamma-1}}, \quad p = \frac{\rho^\gamma}{\gamma M^2}, \quad u = \frac{\beta}{2\pi R} y e^{\frac{r}{2}}, \quad v = -\frac{\beta}{2\pi R} x e^{\frac{r}{2}}, \tag{6.42}$$

where $r = \frac{1-(x^2+y^2)}{R^2}$, $R = 1.5$, $\beta = 13.5$, $\gamma = 1.4$, and $M = 0.4$. With the given initial conditions, the exact solution is stationary and given by (6.42). The L_1 errors in density and the observed convergence rates are reported in Table 6.2. As with the linear advection, we see that the proposed limiter maintains the theoretical convergence rates and introduces only modest errors.

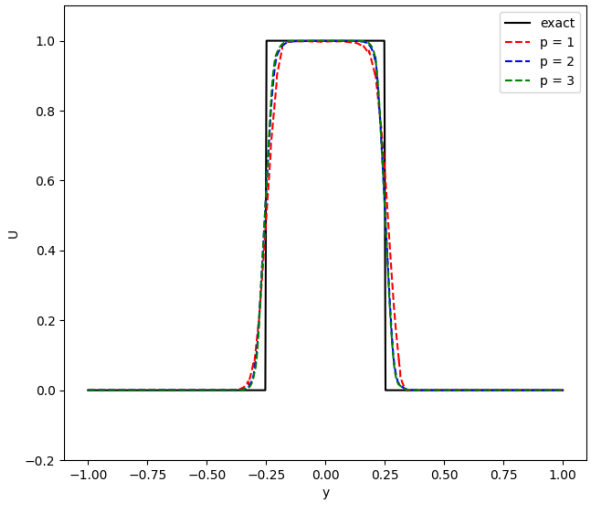

(d) Profile of the solution along $x = 0.5$.

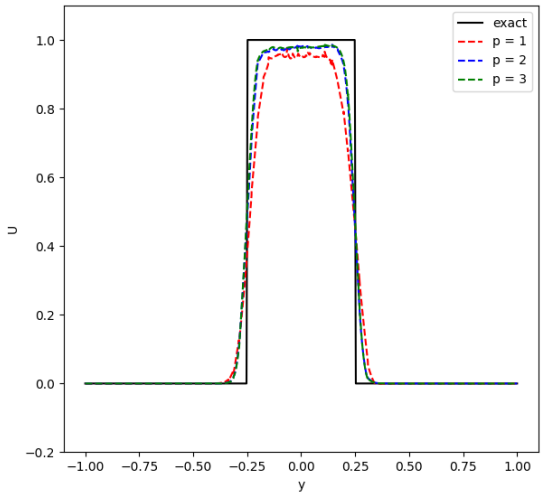

(e) Profile of the solution along $x = 0.55$.

Figure 6.5: Rotating shapes at $t = 1$ on a quadrilateral mesh with 6389 elements.

Mesh	Nb of elem	L1 error					
		p = 1	p = 1 (unlimited)	p = 2	p = 2 (unlimited)	p = 3	p = 3 (unlimited)
A	515	7.15e-02 (-)	1.7e-02 (-)	4.34e-03 (-)	9.29e-04 (-)	2.94e-04 (-)	1.78e-05 (-)
B	2047	1.50e-02 (2.12)	4.06e-03 (2.07)	2.62e-04 (4.00)	1.22e-04 (2.93)	5.59e-06 (5.71)	1.10e-06 (4.02)
C	8372	3.49e-03 (2.11)	1.0e-03 (2.02)	3.07e-05 (3.08)	1.60e-05 (2.93)	1.55e-07 (5.71)	6.45e-08 (4.09)
D	33532	7.28e-04 (2.26)	2.54e-04 (1.98)	3.00e-06 (3.36)	2.1e-06 (2.93)	5.25e-09 (4.88)	4.03e-09 (4.00)

Table 6.2: L_1 errors in density for the stationary isentropic vortex example at $t = 0.5$ on unstructured quadrilateral meshes. The numbers in parentheses are the observed rates of convergence.

6.2.4 Shock-vortex interaction.

Next, we solve the shock-vortex interaction test case to analyze the performance of the proposed limiter in the presence of both discontinuities and smooth flow features. The test case involves interaction of two vortices of strength $M_v = 0.9$ with a stationary shock of strength $M_s = 1.5$ as they pass through it. The initial set-up for the problem (Figure 6.7) is a modification of the one in [52].

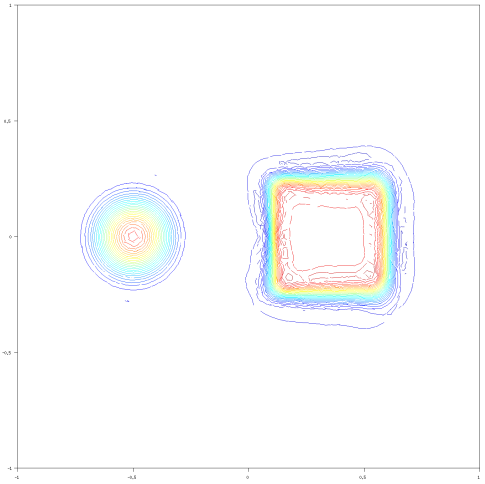

(a) $p = 1$.

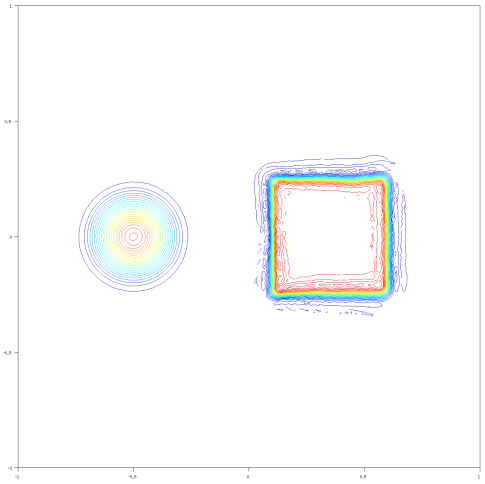

(b) $p = 2$.

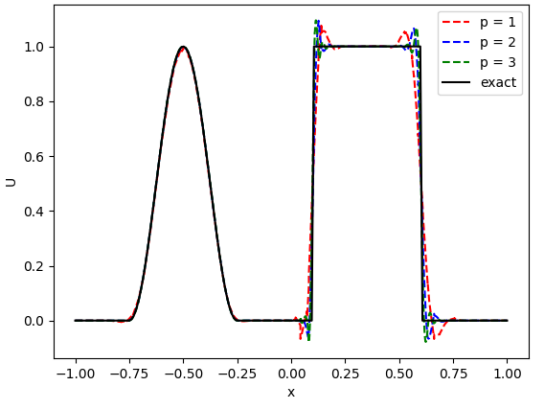

(c) Profile of the solution along $y = 0$.

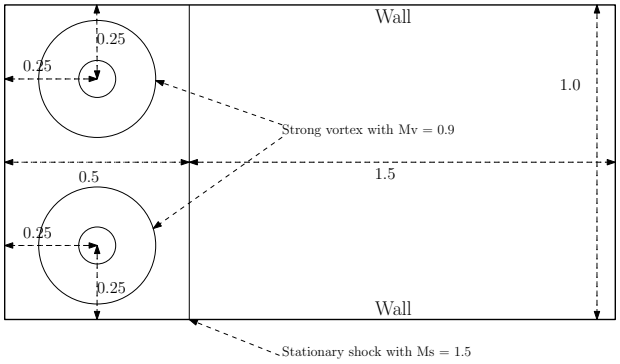

Figure 6.7: Initial set-up for the shock vortex interaction example.

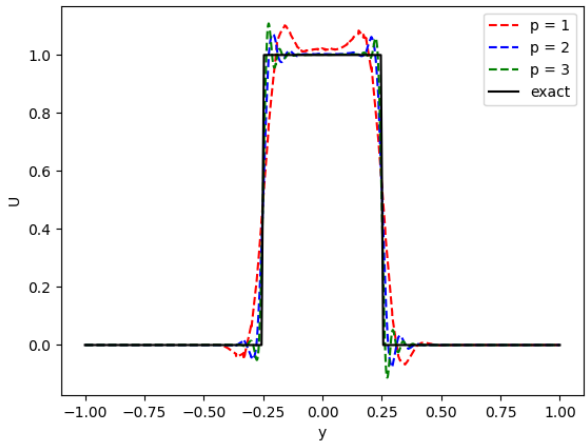

(d) Profile of the solution along $x = 0.5$.

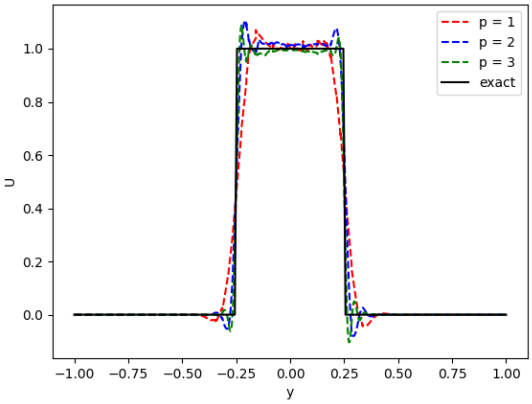

(e) Profile of the solution along $x = 0.55$.

Figure 6.6: Rotating shapes at $t = 1$ on a quadrilateral mesh with 6389 elements.

Initially, the shock is located at $x = 0.5$ while the vortices are located at $(0.25, 0.25)$ and $(0.25, 0.75)$. The upstream conditions are $(\rho_u, u_u, v_u, p_u) = (1, \sqrt{1.4}M_s, 0, 1)$, the vortices rotate with an angular velocity

$$\omega = \begin{cases} \omega_m \dfrac{r}{a}, & r \le a, \\ \omega_m \dfrac{a}{a^2 - b^2}\left(r - \dfrac{b^2}{r}\right), & a \le r \le b, \\ 0, & r \ge b, \end{cases} \tag{6.43}$$

where r is the radial distance from the center of the vortex, $\omega_m = \sqrt{1.4}M_v$ is the maximum angular velocity, and $(a, b) = (0.075, 0.175)$. The density and pressure inside the vortices are

$$\rho = \rho_u \left(\frac{T}{T_u}\right)^{2.5}, \quad p = p_u \left(\frac{T}{T_u}\right)^{3.5}, \tag{6.44}$$

where $T_u = 1$ is the upstream temperature. The temperature inside the vortices can be obtained by solving

$$\frac{dT}{dr} = \frac{2}{7}\frac{\omega^2}{r}, \tag{6.45}$$

where r is the radial distance from the center of the vortex. The simulation is run until

$t = 0.7$ on a mesh of $110,774$ quadrilaterals. Figure 6.8 shows the density isolines at $t = 0.7$ obtained using the second, third, and fourth order DG approximations and the respective moment limiters. From Figure 6.8, we observe that the shock structure and compression waves have been effectively captured in all three simulations. Further, as each vortex passes through the stationary shock, it splits into two vortices. Comparing Figures 6.8a and 6.8b we observe that the high-order discretizations are more effective in capturing the split vortices.

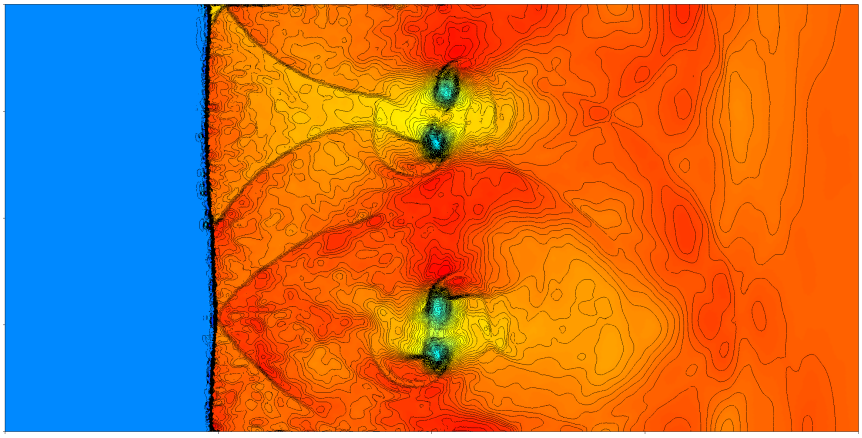

(a) Density isolines with $p = 1$.

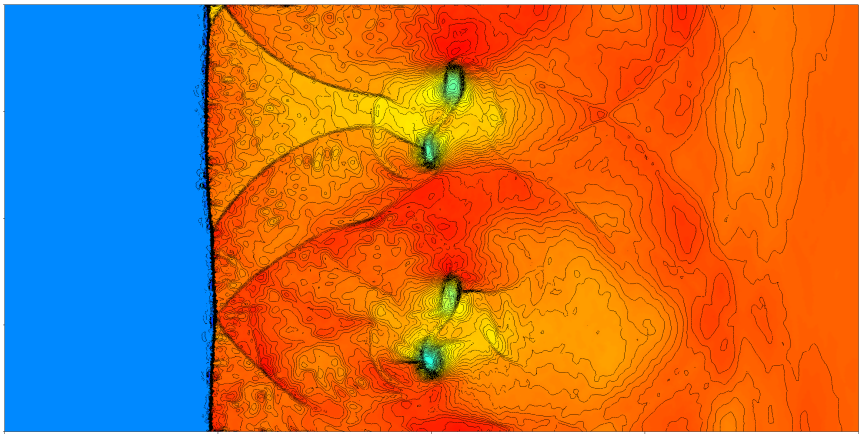

(b) Density isolines with $p = 2$.

6.2.5 Strong shock interactions.

Next, we test the performance of the limiter in the presence of shock-shock interactions. The initial conditions are taken from the two-dimensional Riemann test suite proposed in

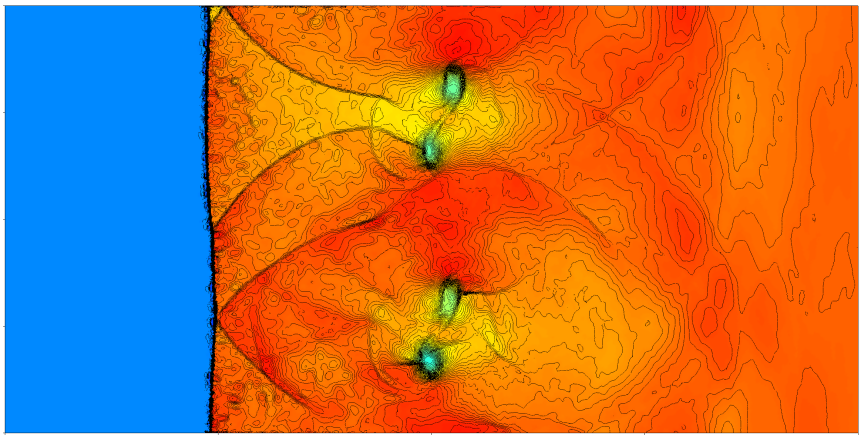

(c) Density isolines with $p = 3$.

Figure 6.8: Density isolines at $t = 0.7$ for the shock vortex interaction example on an unstructured mesh of $110,774$ quads.

[55] and shown in Figure 6.9. The simulation is run until $t = 0.8$ on a mesh of $160,103$ quadrilaterals. Figure 6.10 shows the density isolines at $t = 0.8$ obtained using the second and third-order DG approximations and the respective moment limiters. We note that the higher order method better resolves the vortical structures along the contact discontinuities.

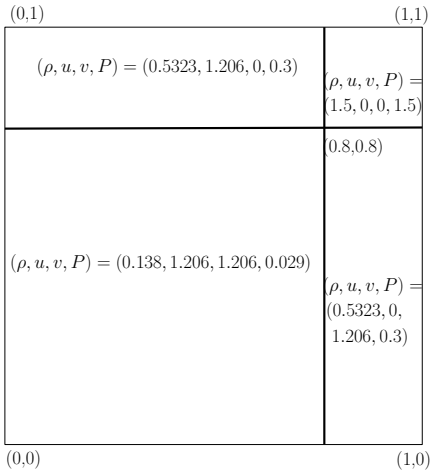

Figure 6.9: Modified initial condition for 2D Riemann problem.

Next, we perform a wall clock timing study to check the computational cost of the limiter. We see that the limiter takes at most about twenty percent of the total run time

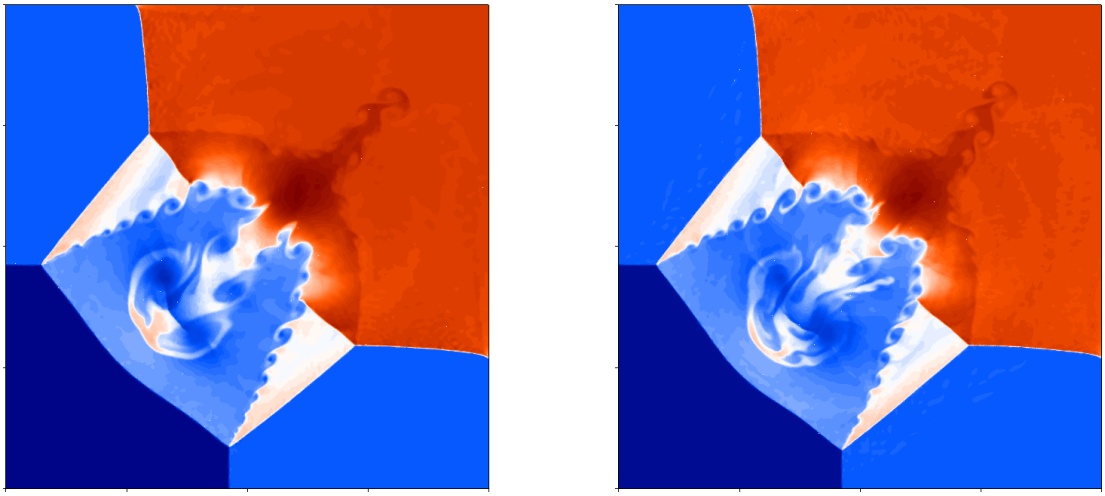

(a) (b)

Figure 6.10: Density isolines at $t = 0.8$ for the shock-shock interaction example for a) $p = 1$, b) $p = 2$, on a mesh of $160,103$ quadrilaterals.

(Table 6.3) of a parallel GPU implementation of the modal discontinuous Galerkin method [54].

p	Run time (s)	Limiting time (s)	Time steps
1	370.88	35.86 (9.6%)	10,062
2	3004.5	564.4 (18.1%)	16,702
3	11,917.5	2,579.6 (21.6%)	20,842

Table 6.3: Limiting time for the shock-shock interaction example for $p = 1,\ 2$, and 3 DG approximations on a mesh of $160,103$ quadrilaterals. The limiting time as a percentage of the total run time is given in parenthesis under "Limiting time".

6.2.6 Double Mach reflection.

Finally, we solve the double Mach reflection problem to test the performance of the proposed moment limiter in the presence of strong discontinuities. The initial set-up for the problem is taken from [25] and is shown in Figure 6.11. The initial condition consists of a Mach 10 shock wave impinging on a reflecting wall at an angle of 60°. The states to the left ($\mathbf{U}_l$) and to the right ($\mathbf{U}_r$) of the shock wave are given in Table 6.4. The computational domain $[0, 3.5] \times [0, 1]$ is discretized into $230,266$ quadrilaterals. The simulation is run

	$\mathbf{U}_l$	$\mathbf{U}_r$
ρ	8	1.4
$s = \mathbf{v} \cdot \mathbf{n}$	8.25	0
p	116.5	1

Table 6.4: States to the left and right of the initial shock for the double Mach test case.

until $t = 0.2$. Figure 6.12 shows the density isolines at $t = 0.2$ obtained using second and third order DG approximations with the moment limiter. The results are comparable to the results in [25] obtained using a moment limiter on Cartesian mesh. We observe that both DG approximations resolve the shock structures well. We also note that the slip line near the primary triple point is tighter for the higher order approximation (Figure 6.13b).

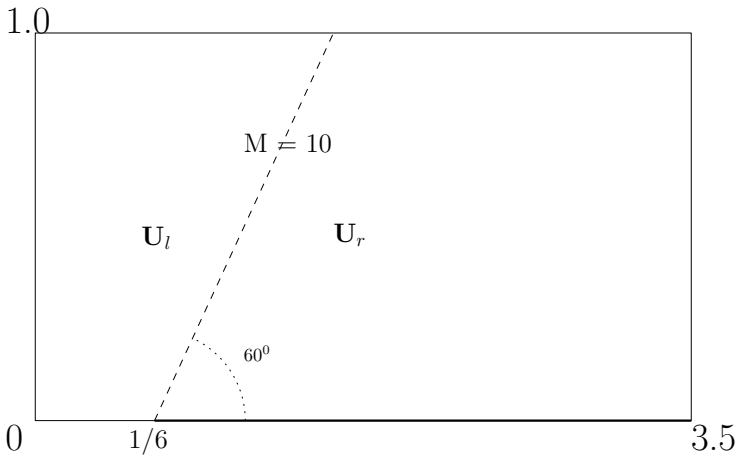

Figure 6.11: The initial set-up for the double mach reflection test case.

6.3 Summary

We have presented a high-order moment limiter for the DG method on unstructured quadrilateral meshes. The limiter works by limiting solution coefficients (moments) hierarchically starting with the highest moment. The limiting stops when either a pair of solution coefficients that are not modified or the zeroth order solution coefficient is encountered. The hierarchical implementation prevents overlimiting, especially near solution extrema where employing a second order limiter leads to 'clipping' thereby damaging the solution. Further, with the proposed limiting directions, the solution coefficients are fully uncoupled

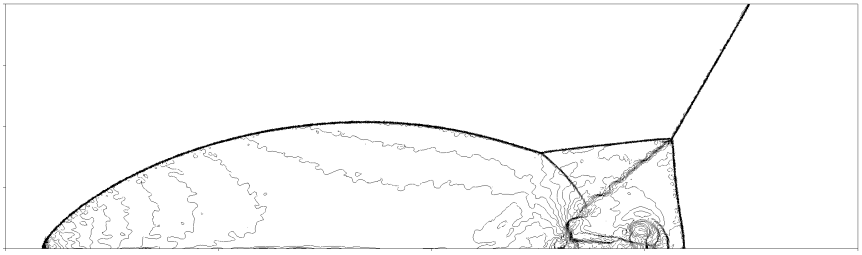

(a) Density isolines with $p = 1$.

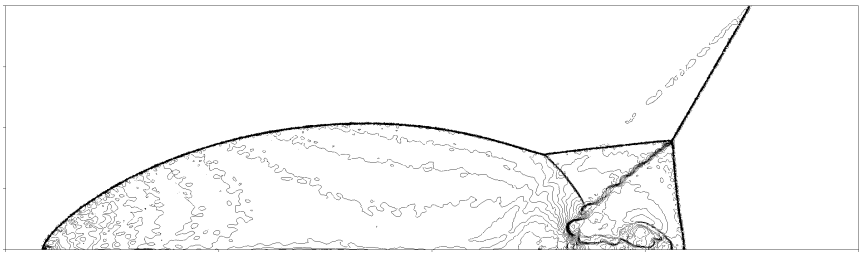

(b) Density isolines with $p = 2$.

Figure 6.12: Density isolines at $t = 0.2$ for the double Mach test case on a final mesh of $230,266$ quads.

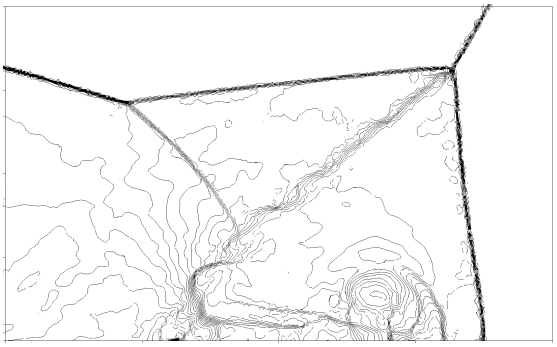

(a) Zoom in near slip line for $p = 1$.

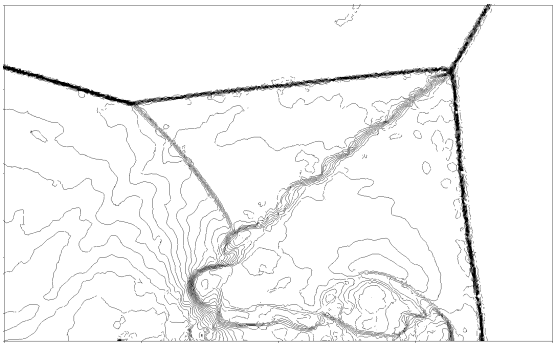

(b) Zoom in near slip line for $p = 2$.

Figure 6.13: Density isolines at $t = 0.2$ for the double Mach test case on a final mesh of $230,266$ quads.

which allows us to selectively limit moments that show excessive growth while retaining solution accuracy.

Numerical experiments presented in Section 6.2 illustrate that the DG method with the proposed limiter eliminates spurious oscillations and is robust in the presence of discontinuities. Further, the experiments also demonstrate that the limited solution retains the theoretical convergence rate for smooth solutions.

The proposed limiter makes use of a compact reconstruction stencil computed [53] once during the preprocessing stage. With the parameters precomputed, the complex formulas involved in the limiter reduces to a simple set of algebraic expressions involving solution coefficients. Thus, the limiter takes only a relatively modest percent of the total computing time ($\approx 20\%$ until $p = 3$ DG approximation) in a parallel implementation on a GPU for solution of Euler equations.

Chapter 7

High-order moment limiter on curvilinear triangular meshes

In the following chapter, we present a high-order moment limiter for the DG method on curvilinear triangular elements. The limiter can be viewed as an extension of the high-order limiter on triangular meshes proposed in [57] to curvilinear triangular meshes. We limit solution coefficients (moments) hierarchically by relating them to reconstructed directional derivatives of the numerical solution along two specified directions (Figure 7.1). The directional derivatives are reconstructed by comparing them to the forward and backward differences of derivatives of one order less. We derive expressions for directional derivatives of U_i in the physical and computational spaces in Section 7.1.1. The moment limiter is then presented in Section 7.1.2 for an arbitrary order of approximation p. We provide a detailed derivation of the limiter for the $p = 2$ DG approximation in Section 7.1.3. Finally, we provide a brief description of the hierarchical implementation of the limiter in 7.1.4. According to [58, 59], for a $p+1$th order DG approximation to retain its theoretical $p+1$th rate of convergence on a curvilinear triangular element Ω_i of order q, the 'curvature' of Ω_i should not exceed $\mathcal{O}(h^{q+1})$, where h is the measure of cell size of Ω_i. Therefore, in this work, we focus on curvilinear elements with the constraint stated above.

7.1 Limiting Algorithm

7.1.1 Directional derivatives

Consider the vectors

$$v_1 = \frac{2}{\sqrt{5}}(1, -1/2), \quad v_2 = (0, 1), \tag{7.1}$$

on the reference element Ω_0 (Figure 7.1). For $p = 1$, it was shown in [2] that the first order directional derivatives along directions (7.1) decouple the linear solution coefficients. This lead to development of the second order moment limiter on triangular meshes. For high-order approximations, these directions significantly simplify relations between solution coefficients and solution derivatives and led to the development of high-order moment limiter on triangular meshes [57].

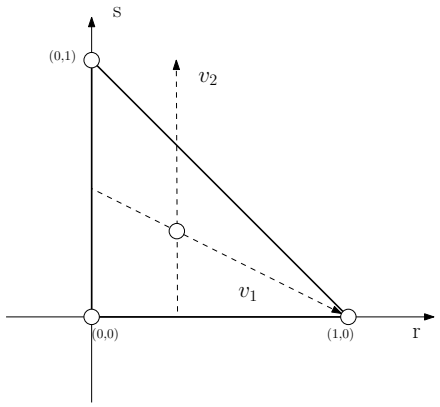

Figure 7.1: Limiting directions v_1 and v_2 on the canonical element Ω_0.

Denote jth directional derivatives along these directions by

$$D^q_{v_1} D^{j-q}_{v_2} U_i(\mathbf{r}) = \frac{\partial^j}{\partial v_1^q \partial v_2^{j-q}} U_i(\mathbf{r}), \quad 0 \le q \le j, \tag{7.2}$$

where $\mathbf{r} = (r, s)$. Following the discussion in [57], the pth directional derivatives of $U_i(\mathbf{r})$

along v_1 and v_2 evaluated at the cell center $\mathbf{r}_0$ can be written as

$$\left(\frac{\sqrt{5}}{2}\right)^q D_{v_2}^{p-q} D_{v_1}^q U_i(\mathbf{r}_0) = \sum_{\gamma=0}^{\lfloor q/2 \rfloor} \hat{U}_{i,p-q+2\gamma}^{q-2\gamma} \left[C_{p-q+2\gamma}^{q-2\gamma} 2^{2(p-q-\gamma)} \frac{d^{p-q}}{db^{p-q}} L_{p-q+2\gamma}(b) \right. \\ \left. \frac{d^q}{da^q} \left((1-a)^{2\gamma} P_{q-2\gamma}^{2(p-q+2\gamma)+1,0}(2a-1) \right) \right] \Big|_{(\frac{1}{3},0)}, \quad 0 \le q \le p, \tag{7.3}$$

where $\lfloor \cdot \rfloor$ is the floor function. Representing the expression within the square brackets by $\theta_{q,q-2\gamma}$, we rewrite (7.3) in the matrix form

$$\begin{pmatrix} D_{v_2}^p U_i(\mathbf{r}_0) \\ \left(\frac{\sqrt{5}}{2}\right) D_{v_2}^{p-1} D_{v_1}^1 U_i(\mathbf{r}_0) \\ \left(\frac{\sqrt{5}}{2}\right)^2 D_{v_2}^{p-2} D_{v_1}^2 U_i(\mathbf{r}_0) \\ \left(\frac{\sqrt{5}}{2}\right)^3 D_{v_2}^{p-3} D_{v_1}^3 U_i(\mathbf{r}_0) \\ \left(\frac{\sqrt{5}}{2}\right)^4 D_{v_2}^{p-4} D_{v_1}^4 U_i(\mathbf{r}_0) \\ \vdots \\ \left(\frac{\sqrt{5}}{2}\right)^p D_{v_1}^p U_i(\mathbf{r}_0) \end{pmatrix} = \begin{bmatrix} \theta_{0,0} & 0 & 0 & 0 & 0 & 0 & 0 & \cdots \\ 0 & \theta_{1,1} & 0 & 0 & 0 & 0 & 0 & \cdots \\ \theta_{2,0} & 0 & \theta_{2,2} & 0 & 0 & 0 & 0 & \cdots \\ 0 & \theta_{3,1} & 0 & \theta_{3,3} & 0 & 0 & 0 & \cdots \\ \theta_{4,0} & 0 & \theta_{4,2} & 0 & \theta_{4,4} & 0 & 0 & \cdots \\ & & & & \vdots & & & \\ & & & & \cdots & \theta_{p,p-2} & 0 & \theta_{p,p} \end{bmatrix} \begin{pmatrix} \hat{U}_{i,p}^0 \\ \hat{U}_{i,p-1}^1 \\ \hat{U}_{i,p-2}^2 \\ \hat{U}_{i,p-3}^3 \\ \hat{U}_{i,p-4}^4 \\ \vdots \\ \hat{U}_{i,0}^p \end{pmatrix}. \tag{7.4}$$

Similarly, the jth directional derivatives of $U_i(\mathbf{r})$, $1 \le j \le p$, along v_1 and v_2 evaluated at $\mathbf{r}_0$ are

$$\left(\frac{\sqrt{5}}{2}\right)^q D_{v_2}^{j-q} D_{v_1}^q U_i(\mathbf{r}_0) = \sum_{k=j}^{p} \sum_{\beta=0}^{\lfloor q/2 \rfloor} \hat{U}_{i,k-q+2\beta}^{q-2\beta} \left[C_{k-q+2\beta}^{q-2\beta} 2^{k+j-2q+2\beta} \frac{d^{j-q}}{db^{j-q}} L_{k-q+2\beta}(b) \right. \\ \left. \frac{d^q}{da^q} \left((1-a)^{k-j+2\beta} P_{q-2\beta}^{2(k-q+2\beta)+1,0}(2a-1) \right) \right] \Big|_{(\frac{1}{3},0)}, \quad 0 \le q \le j. \tag{7.5}$$

As noted in [57], the directional derivatives can be computed in any chosen directions. However, using the directions (7.1) results in a sparse transformation matrix in (7.4).

Next, using (1.29) for element Ω_i, we map the directions v_1 and v_2 defined in (7.1) from

the computational to the physical space and, after normalization, obtain the following unit vectors evaluated at $\mathbf{r}_0$

$$\mathbf{v}_{i,1} = \frac{J_i v_1}{\|J_i v_1\|}\bigg|_{\mathbf{r}_0}, \quad \mathbf{v}_{i,2} = \frac{J_i v_2}{\|J_i v_2\|}\bigg|_{\mathbf{r}_0}, \tag{7.6}$$

where J_i is given by (1.30). Further, we define the element heights as

$$h_{i,1} = \|J_i v_1\|\bigg|_{\mathbf{r}_0}, \quad h_{i,2} = \|J_i v_2\|\bigg|_{\mathbf{r}_0}. \tag{7.7}$$

Finally, using (1.29), (1.30), and (7.6), we express directional derivatives in the computational spaces, evaluated at $\mathbf{r}_0$, in terms of directional derivatives in the physical space

$$\left(\frac{\sqrt{5}}{2h_{i,1}}\right)^l \left(\frac{1}{h_{i,2}}\right)^{j-l} D^l_{v_1} D^{j-l}_{v_2} U_i(\mathbf{r}_0) = D^l_{\mathbf{v}_{i,1}} D^{j-l}_{\mathbf{v}_{i,2}} U_i(\mathbf{x}_{i,0}) + \sum_{s=1}^{q-1} \sum_{d=0}^{j-s} \zeta^d_{i,s} D^d_{\mathbf{v}_{i,1}} D^{j-s-d}_{\mathbf{v}_{i,2}} U_i(\mathbf{x}_{i,0}), \tag{7.8}$$

where $0 \le l \le j$, $1 \le j \le p$, and the coefficients ζ_i depend on the the Jacobian J_i in (1.30) and its derivatives evaluated at $\mathbf{r}_0$. Once we reconstruct the directional derivatives in the physical space, plugging them into (7.8) and using (7.5) we can compute the limited solution coefficients (or moments). In the following section, we describe an algorithm for limiting $D^q_{\mathbf{v}_{i,1}} D^{j-q}_{\mathbf{v}_{i,2}} U_i(\mathbf{x}_{i,0})$.

7.1.2 Reconstructing directional derivatives

For a $p+1$th order DG approximation, we start the limiting process with the highest order solution coefficients $\hat{U}^0_{i,p}, \hat{U}^1_{i,p-1}, ..., \hat{U}^p_{i,0}$. To modify pth order solution coefficients, we need to limit all directional derivatives $D^{j-l}_{\mathbf{v}_{i,1}} D^l_{\mathbf{v}_{i,2}} U_i$, $0 \le l \le j$, $p - q + 1 \le j \le p$, where q is the order of the curvilinear element Ω_i. Consider limiting the pth order directional derivative $D^{p-1}_{\mathbf{v}_{i,1}} D^1_{\mathbf{v}_{i,2}} U_i$. We limit $D^{p-1}_{\mathbf{v}_{i,1}} D^1_{\mathbf{v}_{i,2}} U_i$ by comparing its value at the cell center of Ω_i to the forward and backward differences of $D^{p-1}_{\mathbf{v}_{i,1}} U$ along $\mathbf{v}_{i,2}$ and $D^{p-2}_{\mathbf{v}_{i,1}} D^1_{\mathbf{v}_{i,2}} U$ along $\mathbf{v}_{i,1}$, i.e., the derivatives of one degree less.

The forward and backward differences are computed from the forward ($\mathbf{x}^f_{i,1}$, $\mathbf{x}^f_{i,2}$), and backward ($\mathbf{x}^b_{i,1}$,$\mathbf{x}^b_{i,2}$) interpolation points (Figure 7.2, solid squares) to the cell center (Figure 7.2, solid circle). To compute these points, first, we form a polygon by joining the cell centers of the neighboring elements that share a vertex with Ω_i. Next, we define two lines parallel to $\mathbf{v}_{i,1}$ and $\mathbf{v}_{i,2}$ that pass through the center of Ω_i. The points of intersection of these lines and the faces of the polygon gives the interpolation points $\mathbf{x}^f_{i,k}$, $\mathbf{x}^b_{i,k}$, $k = 1, 2$.

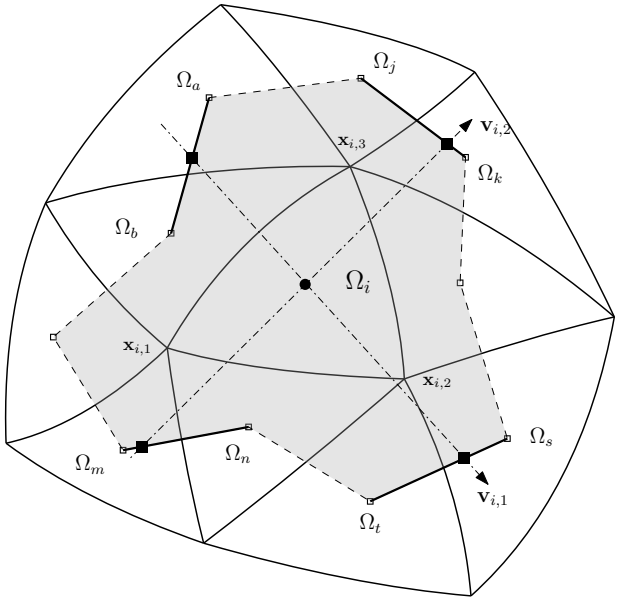

Figure 7.2: Ω_i and the mesh elements sharing a vertex with it. Limiting directions $\mathbf{v}_{i,1}$ and $\mathbf{v}_{i,2}$ are shown as arrows. Backward and forward interpolation points are shown as solid squares. Linear interpolation of directional derivatives at the interpolation points is performed over the thick line segments.

First, let us consider limiting $D^{p-1}_{\mathbf{v}_{i,1}} D^1_{\mathbf{v}_{i,2}} U_i$ along $\mathbf{v}_{i,2}$. To find the values of the $(p-1)$th order derivative $D^{p-1}_{\mathbf{v}_{i,1}} U$ at the interpolation points, we first compute the $(p-1)$th directional derivative $D^{p-1}_{\mathbf{v}_{i,1}} U_f(\mathbf{x}_{f,0})$, $f = \{j,k,m,n\}$ at the cell centers of the neighboring elements Ω_j, Ω_k, Ω_m, and Ω_n (Figure 7.3b). For example, consider element Ω_j. Generally, limiting directions $\mathbf{v}_{j,1}$ and $\mathbf{v}_{j,2}$ on Ω_j will not be the same as $\mathbf{v}_{i,1}$ and $\mathbf{v}_{i,2}$. To obtain directional derivatives along $\mathbf{v}_{i,1}$ and $\mathbf{v}_{i,2}$ on Ω_j, we express directions on Ω_i as linear combinations of directions on Ω_j

$$\mathbf{v}_{i,1} = \alpha^1_{j,1}\mathbf{v}_{j,1} + \alpha^1_{j,2}\mathbf{v}_{j,2}, \quad \mathbf{v}_{i,2} = \alpha^2_{j,1}\mathbf{v}_{j,1} + \alpha^2_{j,2}\mathbf{v}_{j,2}, \tag{7.9}$$

for some coefficients α. Using (7.9) and (7.8), the $(p-1)$th directional derivative $D^{p-1}_{\mathbf{v}_{i,1}} U_j$, evaluated at the cell center $\mathbf{x}_{j,0}$ of Ω_j, is

$$D^{p-1}_{\mathbf{v}_{i,1}} U_j(\mathbf{x}_{j,0}) = \left(\alpha^1_{j,1} D_{\mathbf{v}_{j,1}} + \alpha^1_{j,2} D_{\mathbf{v}_{j,2}}\right)^{p-1} U_j(\mathbf{x}_{j,0}). \tag{7.10}$$

Similarly, we compute the $(p-1)$th directional derivatives $D^{p-1}_{\mathbf{v}_{i,1}} U_k(\mathbf{x}_{k,0})$, $D^{p-1}_{\mathbf{v}_{i,1}} U_m(\mathbf{x}_{m,0})$, and $D^{p-1}_{\mathbf{v}_{i,1}} U_n(\mathbf{x}_{n,0})$ at the centers of Ω_k, Ω_m, and Ω_n (Figure 7.3b). Using the above computed values, we linearly interpolate the $(p-1)$th directional derivatives $D^{p-1}_{\mathbf{v}_{i,1}} U^f_{i,2}$ and $D^{p-1}_{\mathbf{v}_{i,1}} U^b_{i,2}$

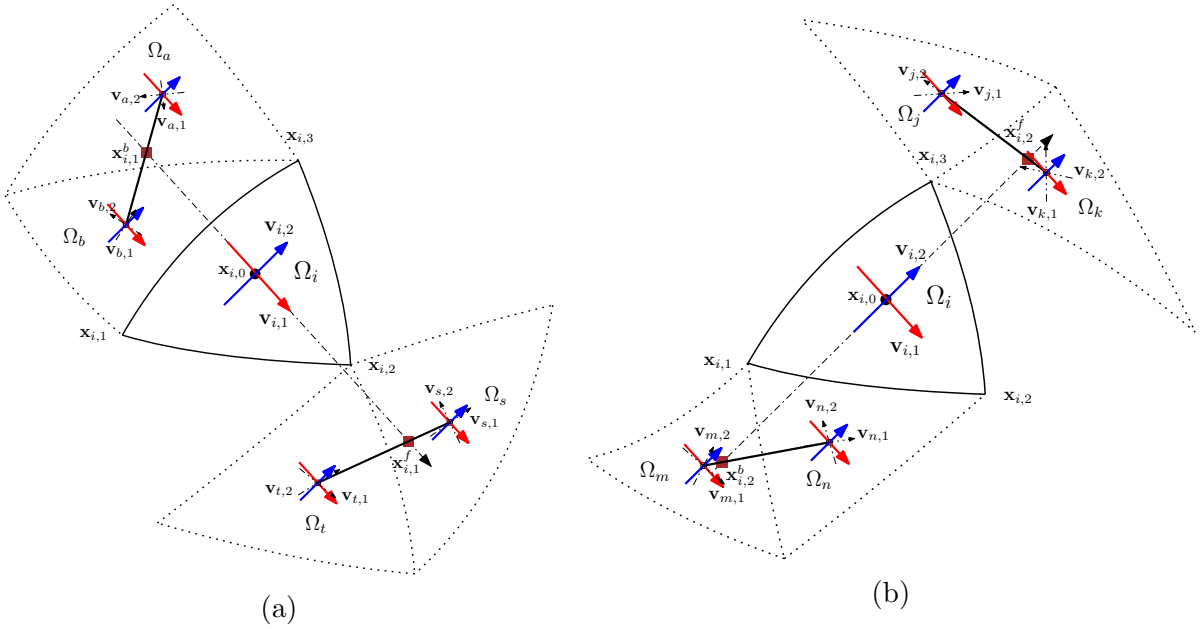

Figure 7.3: (A) Limiting stencil along $\mathbf{v}_{i,1}$, (B) Limiting stencil along $\mathbf{v}_{i,2}$.

at the interpolation points $\mathbf{x}^b_{i,2}$ and $\mathbf{x}^f_{i,2}$ as

$$\begin{aligned} D^{p-1}_{\mathbf{v}_{i,1}} U^f_{i,2} &= \beta^f_{i,2} D^{p-1}_{\mathbf{v}_{i,1}} U_j(\mathbf{x}_{j,0}) + (1-\beta^f_{i,2}) D^{p-1}_{\mathbf{v}_{i,1}} U_k(\mathbf{x}_{k,0}), \\ D^{p-1}_{\mathbf{v}_{i,1}} U^b_{i,2} &= \beta^b_{i,2} D^{p-1}_{\mathbf{v}_{i,1}} U_m(\mathbf{x}_{m,0}) + (1-\beta^b_{i,2}) D^{p-1}_{\mathbf{v}_{i,1}} U_n(\mathbf{x}_{n,0}), \end{aligned} \tag{7.11}$$

where $0 \le \beta^b_{i,2} \le 1$ and $0 \le \beta^f_{i,2} \le 1$ are the backward and forward interpolation weights for the limiting stencil in Figure 7.3b.

Finally, we limit the pth order directional derivative $D^{p-1}_{\mathbf{v}_{i,1}} D^1_{\mathbf{v}_{i,2}} U_i$ by comparing its value to the forward and backward differences in the $(p-1)$th directional derivatives multiplied by scaling parameters $l^f_{i,2}$ and $l^b_{i,2}$

$$\begin{aligned} D^{p-1}_{\mathbf{v}_{i,1}} D^1_{\mathbf{v}_{i,2}} U_i(\mathbf{x}_{i,0}) \leftarrow \operatorname{minmod}\Bigg(& D^{p-1}_{\mathbf{v}_{i,1}} D^1_{\mathbf{v}_{i,2}} U_i(\mathbf{x}_{i,0}), l^f_{i,2} \frac{D^{p-1}_{\mathbf{v}_{i,1}} U^f_{i,2} - D^{p-1}_{\mathbf{v}_{i,1}} U_i(\mathbf{x}_{i,0})}{\left\| \mathbf{x}^f_{i,2} - \mathbf{x}_{i,0} \right\|}, \\ & l^b_{i,2} \frac{D^{p-1}_{\mathbf{v}_{i,1}} U_i(\mathbf{x}_{i,0}) - D^{p-1}_{\mathbf{v}_{i,1}} U^b_{i,2}}{\left\| \mathbf{x}^b_{i,2} - \mathbf{x}_{i,0} \right\|} \Bigg), \end{aligned} \tag{7.12}$$

where the minmod function is

$$\text{minmod}(a,b,c) = \begin{cases} sign(a)\cdot min(|a|,|b|,|c|), & \text{if } sign(a) = sign(b) = sign(c), \\ 0, & \text{otherwise.} \end{cases} \tag{7.13}$$

Next, we limit $D^{p-1}_{\mathbf{v}_{i,1}} D^1_{\mathbf{v}_{i,2}} U_i$ along $\mathbf{v}_{i,1}$. We compute the $(p-1)$th directional derivative $D^{p-2}_{\mathbf{v}_{i,1}} D^1_{\mathbf{v}_{i,2}} U$ at the cell centers of Ω_a, Ω_b, Ω_s, and Ω_t (Figure 7.3a). For example, $D^{p-2}_{\mathbf{v}_{i,1}} D^1_{\mathbf{v}_{i,2}} U_a$ evaluated at $\mathbf{x}_{a,0}$ is

$$D^{p-2}_{\mathbf{v}_{i,1}} D^1_{\mathbf{v}_{i,2}} U_a(\mathbf{x}_{a,0}) = \left(\alpha^1_{a,1} D_{\mathbf{v}_{a,1}} + \alpha^1_{a,2} D_{\mathbf{v}_{a,2}}\right)^{p-2} \left(\alpha^2_{a,1} D_{\mathbf{v}_{a,1}} + \alpha^2_{a,2} D_{\mathbf{v}_{a,2}}\right) U_a(\mathbf{x}_{a,0}). \tag{7.14}$$

Once the values at the cell centers are computed, we use them to linearly interpolate $D^{p-2}_{\mathbf{v}_{i,1}} D^1_{\mathbf{v}_{i,2}} U$ at the forward and backward interpolation points $\mathbf{x}^f_{i,1}$ and $\mathbf{x}^b_{i,1}$

$$\begin{aligned} D^{p-2}_{\mathbf{v}_{i,1}} D^1_{\mathbf{v}_{i,2}} U^f_{i,1} &= \beta^f_{i,1} D^{p-2}_{\mathbf{v}_{i,1}} D^1_{\mathbf{v}_{i,2}} U_s(\mathbf{x}_{s,0}) + (1-\beta^f_{i,1}) D^{p-2}_{\mathbf{v}_{i,1}} D^1_{\mathbf{v}_{i,2}} U_t(\mathbf{x}_{t,0}), \\ D^{p-2}_{\mathbf{v}_{i,1}} D^1_{\mathbf{v}_{i,2}} U^b_{i,1} &= \beta^b_{i,1} D^{p-2}_{\mathbf{v}_{i,1}} D^1_{\mathbf{v}_{i,2}} U_a(\mathbf{x}_{a,0}) + (1-\beta^b_{i,1}) D^{p-2}_{\mathbf{v}_{i,1}} D^1_{\mathbf{v}_{i,2}} U_b(\mathbf{x}_{b,0}), \end{aligned} \tag{7.15}$$

where $0 \le \beta^b_{i,1} \le 1$ and $0 \le \beta^f_{i,1} \le 1$. Finally, we limit $D^{p-1}_{\mathbf{v}_{i,1}} D^1_{\mathbf{v}_{i,2}} U_i$ by comparing it to the forward and backward differences of $D^{p-2}_{\mathbf{v}_{i,1}} D^1_{\mathbf{v}_{i,2}} U$ scaled by the parameters $l^f_{i,1}$ and $l^b_{i,1}$

$$\begin{aligned} D^{p-1}_{\mathbf{v}_{i,1}} D^1_{\mathbf{v}_{i,2}} U_i(\mathbf{x}_{i,0}) \leftarrow \text{minmod}\Bigg(& D^{p-1}_{\mathbf{v}_{i,1}} D^1_{\mathbf{v}_{i,2}} U_i(\mathbf{x}_{i,0}), l^f_{i,1} \frac{D^{p-2}_{\mathbf{v}_{i,1}} D^1_{\mathbf{v}_{i,2}} U^f_{i,1} - D^{p-2}_{\mathbf{v}_{i,1}} D^1_{\mathbf{v}_{i,2}} U_i(\mathbf{x}_{i,0})}{\left\|\mathbf{x}^f_{i,1} - \mathbf{x}_{i,0}\right\|}, \\ & l^b_{i,1} \frac{D^{p-2}_{\mathbf{v}_{i,1}} D^1_{\mathbf{v}_{i,2}} U_i(\mathbf{x}_{i,0}) - D^{p-2}_{\mathbf{v}_{i,1}} D^1_{\mathbf{v}_{i,2}} U^b_{i,1}}{\left\|\mathbf{x}^b_{i,1} - \mathbf{x}_{i,0}\right\|} \Bigg). \end{aligned} \tag{7.16}$$

The scaling parameters $l^f_{i,k}$ and $l^b_{i,k}$, $k = \{1,2\}$, depend on the order of the derivative being limited. For jth order derivatives, $2 \le j \le p$, the admissible range is

$$\begin{aligned} 1 \le l^f_{i,2} \le \gamma^f_{i,2}(2j-1), \quad 1 \le l^b_{i,2} \le \gamma^b_{i,2}(2j-1), \\ 1 \le l^f_{i,1} \le \gamma^f_{i,1}(2j-1), \quad 1 \le l^b_{i,1} \le \gamma^b_{i,1}(2j-1), \end{aligned} \tag{7.17}$$

which is equivalent to the range for the scaling parameters used on Cartesian grids in [25]

and the scaling parameters used in [57]. For first order derivatives, the admissible range is

$$\begin{aligned} 1 \le l_{i,2}^f \le \gamma_{i,2}^f 2, \quad 1 \le l_{i,2}^b \le \gamma_{i,2}^b 2, \\ 1 \le l_{i,1}^f \le \gamma_{i,1}^f \frac{6}{\sqrt{5}}, \quad 1 \le l_{i,1}^b \le \gamma_{i,1}^b \frac{6}{\sqrt{5}}, \end{aligned} \tag{7.18}$$

which is equivalent to the range of scaling parameters used in [2]. The geometric parameters γ_i in (7.17) and (7.18) are

$$\begin{aligned} \gamma_{i,1}^f = \frac{\left\| \mathbf{x}_{i,1}^f - \mathbf{x}_{i,0} \right\|}{h_{i,1}}, \quad \gamma_{i,1}^b = \frac{\left\| \mathbf{x}_{i,1}^b - \mathbf{x}_{i,0} \right\|}{h_{i,1}}, \\ \gamma_{i,2}^f = \frac{\left\| \mathbf{x}_{i,2}^f - \mathbf{x}_{i,0} \right\|}{h_{i,2}}, \quad \gamma_{i,2}^b = \frac{\left\| \mathbf{x}_{i,2}^b - \mathbf{x}_{i,0} \right\|}{h_{i,2}}, \end{aligned} \tag{7.19}$$

where $h_{i,1}$ and $h_{i,2}$ are defined in (7.7). We note that in all experiments presented in Section 7.2, we choose the least restrictive limiter, i.e., the right ends of the intervals in (7.17) and (7.18), to minimize loss in accuracy of the solution.

Similarly, we limit every jth order directional derivative along $\mathbf{v}_{i,1}$ and $\mathbf{v}_{i,2}$, where $p - q + 1 \le j \le p$. Substituting these limited directional derivatives into (7.8) and using (7.4), we obtain the limited pth order moments. If all pth order moments are modified by the limiter, we repeat the process for the $(p-1)$th order moments $\hat{U}_{i,p-1}^0, \hat{U}_{i,p-2}^1, \cdots, \hat{U}_{i,0}^{p-1}$ and the process continues until we reach either a set of kth order moments that are not modified or the zeroth order moment.

Remark 1. For a qth order curvilinear triangular element, if the solution coefficients of order q or lower are limited, then we update the zeroth order solution coefficient $\hat{U}_{i,0}^0$ using (7.20) to ensure that the cell average of U_i in Ω_i, $\overline{U}_i$, remains unmodified.

$$\hat{U}_{i,0}^0 \leftarrow \hat{U}_{i,0}^0 + \frac{\delta_{i,l}^{j-l}}{\delta_{i,0}^0} \left(\hat{U}_{i,l}^{j-l} - \tilde{U}_{i,l}^{j-l} \right), \quad 0 \le l \le j, \quad 1 \le j \le q, \tag{7.20}$$

where the coefficients δ are

$$\delta_{i,l}^{j-l} = \int_{\Omega_0} \varphi_l^{j-l} \det J_i \, d\mathbf{r}. \tag{7.21}$$

To further illustrate the limiting technique discussed above, we give a brief description of the implementation of the third order limiter on second-order curvilinear triangles in the following section.

7.1.3 Third order limiter

The third order DG approximation on element Ω_i, written as a linear combination of the Dubiner basis (1.14), is

$$U_i(r,s) = \sum_{l+k=0}^{2} \hat{U}_{i,k}^{l} \varphi_k^l(r,s). \tag{7.22}$$

The quadratic basis functions are given by

$$\begin{aligned}
\varphi_2^0(r,s) &= \frac{3\sqrt{30}}{2}(2s+r-1)^2 - \frac{\sqrt{30}}{2}(1-r)^2, \\
\varphi_1^1(r,s) &= 3\sqrt{2}(2s+r-1)(5r-1), \\
\varphi_0^2(r,s) &= 3\sqrt{6} + 12\sqrt{6}(r-1) + 10\sqrt{6}(r-1)^2,
\end{aligned} \tag{7.23}$$

and the linear and constant basis functions are

$$\begin{aligned}
\varphi_0^0(r,s) &= \sqrt{2}, \\
\varphi_0^1(r,s) &= -2 + 6r, \\
\varphi_1^0(r,s) &= -2\sqrt{3} + 2\sqrt{3}r + 4\sqrt{3}s.
\end{aligned} \tag{7.24}$$

Using (7.4), the second order moments of U_i can be expressed in terms of the second order directional derivatives along v_1 and v_2 as

$$\begin{pmatrix} D_{v_2}^2 U_i(\mathbf{r}_0) \\ \left(\frac{\sqrt{5}}{2}\right) D_{v_2}^1 D_{v_1}^1 U_i(\mathbf{r}_0) \\ \left(\frac{\sqrt{5}}{2}\right)^2 D_{v_1}^2 U_i(\mathbf{r}_0) \end{pmatrix} = \begin{bmatrix} 12\sqrt{30} & 0 & 0 \\ 0 & 30\sqrt{2} & 0 \\ -\sqrt{30} & 0 & 20\sqrt{6} \end{bmatrix} \begin{pmatrix} \hat{U}_{i,2}^0 \\ \hat{U}_{i,1}^1 \\ \hat{U}_{i,0}^2 \end{pmatrix}. \tag{7.25}$$

Further, using (7.8) and (1.29) with $q = 2$, we can relate the directional derivatives in the computational space and the directional derivatives along $\mathbf{v}_{i,1}$ and $\mathbf{v}_{i,2}$ in the physical

space, evaluated at the cell center $\mathbf{x}_{i,0}$, as

$$
\begin{aligned}
D_{v_2}U_i(\mathbf{r}_0) &= h_{i,2}D^1_{\mathbf{v}_{i,2}}U_i(\mathbf{x}_{i,0}), \quad \left(\frac{\sqrt{5}}{2}\right)D_{v_1}U_i(\mathbf{r}_0) = h_{i,1}D^1_{\mathbf{v}_{i,1}}U_i(\mathbf{x}_{i,0}) \\
D^2_{v_2}U_i(\mathbf{r}_0) &= h^2_{i,2}D^2_{\mathbf{v}_{i,2}}U_i(\mathbf{x}_{i,0}) \\
&\quad + 12\sqrt{30}\left(\eta^{0,0}_{i,2}\frac{2}{\sqrt{5}}h_{i,1}D^1_{\mathbf{v}_{i,1}}U_i(\mathbf{x}_{i,0}) + \eta^{0,1}_{i,2}h_{i,2}D^1_{\mathbf{v}_{i,2}}U_i(\mathbf{x}_{i,0})\right) \\
\left(\frac{\sqrt{5}}{2}\right)D^1_{v_2}D^1_{v_1}U_i(\mathbf{r}_0) &= h_{i,2}h_{i,1}D_{\mathbf{v}_{i,2}}D_{\mathbf{v}_{i,1}}U_i(\mathbf{x}_{i,0}) \\
&\quad + 30\sqrt{2}\left(\eta^{1,0}_{i,1}\frac{2}{\sqrt{5}}h_{i,1}D^1_{\mathbf{v}_{i,1}}U_i(\mathbf{x}_{i,0}) + \eta^{1,1}_{i,1}h_{i,2}D^1_{\mathbf{v}_{i,2}}U_i(\mathbf{x}_{i,0})\right) \\
\left(\frac{\sqrt{5}}{2}\right)^2 D^2_{v_1}U_i(\mathbf{r}_0) &= h^2_{i,1}D^2_{\mathbf{v}_{i,1}}U_i(\mathbf{x}_{i,0}) + \left(20\sqrt{6}\eta^{2,0}_{i,0} - \sqrt{30}\eta^{0,0}_{i,2}\right)\frac{2}{\sqrt{5}}h_{i,1}D^1_{\mathbf{v}_{i,1}}U_i(\mathbf{x}_{i,0}) \\
&\quad + \left(20\sqrt{6}\eta^{2,1}_{i,0} - \sqrt{30}\eta^{0,1}_{i,2}\right)h_{i,2}D^1_{\mathbf{v}_{i,2}}U_i(\mathbf{x}_{i,0}).
\end{aligned}
\tag{7.26}
$$

The coefficients η_i are obtained using

$$
\hat{\mathbf{x}}^2_{i,0} = \eta^{2,0}_{i,0}\mathbf{v}_{i,1} + \eta^{2,1}_{i,0}\mathbf{v}_{i,2}, \quad \hat{\mathbf{x}}^1_{i,1} = \eta^{1,0}_{i,1}\mathbf{v}_{i,1} + \eta^{1,1}_{i,1}\mathbf{v}_{i,2}, \quad \hat{\mathbf{x}}^0_{i,2} = \eta^{0,0}_{i,2}\mathbf{v}_{i,1} + \eta^{0,1}_{i,2}\mathbf{v}_{i,2}, \tag{7.27}
$$

where the mapping coefficients $\hat{\mathbf{x}}_i$ are defined in (1.29). To start the limiting process, first, we compute the first order directional derivatives along $\mathbf{v}_{i,1}$ and $\mathbf{v}_{i,2}$ at the cell centers of the elements in the limiting stencil (Figures 7.2 and 7.3). For example, to limit $D^2_{\mathbf{v}_{i,1}}U_i$ and $D_{\mathbf{v}_{i,2}}D_{\mathbf{v}_{i,1}}U_i$, we need to compute directional derivatives along $\mathbf{v}_{i,1}$ and $\mathbf{v}_{i,2}$ at the cell centers of Ω_a, Ω_b, Ω_s, and Ω_t (Figure 7.3a). Consider element Ω_a. Using (7.5) and (7.8), the first order directional derivatives along $\mathbf{v}_{a,1}$ and $\mathbf{v}_{a,2}$ at $\mathbf{x}_{a,0}$ are

$$
\begin{aligned}
h_{a,1}D^1_{\mathbf{v}_{a,1}}U_a(\mathbf{x}_{a,0}) &= \left(\frac{\sqrt{5}}{2}\right)D^1_{v_1}U_a(\mathbf{r}_0) = 6\left(\hat{U}^1_{a,0} + \frac{\sqrt{30}}{9}\hat{U}^0_{a,2} - \frac{2\sqrt{6}}{9}\hat{U}^2_{a,0}\right), \\
h_{a,2}D^1_{\mathbf{v}_{a,2}}U_a(\mathbf{x}_{a,0}) &= D^1_{v_2}U_a(\mathbf{r}_0) = 4\sqrt{3}\left(\hat{U}^0_{a,1} + \sqrt{\frac{2}{3}}\hat{U}^1_{a,1}\right).
\end{aligned}
\tag{7.28}
$$

Then, we compute the directional derivatives along $\mathbf{v}_{i,1}$ and $\mathbf{v}_{i,2}$ at $\mathbf{x}_{a,0}$ as

$$
\begin{aligned}
D^1_{\mathbf{v}_{i,1}}U_a &= \alpha^1_{a,1}D_{\mathbf{v}_{a,1}}U_a + \alpha^1_{a,2}D_{\mathbf{v}_{a,2}}U_a, \\
D^1_{\mathbf{v}_{i,2}}U_a &= \alpha^2_{a,1}D_{\mathbf{v}_{a,1}}U_a + \alpha^2_{a,2}D_{\mathbf{v}_{a,2}}U_a,
\end{aligned}
\tag{7.29}
$$

where the coefficients α are obtained from

$$\mathbf{v}_{i,1} = \alpha^1_{a,1}\mathbf{v}_{a,1} + \alpha^1_{a,2}\mathbf{v}_{a,2}, \quad \mathbf{v}_{i,2} = \alpha^2_{a,1}\mathbf{v}_{a,1} + \alpha^2_{a,2}\mathbf{v}_{a,2}. \tag{7.30}$$

Similarly, we compute the first order directional derivatives along $\mathbf{v}_{i,1}$ and $\mathbf{v}_{i,2}$ at the cell centers of Ω_b, Ω_s, and Ω_t. Using the above computed values, we linearly interpolate the values at the forward and backward interpolation points $\mathbf{x}^f_{i,1}$ and $\mathbf{x}^b_{i,1}$ as

$$\begin{aligned}
D_{\mathbf{v}_{i,1}}U^f_{i,1} &= \beta^f_{i,1}D_{\mathbf{v}_{i,1}}U_s(\mathbf{x}_{s,0}) + (1-\beta^f_{i,1})D_{\mathbf{v}_{i,1}}U_t(\mathbf{x}_{t,0}),\\
D_{\mathbf{v}_{i,1}}U^b_{i,1} &= \beta^b_{i,1}D_{\mathbf{v}_{i,1}}U_a(\mathbf{x}_{a,0}) + (1-\beta^b_{i,1})D_{\mathbf{v}_{i,1}}U_b(\mathbf{x}_{b,0}),\\
D_{\mathbf{v}_{i,2}}U^f_{i,1} &= \beta^f_{i,1}D_{\mathbf{v}_{i,2}}U_s(\mathbf{x}_{s,0}) + (1-\beta^f_{i,1})D_{\mathbf{v}_{i,2}}U_t(\mathbf{x}_{t,0}),\\
D_{\mathbf{v}_{i,2}}U^b_{i,1} &= \beta^b_{i,1}D_{\mathbf{v}_{i,2}}U_a(\mathbf{x}_{a,0}) + (1-\beta^b_{i,1})D_{\mathbf{v}_{i,2}}U_b(\mathbf{x}_{b,0}).
\end{aligned} \tag{7.31}$$

Finally, the directional derivatives $D^2_{\mathbf{v}_{i,1}}U_i$ and $D_{\mathbf{v}_{i,2}}D_{\mathbf{v}_{i,1}}U_i$ are limited by comparing them to the forward and backward differences along $\mathbf{v}_{i,1}$ as

$$\begin{aligned}
D^2_{\mathbf{v}_{i,1}}U_i(\mathbf{x}_{i,0}) \leftarrow\!\shortmid \text{minmod}\Bigg(&D^2_{\mathbf{v}_{i,1}}U_i(\mathbf{x}_{i,0}), l^f_{i,1}\frac{D_{\mathbf{v}_{i,1}}U^f_{i,1} - D_{\mathbf{v}_{i,1}}U_i(\mathbf{x}_{i,0})}{\left\|\mathbf{x}^f_{i,1} - \mathbf{x}_{i,0}\right\|},\\
&l^b_{i,1}\frac{D_{\mathbf{v}_{i,1}}U_i(\mathbf{x}_{i,0}) - D_{\mathbf{v}_{i,1}}U^b_{i,1}}{\left\|\mathbf{x}^b_{i,1} - \mathbf{x}_{i,0}\right\|}\Bigg),\\
D_{\mathbf{v}_{i,1}}D_{\mathbf{v}_{i,2}}U_i(\mathbf{x}_{i,0}) \leftarrow\!\shortmid \text{minmod}\Bigg(&D_{\mathbf{v}_{i,1}}D_{\mathbf{v}_{i,2}}U_i(\mathbf{x}_{i,0}), l^f_{i,1}\frac{D_{\mathbf{v}_{i,2}}U^f_{i,1} - D_{\mathbf{v}_{i,2}}U_i(\mathbf{x}_{i,0})}{\left\|\mathbf{x}^f_{i,1} - \mathbf{x}_{i,0}\right\|},\\
&l^b_{i,1}\frac{D_{\mathbf{v}_{i,2}}U_i(\mathbf{x}_{i,0}) - D_{\mathbf{v}_{i,2}}U^b_{i,1}}{\left\|\mathbf{x}^b_{i,1} - \mathbf{x}_{i,0}\right\|}\Bigg).
\end{aligned} \tag{7.32}$$

The range for the scaling parameters $l^f_{i,k}$ and $l^b_{i,k}$, $k = \{1,2\}$, is given in (7.17). In a similar way, the first order directional derivatives along $\mathbf{v}_{i,1}$ and $\mathbf{v}_{i,2}$ are computed at the cell centers of Ω_j, Ω_k, Ω_m, and Ω_n (Figure 7.3b), and the values at the cell centers are used to linearly interpolate the values of the first order directional derivatives at the forward and backward interpolation points $\mathbf{x}^f_{i,2}$ and $\mathbf{x}^b_{i,2}$ as

$$\begin{aligned}
D_{\mathbf{v}_{i,1}}U^f_{i,2} &= \beta^f_{i,2}D_{\mathbf{v}_{i,1}}U_j(\mathbf{x}_{j,0}) + (1-\beta^f_{i,2})D_{\mathbf{v}_{i,1}}U_k(\mathbf{x}_{k,0}),\\
D_{\mathbf{v}_{i,1}}U^b_{i,2} &= \beta^b_{i,2}D_{\mathbf{v}_{i,1}}U_m(\mathbf{x}_{m,0}) + (1-\beta^b_{i,2})D_{\mathbf{v}_{i,1}}U_n(\mathbf{x}_{n,0}),\\
D_{\mathbf{v}_{i,2}}U^f_{i,2} &= \beta^f_{i,2}D_{\mathbf{v}_{i,2}}U_j(\mathbf{x}_{j,0}) + (1-\beta^f_{i,2})D_{\mathbf{v}_{i,2}}U_k(\mathbf{x}_{k,0}),\\
D_{\mathbf{v}_{i,2}}U^b_{i,2} &= \beta^b_{i,2}D_{\mathbf{v}_{i,2}}U_m(\mathbf{x}_{m,0}) + (1-\beta^b_{i,2})D_{\mathbf{v}_{i,2}}U_n(\mathbf{x}_{n,0}).
\end{aligned} \tag{7.33}$$

The directional derivatives $D^2_{\mathbf{v}_{i,2}} U_i$ and $D_{\mathbf{v}_{i,1}} D_{\mathbf{v}_{i,2}} U_i$ are limited by comparing them to the forward and backward difference along $\mathbf{v}_{i,2}$ as

$$\begin{aligned} D^2_{\mathbf{v}_{i,2}} U_i(\mathbf{x}_{i,0}) \leftarrow\!\shortmid \text{minmod} \Bigg(& D^2_{\mathbf{v}_{i,2}} U_i(\mathbf{x}_{i,0}), l^f_{i,2} \frac{D_{\mathbf{v}_{i,2}} U^f_{i,2} - D_{\mathbf{v}_{i,2}} U_i(\mathbf{x}_{i,0})}{\left\| \mathbf{x}^f_{i,2} - \mathbf{x}_{i,0} \right\|}, \\ & l^b_{i,2} \frac{D_{\mathbf{v}_{i,2}} U_i(\mathbf{x}_{i,0}) - D_{\mathbf{v}_{i,2}} U^b_{i,2}}{\left\| \mathbf{x}^b_{i,2} - \mathbf{x}_{i,0} \right\|} \Bigg), \\ D_{\mathbf{v}_{i,2}} D_{\mathbf{v}_{i,1}} U_i(\mathbf{x}_{i,0}) \leftarrow\!\shortmid \text{minmod} \Bigg(& D_{\mathbf{v}_{i,2}} D_{\mathbf{v}_{i,1}} U_i(\mathbf{x}_{i,0}), l^f_{i,2} \frac{D_{\mathbf{v}_{i,1}} U^f_{i,2} - D_{\mathbf{v}_{i,1}} U_i(\mathbf{x}_{i,0})}{\left\| \mathbf{x}^f_{i,2} - \mathbf{x}_{i,0} \right\|}, \\ & l^b_{i,2} \frac{D_{\mathbf{v}_{i,1}} U_i(\mathbf{x}_{i,0}) - D_{\mathbf{v}_{i,1}} U^b_{i,2}}{\left\| \mathbf{x}^b_{i,2} - \mathbf{x}_{i,0} \right\|} \Bigg). \end{aligned} \tag{7.34}$$

Next, we limit the first order directional derivatives $D_{\mathbf{v}_{i,1}} U_i$ and $D_{\mathbf{v}_{i,2}} U_i$, evaluated at $\mathbf{x}_{i,0}$. We first compute the numerical solution at the cell centers of the elements in the limiting stencil (Figure 7.3). For example, to limit $D_{\mathbf{v}_{i,1}} U_i$, we compute the solution values at the cell centers of Ω_a, Ω_b, Ω_s, and Ω_t and use them to linearly interpolate the solution values at the forward and backward interpolation points $\mathbf{x}^f_{i,1}$ and $\mathbf{x}^b_{i,1}$ as

$$U^f_{i,1} = \beta^f_{i,1} U_s(\mathbf{x}_{s,0}) + (1 - \beta^f_{i,1}) U_t(\mathbf{x}_{t,0}), \quad U^b_{i,1} = \beta^b_{i,1} U_a(\mathbf{x}_{a,0}) + (1 - \beta^b_{i,1}) U_b(\mathbf{x}_{b,0}). \tag{7.35}$$

Finally, the directional derivative $D_{\mathbf{v}_{i,1}} U_i$ is limited by comparing it to the forward and backward differences along $\mathbf{v}_{i,1}$ as

$$D_{\mathbf{v}_{i,1}} U_i(\mathbf{x}_{i,0}) \leftarrow\!\shortmid \text{minmod} \left(D_{\mathbf{v}_{i,1}} U_i(\mathbf{x}_{i,0}), l^f_{i,1} \frac{U^f_{i,1} - U_i(\mathbf{x}_{i,0})}{\left\| \mathbf{x}^f_{i,1} - \mathbf{x}_{i,0} \right\|}, l^b_{i,1} \frac{U_i(\mathbf{x}_{i,0}) - U^b_{i,1}}{\left\| \mathbf{x}^b_{i,1} - \mathbf{x}_{i,0} \right\|} \right). \tag{7.36}$$

The range for the scaling parameters $l^f_{i,k}$ and $l^b_{i,k}$, $k = \{1, 2\}$, is given in (7.18). In a similar way, the solution values at the cell centers of Ω_j, Ω_k, Ω_m, and Ω_n are computed and used to linearly interpolate the solution values at the forward and backward interpolation points $\mathbf{x}^f_{i,2}$ and $\mathbf{x}^b_{i,2}$ as

$$U^f_{i,2} = \beta^f_{i,2} U_j(\mathbf{x}_{j,0}) + (1 - \beta^f_{i,2}) U_k(\mathbf{x}_{k,0}), \quad U^b_{i,2} = \beta^b_{i,2} U_m(\mathbf{x}_{m,0}) + (1 - \beta^b_{i,2}) U_n(\mathbf{x}_{n,0}). \tag{7.37}$$

The directional derivative $D_{\mathbf{v}_{i,2}} U_i$ is limited by comparing it to the forward and backward

differences along $\mathbf{v}_{i,2}$ as

$$D_{\mathbf{v}_{i,2}} U_i(\mathbf{x}_{i,0}) \leftarrow \text{minmod}\left(D_{\mathbf{v}_{i,2}} U_i(\mathbf{x}_{i,0}), l_{i,2}^f \frac{U_{i,2}^f - U_i(\mathbf{x}_{i,0})}{\left\| \mathbf{x}_{i,2}^f - \mathbf{x}_{i,0} \right\|}, l_{i,2}^b \frac{U_i(\mathbf{x}_{i,0}) - U_{i,2}^b}{\left\| \mathbf{x}_{i,2}^b - \mathbf{x}_{i,0} \right\|} \right). \tag{7.38}$$

Finally, the modified second order moments $\hat{U}_{i,0}^2$, $\hat{U}_{i,1}^1$, and $\hat{U}_{i,2}^0$ are computed by substituting the limited directional derivatives into (7.26) and (7.25)

$$\begin{aligned}
\hat{U}_{i,2}^0 &= \frac{h_{i,2}^2}{12\sqrt{30}} D_{\mathbf{v}_{i,2}}^2 U_i + \eta_{i,2}^{0,0} \frac{2}{\sqrt{5}} h_{i,1} D_{\mathbf{v}_{i,1}}^1 U_i + \eta_{i,2}^{0,1} h_{i,2} D_{\mathbf{v}_{i,2}}^1 U_i, \\
\hat{U}_{i,1}^1 &= \frac{h_{i,2} h_{i,1}}{30\sqrt{2}} D_{\mathbf{v}_{i,2}} D_{\mathbf{v}_{i,1}} U_i + \eta_{i,1}^{1,0} \frac{2}{\sqrt{5}} h_{i,1} D_{\mathbf{v}_{i,1}}^1 U_i + \eta_{i,1}^{1,1} h_{i,2} D_{\mathbf{v}_{i,2}}^1 U_i, \\
\hat{U}_{i,0}^2 &= \frac{h_{i,1}^2}{20\sqrt{6}} D_{\mathbf{v}_{i,1}}^2 U_i + \frac{h_{i,2}^2}{240\sqrt{6}} D_{\mathbf{v}_{i,2}}^2 U_i + \eta_{i,0}^{2,0} \frac{2}{\sqrt{5}} h_{i,1} D_{\mathbf{v}_{i,1}}^1 U_i + \eta_{i,0}^{2,1} h_{i,2} D_{\mathbf{v}_{i,2}}^1 U_i.
\end{aligned} \tag{7.39}$$

If any of the solution coefficients have been modified, we update the zeroth order solution coefficient $\hat{U}_{i,0}^0$ using (7.20). If all second order solution coefficients have been modified by the limiter, then the linear moments are limited using the second order moment limiter [2]

$$\begin{aligned}
\hat{U}_{i,1}^0 &\leftarrow \text{minmod}\left(\frac{U_{i,1}^f - U_i(\mathbf{x}_{i,0})}{2}, \hat{U}_{i,1}^0, \frac{U_i(\mathbf{x}_{i,0}) - U_{i,1}^b}{2} \right), \\
\hat{U}_{i,2}^0 &\leftarrow \text{minmod}\left(\frac{U_{i,2}^f - U_i(\mathbf{x}_{i,0})}{2\sqrt{3}}, \hat{U}_{i,2}^0, \frac{U_i(\mathbf{x}_{i,0}) - U_{i,2}^b}{2\sqrt{3}} \right),
\end{aligned} \tag{7.40}$$

and the zeroth order solution coefficient $\hat{U}_{i,0}^0$ is updated using (7.20). The forward and backward interpolation values $U_{i,q}^f$ and $U_{i,q}^b$, $q = \{1, 2\}$, are linearly interpolated using the values at the cell centers from respective neighboring elements (Figure 7.2). For example, the forward and backward interpolation values along $\mathbf{v}_{i,2}$ are given by

$$\begin{aligned}
U_{i,2}^f &= \beta_{i,2}^f U_j(\mathbf{x}_{j,0}) + (1 - \beta_{i,2}^f) U_k(\mathbf{x}_{k,0}), \\
U_{i,2}^b &= \beta_{i,2}^b U_m(\mathbf{x}_{m,0}) + (1 - \beta_{i,2}^b) U_n(\mathbf{x}_{n,0}),
\end{aligned} \tag{7.41}$$

with $0 \leq \beta_{i,2}^f, \beta_{i,2}^b \leq 1$.

7.1.4 Implementation Strategy

For each mesh element, we compute the limiting stencil (Figures 7.2 and 7.3) in the preprocessing stage [53], i.e., for each Ω_i, we store the access IDs to the eight mesh elements involved in the limiting stencil. Then, we compute and store the constants α in (7.30), the constants η in (7.26) (for $q = 2$) and interpolation weights β in (7.31). For example, to apply the limiter for $p = 2$ on a mesh element of order $q = 2$, we

1. Compute first- and second-order derivatives using (7.25) and (7.26).
2. Compute lower order derivatives using (7.28).
3. Compute the directional derivatives along the required direction on neighboring elements using (7.29).
4. Interpolate lower order derivatives and solution values at the interpolation points using (7.31), (7.35), and (7.37).
5. Apply the minmod function.

7.2 Numerical Results

In this section, we present numerical experiments to analyze the performance of the proposed high-order moment limiter. We perform convergence studies to show that the limiter maintains the theoretical rate of convergence for smooth problems. Further, we run tests to show the robustness of the proposed limiter in the presence of discontinuities. In all presented cases, time-stepping was performed using an explicit Runge-Kutta method of order $p+1$ with the CFL condition [50]. Finally, unless stated otherwise, the local Lax-Friedrichs flux was used.

7.2.1 Advecting hill.

We consider the advecting hill problem on the domain Ω obtained by applying the transformation

$$\mathbf{T}(x,y) = \left(3x - 0.3\sin(2\pi\frac{(1+y)}{2}), 3y + 0.3\sin(2\pi\frac{(1+x)}{2})\right) \tag{7.42}$$

to the square domain $[-1,1] \times [-1,1]$. For this test case, the flux in (1.8) is given by $\mathbf{F} = [u,u]$ and the initial condition is $u_0(x,y) = 2.5\exp\left(\frac{-r^2}{2R^2}\right)$, where $R = 0.15$ and $r = \sqrt{(x-0.25)^2 + (y-0.25)^2}$. We solve the problem on a sequence of curvilinear meshes A-F

of order $q = 2$ and $q = 3$. Mesh A is a coarse unstructured curvilinear mesh consisting of 240 triangular elements (Figure 7.4). Meshes B-F are obtained by nested refinement of the preceding mesh.

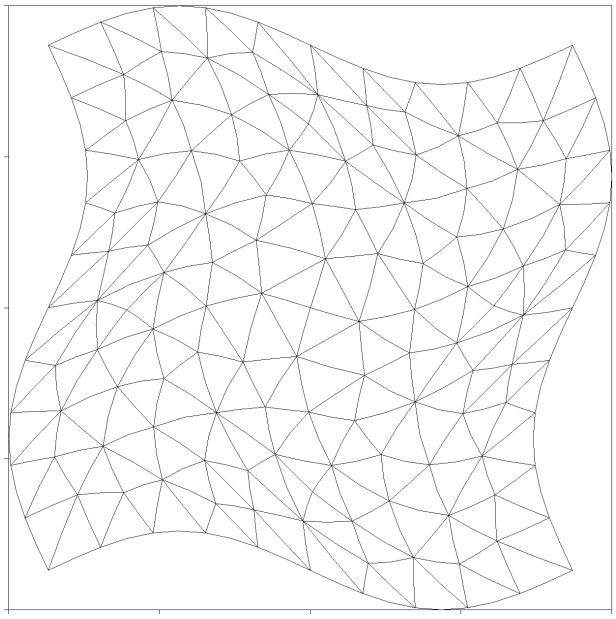

Figure 7.4: Mesh A, consisting of 240 second-order triangular elements, for the advecting hill problem

Tables 7.1 and 7.2 show, respectively, the L_1 errors and rates of convergence for $p = 1$, $p = 2$, and $p = 3$ DG approximations at $t = 0.4$ with and without limiting on second- and third-order triangular meshes. We observe that limited solutions converge with the theoretical rates. It is expected that a limiter will increase the magnitude of the numerical error. We note that such an increase in the error is modest.

Mesh	Nb	L1 error					
		p = 1	p = 1 (unlimited)	p = 2	p = 2 (unlimited)	p = 3	p = 3 (unlimited)
A	240	3.46e-02 (-)	1.21e-02 (-)	1.49e-02 (-)	1.09e-03 (-)	1.69e-02 (-)	1.06e-04 (-)
B	952	6.88e-03 (2.33)	2.61e-03 (2.21)	5.93e-04 (4.65)	1.39e-04 (2.97)	1.36e-04 (6.95)	7.58e-06 (3.8)
C	3,814	1.45e-03 (2.25)	6.10e-04 (2.09)	5.72e-05 (3.37)	1.78e-05 (2.97)	1.94e-06 (6.13)	5.64e-07 (3.75)
D	15,576	2.66e-04 (2.44)	1.41e-04 (2.11)	5.54e-06 (3.37)	2.15e-06 (3.05)	8.13e-08 (4.57)	3.35e-08 (4.07)
E	62,104	5.61e-05 (2.24)	3.62e-05 (1.96)	5.58e-07 (3.31)	2.72e-07 (2.98)	4.02e-09 (4.34)	2e-09 (4.07)
F	247,688	1.22e-05 (2.20)	9.15e-06 (1.98)	5.23e-08 (3.41)	3.36e-08 (3.01)	1.94e-10 (4.37)	1.32e-10 (3.92)

Table 7.1: L_1 errors for the linear advection of an advecting hill at $t = 0.4$ on an unstructured curvilinear triangular mesh of order $q = 2$. The numbers in parentheses are the observed rates of convergence.

Mesh	Nb	L1 error					
		p = 1	p = 1 (unlimited)	p = 2	p = 2 (unlimited)	p = 3	p = 3 (unlimited)
A	240	3.46e-02 (-)	1.21e-02 (-)	1.58e-02 (-)	1.11e-03 (-)	1.69e-02 (-)	1.09e-04 (-)
B	952	6.89e-03 (2.33)	2.61e-03 (2.21)	5.94e-04 (4.65)	1.42e-04 (2.97)	1.18e-04 (6.95)	7.97e-06 (3.8)
C	3,814	1.45e-03 (2.25)	6.15e-04 (2.09)	5.74e-05 (3.37)	1.81e-05 (2.97)	1.89e-06 (6.13)	5.96e-07 (3.75)
D	15,576	2.67e-04 (2.44)	1.42e-04 (2.11)	5.55e-06 (3.37)	2.19e-06 (3.05)	7.95e-08 (4.57)	3.53e-08 (4.07)
E	62,104	5.63e-05 (2.24)	3.65e-05 (1.96)	5.60e-07 (3.31)	2.75e-07 (2.98)	3.95e-09 (4.34)	2.11e-09 (4.07)
F	247,688	1.23e-05 (2.20)	9.21e-06 (1.98)	5.26e-08 (3.41)	3.39e-08 (3.01)	1.93e-10 (4.37)	1.39e-10 (3.92)

Table 7.2: L_1 errors for the linear advection of an advecting hill at $t = 0.4$ on an unstructured curvilinear triangular mesh of order $q = 3$. The numbers in parentheses are the observed rates of convergence.

7.2.2 Rotating shapes.

Next, we solve the rotating shapes problem with the flux in (1.8) given by $\mathbf{F} = [-2\pi yu, 2\pi xu]$. The initial condition consists of a hill and a square pulse (Figure 7.5) and is given by

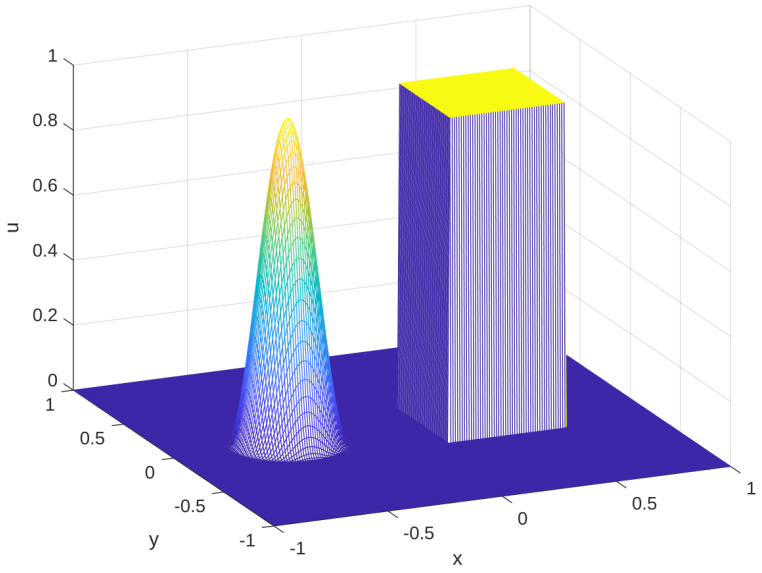

Figure 7.5: Initial condition for the rotating shapes problem.

$$u_0(x,y) = \begin{cases} \cos^2(2\pi r), & \text{if } r \le 0.25, \\ 1, & \text{if } \max(|x-0.35|, |y|) \le 0.25, \\ 0, & \text{otherwise,} \end{cases} \tag{7.43}$$

where $r = \sqrt{(x+0.5)^2 + y^2}$. The exact solution is a rotation of the initial condition about the origin. The problem is solved on the domain Ω obtained by applying the transformation

$$\mathbf{T}(x,y) = \left(x - 0.1\cos(2\pi\frac{(1+y)}{2}), 1y + 0.1\cos(2\pi\frac{(1+x)}{2})\right) \tag{7.44}$$

to the square domain $[-1,1] \times [-1,1]$. The problem is solved until $t = 1$ on curvilinear meshes of $12,800$ triangular elements of order $q = 2$ (Figure 7.6) and $q = 3$.

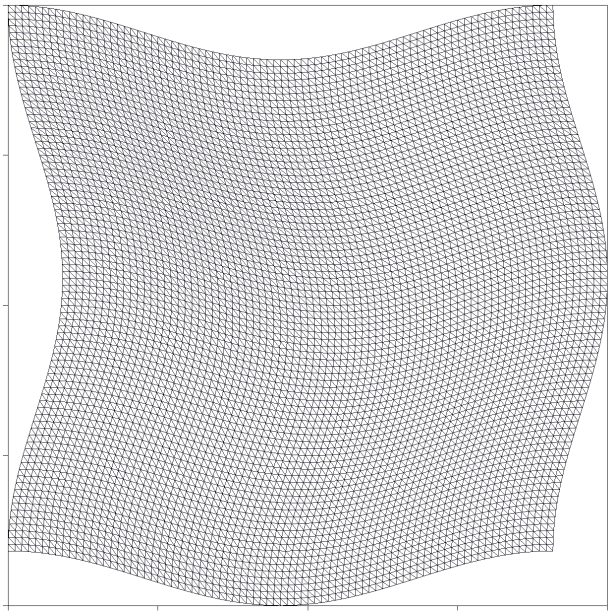

Figure 7.6: Second-order curvilinear mesh of $12,800$ elements, for the rotating shapes problem.

Figures 7.7 and 7.8 show the isolines and the solution profiles at $y = 0$, $x = 0.5, 0.55$, obtained using second, third, and fourth order DG approximations with and without limiting on the second-order mesh while Figure 7.9 shows the corresponding isolines and solution profiles obtained on the third-order mesh with limiting. The quality of the solution is comparable to the results obtained on a 80×80 Cartesian mesh using the moment limiter described in [25] and to the results obatined on an unstructured triangular mesh using the moment limiter described in [57]. We note that while the discontinuities are resolved well by all three moment limiters, the peak of the hill is captured well only by the third and fourth order moment limiters. This can be attributed to the phenomenon of clipping at the local extrema by a second order slope limiter. Moreover, while all three limiters are successful in reducing the spurious oscillations near discontinuities, from Figures 7.7b and

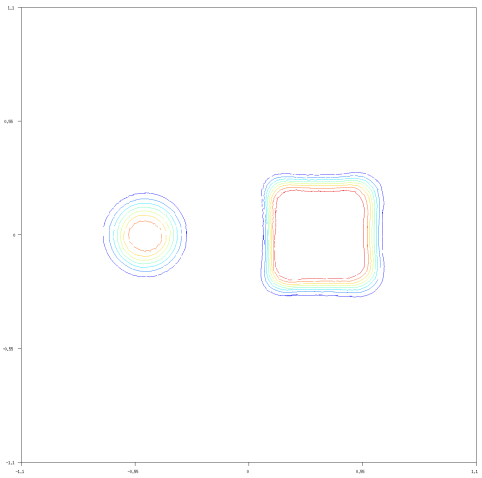

(a) Isolines with second order moment limiter.

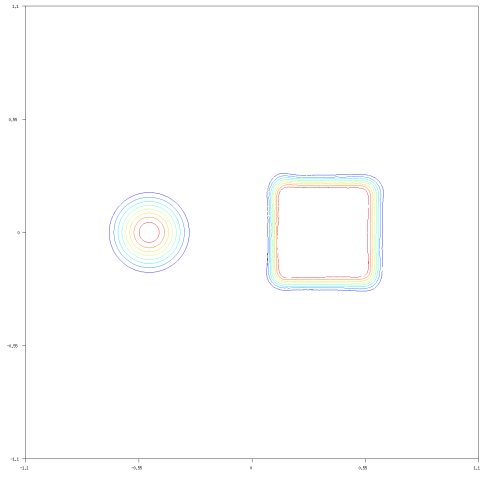

(b) Isolines with third order moment limiter.

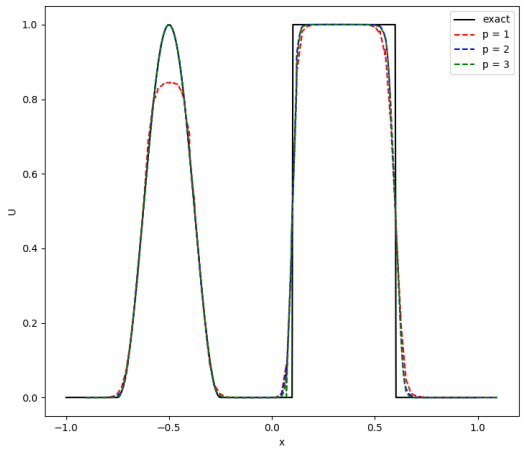

(c) Profile of the solution along $y = 0$.

7.9b we see that discontinuities are sharper with high-order limiters. The above observation is further supported by the solution profiles shown in Figures 7.7e and 7.9e.

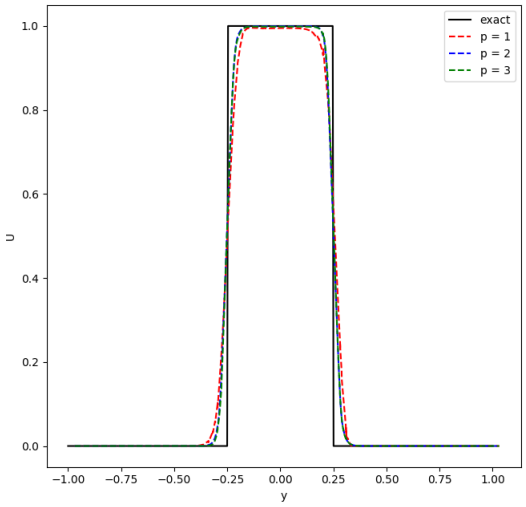

(d) Profile of the solution along $x = 0.5$.

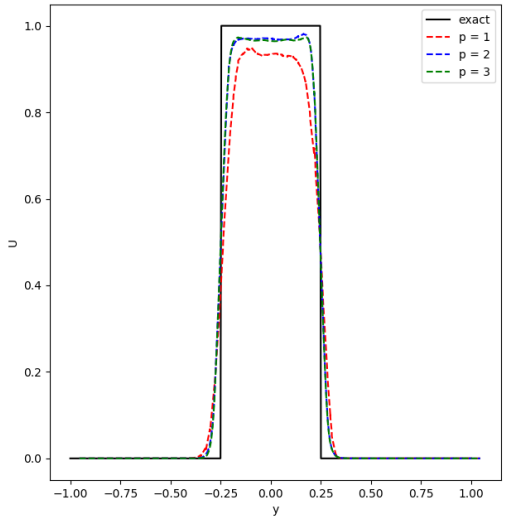

(e) Profile of the solution along $x = 0.55$.

Figure 7.7: Rotating shapes at $t = 1$ with limiting on a curvilinear mesh with $12,800$ triangular elements of order $q = 2$.

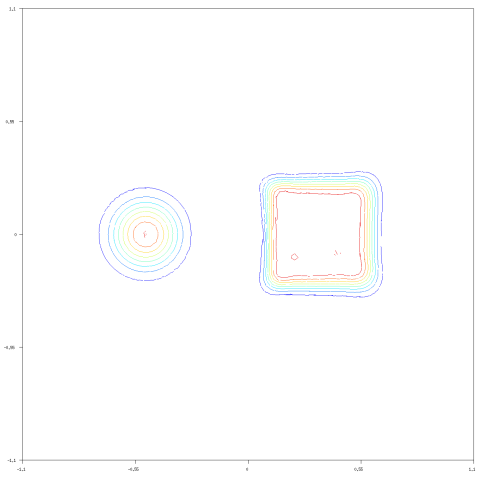

(a) $p = 1$.

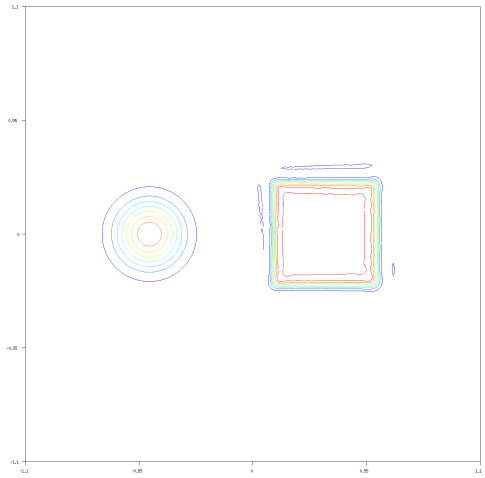

(b) $p = 2$.

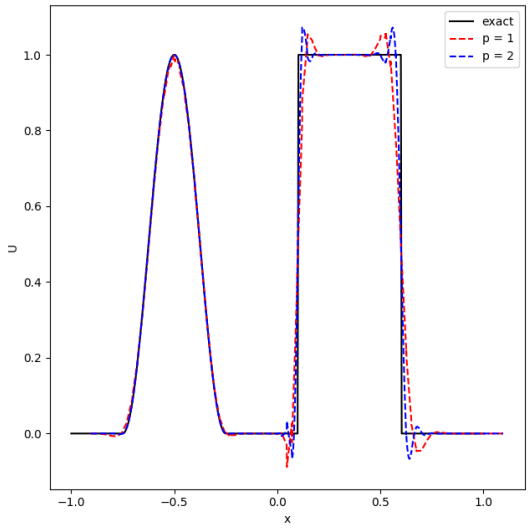

(c) Profile of the solution along $y = 0$.

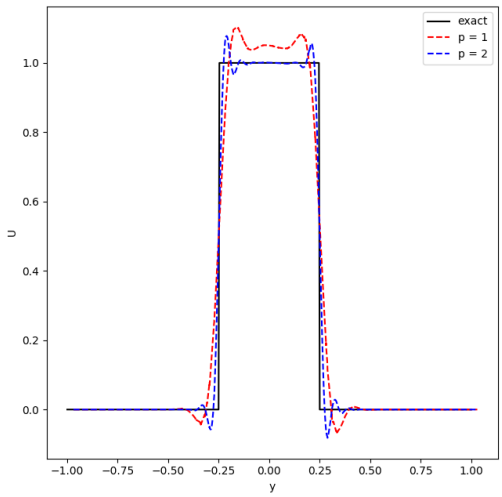

(d) Profile of the solution along $x = 0.5$.

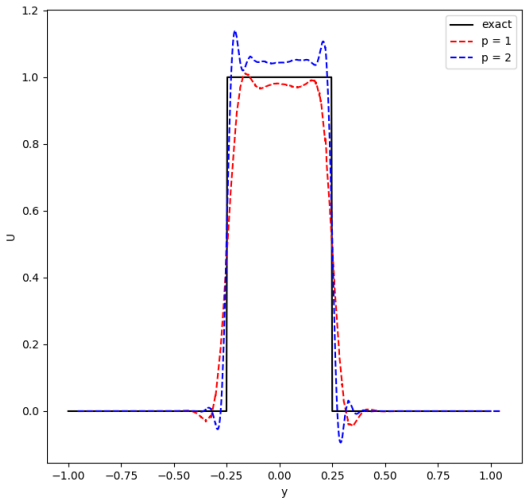

(e) Profile of the solution along $x = 0.55$.

Figure 7.8: Rotating shapes at $t = 1$ without limiting on a curvilinear mesh with $12,800$ triangular elements of order $q = 2$.

7.2.3 Isentropic vortex.

Next, we test the performance of the high-order limiter when applied to a system of non-linear equations, for example, the Euler equations given by

$$\frac{\partial}{\partial t}\begin{pmatrix}\rho\\ \rho u\\ \rho v\\ E\end{pmatrix}+\frac{\partial}{\partial x}\begin{pmatrix}\rho u\\ \rho u^2+p\\ \rho uv\\ (E+p)u\end{pmatrix}+\frac{\partial}{\partial y}\begin{pmatrix}\rho v\\ \rho uv\\ \rho v^2+p\\ (E+p)v\end{pmatrix}=0, \tag{7.45}$$

where ρ is the density, ρu and ρv are the x- and y-direction momenta, E is the energy, and the pressure, p, is given by the equation of state $p = (\gamma-1)\left(E-\frac{\rho}{2}(u^2+v^2)\right)$.

We solve the smooth isentropic vortex problem described in [51] with the initial conditions

$$\rho=\left(1-\frac{(\gamma-1)}{8\pi^2}(M\beta)^2e^r\right)^{\frac{1}{\gamma-1}},\quad p=\frac{\rho^\gamma}{\gamma M^2},\quad u=\frac{\beta}{2\pi R}ye^{\frac{r}{2}},\quad v=-\frac{\beta}{2\pi R}xe^{\frac{r}{2}}, \tag{7.46}$$

where $r = \frac{1-(x^2+y^2)}{R^2}$, $R = 1.5$, $\beta = 13.5$, $\gamma = 1.4$, and $M = 0.4$. With the given initial

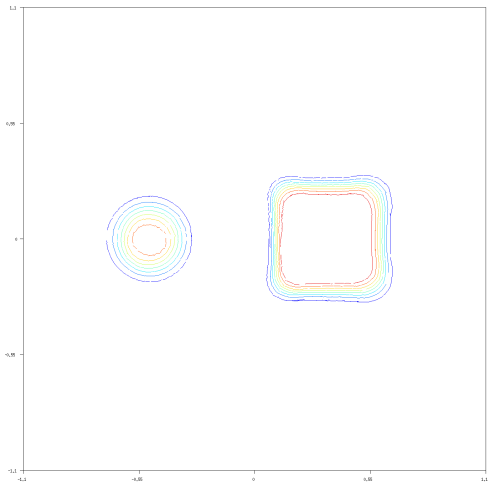

(a) Isolines with second order moment limiter.

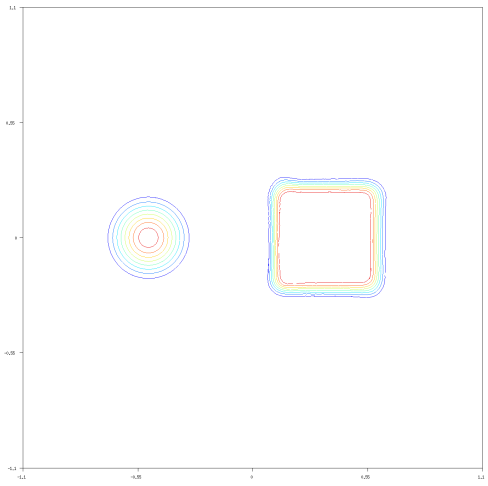

(b) Isolines with third order moment limiter.

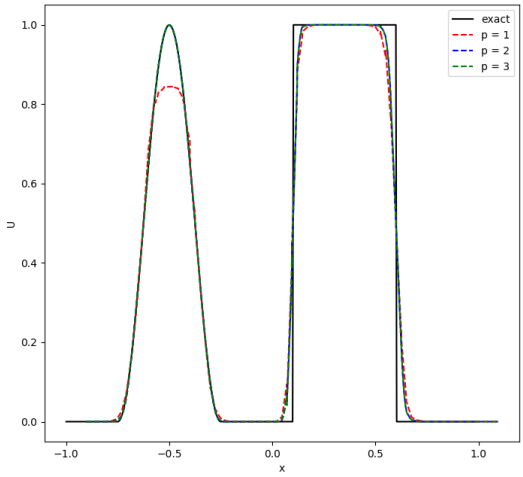

(c) Profile of the solution along $y = 0$.

conditions, the exact solution is stationary and given by (7.46). We solve the problem on domain Ω obtained by applying the transformation

$$\mathbf{T}(x, y) = \left(3x - 0.3\sin(2\pi\frac{(1+y)}{2}), 3y + 0.3\sin(2\pi\frac{(1+x)}{2})\right) \tag{7.47}$$

to the square domain $[-3, 3]\times[-3, 3]$. The L_1 errors in density and the observed convergence rates for $p = 1$, $p = 2$, and $p = 3$ DG approximations at the final time are reported in Table 7.3 for second-order meshes and in Table 7.4 for third-order meshes. As with the linear

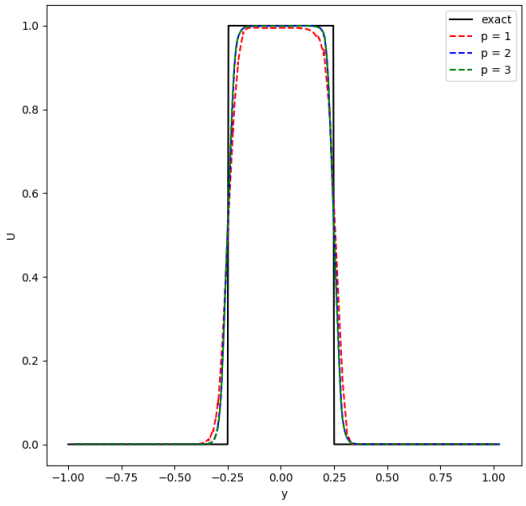

(d) Profile of the solution along $x = 0.5$.

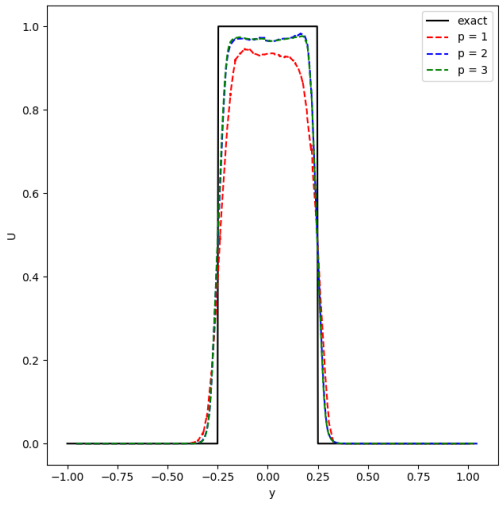

(e) Profile of the solution along $x = 0.55$.

Figure 7.9: Rotating shapes at $t = 1$ with limiting on a curvilinear mesh with $12,800$ triangular elements of order $q = 3$.

advection, we see that the proposed limiter maintains the theoretical convergence rates and introduces only modest errors.

Mesh	Nb	L1 error					
		p = 1	p = 1 (unlimited)	p = 2	p = 2 (unlimited)	p = 3	p = 3 (unlimited)
A	240	2.81e-01 (-)	6.83e-02 (-)	8.6e-02 (-)	5.63e-03 (-)	7.35e-02 (-)	3.45e-04 (-)
B	952	8.09e-02 (1.8)	1.64e-02 (2.06)	1.26e-02 (2.77)	7.55e-04 (2.89)	5.96e-04 (6.95)	2.15e-05 (4.0)
C	3,814	1.98e-02 (2.03)	3.98e-03 (2.04)	6.51e-04 (4.27)	1.02e-04 (2.89)	1.97e-05 (4.91)	1.41e-06 (3.93)
D	15,576	4.71e-03 (2.07)	9.67e-04 (2.04)	7.86e-05 (3.05)	1.26e-05 (3.02)	1.05e-06 (4.23)	8.31e-08 (4.08)
E	62,104	1.18e-03 (1.99)	2.42e-04 (1.99)	1.02e-05 (2.95)	1.67e-06 (2.92)	6.18e-08 (4.09)	5.42e-09 (3.94)
F	247,688	3.28e-04 (1.85)	6e-05 (2.01)	1.23e-06 (3.05)	2.16e-07 (2.95)	3.07e-09 (4.33)	3.42e-10 (3.97)

Table 7.3: L_1 errors for the isentropic vortex problem at $t = 0.5$ on an unstructured curvilinear triangular mesh of order $q = 2$. The numbers in parentheses are the observed rates of convergence.

7.2.4 Shock-cylinder interaction.

Next, we solve the interaction of a Mach 2 shock wave with a cylinder to test the performance of the proposed limiter in the presence of discontinuities. The setup for the problem,

Mesh	Nb	L1 error					
		p = 1	p = 1 (unlimited)	p = 2	p = 2 (unlimited)	p = 3	p = 3 (unlimited)
A	240	2.81e-01 (-)	6.81e-02 (-)	8.85e-02 (-)	5.74e-03 (-)	6.20e-02 (-)	3.70e-04 (-)
B	952	8.09e-02 (1.8)	1.62e-02 (2.06)	1.29e-02 (2.77)	7.73e-04 (2.89)	7.51e-04 (6.95)	2.29e-05 (4.0)
C	3,814	1.98e-02 (2.03)	3.92e-03 (2.04)	6.56e-04 (4.27)	1.05e-04 (2.89)	1.94e-05 (4.91)	1.49e-06 (3.93)
D	15,576	4.71e-03 (2.07)	9.52e-04 (2.04)	7.95e-05 (3.05)	1.33e-05 (3.02)	1.01e-06 (4.23)	8.83e-08 (4.08)
E	62,104	1.18e-03 (1.99)	2.38e-04 (1.99)	1.03e-05 (2.95)	1.74e-06 (2.92)	6.07e-08 (4.09)	5.73e-09 (3.94)
F	247,688	3.29e-04 (1.85)	5.92e-05 (2.01)	1.25e-06 (3.05)	2.21e-07 (2.95)	3.02e-09 (4.33)	3.61e-10 (3.97)

Table 7.4: L_1 errors for the isentropic vortex problem at $t = 0.5$ on an unstructured curvilinear triangular mesh of order $q = 3$. The numbers in parentheses are the observed rates of convergence.

described in [24], consists of a Mach 2 shock starting at $x = 0.2$ and a cylinder of radius $r = 0.15$ centered at $(0.5, 0.5)$. The states to the left $\mathbf{U}_l$ and right $\mathbf{U}_r$ of the shock wave are given in Table 7.5. The problem is run until $t = 0.3$. We solve the problem on an annular

	$\mathbf{U}_l$	$\mathbf{U}_r$
ρ	11.2/3	1.4
u	1.25	0
v	0	0
p	4.5	1

Table 7.5: States to the left and right of the initial shock for the shock cylinder interaction test case.

domain Ω of inner radius $r = 0.15$ and outer radius $R = \sqrt{2}/2$. The domain is discretized into a structured polar mesh of $209,300$ second-order triangular elements. Figures 7.10 show the density isolines at $t = 0.3$ obtained using $p = 1$ and $p = 2$ DG approximations on the second-order curvilinear mesh. Once again, we observe that both approximations capture the shock structures and their interactions well.

7.2.5 Strong shock interactions.

Next, we test the performance of the limiter in the presence of shock-shock interactions. The initial conditions for the test problem are taken from the two-dimensional Riemann test suite proposed in [55] and shown in Figure 7.11. The simulation is run until $t = 0.8$ on a mesh of $247,688$ second-order triangular elements. Figure 7.12 shows the density isolines at $t = 0.8$ obtained using the second and third-order DG approximations and the respective moment limiters. We note that the higher order method better resolves the vortical structures along the contact discontinuities.

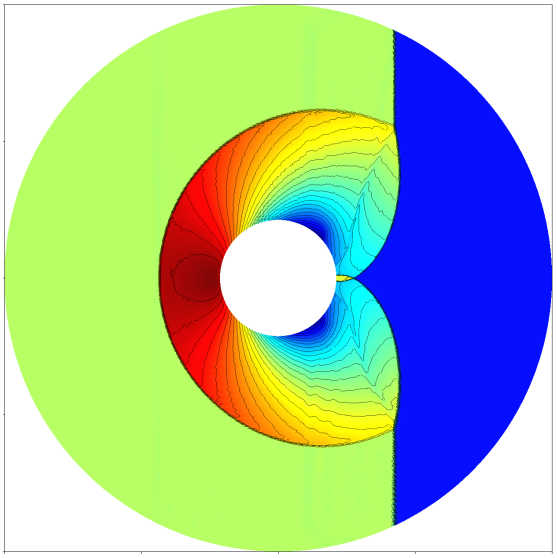

(a) Density isolines with $p = 1$.

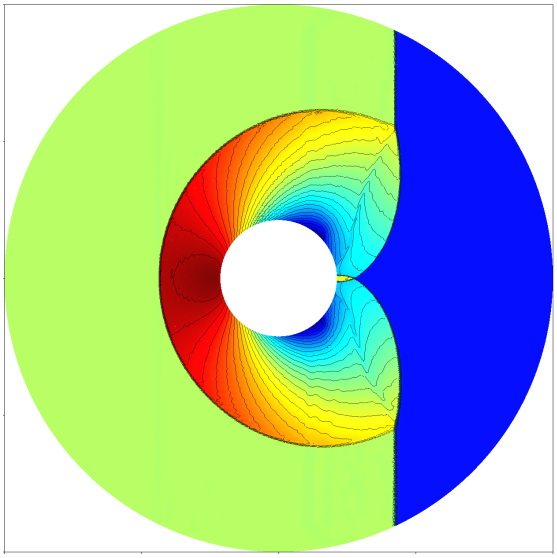

(b) Density isolines with $p = 2$.

7.2.6 Double Mach reflection.

Finally, we solve the double Mach reflection problem to test the performance of the proposed moment limiter in the presence of strong discontinuities. The initial set-up for the problem (Figure 7.13) is taken from [25]. The initial condition consists of a Mach 10 shock wave impinging on a reflecting wall at an angle of 60°. The states to the left ($\mathbf{U}_l$) and to the right ($\mathbf{U}_r$) of the shock wave are given in Table 7.6. The simulation is run until $t = 0.2$ on a computational domain $[0, 3.5] \times [0, 1]$ discretized into $252,232$ second-order triangular elements. Figure 7.14 shows the density isolines at $t = 0.2$ obtained using second

	$\mathbf{U}_l$	$\mathbf{U}_r$
ρ	8	1.4
$s = \mathbf{v} \cdot \mathbf{n}$	8.25	0
p	116.5	1

Table 7.6: States to the left and right of the initial shock for the double Mach test case.

and third order DG approximations with the respective moment limiters. The results are comparable to the results in [25] obtained using a moment limiter on Cartesian mesh and to the results in [57] obtained using a moment limiter on triangular meshes. We observe that both DG approximations resolve the shock structures well. We also note that the slip line near the primary triple point is tighter for the higher order approximation (Figure 7.15b). Finally, we report the computational cost of limiting in Table 7.7. The limiter

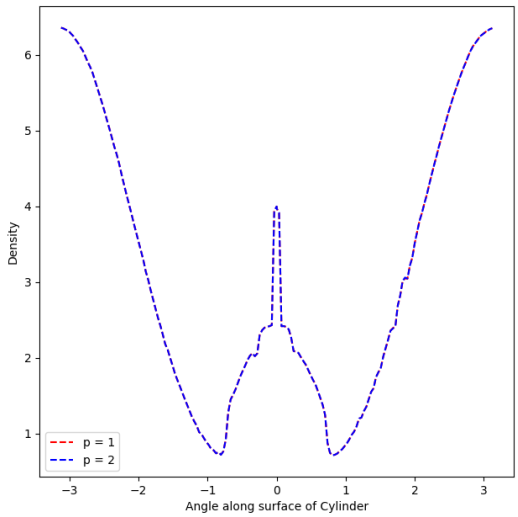

(c) Density along surface of the cylinder.

Figure 7.10: Density isolines at $t = 0.3$ for the shock cylinder interaction example on an structured polar mesh of $209,300$ second-order triangular elements.

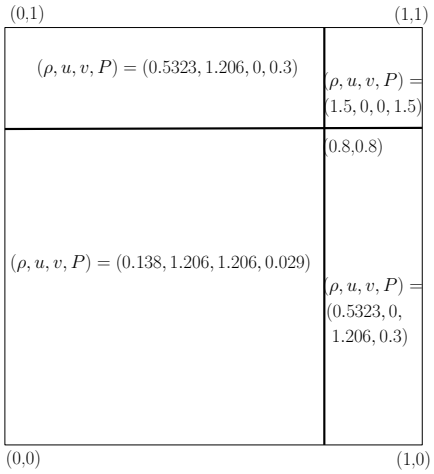

Figure 7.11: Modified initial condition for 2D Riemann problem.

takes at most sixteen percent of the total run time of a parallel GPU implementation of the modal discontinuous Galerkin method [54].

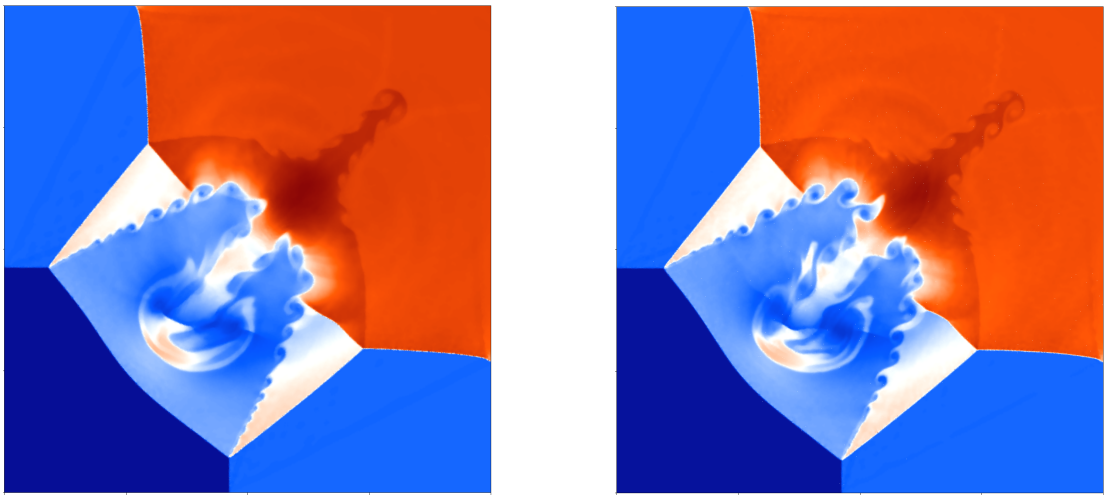

(a) (b)

Figure 7.12: Density isolines at $t = 0.8$ for the shock-shock interaction example for a) $p = 1$, b) $p = 2$, on a mesh of $247,688$ second-order triangular elements.

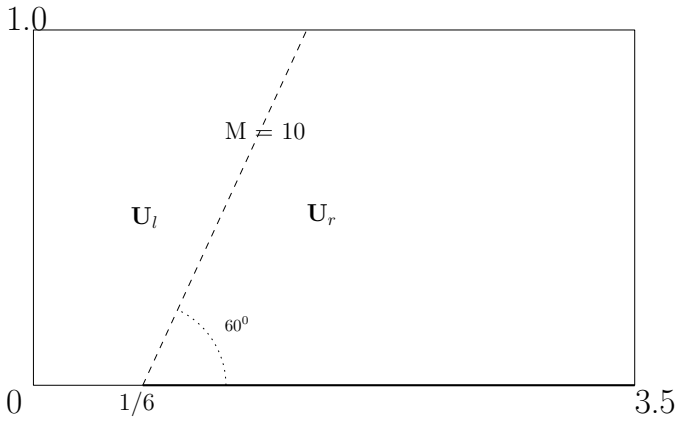

Figure 7.13: The initial set-up for the double mach reflection test case.

7.3 Summary

We have presented a high-order moment limiter for the DG method on unstructured curvilinear triangular meshes. The limiter works by limiting solution coefficients (moments) hierarchically starting with the highest. The limiter stops when either a set of solution coefficients that are not modified or the zeroth order moment is encountered. The hierarchical implementation prevents overlimiting, especially near solution extrema where employing a second order limiter leads to 'clipping' of the extrema.

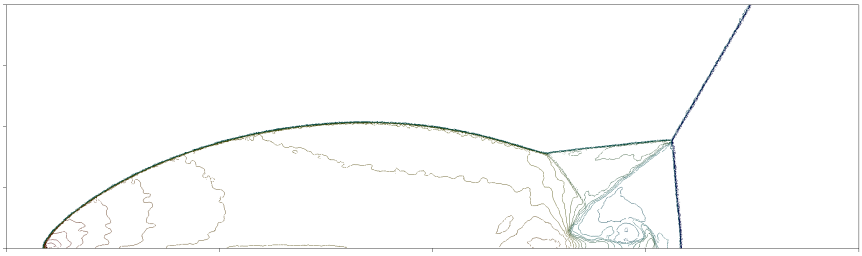

(a) Density isolines with $p = 1$.

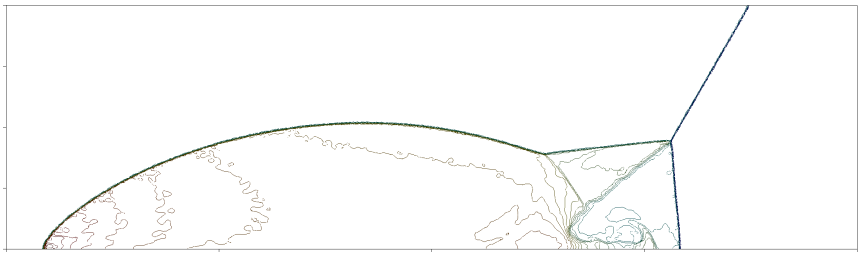

(b) Density isolines with $p = 2$.

Figure 7.14: Density isolines at $t = 0.2$ for the double Mach test case on a final mesh of $252,232$ second-order triangular elements.

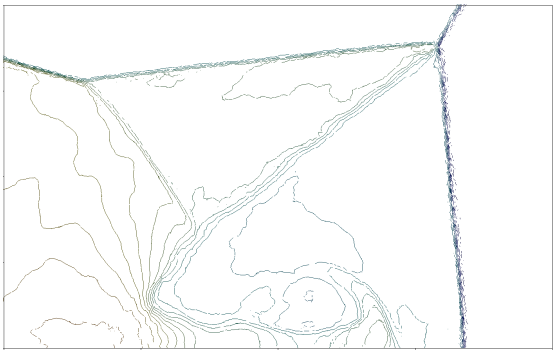

(a) Zoom in near slip line for $p = 1$.

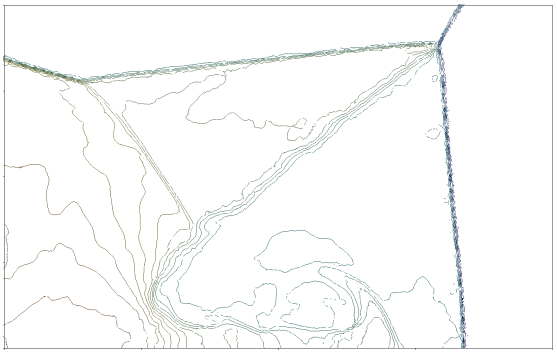

(b) Zoom in near slip line for $p = 2$.

Figure 7.15: Density isolines at $t = 0.2$ for the double Mach test case on a final mesh of $252,232$ second-order triangular elements.

Numerical experiments presented in Section 7.2 demonstrate that the DG method with the proposed limiter eliminates spurious oscillations and is robust in the presence of discontinuities. Further, the experiments also show that the limiter solution retains the theoretical convergence rate for smooth solutions.

The proposed limiter makes use of a compact reconstruction stencil computed [53] once during the preprocessing stage. The implementation of the limiting strategy involves only a

p	Run time (s)	Limiting time (s)	Time steps
1	228.4	16.2 (7.1%)	10,062
2	1566.65	222.81 (14.2%)	16,702
3	4,131.3	672.9 (16.2%)	20,842

Table 7.7: Limiting time for the double Mach reflection example for $p = 1,\ 2$, and 3 DG approximations on a mesh of $252,232$ second-order triangular elements. The limiting time as a percentage of the total run time is given in parenthesis under "Limiting time".

simple set of algebraic expressions involving the solution coefficients and some precomputed parameters. Thus, the limiter takes only a small percent of the total computing time ($\approx 16\%$) in a parallel implementation, which is relatively modest.

Chapter 8

Slope limiter on tetrahedral meshes

In this chapter, we present and analyze a class of scalar slope limiters for the DG method on unstructured tetrahedral meshes. The limiter works by multiplying linear solution coefficients by a scaling factor $\alpha_i \in [0,1]$ such that the value of numerical solution at select limiting points along the element boundary remains bounded by solution averages from a neighborhood of the element. The above limiter along with a valid time step ensure that the numerical solution satisfies local maximum principle (LMP) (8.18) in means. The performance of the limiter depends on the choice of the limiting points as well as the limiting neighborhood. For a triangular mesh, it was shown in [22] that for the limited solution to retain its second order accuracy, the limiting points must lie within the convex hull formed by the cell centroids of the elements in the limiting neighborhood. The same proof and conclusion follows for a tetrahedral mesh. A simple choice for a neighborhood that always satisfies the above condition is the vertex neighborhood, i.e., the neighborhood consisting of elements sharing a vertex with the element.

We give a short description of the second order slope limiter in Section 8.1. We analyze the stability of the limited solution for scalar linear conservation laws in Section 8.1.2 and scalar nonlinear conservation laws in Section 8.1.3. Finally, we present numerical experiments in Section 8.2 to verify the performance of the proposed limiter.

8.1 Limiting Algorithm

The second order DG approximation on Ω_i, written as a linear combination of polynomial basis, is

$$U_i^n(r,s,t) = \hat{U}_{i,0}^n\varphi_0(r,s,t) + \hat{U}_{i,1}^n\varphi_1(r,s,t) + \hat{U}_{i,2}^n\varphi_2(r,s,t) + \hat{U}_{i,3}^n\varphi_3(r,s,t), \tag{8.1}$$

where the constant and linear basis functions are given by

$$\begin{aligned}
\varphi_0 &= \sqrt{6} \\
\varphi_1 &= -\sqrt{10} + 4\sqrt{10}r \\
\varphi_2 &= -2\sqrt{5} + 2\sqrt{5}r + 6\sqrt{5}s \\
\varphi_3 &= -2\sqrt{15} + 2\sqrt{15}r + 2\sqrt{15}s + 4\sqrt{15}t.
\end{aligned} \tag{8.2}$$

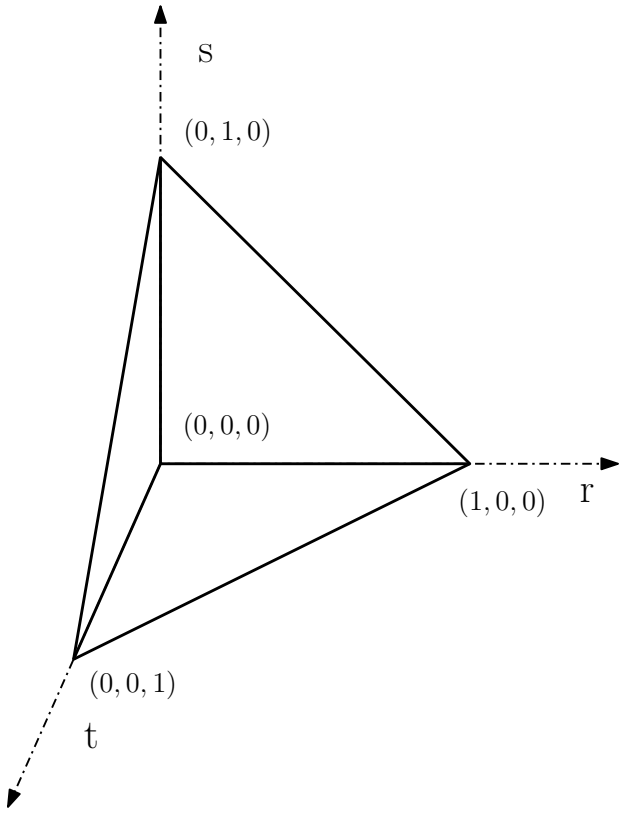

Figure 8.1: Reference tetrahedral element Ω_0.

The limited numerical solution is given by

$$\tilde{U}_i^n = \hat{U}_{i,0}^n \varphi_0(r,s,t) + \alpha_i \left(\hat{U}_{i,1}^n \varphi_1(r,s,t) + \hat{U}_{i,2}^n \varphi_2(r,s,t) + \hat{U}_{i,3}^n \varphi_3(r,s,t) \right), \tag{8.3}$$

where α_i is a scalar multiplier that lies in the interval $[0,1]$ and is computed using the following algorithm

1. Compute the minimum and maximum cell averages in a neighborhood of Ω_i, i.e.,

$$m_i = \min_{j \in N_i} \overline{U}_j \text{ and } M_i = \max_{j \in N_i} \overline{U}_j, \tag{8.4}$$

where N_i is a set containing the indices of Ω_i and elements in the neighborhood of Ω_i, e.g., vertex neighborhood and $\overline{U}_i$ is the solution average in Ω_i.

2. Compute the coefficient $y_i(\mathbf{x}_k)$ at each limiting point $\mathbf{x}_k$, e.g., face midpoints, quadrature points, etc., as

$$y_i(\mathbf{x}_k) = \begin{cases} \dfrac{M_i - \overline{U}_i}{U_i(\mathbf{x}_k) - \overline{U}_i}, & \text{if } U_i(\mathbf{x}_k) - \overline{U}_i > 0, \\ \dfrac{m_i - \overline{U}_i}{U_i(\mathbf{x}_k) - \overline{U}_i}, & \text{if } U_i(\mathbf{x}_k) - \overline{U}_i < 0, \\ 1 \qquad \text{otherwise.} \end{cases} \tag{8.5}$$

3. Finally, compute the scalar multiplier α_i as

$$\alpha_i = \min(1, \min_k y_i(\mathbf{x}_k)). \tag{8.6}$$

Remark 1. We note that limiting the solution U_i^n using (8.3) doesn't change the cell average $\overline{U}_i^n$ in Ω_i and thus, doesn't affect conservation.

8.1.1 Second order accuracy

For a triangular element in two dimension, it was shown in [22] that for the slope limiter to be second order accurate, the limiting points must lie within the region enclosed by the cell centroids of the neighborhood used in limiting. The same result extends to slope limiting on terahedral elements.

For the slope limiter to be second order accurate, the scaling coefficient α_i should be equal to one for exact linear solutions. Let's assume that the limiting points on Ω_i lie within the region enclosed by the cell centroids of the neighborhood used in limiting, N_i. Now, assume that the exact solution $u(\mathbf{x})$ is linear. Therefore, on Ω_i, the numerical solution $U_i(\mathbf{x}) = u(\mathbf{x})$. From the above two assumptions, the solution at the limiting points on Ω_i will be bounded by the maximum and minimum solutions values at the cell centroids in N_i, i.e.,

$$m_i \leq U_i(\mathbf{x}_k) \leq M_i, \tag{8.7}$$

where $m_i = \min_{j \in N_i} \overline{U}_j$ and $M_i = \max_{j \in N_i} \overline{U}_j$. Subtracting the cell average $\overline{U}_i$ from (8.7) gives

$$m_i - \overline{U}_i \leq U_i(\mathbf{x}_k) - \overline{U}_i \leq M_i - \overline{U}_i. \tag{8.8}$$

From (8.8), we observe that the coefficient $y_i(\mathbf{x}_k)$ in (8.5) evaluated at limiting point $\mathbf{x}_k$ will always be greater than one. Therefore, from (8.6), the scaling coefficient α_i will be one and the solution remains unchanged. However, if any of the limiting points, say $\mathbf{x}_l$, lies outside the region enclosed by the cell centroids in N_i, then (8.7) and thus, (8.8) may no longer be satisfied at $\mathbf{x}_l$. Therefore, either $m_i - \overline{U}_i \geq U_i(\mathbf{x}_l) - \overline{U}_i$ or $U_i(\mathbf{x}_l) - \overline{U}_i \geq M_i - \overline{U}_i$ and following the algorithm to compute the scalar multiplier, α_i could end up being less than one.

8.1.2 Stability analysis for linear advection

Consider the case where (1.8) is a scalar linear advection equation, i.e.,

$$u_t + \nabla \cdot (\mathbf{a}u) = 0. \tag{8.9}$$

Setting $k = 0$ in (1.38) and multiplying with $\sqrt{6}$, we get

$$\frac{d\overline{U}_i^n}{dt} = -\frac{1}{|\Omega_i|} \sum_{j \in N_i^e} \int_{\delta\Omega_{i,j}} \mathbf{F}^*(U_i^n, U_j^n) \cdot \mathbf{n}_{i,j} dl, \tag{8.10}$$

where $\overline{U}_i^n = \sqrt{6}\hat{U}_0^n$ is the cell average and $|\Omega_i| = 6 \det J_i$ is the volume of the tetrahedron Ω_i. After one Euler time step, the cell average in Ω_i is

$$\overline{U}_i^{n+1} = \overline{U}_i^n - \frac{\Delta t}{|\Omega_i|} \sum_{j \in N_i^e} \int_{\delta\Omega_{i,j}} \mathbf{F}^*(U_i, U_j) \cdot \mathbf{n}_{i,j} dl. \tag{8.11}$$

For linear advection, the flux in (1.8) is given by $\mathbf{F}(u) = u\mathbf{a}$, where $\mathbf{a}$ is the flow direction. Choosing the upwind flux as the numerical flux gives us

$$\mathbf{F}^*(U_i, U_j) \cdot \mathbf{n}_{i,j} = \begin{cases} (\mathbf{a} \cdot \mathbf{n}_{i,j}) U_i, & \text{if } j \in N_i^+, \\ (\mathbf{a} \cdot \mathbf{n}_{i,j}) U_j, & \text{if } j \in N_i^-, \end{cases} \tag{8.12}$$

where N_i^+ and N_i^- are, respectively, the indices of the outflow and inflow neighbors of Ω_i, i.e., $N_i^{\pm} = \{j \in N_i^e \Big| \pm (\mathbf{a}\cdot\mathbf{n}_{i,j}) > 0\}$. Further, from the divergence theorem we have

$$\sum_{j\in N_i^e} \int_{\delta\Omega_{i,j}} \overline{U}_i^n \mathbf{a}\cdot\mathbf{n}_{i,j} dl = \sum_{j\in N_i^+} \overline{U}_i^n |\mathbf{a}\cdot\mathbf{n}_{i,j}||\delta\Omega_{i,j}| - \sum_{j\in N_i^-} \overline{U}_i^n |\mathbf{a}\cdot\mathbf{n}_{i,j}||\delta\Omega_{i,j}| = 0. \tag{8.13}$$

Substituting (8.12) and (8.13) in (8.11), we get

$$\overline{U}_i^{n+1} = \overline{U}_i^n + \frac{\Delta t}{|\Omega_i|}\left[\sum_{j\in N_i^-} \left(U_j^n(\mathbf{x}_{i,j}) - \overline{U}_i^n\right)|\mathbf{a}\cdot\mathbf{n}_{j,i}||\delta\Omega_{i,j}| - \sum_{j\in N_i^+} \left(U_i^n(\mathbf{x}_{i,j}) - \overline{U}_i^n\right)|\mathbf{a}\cdot\mathbf{n}_{i,j}||\delta\Omega_{i,j}|\right], \tag{8.14}$$

where the midpoint of the face $\delta\Omega_{i,j}$ is chosen as the quadrature point $\mathbf{x}_{i,j}$. If the solution is limited at time t_n, then (8.14) becomes

$$\overline{U}_i^{n+1} = \overline{U}_i^n + \frac{\Delta t}{|\Omega_i|}\left[\sum_{j\in N_i^-} \left(\tilde{U}_j^n(\mathbf{x}_{i,j}) - \overline{U}_i^n\right)|\mathbf{a}\cdot\mathbf{n}_{j,i}||\delta\Omega_{i,j}| - \sum_{j\in N_i^+} \left(\tilde{U}_i^n(\mathbf{x}_{i,j}) - \overline{U}_i^n\right)|\mathbf{a}\cdot\mathbf{n}_{i,j}||\delta\Omega_{i,j}|\right], \tag{8.15}$$

where $\tilde{U}^n$ is the limited solution. We aim to rewrite (8.15) in the form

$$\overline{U}_i^{n+1} = \delta_0 \overline{U}_i^n + \sum_k \delta_k U_k, \tag{8.16}$$

where U_k is either the cell average or a convex combination of cell averages in some neighborhood of Ω_i. If the scaling coefficients δ_k satisfy

$$\delta_k \geq 0, \quad \delta_0 \geq 0, \quad \text{and} \quad \delta_0 + \sum_k \delta_k = 1, \tag{8.17}$$

then the right hand side of (8.16) is a convex combination of cell averages in some neighborhood of Ω_i, and thus, the numerical solution in Ω_i satisfies the local maximum principle (LMP) in the means, i.e.,

$$\min_{k\in\mathcal{N}_i} \overline{U}_k^n \leq \overline{U}_i^{n+1} \leq \max_{k\in\mathcal{N}_i} \overline{U}_k^n, \tag{8.18}$$

where $\mathcal{N}_i$ is a set containing the indices of Ω_i and its neighbors.

For a scalar linear conservation law, we choose the face centers as the limiting points while computing the scalar multiplier α_i in (8.3). Consider the following proposition, proof of which is provided in Section 8.4.1.

Proposition 1

For a face center $\mathbf{x}_{i,j}$, there exists a scalar multiplier r_{fc} and another face center $\mathbf{x}_{i,k}$ such that

$$U_i(\mathbf{x}_{i,j}) - \overline{U}_i = r_{fc}\left(\overline{U}_i - U_i(\mathbf{x}_{i,k})\right), \quad 0 \le r_{fc} \le 3. \tag{8.19}$$

Using (8.13) and (8.19), the expression on the right hand side of (8.15) can be rewritten as

$$\begin{aligned}
\overline{U}_i^{n+1} &= \overline{U}_i^n + \frac{\Delta t}{|\Omega_i|}\left[\sum_{j\in N_i^-}\left(\tilde{U}_j^n(\mathbf{x}_{i,j}) - \overline{U}_i^n\right)|\mathbf{a}\cdot\mathbf{n}_{j,i}||\delta\Omega_{i,j}| - \sum_{j\in N_i^+}\left(\tilde{U}_i^n(\mathbf{x}_{i,j}) - \overline{U}_i^n\right)|\mathbf{a}\cdot\mathbf{n}_{i,j}||\delta\Omega_{i,j}|\right], \\
&= \overline{U}_i^n + \frac{\Delta t}{|\Omega_i|}\left[\sum_{j\in N_i^-}\left(\tilde{U}_j^n(\mathbf{x}_{i,j}) - \overline{U}_i^n\right)|\mathbf{a}\cdot\mathbf{n}_{j,i}||\delta\Omega_{i,j}| + \sum_{j\in N_i^+} r_{fc}\left(\tilde{U}_i^n(\mathbf{x}_{i,j'}) - \overline{U}_i^n\right)|\mathbf{a}\cdot\mathbf{n}_{i,j}||\delta\Omega_{i,j}|\right], \\
&= \left[1 - \frac{\Delta t}{|\Omega_i|}\sum_{j\in N_i^-}|\mathbf{a}\cdot\mathbf{n}_{j,i}||\delta\Omega_{i,j}| - \frac{\Delta t}{|\Omega_i|}\sum_{j\in N_i^+} r_{fc}|\mathbf{a}\cdot\mathbf{n}_{i,j}||\delta\Omega_{i,j}|\right]\overline{U}_i^n \\
&+ \frac{\Delta t}{|\Omega_i|}\left[\sum_{j\in N_i^-}\tilde{U}_j^n(\mathbf{x}_{i,j})|\mathbf{a}\cdot\mathbf{n}_{j,i}||\delta\Omega_{i,j}| + \sum_{j\in N_i^+} r_{fc}\tilde{U}_i^n(\mathbf{x}_{i,j'})|\mathbf{a}\cdot\mathbf{n}_{i,j}||\delta\Omega_{i,j}|\right], \\
&= \left[1 - \frac{\Delta t}{|\Omega_i|}(1+r_{fc})\sum_{j\in N_i^-}|\mathbf{a}\cdot\mathbf{n}_{j,i}||\delta\Omega_{i,j}|\right]\overline{U}_i^n + \frac{\Delta t}{|\Omega_i|}\left[\sum_{j\in N_i^-}\tilde{U}_j^n(\mathbf{x}_{i,j})|\mathbf{a}\cdot\mathbf{n}_{j,i}||\delta\Omega_{i,j}|\right. \\
&\left. + \sum_{j\in N_i^+} r_{fc}\tilde{U}_i^n(\mathbf{x}_{i,j'})|\mathbf{a}\cdot\mathbf{n}_{i,j}||\delta\Omega_{i,j}|\right]
\end{aligned} \tag{8.20}$$

which is of the form (8.16). We note that all of the scaling coefficients on the right hand side of (8.20) add up to one. As a result of limiting, the solution values at face centers are bounded by the minimum and maximum cell averages in a neighborhood of Ω_i. Further, by construction, the scaling coefficients of the values of the limited solution at face centers are non negative. Therefore, to satisfy (8.17), the scaling coefficient of $\overline{U}_i^n$ should satisfy

$$\begin{aligned}
(1+r_{fc})\frac{\Delta t}{|\Omega_i|}\sum_{j\in N_i^-}|\mathbf{a}\cdot\mathbf{n}_{j,i}||\delta\Omega_{i,j}| &\le 1 \\
\Delta t &\le \frac{1}{1+r_{fc}}\frac{|\Omega_i|}{\sum_{j\in N_i^-}|\mathbf{a}\cdot\mathbf{n}_{j,i}||\delta\Omega_{i,j}|}.
\end{aligned} \tag{8.21}$$

From (8.19), we note that $r_{fc} \le 3$. Applying this in (8.21), we obtain a slightly restrictive

condition on the time step

$$\Delta t \leq \frac{1}{4} \frac{|\Omega_i|}{\sum_{j \in N_i^-} |\mathbf{a} \cdot \mathbf{n}_{j,i}| |\delta\Omega_{i,j}|} \tag{8.22}$$

In general, the expression for the measure of cell size on the right hand side of (8.22) depends on the direction of wave propagation. Instead, as noted and proved in [23], we can use a slightly restrictive but simpler measure of cell size

$$h_i = 3 \frac{|\Omega_i|}{|\delta\Omega_{i,1}| + |\delta\Omega_{i,2}|}, \tag{8.23}$$

where $|\delta\Omega_{i,1}|$ and $|\delta\Omega_{i,1}|$ are the two largest face areas of Ω_i. Combining (8.22) and (8.23), we have

$$\Delta t \leq \frac{1}{12} \frac{h_i}{|\mathbf{a}|}. \tag{8.24}$$

8.1.3 Stability analysis for scalar nonlinear conservation laws

Consider the case where (1.8) is a scalar nonlinear hyperbolic equation, i.e.,

$$u_t + \nabla \cdot (\mathbf{F}(u)) = 0. \tag{8.25}$$

Setting $k = 0$ in (1.38) and multiplying with $\sqrt{6}$, we get

$$\frac{d\overline{U}_i^n}{dt} = -\frac{1}{|\Omega_i|} \sum_{j \in N_i^e} \int_{\delta\Omega_{i,j}} \mathbf{F}^*(U_i^n, U_j^n) \cdot \mathbf{n}_{i,j} dl. \tag{8.26}$$

Therefore, after one Euler time step, the cell average in Ω_i is given by

$$\overline{U}_i^{n+1} = \overline{U}_i^n - \frac{\Delta t}{|\Omega_i|} \sum_{j \in N_i^e} \int_{\delta\Omega_{i,j}} \mathbf{F}^*(U_i^n, U_j^n) \cdot \mathbf{n}_{i,j} dl. \tag{8.27}$$

As the cell average $\overline{U}_i^n$ is a constant, from the divergence theorem we have

$$\sum_{j \in N_i^e} \int_{\delta\Omega_{i,j}} \mathbf{F}^*(\overline{U}_i^n, \overline{U}_i^n) \cdot \mathbf{n}_{i,j} dl = 0. \tag{8.28}$$

Using (8.28), a three point quadrature rule to compute the nonlinear flux on face $\delta\Omega_{i,j}$, and denoting the normal flux at a quadrature point $\mathbf{x}_{i,j}^q$ on $\delta\Omega_{i,j}$ as

$$\hat{\mathbf{F}}_q(U_i, U_j) = \mathbf{F}_q^*(U_i, U_j) \cdot \mathbf{n}_{i,j}, \tag{8.29}$$

we get

$$\overline{U}_i^{n+1} = \overline{U}_i^n - \frac{\Delta t}{3|\Omega_i|} \sum_{j \in N_i^e} \sum_{q=1}^{3} \left(\hat{\mathbf{F}}_q(U_i^n, U_j^n) - \hat{\mathbf{F}}_q(\overline{U}_i^n, \overline{U}_i^n) \right) |\delta\Omega_{i,j}|. \tag{8.30}$$

If the solution is limited at time t_n, then (8.30) becomes

$$\overline{U}_i^{n+1} = \overline{U}_i^n - \frac{\Delta t}{3|\Omega_i|} \sum_{j \in N_i^e} \sum_{q=1}^{3} \left(\hat{\mathbf{F}}_q(\tilde{U}_i^n, \tilde{U}_j^n) - \hat{\mathbf{F}}_q(\overline{U}_i^n, \overline{U}_i^n) \right) |\delta\Omega_{i,j}|, \tag{8.31}$$

where $\tilde{U}^n$ is the limited solution. Next, adding and subtracting $\hat{\mathbf{F}}_q(\overline{U}_i^n, \tilde{U}_j^n)$ at each quadrature point in (8.31), we get

$$\begin{aligned}
\overline{U}_i^{n+1} &= \overline{U}_i^n - \frac{\Delta t}{3|\Omega_i|} \sum_{j \in N_i^e} \sum_{q=1}^{3} \left(\hat{\mathbf{F}}_q(\tilde{U}_i^n, \tilde{U}_j^n) \pm \hat{\mathbf{F}}_q(\overline{U}_i^n, \tilde{U}_j^n) - \hat{\mathbf{F}}_q(\overline{U}_i^n, \overline{U}_i^n) \right) |\delta\Omega_{i,j}|, \\
&= \overline{U}_i^n + \frac{\Delta t}{3|\Omega_i|} \sum_{j \in N_i^e} \sum_{q=1}^{3} \frac{\partial \hat{\mathbf{F}}_q}{\partial U_1}(\theta_{i,1q}, \tilde{U}_j^n) \left(\overline{U}_i^n - \tilde{U}_i^n(\mathbf{x}_{i,j}^q) \right) |\delta\Omega_{i,j}| \\
&- \frac{\Delta t}{3|\Omega_i|} \sum_{j \in N_i^e} \sum_{q=1}^{3} \frac{\partial \hat{\mathbf{F}}_q}{\partial U_2}(\tilde{U}_i^n, \theta_{j,1q}) \left(\tilde{U}_j^n(\mathbf{x}_{i,j}^q) - \overline{U}_i^n \right) |\delta\Omega_{i,j}|,
\end{aligned} \tag{8.32}$$

where $\theta_{i,1q}$ lies between $\tilde{U}_i^n(\mathbf{x}_{i,j}^q)$ and $\overline{U}_i^n$, $\theta_{j,1q}$ lies between $\tilde{U}_j^n(\mathbf{x}_{i,j}^q)$ and $\overline{U}_i^n$. By the monotonicity property of the numerical flux, the partial derivatives of $\hat{\mathbf{F}}_q$ satisfy

$$\hat{\mathbf{F}}_{U_1,q} = \frac{\partial \hat{\mathbf{F}}_q}{\partial U_1} \geq 0, \quad \hat{\mathbf{F}}_{U_2,q} = -\frac{\partial \hat{\mathbf{F}}_q}{\partial U_2} \geq 0. \tag{8.33}$$

We aim to rewrite (8.32) in the form

$$\overline{U}_i^{n+1} = \overline{U}_i^n + \sum_k \omega_k \left(U_k - \overline{U}_i^n \right), \tag{8.34}$$

where U_k is either the cell average or a convex combination of cell averages in some neighborhood of Ω_i. If the scaling coefficients ω_k satisfy

$$\omega_k \geq 0, \quad \text{and} \quad \sum_k \omega_k \leq 1, \tag{8.35}$$

then the right hand side of (8.16) is a convex combination of cell averages in some neighborhood of Ω_i, and thus, the numerical solution in Ω_i satisfies the local maximum principle (LMP) (8.18) in means.

For a scalar nonlinear conservation law, we choose the three point quadrature points on each face as the limiting points while computing the scalar multiplier α_i in (8.3). Consider the following proposition, whose proof is provided in Section 8.4.2.

Proposition 2

For a quadrature point $\mathbf{x}_{i,j}$ from the three point quadrature rule on face $\delta\Omega_{i,j}$, there exists a scalar multiplier r_{3q} and another quadrature point $\mathbf{x}_{i,k}$, possibly on a different face, such that

$$U_i(\mathbf{x}_{i,j}) - \overline{U}_i = r_{3q}\left(\overline{U}_i - U_i(\mathbf{x}_{i,k})\right), \quad 0 \le r_{3q} \le 5/3. \tag{8.36}$$

Using (8.36) and (8.33) in (8.32), we get

$$\begin{aligned}\overline{U}_i^{n+1} = \overline{U}_i &+ \frac{\Delta t}{3|\Omega_i|}\sum_{j\in N_i^e}\sum_{q=1}^{3}\hat{\mathbf{F}}_{U_1,q}\left[r_{3q}\left(\tilde{U}_i^n(\mathbf{x}_{i,j'}^{q'}) - \overline{U}_i^n\right)\right]|\delta\Omega_{i,j}| \\ &+ \frac{\Delta t}{3|\Omega_i|}\sum_{j\in N_i^e}\sum_{q=1}^{3}\hat{\mathbf{F}}_{U_2,q}\left(\tilde{U}_j^n(\mathbf{x}_{i,j}^{q}) - \overline{U}_i^n\right)|\delta\Omega_{i,j}|,\end{aligned} \tag{8.37}$$

which is of the form (8.34). As a result of limiting, the solution values at the quadrature points on all faces are bounded by the minimum and maximum cell averages in the limiting neighborhood of Ω_i. Moreover, we require the scaling coefficients to satisfy (8.35). To do so, we need to impose the following restriction on the time step size

$$\begin{aligned}&\frac{\Delta t}{3|\Omega_i|}\sum_{j\in N_i^e}\left[\sum_{q=1}^{3}\left(\hat{\mathbf{F}}_{U_1,q}r_{3q} + \hat{\mathbf{F}}_{U_2,q}\right)\right]|\delta\Omega_{i,j}| \le 1 \\ &\frac{\Delta t}{3|\Omega_i|}\lambda_i\sum_{j\in N_i^e}3\left(r_{3q}+1\right)|\delta\Omega_{i,j}| \le 1 \\ &\Delta t \le \frac{1}{(1+r_{3q})}\frac{|\Omega_i|}{\lambda_i\sum_{j\in N_i^e}|\delta\Omega_{i,j}|} \\ &\Delta t \le \frac{1}{8}\frac{h_{i,c}}{\lambda_i},\end{aligned} \tag{8.38}$$

where λ_i is the maximum wavespeed in the element and $h_{i,c} = 3\dfrac{|\Omega_i|}{\sum_{j\in N_i^e}|\delta\Omega_{i,j}|}$.

8.2 Results

In this section, we present numerical experiments to analyze the performance of the proposed scalar limiter. We show numerically that the derived restrictions on the time step for linear stability is valid. Through convergence studies, we show that the limited solution retains second order rate of convergence for smooth problems. Finally, we also run tests to show the robustness of the proposed limiter in the presence of discontinuities. In all presented cases, unless stated otherwise, time-stepping was performed using an explicit second order Runge-Kutta method with the CFL condition (8.21).

8.2.1 CFL verification.

We provide numerical examples to show that the time step restriction derived in Section 8.1.2 for linear stability is tight. To do so, we construct a structured and tiled tetrahedral mesh with the same minimum cell width for every tetrahedron. To construct the mesh, we first divide a cube of side $a = 1/30$ into six tetrahedra using the decomposition shown in Figure 8.2. Next, the tetrahedral decomposition of the cube is tiled on the domain $[-1, 1]^3$ resulting in a structured mesh of $1,296,000$ elements. For the decomposition in Figure 8.2, the minimum cell height for each tetrahedron in the cube is $h_i = \frac{1}{30}\sqrt{2}$, along the direction $[1, 1, 0]$.On the tiled mesh, we solve the scalar advection equation, with the flux in (1.8) given by $\mathbf{F} = [u, u, 0]$ until the final time $t = 0.25$.The initial condition is given by

$$u_0(x, y, z) = \begin{cases} 1, & \text{if} \sqrt{x^2 + y^2 + z^2} \leq 0.25, \\ 0, & \text{otherwise.} \end{cases} \tag{8.39}$$

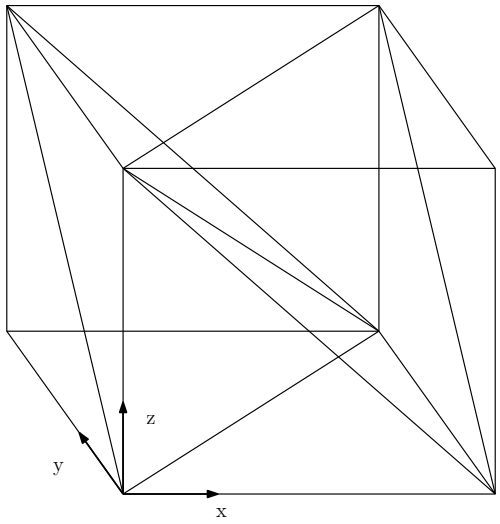

Figure 8.2: Decomposition of cube into tetrahedra.

Table 8.1 shows the maximum and minimum cell averages of the numerical solution observed until the final time. We note that the numerical solution remains bounded within the initial global bounds at the CFL of 1/12 for the forward Euler time stepping, agreeing with the analysis. For RK2 timestepping, we note that it is possible to take larger CFL and the solution averages still remain within the initial global bounds.

1/CFL	Maximum	Minimum
6	1+8.896752e-04	-3.440212e-04
8	1+1.889171e-04	-1.254546e-05
10	1+7.426556e-06	-8.941661e-17
11	1+1.554312e-15	-8.004176e-17
11.5	1+1.332268e-15	-8.053579e-17
12	1+1.332268e-15	-7.328884e-17

(a) RK2.

1/CFL	Maximum	Minimum
6	1+2.359015e-02	-6.377838e-04
8	1+5.951599e-03	-5.951599e-03
10	1+1.091354e-08	-7.366143e-16
11	1+1.842021e-08	-5.316378e-16
11.5	1+4.628808e-11	-4.064670e-16
12	1+2.220446e-15	-5.299669e-16

(b) Forward Euler.

Table 8.1: Global bounds of solution averages until $t = 0.25$ on a mesh of $1,296,000$ tetrahedra for the advecting spherical pulse problem.

8.2.2 Advecting hill.

We solve the scalar advection equation on the domain $\Omega = [-1,1]^3$, with the flux in (1.8) given by $\mathbf{F} = [u,u,u]$. The initial condition is

$$u_0(x,y,z) = \begin{cases} cos(\frac{\pi}{2}r)^2, & \text{r} \leq 1, \\ 0, & \text{otherwise} \end{cases}, \tag{8.40}$$

where $r = 2\sqrt{(x)^2+(y)^2+(z)^2}$. The problem is solved until $t = 0.25$ on a series of unstructured tetrahedral meshes $A-D$. Mesh A is the coarsest with 4485 tetrahedra while meshes B-D are obtained by the nested refinement of the preceding mesh. Tables 8.2 and 8.3 show the L_1 errors and the observed convergence rates for the second order DG approximation with and without limiting. We observe that the limited solution retains the second order rate of convergence, when the solution is limited at face midpoints as well as second degree quadrature points. Applying a limiter is expected to introduce errors in the solution. However, we note that such errors are relatively modest.

Mesh	Number of elements	L1 error	
		limited	unlimited
A	4,485	1.56e-02 (-)	1.5e-02 (-)
B	35,347	4.1e-03 (1.93)	4.6e-03 (1.7)
C	271,899	9.66e-04 (2.08)	1.1e-03 (2.06)
D	2,178,457	2.04e-04 (2.24)	2.5e-04 (2.14)

Table 8.2: L_1 errors for the advecting hill problem at $t = 0.25$ with and without limiting, using vertex neighborhood and face midpoints as limiting points. The numbers in parentheses are the observed rates of convergence.

Mesh	Number of elements	L1 error	
		limited	unlimited
A	4,485	2.12e-02 (-)	1.5e-02 (-)
B	35,347	5.7e-03 (1.89)	4.6e-03 (1.7)
C	271,899	1.28e-03 (2.15)	1.1e-03 (2.06)
D	2,178,457	2.51e-04 (2.35)	2.5e-04 (2.14)

Table 8.3: L_1 errors for the advecting hill problem at $t = 0.25$ with and without limiting, using vertex neighborhood and second degree quadrature points as limiting points. The numbers in parentheses are the observed rates of convergence.

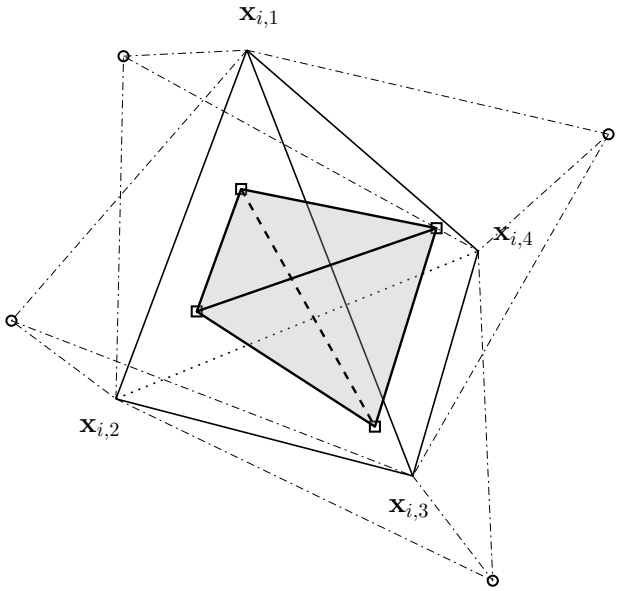

Figure 8.3: The edge neighborhood for element Ω_i.

To show the effect of the choice of limiting neighborhood on the solution accuracy, we repeat the convergence study with the edge neighborhood i.e., all elements that share a face with Ω_i (Figure 8.3, shaded region), as the limiting neighborhood and the face centers as the limiting points. Table 8.4 shows the L_1 errors and the observed convergence rates for the second order DG approximation with and without limiting. We note that for the chosen limiting configuration, the limited solution does not retain the second order convergence rate, thus corroborating the discussion in Section 8.1.1.

Mesh	Number of elements	L1 error	
		limited	unlimited
A	4,485	2.35e-02 (-)	1.5e-02 (-)
B	35,347	8.677e-03 (1.44)	4.6e-03 (1.7)
C	271,899	3.62e-03 (1.26)	1.1e-03 (2.06)
D	2,178,457	1.66e-03 (1.12)	2.5e-04 (2.14)

Table 8.4: L_1 errors for the advecting hill problem at $t = 0.25$ with and without limiting, using edge neighborhood and face midpoints as limiting points. The numbers in parentheses are the observed rates of convergence.

8.2.3 Rotating Shapes.

We solve the rotating shapes problem with the flux in (1.8) given by $\mathbf{F} = [-2\pi yu, 2\pi xu, 0]$. The initial condition consists of a hill and a square pulse given by

$$u_0(x,y,z) = \begin{cases} \cos^2(2\pi r), & \text{if } r \le 0.25, \\ 1, & \text{if } \max\left(|x-0.35|, |y|, |z|\right) \le 0.25, \\ 0, & \text{otherwise}, \end{cases} \tag{8.41}$$

where $r = \sqrt{(x+0.5)^2 + y^2 + z^2}$. The exact solution is a rotation of the initial condition about the origin. The problem is solved until $t = 1$ on an unstructured mesh of $3,150,670$ tetrahedral elements. Figure 8.4 shows the isosurface of the limited solution for $z < 0$ at the final time while Figure 8.5 shows the isolines and the solution profiles at $z = y = 0$, $z = 0, x = 0.5$, and $z = 0, x = 0.55$, obtained using $p = 1$ DG approximation with and without the limiter. The quality of the solution is comparable to the results obtained using the moment limiter described in [25] on a 80×80 Cartesian mesh and the second order moment limiter described in [23] on an unstructured mesh of $3,049,851$ tetrahedral elements. From Figures 8.5a, 8.5b and 8.5c, we note that the limiter successfully reduces

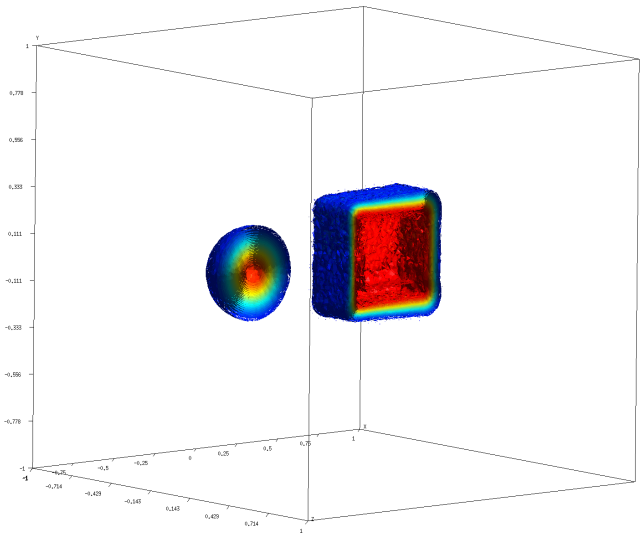

Figure 8.4: Isosurfaces of the limited solution to the rotating shapes problem for $z < 0$ at $t = 1$.

oscillations near the discontinuities. This is further supported by the solution profiles in Figures 8.5d and 8.5f. We note that the accuracy near the peak of the hill has reduced

which can be attributed to the well known phenomenon of 'clipping' at local extrema by a second order slope limiter. Furthermore, from the profiles of the limited solutions in 8.5d and 8.5e, we observe that the solution is better resolved when we choose the face midpoints as the limiting points over the second degree quadrature points. This is to be expected as limiting at second degree quadrature points is more restrictive compared to applying the limiter at face centers.

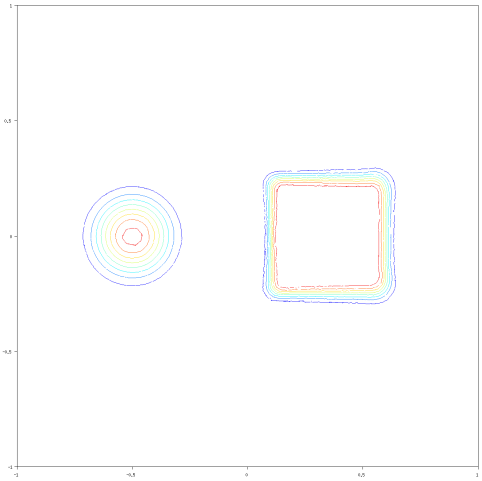

(a) Isolines with second order limiter, midpoint as limiting points.

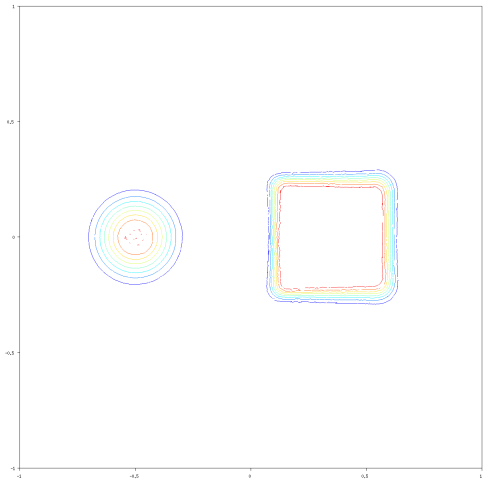

(b) Isolines with second order limiter, quadrature points as limiting points.

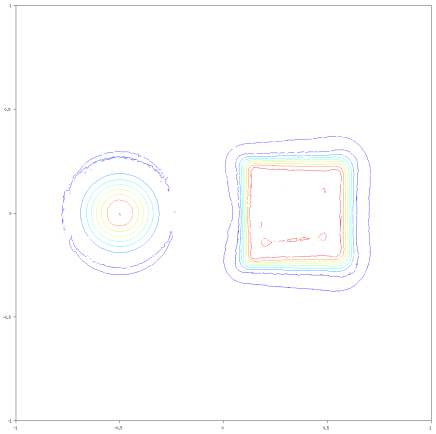

(c) Isolines without limiting.

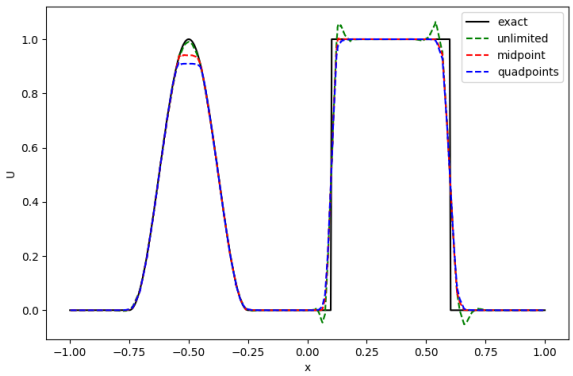

(d) Profile of the solution at $y = 0$.

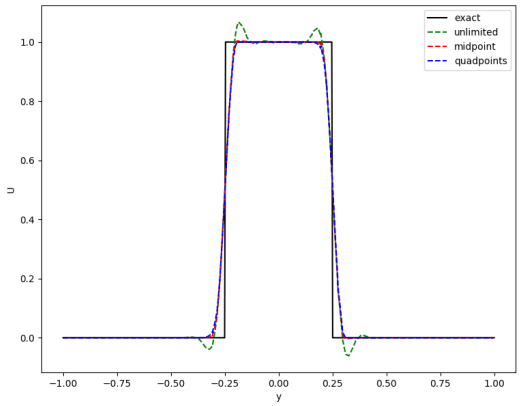

(e) Profile of the solution at $x = 0.5$.

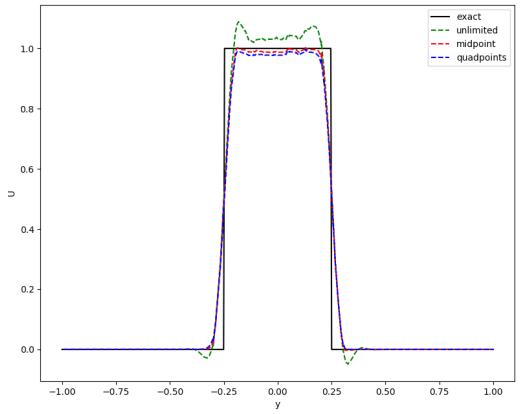

(f) Profile of the solution at $x = 0.55$.

Figure 8.5: Isolines and profiles of the solution for the rotating shapes problem, with and without limiting, at $t = 1$ on an unstructured mesh of $3,150,670$ tetrahedras.

8.2.4 Shock-bubble interaction.

Next, we test the performance of the second order limiter when applied to a system of nonlinear equations, for example, the Euler equations given by

$$\frac{\partial}{\partial t}\begin{pmatrix}\rho\\ \rho u\\ \rho v\\ \rho w\\ E\end{pmatrix}+\frac{\partial}{\partial x}\begin{pmatrix}\rho u\\ \rho u^2+p\\ \rho uv\\ \rho uw\\ (E+p)u\end{pmatrix}+\frac{\partial}{\partial y}\begin{pmatrix}\rho v\\ \rho uv\\ \rho v^2+p\\ \rho vw\\ (E+p)v\end{pmatrix}+\frac{\partial}{\partial y}\begin{pmatrix}\rho w\\ \rho uw\\ \rho vw\\ \rho w^2+p\\ (E+p)w\end{pmatrix}=0, \tag{8.42}$$

where ρ is the density, ρu, ρv and ρw are the x-, y-, and z-direction momenta, E is the energy, and the pressure, p, is given by the equation of state $p = (\gamma-1)\left(E - \frac{\rho}{2}(u^2+v^2+w^2)\right)$. In this example, we simulate the interaction between a Mach 10 shock and a spherical bubble. The initial setup consists of a spherical bubble of radius $R = 0.55$ centered at $(-0.4, 0, 0)$ in the domain $[-1,1]^3$ and the incident shock located at $x = -0.95$ (Figure 8.6). Table 8.5 provides the initial incident, quiescent, and bubble states. $\mathbf{U}_B$ and $\mathbf{U}_Q$ respectively denote the initial states inside and outside the bubble, while $\mathbf{U}_I$ gives the state to the right of the left moving shock. Due to the symmetry of the problem, we can run the test case on a quarter of the original domain, i.e., $[-1,1]\times[0,1]^2$. The problem is run until the final time $t = 0.125$ on an unstructured mesh of $11,530,455$ tetrahedra. A cross section of the density on the plane $z = 0$ at various times between $t = 0$ and the final time $t = 0.125$

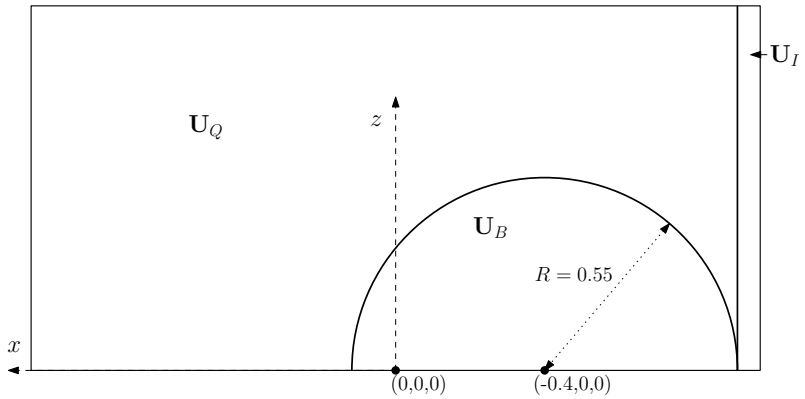

Figure 8.6: Initial setup for the bubble-shock interaction case.

	$\mathbf{U}_Q$	$\mathbf{U}_B$	$\mathbf{U}_I$
ρ	1.4	0.5	8
u	0	0	-8.25
v	0	0	0
w	0	0	0
p	1	1	116.5

Table 8.5: The initial states for the shock-bubble interaction test case.

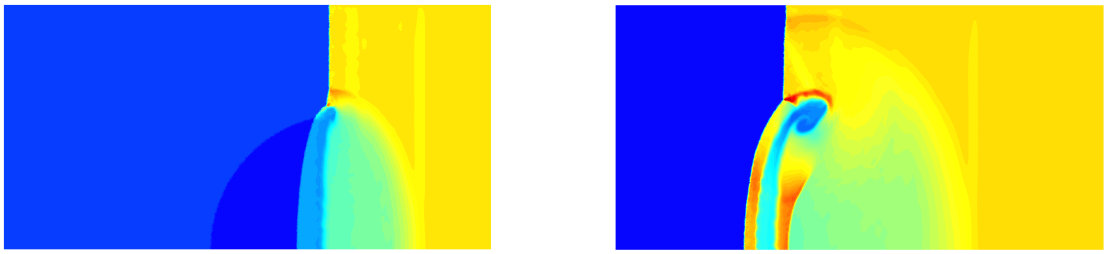

(a) $t = 0.06125$. (b) $t = 0.125$.

Figure 8.7: Density profile along $z = 0$ for the bubble shock interaction case on an unstructured mesh of $11,530,455$ tetrahedra.

are shown in Figure 8.7, displaying a complex interaction where the shock compresses the initial bubble. Isosurfaces of the density at the final time are provided in Figure 8.8.

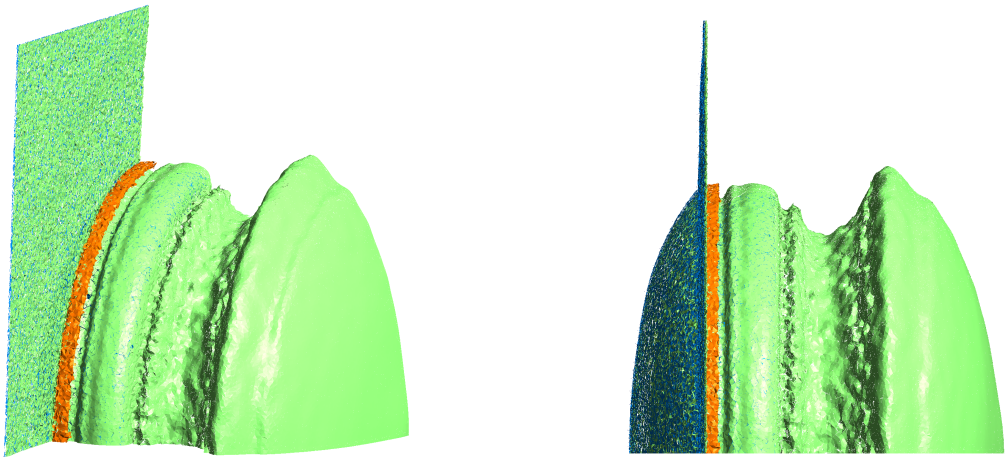

(a) View 1. (b) View 2.

Figure 8.8: Isosurfaces of density for the bubble shock interaction case, at $t = 0.125$ on an unstructured mesh of $11,530,455$ tetrahedra.

8.3 Summary

We have presented the stability analysis for a class of second order scalar slope limiters for the DG method on unstructured tetrahedral meshes. The limiter works by scaling the linear solution coefficients by a constant scaling factor $\alpha_i \in [0,1]$. Further, we derive conditions on the limiter as well as the time step that ensure the solution satisfies the local maximum principle in the means. Numerical experiments presented in Section 8.2 confirm that the DG method with the proposed limiter eliminates spurious oscillations and is robust in the presence of discontinuities. Further, the experiments also demonstrate that the limiter solution retains the second order convergence rate for smooth solutions.

8.4 Proofs

8.4.1 Proof of Proposition 1

Proposition 1

For a face center $\mathbf{x}_{i,j}$, there exists a scalar multiplier $0 \leq r_{fc} \leq 3$ and another face center $\mathbf{x}_{i,k}$ such that

$$U_i(\mathbf{x}_{i,j}) - \overline{U}_i = r_{fc}\left(\overline{U}_i - U_i(\mathbf{x}_{i,k})\right). \tag{8.43}$$

Let $\mathbf{x}_i^j,\ j = \{1,2,3,4\}$, be the four face centers of the tetrahedron Ω_i. Following convention, $\mathbf{x}_i^j$ is the face center corresponding to the face opposite the vertex $\mathbf{x}_{i,j}$. The four face centers form vertices of a tetrahedron and thus, can be mapped to the canonical tetrahedral element Ω_0 under an affine map similar to (1.34) (Figure 8.9a). Further, as the map is affine, all geometrical ratios remain constant under the transformation. Now, without loss of generality, let's assume that $\mathbf{x}_i^1$ maps to the vertex $(0,0,0)$ on Ω_0. On Ω_0, the line

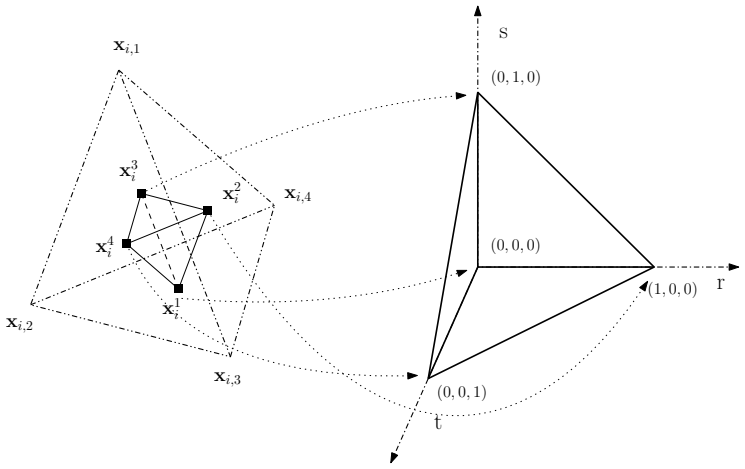

(a) Mapping tetrahedron formed by joining face centers to reference element Ω_0.

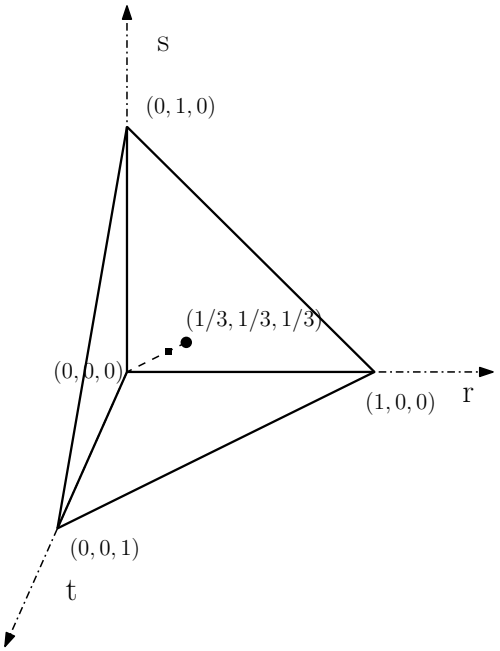

(b) Reference tetrahedral element Ω_0.

joining the vertex $(0,0,0)$ and cell centroid $(1/4,1/4,1/4)$ passes through the face center $\mathbf{r}^q = (1/3,1/3,1/3)$ (Figure 8.9b). Therefore, for a linear solution, the solution values at these points are related as

$$U_i\left(\mathbf{x}_i^1\right) + 3U_i\left(\mathbf{r}^q\right) = 4\overline{U}_i. \tag{8.44}$$

Note that as the solution is linear and $\mathbf{r}^q$ is the center of the face corresponding to the points $\mathbf{x}_i^j,\ j = \{2,3,4\}$, we can write the solution value at $\mathbf{r}^q$ as

$$U_i\left(\mathbf{r}^q\right) = \frac{1}{3}\left(U_i\left(\mathbf{x}_i^2\right) + U_i\left(\mathbf{x}_i^3\right) + U_i\left(\mathbf{x}_i^4\right)\right). \tag{8.45}$$

Plugging (8.45) into (8.44) and rearranging, we get

$$U_i\left(\mathbf{x}_i^1\right) - \overline{U}_i = \left(U_i\left(\mathbf{x}_i^2\right) - \overline{U}_i\right) + \left(U_i\left(\mathbf{x}_i^3\right) - \overline{U}_i\right) + \left(U_i\left(\mathbf{x}_i^4\right) - \overline{U}_i\right). \tag{8.46}$$

Consider the scenario where the difference $U_i\left(\mathbf{x}_i^1\right) - \overline{U}_i$ is non negative. For (8.46) to hold, atleast one of the differences on the right hand side should be non negative. Let $U_i\left(\mathbf{x}_i^k\right) - \overline{U}_i$ be the maximum of the differences on the right hand side i.e.,

$$U_i\left(\mathbf{x}_i^k\right) - \overline{U}_i = \max\left(U_i\left(\mathbf{x}_i^2\right) - \overline{U}_i, U_i\left(\mathbf{x}_i^3\right) - \overline{U}_i, U_i\left(\mathbf{x}_i^4\right) - \overline{U}_i\right) \geq 0. \tag{8.47}$$

Defining the ratio r_{fc} as

$$r_{fc} = \frac{U_i\left(\mathbf{x}_i^1\right) - \overline{U}_i}{U_i\left(\mathbf{x}_i^k\right) - \overline{U}_i}, \tag{8.48}$$

and combining (8.47) and (8.46), we get

$$\begin{aligned} &0 \leq U_i\left(\mathbf{x}_i^1\right) - \overline{U}_i \leq 3\left(U_i\left(\mathbf{x}_i^k\right) - \overline{U}_i\right) \\ &0 \leq r_{fc} \leq 3. \end{aligned} \tag{8.49}$$

Next, consider the case when the difference $U_i\left(\mathbf{x}_i^1\right) - \overline{U}_i$ is negative. Multiplying (8.46) with -1, we get

$$\overline{U}_i - U_i\left(\mathbf{x}_i^1\right) = \left(\overline{U}_i - U_i\left(\mathbf{x}_i^2\right)\right) + \left(\overline{U}_i - U_i\left(\mathbf{x}_i^3\right)\right) + \left(\overline{U}_i - U_i\left(\mathbf{x}_i^4\right)\right), \tag{8.50}$$

where the difference on the left hand side is now positive. Now, proceeding in a way similar to when the difference $U_i\left(\mathbf{x}_i^1\right) - \overline{U}_i$ is non negative, we arrive at

$$\begin{aligned} &0 \leq \overline{U}_i - U_i\left(\mathbf{x}_i^1\right) \leq 3\left(\overline{U}_i - U_i\left(\mathbf{x}_i^k\right)\right) \\ &0 \leq r_{fc} \leq 3. \end{aligned} \tag{8.51}$$

Remark 1. Note that the ratio r_{fc} is not defined if $U_i(\mathbf{x}_i^k) = \overline{U}_i$. However, in this scenario, all of the differences in (8.46) are zero and hence, (8.43) is trivially satisfied.

Finally, as the face center $\mathbf{x}_i^1$ was arbitrarily chosen, the above steps hold for any face center, thus proving the proposition (8.43).

8.4.2 Proof of Proposition 2

Proposition 2

For a quadrature point $\mathbf{x}_{i,j}$ from the three point quadrature rule on face $\delta\Omega_{i,j}$, there exists a scalar multiplier $0 \leq r_{3q} \leq 5/3$ and another quadrature point $\mathbf{x}_{i,k}$, possibly on a different face, such that

$$U_i(\mathbf{x}_{i,j}) - \overline{U}_i = r_{3q}\left(\overline{U}_i - U_i(\mathbf{x}_{i,k})\right). \tag{8.52}$$

Let $\mathbf{x}_i^{j,q}$, $j = \{1,2,3,4\}$, $q = \{1,2,3\}$, be the quadrature points on the faces of the tetrahedron Ω_i. Following convention, $\mathbf{x}_i^{j,q}$ lies on the face opposite the vertex $\mathbf{x}_{i,j}$. Ω_i can be mapped to the canonical tetrahedral element Ω_0 using the affine map (1.34). Further, as the transformation is affine, all geometrical ratios remain constant under the map. Now, without loss of generality, let's assume that $\mathbf{x}_i^{1,1}$ maps to the point $\mathbf{r}^{1,1} = (1/6, 1/6, 2/3)$ on Ω_0. We note that the above mapping depends on how the vertices of Ω_i are ordered and are mapped onto the vertices of Ω_i. Thus, depending on the choice, any quadrature point on the faces on Ω_i can be mapped to $\mathbf{r}^{1,1}$. On Ω_0, the line joining the point $\mathbf{r}^{1,1}$ and the cell centroid $(1/4, 1/4, 1/4)$ intercepts the r,s-plane at the point $\mathbf{r}^q = (3/10, 3/10, 0)$ (Figure 8.10). Therefore, for a linear solution, the solution values at these points are related as

$$3U_i\left(\mathbf{r}_i^{1,1}\right) + 5U_i\left(\mathbf{r}^q\right) = 8\overline{U}_i. \tag{8.53}$$

Note that as the solution is linear and $\mathbf{r}^q$ lies in the region enclosed by the quadrature points $\mathbf{r}^{4,q}$ on the face of Ω_0 on (r,s)-plane, we can write the value of the solution at $\mathbf{r}^q$ as

$$U_i\left(\mathbf{r}^q\right) = \gamma_{4,1}U_i\left(\mathbf{r}^{4,1}\right) + \gamma_{4,2}U_i\left(\mathbf{r}^{4,2}\right) + \left(1 - \gamma_{4,1} - \gamma_{4,2}\right)U_i\left(\mathbf{r}^{4,3}\right), \tag{8.54}$$

where $0 \leq \gamma_{4,1}, \gamma_{4,2} \leq 1$. Plugging (8.54) into (8.53) and rearranging, we get

$$U_i\left(\mathbf{r}_i^{1,1}\right) - \overline{U}_i = \frac{5}{3}\left[\gamma_{4,1}\left(U_i\left(\mathbf{r}_i^{4,1}\right) - \overline{U}_i\right) + \gamma_{4,2}\left(U_i\left(\mathbf{r}_i^{4,2}\right) - \overline{U}_i\right) + \left(1 - \gamma_{4,1} - \gamma_{4,2}\right)\left(U_i\left(\mathbf{x}_i^{4,3}\right) - \overline{U}_i\right)\right]. \tag{8.55}$$

Now, consider the case when the difference $U_i\left(\mathbf{r}_i^{1,1}\right) - \overline{U}_i$ is non negative. For (8.55) to hold, atleast one of the differences on the right hand side should be non negative. Let

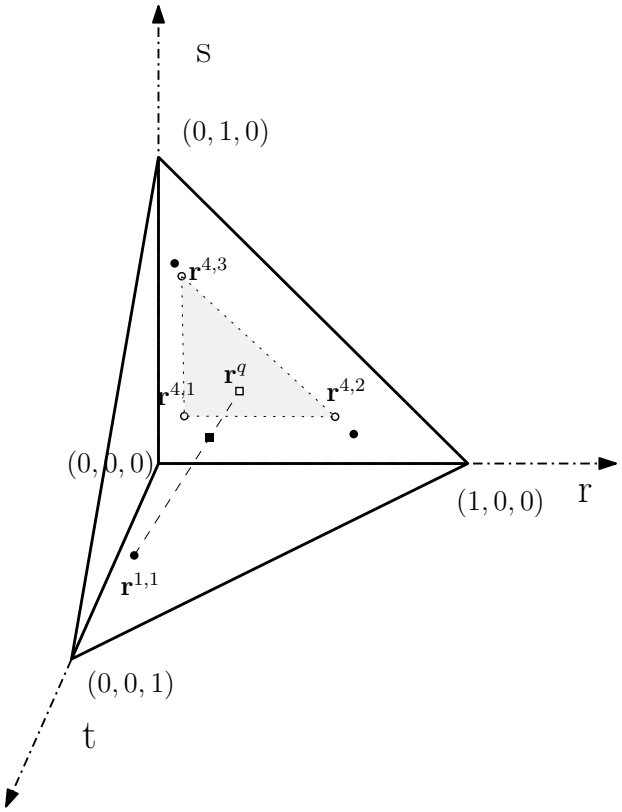

Figure 8.10: Mapping of face quadrature points by (1.34).

$U_i\left(\mathbf{r}_i^{4,k}\right) - \overline{U}_i$ be the maximum of the differences on the right hand side i.e.,

$$U_i\left(\mathbf{r}_i^{4,k}\right) - \overline{U}_i = \max\left(U_i\left(\mathbf{r}_i^{4,1}\right) - \overline{U}_i, U_i\left(\mathbf{r}_i^{4,2}\right) - \overline{U}_i, U_i\left(\mathbf{r}_i^{4,3}\right) - \overline{U}_i\right) \geq 0. \tag{8.56}$$

Defining the ratio r_{3q} as

$$r_{3q} = \frac{U_i\left(\mathbf{r}_i^{1,1}\right) - \overline{U}_i}{U_i\left(\mathbf{r}_i^{4,k}\right) - \overline{U}_i} = \frac{U_i\left(\mathbf{x}_i^{1,1}\right) - \overline{U}_i}{U_i\left(\mathbf{x}_i^{4,k}\right) - \overline{U}_i}, \tag{8.57}$$

and combining (8.56) and (8.55), we get

$$\begin{aligned} &0 \leq U_i\left(\mathbf{x}_i^{1,1}\right) - \overline{U}_i \leq \frac{5}{3}\left(U_i\left(\mathbf{x}_i^{4,k}\right) - \overline{U}_i\right) \\ &0 \leq r_{3q} \leq \frac{5}{3}. \end{aligned} \tag{8.58}$$

Next, consider the case when the difference $U_i\left(\mathbf{x}_i^{1,1}\right) - \overline{U}_i$ is negative. Multiplying (8.55) with -1, we get

$$\overline{U}_i - U_i\left(\mathbf{r}_i^{1,1}\right) = \frac{5}{3}\left[\gamma_{4,1}\left(\overline{U}_i - U_i\left(\mathbf{r}_i^{4,1}\right)\right) + \gamma_{4,2}\left(\overline{U}_i - U_i\left(\mathbf{r}_i^{4,2}\right)\right) + \left(1 - \gamma_{4,1} - \gamma_{4,2}\right)\left(\overline{U}_i - U_i\left(\mathbf{x}_i^{4,3}\right)\right)\right], \tag{8.59}$$

where the difference on the left hand side is now positive. Now, proceeding in a way similar to the case when the difference $U_i\left(\mathbf{x}_i^{1,1}\right) - \overline{U}_i$ is non negative, we arrive at

$$\begin{aligned} 0 \le \overline{U}_i - U_i\left(\mathbf{x}_i^{1,1}\right) &\le \frac{5}{3}\left(\overline{U}_i - U_i\left(\mathbf{x}_i^{4,k}\right)\right) \\ 0 \le r_{3q} &\le \frac{5}{3}. \end{aligned} \tag{8.60}$$

Remark 1. Note that the ratio r_{3q} is not defined if $U_i\left(\mathbf{x}_i^{4,k}\right) = \overline{U}_i$. However, in this scenario, all of the differences in (8.55) are zero and hence, (8.52) is trivially satisfied.

Finally, as noted before, depending on the choice of vertex ordering and mapping, quadrature point on any face can be mapped to $\mathbf{r}^{1,1}$ and thus, the above result holds for every quadrature point on the faces of Ω_i, thus proving the proposition (8.52).

Chapter 9

High-order moment limiter on tetrahedral meshes

In this chapter, we describe a high-order moment limiter for the DG method on unstructured tetrahedral meshes. The limiter can be viewed as an extension of the high-order limiter on triangular meshes [57] and an extension of the high-order moment limiter on Cartesian grids [25] to tetrahedral meshes. The limiter works by relating the solution coefficients (moments) to the directional derivatives of the numerical solution in three specially chosen directions (Figure 9.1) and limiting the derivatives by comparing them to forward and backward differences of the directional derivatives of one order less. Starting with the highest solution coefficient, the limiter is applied hierarchically thus ensuring that the solution is not overlimited. The choice of limiting directions is described in 9.1.1, while the compact reconstruction stencil and the generalized moment limiter are described in 9.1.2. Finally, we provide a brief description of the hierarchical implementation of the limiter in 9.1.4.

9.1 Limiting Algorithm

9.1.1 Directional derivatives

Consider the directions given by the vectors

$$v_1 = \frac{3}{\sqrt{11}}(1, -1/3, -1/3), \quad v_2 = \frac{2}{\sqrt{5}}(0, 1, -1/2), \quad v_3 = (0, 0, 1), \tag{9.1}$$

on Ω_0 (Figure 9.1). It was shown in [23] that the first order directional derivatives along the directions (9.1) fully uncouple linear solution coefficients, which lead to the development of a second order moment limiter on tetrahedral meshes. While higher order solution coefficients cannot be fully uncoupled, these directions significantly simplify relations between solution coefficients and solution derivatives.

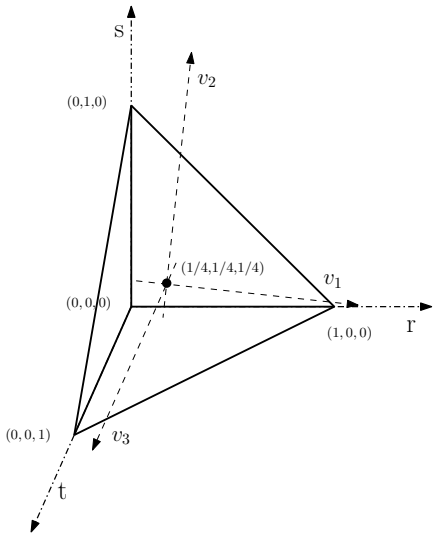

Figure 9.1: Limiting directions v_1, v_2 and v_3 on the canonical element Ω_0.

Denote jth directional derivatives along these directions by

$$D_{v_1}^g D_{v_2}^h D_{v_3}^{j-g-h} U_i(\mathbf{r}) = \frac{\partial^j}{\partial v_1^g \partial v_1^h \partial v_3^{j-g-h}} U_i(\mathbf{r}), \quad 0 \le g, h, g+h \le j, \tag{9.2}$$

where $\mathbf{r} = (r, s, t)$. Using (9.2) and (1.37), the jth directional derivatives of $U_i(\mathbf{r})$, $1 \le j \le p$, along v_1, v_2, and v_3 evaluated at the cell centroid of Ω_0, $\mathbf{r}_0 = (\frac{1}{4}, \frac{1}{4}, \frac{1}{4})$ are

$$\left(\frac{\sqrt{11}}{3}\right)^g \left(\frac{\sqrt{5}}{2}\right)^h D_{v_1}^g D_{v_2}^h D_{v_3}^{j-g-h} U_i(\mathbf{r}_0) = \sum_{l+k+m=0}^{p} \hat{U}_{i,k}^{l,m} \frac{\partial^j}{\partial v_1^g \partial v_1^h \partial v_3^{j-g-h}} \varphi_k^{l,m}(\mathbf{r}_0), \tag{9.3}$$

where $0 \le g, h, g+h \le j$. Setting $j = p$ in (9.3), we obtain the pth directional derivatives of $U_i(\mathbf{r})$ along v_1, v_2, and v_3 evaluated at $\mathbf{r}_0$

$$\left(\frac{\sqrt{11}}{3}\right)^g \left(\frac{\sqrt{5}}{2}\right)^h D_{v_1}^g D_{v_2}^h D_{v_3}^{p-g-h} U_i(\mathbf{r}_0) = \sum_{l+k+m=p} \hat{U}_{i,k}^{l,m} \frac{\partial^j}{\partial v_1^g \partial v_1^h \partial v_3^{p-g-h}} \varphi_k^{l,m}(\mathbf{r}_0), \tag{9.4}$$

where $0 \le k, l, m, g, h, g+h \le p$. Next, we use (1.34) to map the directions v_1, v_2, and v_3

defined in (9.1) from the computational to physical space and after normalization, obtain the following unit vectors

$$\mathbf{v}_{i,1} = \frac{J_i v_1}{\|J_i v_1\|}, \quad \mathbf{v}_{i,2} = \frac{J_i v_2}{\|J_i v_2\|}, \quad \mathbf{v}_{i,3} = \frac{J_i v_3}{\|J_i v_3\|}, \tag{9.5}$$

where J_i is given by (1.35). Using (1.34), (1.35), and (9.1), (9.5) can be simplified to

$$\begin{aligned} \mathbf{v}_{i,1} &= \frac{1}{h_{i,1}}\left(\mathbf{x}_{i,2} - \frac{1}{3}(\mathbf{x}_{i,1} + \mathbf{x}_{i,3} + \mathbf{x}_{i,4})\right), \quad \mathbf{v}_{i,2} = \frac{1}{h_{i,2}}\left(\mathbf{x}_{i,3} - \frac{1}{2}(\mathbf{x}_{i,1} + \mathbf{x}_{i,4})\right), \\ \mathbf{v}_{i,3} &= \frac{1}{h_{i,3}}\left(\mathbf{x}_{i,4} - \mathbf{x}_{i,1}\right), \end{aligned} \tag{9.6}$$

where $\mathbf{x}_{i,k},\ k = \{1,2,3,4\}$, are the vertices of Ω_i and

$$h_{i,1} = \left\|\mathbf{x}_{i,2} - \frac{1}{3}(\mathbf{x}_{i,1} + \mathbf{x}_{i,3} + \mathbf{x}_{i,4})\right\|, \quad h_{i,2} = \left\|\mathbf{x}_{i,3} - \frac{1}{2}(\mathbf{x}_{i,1} + \mathbf{x}_{i,4})\right\|, \quad h_{i,3} = \|\mathbf{x}_{i,4} - \mathbf{x}_{i,1}\|. \tag{9.7}$$

Using (1.34), (1.35), and (9.5), we relate directional derivatives in the physical and computational spaces

$$D^g_{\mathbf{v}_{i,1}} D^h_{\mathbf{v}_{i,2}} D^{j-g-h}_{\mathbf{v}_{i,3}} U_i(\mathbf{x}) = \left(\frac{\sqrt{11}}{3h_{i,1}}\right)^g \left(\frac{\sqrt{5}}{2h_{i,2}}\right)^h \left(\frac{1}{h_{i,3}}\right)^{j-g-h} D^q_{v_1} D^h_{v_2} D^{j-g-h}_{v_2} U_i(\mathbf{r}), \tag{9.8}$$

where $0 \le g, h, g+h \le j,\ 1 \le j \le p.$. In the next section, we derive an algorithm for limiting $D^q_{\mathbf{v}_{i,1}} D^{j-q}_{\mathbf{v}_{i,2}} U_i(\mathbf{x}_0)$.

Remark 1. The process outlined above can be used to compute directional derivatives in any given directions. The advantage of using directions (9.1) is sparsity of the transformation in (9.4).

9.1.2 Derivation of the moment limiter

For the $p+1$th order DG approximation, we start the limiting process with the highest order solution coefficients $\hat{U}^{0,0}_{i,p}, \hat{U}^{1,0}_{i,p-1}, ..., \hat{U}^{0,p}_{i,0}$. For example, consider limiting the pth order directional derivative $D^{p-2}_{\mathbf{v}_{i,1}} D^1_{\mathbf{v}_{i,2}} D^1_{\mathbf{v}_{i,3}} U_i$. We limit $D^{p-2}_{\mathbf{v}_{i,1}} D^1_{\mathbf{v}_{i,2}} D^1_{\mathbf{v}_{i,3}} U_i$ by comparing its value at the cell centroid of Ω_i to the forward and backward differences of $D^{p-2}_{\mathbf{v}_{i,1}} D^1_{\mathbf{v}_{i,2}} U$ along $\mathbf{v}_{i,3}$, $D^{p-2}_{\mathbf{v}_{i,1}} D^1_{\mathbf{v}_{i,3}} U$ along $\mathbf{v}_{i,2}$, and $D^{p-3}_{\mathbf{v}_{i,1}} D^1_{\mathbf{v}_{i,2}} D^1_{\mathbf{v}_{i,3}} U$ along $\mathbf{v}_{i,1}$, i.e., the derivatives of one degree less along $\mathbf{v}_{i,3}$, $\mathbf{v}_{i,2}$ and $\mathbf{v}_{i,1}$, respectively.

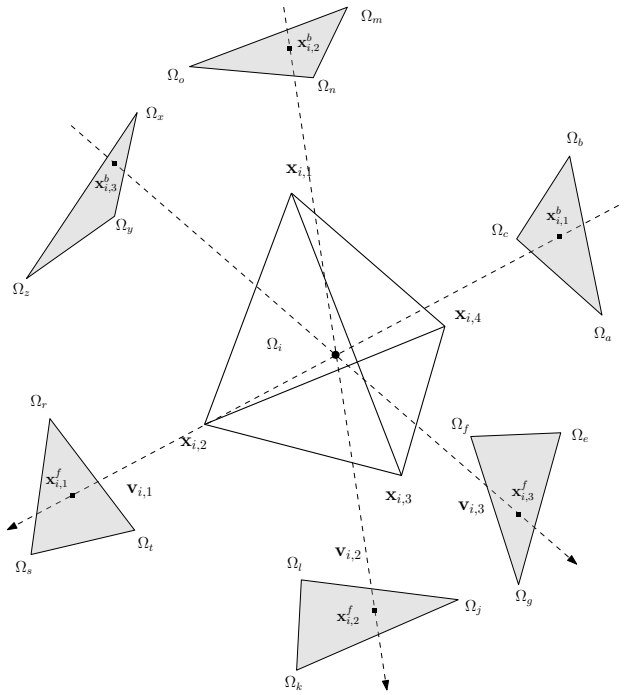

Figure 9.2: The reconstruction stencil for Ω_i. Limiting directions $\mathbf{v}_{i,1}$, $\mathbf{v}_{i,2}$, and $\mathbf{v}_{i,3}$ are shown as arrows. Backward and forward interpolation points are shown as solid squares. Linear interpolation of directional derivatives at the interpolation points is performed over the shaded triangular regions.

The forward and backward differences are computed from the forward ($\mathbf{x}^f_{i,1}$, $\mathbf{x}^f_{i,2}$, and $\mathbf{x}^f_{i,3}$) and backward ($\mathbf{x}^b_{i,1}$, $\mathbf{x}^b_{i,2}$, and $\mathbf{x}^b_{i,3}$) interpolation points (Figure 9.2, solid squares) to the cell centroid (Figure 9.2, solid circle). To find the interpolation points, we form a polygon by joining the cell centroids of the convex hull of the neighboring elements that share a vertex with Ω_i. Next, we define three lines parallel to $\mathbf{v}_{i,1}$, $\mathbf{v}_{i,2}$, and $\mathbf{v}_{i,3}$ that pass through the centroid of Ω_i. The interpolation points $\mathbf{x}^f_{i,k}$, $\mathbf{x}^b_{i,k}$, $k = \{1, 2, 3\}$, are then the points of intersection of these lines and the faces of the polygon.

Let us consider limiting $D^{p-2}_{\mathbf{v}_{i,1}} D^1_{\mathbf{v}_{i,2}} D^1_{\mathbf{v}_{i,3}} U_i$ in the direction $\mathbf{v}_{i,2}$. In order to find the values of the $(p-1)$th order derivative $D^{p-2}_{\mathbf{v}_{i,1}} D^1_{\mathbf{v}_{i,3}} U$ at the interpolation points, we first compute the $(p-1)$th directional derivative $D^{p-2}_{\mathbf{v}_{i,1}} D^1_{\mathbf{v}_{i,3}} U_f(\mathbf{x}_{f,0})$, $f = \{j, k, l, m, n, o\}$ at the cell centroids of the neighbouring elements Ω_j, Ω_k, Ω_l, Ω_m, Ω_n, and Ω_o (Figure 9.3b). For example, consider element Ω_m. To obtain directional derivatives along $\mathbf{v}_{i,1}$, $\mathbf{v}_{i,2}$, and $\mathbf{v}_{i,3}$ on Ω_m, we express the limiting directions on Ω_i as linear combinations of limiting directions

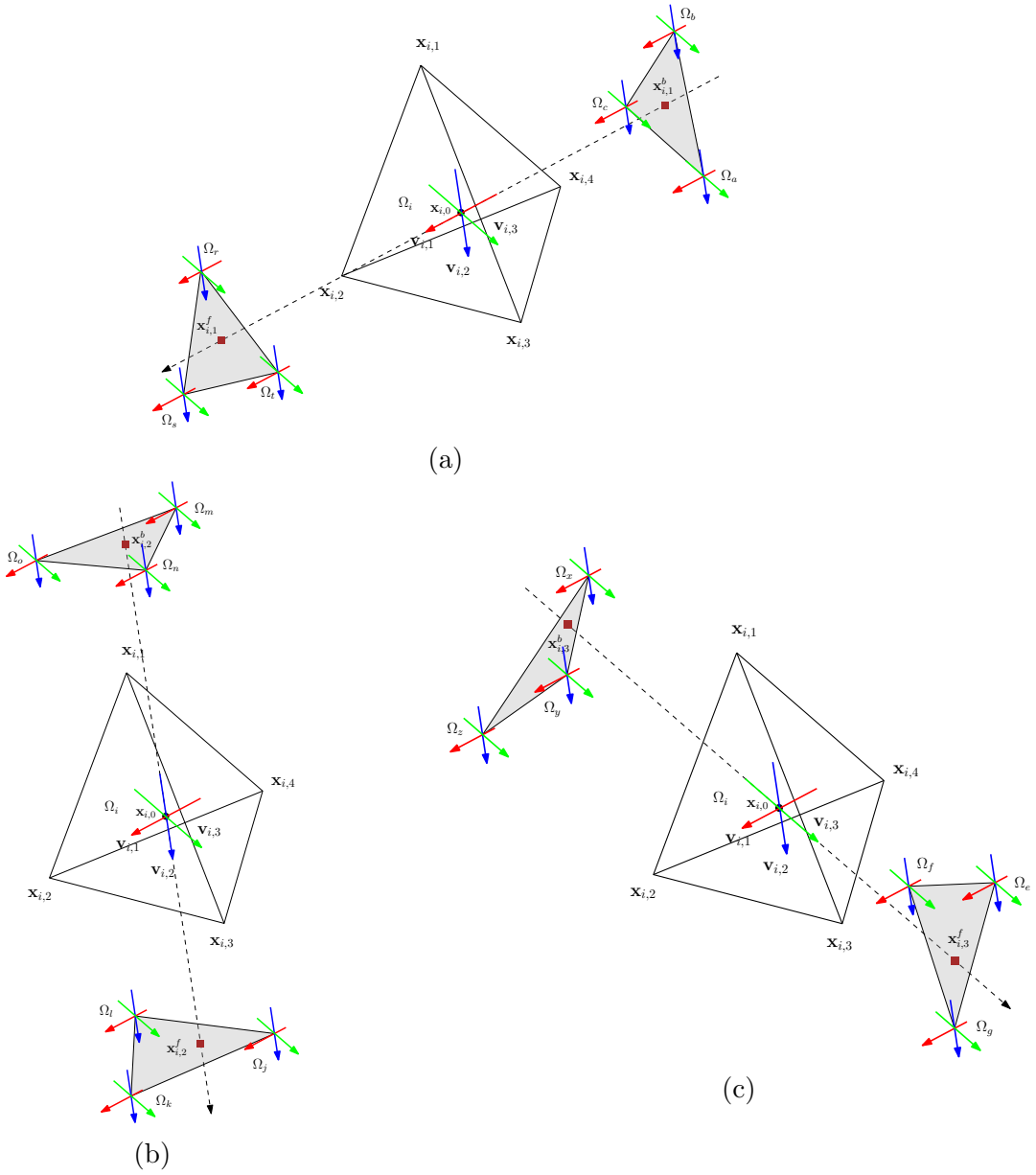

Figure 9.3: (A) Limiting stencil along $\mathbf{v}_{i,1}$, (B) Limiting stencil along $\mathbf{v}_{i,2}$, (C) Limiting stencil along $\mathbf{v}_{i,3}$.

$\mathbf{v}_{m,1}$, $\mathbf{v}_{m,2}$, and $\mathbf{v}_{m,3}$ on Ω_m

$$\begin{aligned}\mathbf{v}_{i,1} &= \alpha^1_{m,1}\mathbf{v}_{m,1} + \alpha^1_{m,2}\mathbf{v}_{m,2} + \alpha^1_{m,3}\mathbf{v}_{m,3}, \quad \mathbf{v}_{i,2} = \alpha^2_{m,1}\mathbf{v}_{m,1} + \alpha^2_{m,2}\mathbf{v}_{m,2} + \alpha^2_{m,3}\mathbf{v}_{m,3}, \\ \mathbf{v}_{i,3} &= \alpha^3_{m,1}\mathbf{v}_{m,1} + \alpha^3_{m,2}\mathbf{v}_{m,2} + \alpha^3_{m,3}\mathbf{v}_{m,3},\end{aligned} \tag{9.9}$$

for some scaling coefficients α. Using (9.9) and (9.8), the $(p-1)$th directional derivative $D^{p-2}_{\mathbf{v}_{i,1}} D^1_{\mathbf{v}_{i,3}} U_m$, evaluated at the cell centroid $\mathbf{x}_{m,0}$ of Ω_m, is

$$
\begin{aligned}
D^{p-2}_{\mathbf{v}_{i,1}} D^1_{\mathbf{v}_{i,3}} U_m(\mathbf{x}_{m,0}) &= \left(\alpha^1_{m,1} D_{\mathbf{v}_{m,1}} + \alpha^1_{m,2} D_{\mathbf{v}_{m,2}} + \alpha^1_{m,3} D_{\mathbf{v}_{m,3}}\right)^{p-2} \left(\alpha^3_{m,1} D_{\mathbf{v}_{m,1}} + \alpha^3_{m,2} D_{\mathbf{v}_{m,2}} \right. \\
&\left. + \alpha^3_{m,3} D_{\mathbf{v}_{m,3}}\right) U_m(\mathbf{x}_{m,0}) \qquad (9.10) \\
&= \left(\alpha^1_{m,1} \frac{\sqrt{11}}{3h_{m,1}} D_{v_1} + \alpha^1_{m,2} \frac{\sqrt{5}}{2h_{m,2}} D_{v_2} + \alpha^1_{m,3} \frac{1}{h_{m,3}} D_{v_3}\right)^{p-2} \left(\alpha^3_{m,1} \frac{\sqrt{11}}{3h_{m,1}} D_{v_1} \right. \\
&\left. + \alpha^3_{m,2} \frac{\sqrt{5}}{2h_{m,2}} D_{v_2} + \alpha^3_{m,3} \frac{1}{h_{m,3}} D_{v_3}\right) U_m(\mathbf{r}_0). \qquad (9.11)
\end{aligned}
$$

Similarly, we compute the $(p-1)$th directional derivatives $D^{p-2}_{\mathbf{v}_{i,1}} D^1_{\mathbf{v}_{i,3}} U_t(\mathbf{x}_{t,0})$, $t = \{j,k,l,n,o\}$, at the centroids of Ω_j, Ω_k, Ω_l, Ω_n, and Ω_o (Figure 9.3b). We use these values to linearly interpolate the $(p-1)$th directional derivatives $D^{p-1}_{\mathbf{v}_{i,1}} D^1_{\mathbf{v}_{i,3}} U^b_{i,2}$ and $D^{p-1}_{\mathbf{v}_{i,1}} D^1_{\mathbf{v}_{i,3}} U^f_{i,2}$ at the backward and forward interpolation points $\mathbf{x}^b_{i,2}$ and $\mathbf{x}^f_{i,2}$ as

$$\begin{aligned} D^{p-2}_{\mathbf{v}_{i,1}} D^1_{\mathbf{v}_{i,3}} U^f_{i,2} &= \beta^f_{i,2,1} D^{p-2}_{\mathbf{v}_{i,1}} D^1_{\mathbf{v}_{i,3}} U_j(\mathbf{x}_{j,0}) + \beta^f_{i,2,2} D^{p-2}_{\mathbf{v}_{i,1}} D^1_{\mathbf{v}_{i,3}} U_k(\mathbf{x}_{k,0}) \\ &\quad + (1 - \beta^f_{i,2,1} - \beta^f_{i,2,2}) D^{p-2}_{\mathbf{v}_{i,1}} D^1_{\mathbf{v}_{i,3}} U_l(\mathbf{x}_{l,0}), \\ D^{p-2}_{\mathbf{v}_{i,1}} D^1_{\mathbf{v}_{i,3}} U^b_{i,2} &= \beta^b_{i,2,1} D^{p-2}_{\mathbf{v}_{i,1}} D^1_{\mathbf{v}_{i,3}} U_m(\mathbf{x}_{m,0}) + \beta^b_{i,2,2} D^{p-2}_{\mathbf{v}_{i,1}} D^1_{\mathbf{v}_{i,3}} U_n(\mathbf{x}_{n,0}) \\ &\quad + (1 - \beta^b_{i,2,1} - \beta^b_{i,2,2}) D^{p-2}_{\mathbf{v}_{i,1}} D^1_{\mathbf{v}_{i,3}} U_o(\mathbf{x}_{o,0}), \end{aligned} \tag{9.12}$$

where $0 \le \beta^b_{i,2,1}, \beta^b_{i,2,2} \le 1$ and $0 \le \beta^f_{i,2,1}, \beta^f_{i,2,2} \le 1$ are the backward and forward interpolation weights for the limiting stencil in Figure 9.3b. Finally, the limited pth order directional derivative $D^{p-2}_{\mathbf{v}_{i,1}} D^1_{\mathbf{v}_{i,2}} D^1_{\mathbf{v}_{i,3}} U_i$ is obtained by comparing its value to the forward and backward differences in the $(p-1)$th directional derivatives multiplied by the scaling parameters $l^f_{i,2}$ and $l^b_{i,2}$

$$\begin{aligned} &D^{p-2}_{\mathbf{v}_{i,1}} D^1_{\mathbf{v}_{i,2}} D^1_{\mathbf{v}_{i,3}} U_i(\mathbf{x}_{i,0}) \leftarrow \text{minmod}\left(D^{p-2}_{\mathbf{v}_{i,1}} D^1_{\mathbf{v}_{i,2}} D^1_{\mathbf{v}_{i,3}} U_i(\mathbf{x}_{i,0}), \right. \\ &\left. l^f_{i,2} \frac{D^{p-2}_{\mathbf{v}_{i,1}} D^1_{\mathbf{v}_{i,3}} U^f_{i,2} - D^{p-2}_{\mathbf{v}_{i,1}} D^1_{\mathbf{v}_{i,3}} U_i(\mathbf{x}_{i,0})}{\left\| \mathbf{x}^f_{i,2} - \mathbf{x}_{i,0} \right\|}, l^b_{i,2} \frac{D^{p-2}_{\mathbf{v}_{i,1}} D^1_{\mathbf{v}_{i,3}} U_i(\mathbf{x}_{i,0}) - D^{p-2}_{\mathbf{v}_{i,1}} D^1_{\mathbf{v}_{i,3}} U^b_{i,2}}{\left\| \mathbf{x}^b_{i,2} - \mathbf{x}_{i,0} \right\|} \right), \end{aligned} \tag{9.13}$$

where the minmod function is

$$\text{minmod}(a,b,c) = \begin{cases} sign(a) \cdot min(|a|,|b|,|c|), & \text{if } sign(a) = sign(b) = sign(c), \\ 0, & \text{otherwise.} \end{cases} \tag{9.14}$$

Next, we limit $D^{p-2}_{\mathbf{v}_{i,1}} D^1_{\mathbf{v}_{i,2}} D^1_{\mathbf{v}_{i,3}} U_i$ along $\mathbf{v}_{i,3}$. We compute the $(p-1)$th directional derivative $D^{p-2}_{\mathbf{v}_{i,1}} D^1_{\mathbf{v}_{i,2}} U$ at the cell centroids of Ω_e, Ω_f, Ω_g, Ω_x, Ω_y and Ω_z (Figure 9.3c), e.g., $D^{p-2}_{\mathbf{v}_{i,1}} D^1_{\mathbf{v}_{i,2}} U_e$, evaluated at $\mathbf{x}_{e,0}$, is

$$\begin{aligned} D^{p-2}_{\mathbf{v}_{i,1}} D^1_{\mathbf{v}_{i,2}} U_e(\mathbf{x}_{e,0}) &= \left(\alpha^1_{e,1} D_{\mathbf{v}_{e,1}} + \alpha^1_{e,2} D_{\mathbf{v}_{e,2}} + \alpha^1_{e,3} D_{\mathbf{v}_{e,3}} \right)^{p-2} \left(\alpha^2_{e,1} D_{\mathbf{v}_{e,1}} + \alpha^2_{e,2} D_{\mathbf{v}_{e,2}} \right. \\ &\quad \left. + \alpha^2_{e,3} D_{\mathbf{v}_{e,3}} \right) U_e(\mathbf{x}_{e,0}) \\ &= \left(\alpha^1_{e,1} \frac{\sqrt{11}}{3h_{e,1}} D_{v_1} + \alpha^1_{e,2} \frac{\sqrt{5}}{2h_{e,2}} D_{v_2} + \alpha^1_{e,3} \frac{1}{h_{e,3}} D_{v_3} \right)^{p-2} \left(\alpha^2_{e,1} \frac{\sqrt{11}}{3h_{e,1}} D_{v_1} \right. \\ &\quad \left. + \alpha^2_{e,2} \frac{\sqrt{5}}{2h_{e,2}} D_{v_2} + \alpha^2_{e,3} \frac{1}{h_{e,3}} D_{v_3} \right) U_e(\mathbf{r}_0). \end{aligned} \tag{9.15}$$

Then, we linearly interpolate $D^{p-2}_{\mathbf{v}_{i,1}} D^1_{\mathbf{v}_{i,2}} U$ at the forward and backward interpolation points $\mathbf{x}^f_{i,3}$ and $\mathbf{x}^b_{i,3}$ using the computed values at the cell centroids

$$\begin{aligned} D^{p-2}_{\mathbf{v}_{i,1}} D^1_{\mathbf{v}_{i,2}} U^f_{i,3} &= \beta^f_{i,3,1} D^{p-2}_{\mathbf{v}_{i,1}} D^1_{\mathbf{v}_{i,2}} U_e(\mathbf{x}_{e,0}) + \beta^f_{i,3,2} D^{p-2}_{\mathbf{v}_{i,1}} D^1_{\mathbf{v}_{i,2}} U_f(\mathbf{x}_{f,0}) \\ &\quad + (1 - \beta^f_{i,3,1} - \beta^f_{i,3,2}) D^{p-2}_{\mathbf{v}_{i,1}} D^1_{\mathbf{v}_{i,2}} U_g(\mathbf{x}_{g,0}), \\ D^{p-2}_{\mathbf{v}_{i,1}} D^1_{\mathbf{v}_{i,2}} U^b_{i,3} &= \beta^b_{i,3,1} D^{p-2}_{\mathbf{v}_{i,1}} D^1_{\mathbf{v}_{i,2}} U_x(\mathbf{x}_{x,0}) + \beta^b_{i,3,2} D^{p-2}_{\mathbf{v}_{i,1}} D^1_{\mathbf{v}_{i,2}} U_y(\mathbf{x}_{y,0}) \\ &\quad + (1 - \beta^b_{i,3,1} - \beta^b_{i,3,2}) D^{p-2}_{\mathbf{v}_{i,1}} D^1_{\mathbf{v}_{i,2}} U_z(\mathbf{x}_{z,0}), \end{aligned} \tag{9.16}$$

where $0 \leq \beta^b_{i,3,1}, \beta^b_{i,3,2} \leq 1$ and $0 \leq \beta^f_{i,3,1}, \beta^f_{i,3,2} \leq 1$. Finally, we limit $D^{p-2}_{\mathbf{v}_{i,1}} D^1_{\mathbf{v}_{i,2}} D^1_{\mathbf{v}_{i,3}} U_i$ by comparing it to the forward and backward differences of $D^{p-2}_{\mathbf{v}_{i,1}} D^1_{\mathbf{v}_{i,2}} U$ scaled by the parameters $l^f_{i,3}$ and $l^b_{i,3}$

$$\begin{aligned} &D^{p-2}_{\mathbf{v}_{i,1}} D^1_{\mathbf{v}_{i,2}} D^1_{\mathbf{v}_{i,3}} U_i(\mathbf{x}_{i,0}) \leftarrow \operatorname{minmod}\Big(D^{p-2}_{\mathbf{v}_{i,1}} D^1_{\mathbf{v}_{i,2}} D^1_{\mathbf{v}_{i,3}} U_i(\mathbf{x}_{i,0}), \\ &l^f_{i,3} \frac{D^{p-2}_{\mathbf{v}_{i,1}} D^1_{\mathbf{v}_{i,2}} U^f_{i,3} - D^{p-2}_{\mathbf{v}_{i,1}} D^1_{\mathbf{v}_{i,2}} U_i(\mathbf{x}_{i,0})}{\left\| \mathbf{x}^f_{i,3} - \mathbf{x}_{i,0} \right\|}, l^b_{i,3} \frac{D^{p-2}_{\mathbf{v}_{i,1}} D^1_{\mathbf{v}_{i,2}} U_i(\mathbf{x}_{i,0}) - D^{p-2}_{\mathbf{v}_{i,1}} D^1_{\mathbf{v}_{i,2}} U^b_{i,3}}{\left\| \mathbf{x}^b_{i,3} - \mathbf{x}_{i,0} \right\|} \Bigg). \end{aligned} \tag{9.17}$$

Finally, we limit $D^{p-2}_{\mathbf{v}_{i,1}} D^1_{\mathbf{v}_{i,2}} D^1_{\mathbf{v}_{i,3}} U_i$ along $\mathbf{v}_{i,1}$. We compute the $(p-1)$th directional derivative $D^{p-3}_{\mathbf{v}_{i,1}} D^1_{\mathbf{v}_{i,2}} D^1_{\mathbf{v}_{i,3}} U$ at the cell centroids of Ω_a, Ω_b, Ω_c, Ω_r, Ω_s, and Ω_t (Figure 9.3a), e.g., $D^{p-3}_{\mathbf{v}_{i,1}} D^1_{\mathbf{v}_{i,2}} D^1_{\mathbf{v}_{i,3}} U_s$, evaluated at $\mathbf{x}_{s,0}$, is

$$\begin{aligned} D^{p-3}_{\mathbf{v}_{i,1}} D^1_{\mathbf{v}_{i,2}} D^1_{\mathbf{v}_{i,3}} U_s(\mathbf{x}_{s,0}) &= \left(\alpha^1_{s,1} D_{\mathbf{v}_{s,1}} + \alpha^1_{s,2} D_{\mathbf{v}_{s,2}} + \alpha^1_{s,3} D_{\mathbf{v}_{s,3}} \right)^{p-3} \left(\alpha^2_{s,1} D_{\mathbf{v}_{s,1}} + \alpha^2_{s,2} D_{\mathbf{v}_{s,2}} + \right. \\ &\quad \left. \alpha^2_{s,3} D_{\mathbf{v}_{s,3}} \right) \left(\alpha^3_{s,1} D_{\mathbf{v}_{s,1}} + \alpha^3_{s,2} D_{\mathbf{v}_{s,2}} + \alpha^3_{s,3} D_{\mathbf{v}_{s,3}} \right) U_s(\mathbf{x}_{s,0}) \\ &= \left(\alpha^1_{s,1} \frac{\sqrt{11}}{3h_{s,1}} D_{v_1} + \alpha^1_{s,2} \frac{\sqrt{5}}{2h_{s,2}} D_{v_2} + \alpha^1_{s,3} \frac{1}{h_{s,3}} D_{v_3} \right)^{p-3} \\ &\quad \left(\alpha^2_{s,1} \frac{\sqrt{11}}{3h_{s,1}} D_{v_1} + \alpha^2_{s,2} \frac{\sqrt{5}}{2h_{s,2}} D_{v_2} + \alpha^2_{s,3} \frac{1}{h_{s,3}} D_{v_3} \right) \\ &\quad \left(\alpha^3_{s,1} \frac{\sqrt{11}}{3h_{s,1}} D_{v_1} + \alpha^3_{s,2} \frac{\sqrt{5}}{2h_{s,2}} D_{v_2} + \alpha^3_{s,3} \frac{1}{h_{s,3}} D_{v_3} \right) U_s(\mathbf{r}_0). \end{aligned} \tag{9.18}$$

Then, we linearly interpolate $D^{p-3}_{\mathbf{v}_{i,1}} D^1_{\mathbf{v}_{i,2}} D^1_{\mathbf{v}_{i,3}} U$ at the forward and backward interpolation

points $\mathbf{x}_{i,1}^f$ and $\mathbf{x}_{i,1}^b$ using the values at the cell centroids

$$\begin{aligned} D^{p-3}_{\mathbf{v}_{i,1}} D^1_{\mathbf{v}_{i,2}} D^1_{\mathbf{v}_{i,3}} U^f_{i,1} &= \beta^f_{i,1,1} D^{p-3}_{\mathbf{v}_{i,1}} D^1_{\mathbf{v}_{i,2}} D^1_{\mathbf{v}_{i,3}} U_r(\mathbf{x}_{r,0}) + \beta^f_{i,1,2} D^{p-3}_{\mathbf{v}_{i,1}} D^1_{\mathbf{v}_{i,2}} D^1_{\mathbf{v}_{i,3}} U_s(\mathbf{x}_{s,0}) \\ &\quad + (1 - \beta^f_{i,1,1} - \beta^f_{i,1,2}) D^{p-3}_{\mathbf{v}_{i,1}} D^1_{\mathbf{v}_{i,2}} D^1_{\mathbf{v}_{i,3}} U_t(\mathbf{x}_{t,0}), \\ D^{p-3}_{\mathbf{v}_{i,1}} D^1_{\mathbf{v}_{i,2}} D^1_{\mathbf{v}_{i,3}} U^b_{i,1} &= \beta^b_{i,1,1} D^{p-3}_{\mathbf{v}_{i,1}} D^1_{\mathbf{v}_{i,2}} D^1_{\mathbf{v}_{i,3}} U_a(\mathbf{x}_{a,0}) + \beta^b_{i,1,2} D^{p-3}_{\mathbf{v}_{i,1}} D^1_{\mathbf{v}_{i,2}} D^1_{\mathbf{v}_{i,3}} U_b(\mathbf{x}_{b,0}) \\ &\quad + (1 - \beta^b_{i,1,1} - \beta^b_{i,1,2}) D^{p-3}_{\mathbf{v}_{i,1}} D^1_{\mathbf{v}_{i,2}} D^1_{\mathbf{v}_{i,3}} U_c(\mathbf{x}_{c,0}), \end{aligned} \tag{9.19}$$

where $0 \leq \beta^b_{i,1,1}, \beta^b_{i,1,2} \leq 1$ and $0 \leq \beta^f_{i,1,1}, \beta^f_{i,1,2} \leq 1$. Finally, we limit $D^{p-1}_{\mathbf{v}_{i,1}} D^1_{\mathbf{v}_{i,2}} D^1_{\mathbf{v}_{i,3}} U_i$ by comparing it to the forward and backward differences of $D^{p-3}_{\mathbf{v}_{i,1}} D^1_{\mathbf{v}_{i,2}} D^1_{\mathbf{v}_{i,3}} U$ scaled by the parameters $l^f_{i,1}$ and $l^b_{i,1}$

$$\begin{aligned} D^{p-2}_{\mathbf{v}_{i,1}} D^1_{\mathbf{v}_{i,2}} D^1_{\mathbf{v}_{i,3}} U_i(\mathbf{x}_{i,0}) &\leftarrow \operatorname{minmod}\left(D^{p-2}_{\mathbf{v}_{i,1}} D^1_{\mathbf{v}_{i,2}} D^1_{\mathbf{v}_{i,3}} U_i(\mathbf{x}_{i,0}), D^+, D^-\right), \\ D^+ &= l^f_{i,1} \frac{D^{p-3}_{\mathbf{v}_{i,1}} D^1_{\mathbf{v}_{i,2}} D^1_{\mathbf{v}_{i,3}} U^f_{i,1} - D^{p-3}_{\mathbf{v}_{i,1}} D^1_{\mathbf{v}_{i,2}} D^1_{\mathbf{v}_{i,3}} U_i(\mathbf{x}_{i,0})}{\left\|\mathbf{x}^f_{i,1} - \mathbf{x}_{i,0}\right\|}, \\ D^- &= l^b_{i,1} \frac{D^{p-3}_{\mathbf{v}_{i,1}} D^1_{\mathbf{v}_{i,2}} D^1_{\mathbf{v}_{i,3}} U_i(\mathbf{x}_{i,0}) - D^{p-3}_{\mathbf{v}_{i,1}} D^1_{\mathbf{v}_{i,2}} D^1_{\mathbf{v}_{i,3}} U^b_{i,1}}{\left\|\mathbf{x}^b_{i,1} - \mathbf{x}_{i,0}\right\|}. \end{aligned} \tag{9.20}$$

The admissible range for the scaling parameters $l^f_{i,k}$ and $l^b_{i,k}$, $k = \{1, 2, 3\}$, is

$$\begin{aligned} 1 \leq l^f_{i,3} \leq \gamma^f_{i,3}, \quad 1 \leq l^b_{i,3} \leq \gamma^b_{i,3}, \\ 1 \leq l^f_{i,2} \leq \gamma^f_{i,2}, \quad 1 \leq l^b_{i,2} \leq \gamma^b_{i,2}, \\ 1 \leq l^f_{i,1} \leq \gamma^f_{i,1}, \quad 1 \leq l^b_{i,1} \leq \gamma^b_{i,1}, \end{aligned} \tag{9.21}$$

which is equivalent to the range for the scaling parameters used on Cartesian grids in [25] and the scaling parameters used on unstructured two-dimensional mesh in [57, 60]. The geometric parameters γ_i in (9.21) are

$$\begin{aligned} \gamma^f_{i,1} &= \frac{\left\|\mathbf{x}^f_{i,1} - \mathbf{x}_{i,0}\right\|}{h_{i,1}}, \quad \gamma^b_{i,1} = \frac{\left\|\mathbf{x}^b_{i,1} - \mathbf{x}_{i,0}\right\|}{h_{i,1}}, \\ \gamma^f_{i,2} &= \frac{\left\|\mathbf{x}^f_{i,2} - \mathbf{x}_{i,0}\right\|}{h_{i,2}}, \quad \gamma^b_{i,2} = \frac{\left\|\mathbf{x}^b_{i,2} - \mathbf{x}_{i,0}\right\|}{h_{i,2}}, \\ \gamma^f_{i,3} &= \frac{\left\|\mathbf{x}^f_{i,3} - \mathbf{x}_{i,0}\right\|}{h_{i,3}}, \quad \gamma^b_{i,3} = \frac{\left\|\mathbf{x}^b_{i,3} - \mathbf{x}_{i,0}\right\|}{h_{i,3}}, \end{aligned} \tag{9.22}$$

where $h_{i,1}$, $h_{i,2}$, and $h_{i,3}$ are given in (9.7). In all experiments in Section 9.2 we choose the

least restrictive limiter, i.e., the right hand side of the intervals in (9.21).

Following a similar strategy, we limit every pth order directional derivative along $\mathbf{v}_{i,1}$, $\mathbf{v}_{i,2}$, and $\mathbf{v}_{i,3}$. Substituting these limited directional derivatives into (9.4), we obtain the limited pth order moments. If all pth order directional derivatives are modified by the limiter, we repeat the process for the $(p-1)$th order moments $\hat{U}^{0,0}_{i,p-1}, \hat{U}^{0,1}_{i,p-2}, \cdots, \hat{U}^{0,p-1}_{i,0}$. We limit the $(p-1)$th directional derivatives along $\mathbf{v}_{i,1}$, $\mathbf{v}_{i,2}$, and $\mathbf{v}_{i,3}$ by comparing them to the forward and backward differences in $(p-2)$th directional derivatives. We find modified values of $(p-1)$th order moments by substituting the limited $(p-1)$th directional derivatives into a system of equations similar to (9.4), obtained by ignoring the contribution of pth order moments in (9.3). The process continues until we reach either a set of kth order directional derivatives that are not modified or the zeroth order moment.

To further elaborate the limiting technique discussed above, we give a brief description of the implementation of the third order limiter in the next section.

9.1.3 Third order limiter

The third order DG approximation on element Ω_i, written as a linear combination of the Dubiner basis (1.36), is

$$U_i(r,s,t) = \sum_{l+k=0}^{2} \hat{U}^{l,m}_{i,k} \varphi^{l,m}_k(r,s,t). \tag{9.23}$$

The quadratic basis functions are given by

$$\begin{aligned}
\varphi^{0,0}_2(r,s,t) &= \sqrt{\frac{105}{128}} 8 \left(3\left(2t+s+r-1\right)^2 - \left(1-s-r\right)^2\right), \\
\varphi^{2,0}_0(r,s,t) &= \sqrt{\frac{21}{8}} \left(12\left(1-r\right)^2 + 48\left(s+r-1\right)\left(1-r\right) + 40\left(s+r-1\right)^2\right), \\
\varphi^{0,2}_0(r,s,t) &= \sqrt{14}\left(6 + 20\left(r-1\right) + 15\left(r-1\right)^2\right), \\
\varphi^{1,0}_1(r,s,t) &= \sqrt{\frac{63}{32}} 8 \left(2t+s+r-1\right)\left(4\left(1-r\right) + 5\left(s+r-1\right)\right), \\
\varphi^{0,1}_1(r,s,t) &= \sqrt{\frac{21}{4}} 4 \left(2t+s+r-1\right)\left(5 + 6\left(r-1\right)\right), \\
\varphi^{1,1}_0(r,s,t) &= \sqrt{72}\left(2\left(1-r\right) + 3\left(s+r-1\right)\right)\left(5 + 6\left(r-1\right)\right),
\end{aligned} \tag{9.24}$$

and the linear and constant basis functions are given by

$$\begin{aligned}
\varphi_0^{0,0} &= \sqrt{6} \\
\varphi_1^{0,0} &= -\sqrt{10} + 4\sqrt{10}r \\
\varphi_0^{1,0} &= -2\sqrt{5} + 2\sqrt{5}r + 6\sqrt{5}s \\
\varphi_0^{0,1} &= -2\sqrt{15} + 2\sqrt{15}r + 2\sqrt{15}s + 4\sqrt{15}t.
\end{aligned} \tag{9.25}$$

Using (9.4), the second order moments of U_i can be expressed in terms of the second order directional derivatives along $\mathbf{v}_{i,1}$, $\mathbf{v}_{i,2}$, and $\mathbf{v}_{i,3}$ as

$$\begin{pmatrix}
h_{i,3}^2 D_{\mathbf{v}_{i,3}}^2 U_i(\mathbf{x}_{i,0}) \\
h_{i,3}h_{i,2} D_{\mathbf{v}_{i,3}} D_{\mathbf{v}_{i,2}} U_i(\mathbf{x}_{i,0}) \\
h_{i,2}^2 D_{\mathbf{v}_{i,2}}^2 U_i(\mathbf{x}_{i,0}) \\
h_{i,3}h_{i,1} D_{\mathbf{v}_{i,3}} D_{\mathbf{v}_{i,1}} U_i(\mathbf{x}_{i,0}) \\
h_{i,1}^2 D_{\mathbf{v}_{i,1}}^2 U_i(\mathbf{x}_{i,0}) \\
h_{i,2}h_{i,1} D_{\mathbf{v}_{i,2}} D_{\mathbf{v}_{i,1}} U_i(\mathbf{x}_{i,0})
\end{pmatrix} = \mathcal{A} \begin{pmatrix}
\hat{U}_{i,2}^{0,0} \\
\hat{U}_{i,1}^{1,0} \\
\hat{U}_{i,0}^{2,0} \\
\hat{U}_{i,1}^{0,1} \\
\hat{U}_{i,0}^{0,2} \\
\hat{U}_{i,0}^{1,1}
\end{pmatrix}, \tag{9.26}$$

where the matrix $\mathcal{A}$ is given by

$$\begin{bmatrix}
192\sqrt{\frac{105}{128}} & 0 & 0 & 0 & 0 & 0 \\
0 & 80\sqrt{\frac{63}{32}} & 0 & 0 & 0 & 0 \\
-16\sqrt{\frac{105}{128}} & 0 & 80\sqrt{\frac{21}{8}} & 0 & 0 & 0 \\
0 & -\frac{32}{3}\sqrt{\frac{63}{32}} & 0 & 48\sqrt{\frac{21}{4}} & 0 & 0 \\
-\frac{64}{9}\sqrt{\frac{105}{128}} & 0 & -\frac{40}{9}\sqrt{\frac{21}{8}} & 0 & 30\sqrt{14} & 0 \\
-\frac{32}{3}\sqrt{\frac{105}{128}} & 0 & \frac{16}{3}\sqrt{\frac{21}{8}} & 0 & 0 & 36\sqrt{7}
\end{bmatrix}. \tag{9.27}$$

To limit the second order solution coefficients, we start by computing the first order directional derivatives along $\mathbf{v}_{i,1}$, $\mathbf{v}_{i,2}$, and $\mathbf{v}_{i,3}$ at the cell centroids of the elements involved in the limiting stencil (Figures 9.2 and 9.3). For example, to limit $D_{\mathbf{v}_{i,2}}^2 U_i$, $D_{\mathbf{v}_{i,2}} D_{\mathbf{v}_{i,1}} U_i$, and $D_{\mathbf{v}_{i,2}} D_{\mathbf{v}_{i,3}} U_i$, we need to compute directional derivatives along $\mathbf{v}_{i,1}$, $\mathbf{v}_{i,2}$, and $\mathbf{v}_{i,3}$ at the cell

centroids of Ω_j, Ω_k, Ω_l, Ω_m, Ω_n, and Ω_o (Figure 9.3b). Consider element Ω_n. Using (9.3), the first order directional derivatives along $\mathbf{v}_{n,1}$, $\mathbf{v}_{n,2}$, and $\mathbf{v}_{n,3}$ at the cell centroid $\mathbf{x}_{n,0}$ are

$$\begin{aligned}
h_{n,1}D^1_{\mathbf{v}_{n,1}}U_n(\mathbf{x}_{n,0}) &= 4\sqrt{10}\hat{U}^{0,0}_{n,1} + \frac{16}{3}\sqrt{\frac{105}{128}}\hat{U}^{0,0}_{n,2} + \frac{10}{3}\sqrt{\frac{21}{8}}\hat{U}^{2,0}_{n,0} - \frac{5}{2}\sqrt{14}\hat{U}^{0,2}_{n,0},\\
h_{n,2}D^1_{\mathbf{v}_{n,2}}U_n(\mathbf{x}_{n,0}) &= 6\sqrt{5}\hat{U}^{1,0}_{n,0} + 8\sqrt{\frac{105}{128}}\hat{U}^{0,0}_{n,2} + 4\sqrt{\frac{21}{8}}\hat{U}^{2,0}_{n,0} + 3\sqrt{7}\hat{U}^{1,1}_{n,0},\\
h_{n,3}D^1_{\mathbf{v}_{n,3}}U_n(\mathbf{x}_{n,0}) &= 4\sqrt{15}\hat{U}^{0,1}_{n,0} + 4\sqrt{\frac{21}{4}}\hat{U}^{0,1}_{n,1} + 8\sqrt{\frac{63}{32}}\hat{U}^{1,0}_{n,1}.
\end{aligned} \tag{9.28}$$

Then, the first order directional derivatives along $\mathbf{v}_{i,1}$, $\mathbf{v}_{i,2}$, and $\mathbf{v}_{i,3}$ at $\mathbf{x}_{n,0}$ are computed as

$$\begin{aligned}
D^1_{\mathbf{v}_{i,1}}U_n &= \alpha^1_{n,1}D_{\mathbf{v}_{n,1}}U_n + \alpha^1_{n,2}D_{\mathbf{v}_{n,2}}U_n\alpha^1_{n,3}D_{\mathbf{v}_{n,3}}U_n,\\
D^1_{\mathbf{v}_{i,2}}U_n &= \alpha^2_{n,1}D_{\mathbf{v}_{n,1}}U_n + \alpha^2_{n,2}D_{\mathbf{v}_{n,2}}U_n + \alpha^2_{n,3}D_{\mathbf{v}_{n,3}}U_n,\\
D^1_{\mathbf{v}_{i,3}}U_n &= \alpha^3_{n,1}D_{\mathbf{v}_{n,1}}U_n + \alpha^3_{n,2}D_{\mathbf{v}_{n,2}}U_n + \alpha^3_{n,3}D_{\mathbf{v}_{n,3}}U_n,
\end{aligned} \tag{9.29}$$

where the coefficients α are obtained from

$$\begin{aligned}
&\mathbf{v}_{i,1} = \alpha^1_{n,1}\mathbf{v}_{n,1} + \alpha^1_{n,2}\mathbf{v}_{n,2} + \alpha^1_{n,3}\mathbf{v}_{n,3}, \quad \mathbf{v}_{i,2} = \alpha^2_{n,1}\mathbf{v}_{n,1} + \alpha^2_{n,2}\mathbf{v}_{n,2} + \alpha^2_{n,3}\mathbf{v}_{n,3},\\
&\mathbf{v}_{i,3} = \alpha^3_{n,1}\mathbf{v}_{n,1} + \alpha^3_{n,2}\mathbf{v}_{n,2} + \alpha^3_{n,3}\mathbf{v}_{n,3}.
\end{aligned} \tag{9.30}$$

Following similar steps, the first order directional derivatives along $\mathbf{v}_{i,1}$, $\mathbf{v}_{i,2}$, and $\mathbf{v}_{i,3}$ are computed at the cell centroids of $\Omega_j, \Omega_k, \Omega_l, \Omega_m$, and Ω_o. The computed values are then used to linearly interpolate the values at the forward and backward interpolation points $\mathbf{x}^f_{i,2}$ and $\mathbf{x}^b_{i,2}$ as

$$\begin{aligned}
D_{\mathbf{v}_{i,1}}U^f_{i,2} &= \beta^f_{i,2,1}D_{\mathbf{v}_{i,1}}U_j(\mathbf{x}_{j,0}) + \beta^f_{i,2,2}D_{\mathbf{v}_{i,1}}U_k(\mathbf{x}_{k,0}) + (1-\beta^f_{i,2,1}-\beta^f_{i,2,2})D_{\mathbf{v}_{i,1}}U_l(\mathbf{x}_{l,0}),\\
D_{\mathbf{v}_{i,1}}U^b_{i,2} &= \beta^b_{i,2,1}D_{\mathbf{v}_{i,1}}U_m(\mathbf{x}_{m,0}) + \beta^b_{i,2,2}D_{\mathbf{v}_{i,1}}U_n(\mathbf{x}_{n,0}) + (1-\beta^b_{i,2,1}-\beta^b_{i,2,2})D_{\mathbf{v}_{i,1}}U_o(\mathbf{x}_{o,0}),\\
D_{\mathbf{v}_{i,2}}U^f_{i,2} &= \beta^f_{i,2,1}D_{\mathbf{v}_{i,2}}U_j(\mathbf{x}_{j,0}) + \beta^f_{i,2,2}D_{\mathbf{v}_{i,2}}U_k(\mathbf{x}_{k,0}) + (1-\beta^f_{i,2,1}-\beta^f_{i,2,2})D_{\mathbf{v}_{i,2}}U_l(\mathbf{x}_{l,0}),\\
D_{\mathbf{v}_{i,2}}U^b_{i,2} &= \beta^b_{i,2,1}D_{\mathbf{v}_{i,2}}U_m(\mathbf{x}_{m,0}) + \beta^b_{i,2,2}D_{\mathbf{v}_{i,2}}U_n(\mathbf{x}_{n,0}) + (1-\beta^b_{i,2,1}-\beta^b_{i,2,2})D_{\mathbf{v}_{i,2}}U_o(\mathbf{x}_{o,0}),\\
D_{\mathbf{v}_{i,3}}U^f_{i,2} &= \beta^f_{i,2,1}D_{\mathbf{v}_{i,3}}U_j(\mathbf{x}_{j,0}) + \beta^f_{i,2,2}D_{\mathbf{v}_{i,3}}U_k(\mathbf{x}_{k,0}) + (1-\beta^f_{i,2,1}-\beta^f_{i,2,2})D_{\mathbf{v}_{i,3}}U_l(\mathbf{x}_{l,0}),\\
D_{\mathbf{v}_{i,3}}U^b_{i,2} &= \beta^b_{i,2,1}D_{\mathbf{v}_{i,3}}U_m(\mathbf{x}_{m,0}) + \beta^b_{i,2,2}D_{\mathbf{v}_{i,3}}U_n(\mathbf{x}_{n,0}) + (1-\beta^b_{i,2,1}-\beta^b_{i,2,2})D_{\mathbf{v}_{i,3}}U_o(\mathbf{x}_{o,0}).
\end{aligned} \tag{9.31}$$

Finally, the directional derivatives $D^2_{\mathbf{v}_{i,2}}U_i$, $D_{\mathbf{v}_{i,2}}D_{\mathbf{v}_{i,1}}U_i$, and $D_{\mathbf{v}_{i,2}}D_{\mathbf{v}_{i,3}}U_i$ are limited by

comparing them to the forward and backward differences along $\mathbf{v}_{i,2}$ as

$$
\begin{aligned}
D^2_{\mathbf{v}_{i,2}} U_i(\mathbf{x}_{i,0}) \leftarrow \text{minmod} \Bigg(& D^2_{\mathbf{v}_{i,2}} U_i(\mathbf{x}_{i,0}), l^f_{i,2} \frac{D_{\mathbf{v}_{i,2}} U^f_{i,2} - D_{\mathbf{v}_{i,2}} U_i(\mathbf{x}_{i,0})}{\left\| \mathbf{x}^f_{i,2} - \mathbf{x}_{i,0} \right\|}, \\
& l^b_{i,2} \frac{D_{\mathbf{v}_{i,2}} U_i(\mathbf{x}_{i,0}) - D_{\mathbf{v}_{i,2}} U^b_{i,2}}{\left\| \mathbf{x}^b_{i,2} - \mathbf{x}_{i,0} \right\|} \Bigg), \\
D_{\mathbf{v}_{i,2}} D_{\mathbf{v}_{i,1}} U_i(\mathbf{x}_{i,0}) \leftarrow \text{minmod} \Bigg(& D_{\mathbf{v}_{i,2}} D_{\mathbf{v}_{i,1}} U_i(\mathbf{x}_{i,0}), l^f_{i,2} \frac{D_{\mathbf{v}_{i,1}} U^f_{i,2} - D_{\mathbf{v}_{i,1}} U_i(\mathbf{x}_{i,0})}{\left\| \mathbf{x}^f_{i,2} - \mathbf{x}_{i,0} \right\|}, \\
& l^b_{i,2} \frac{D_{\mathbf{v}_{i,1}} U_i(\mathbf{x}_{i,0}) - D_{\mathbf{v}_{i,1}} U^b_{i,2}}{\left\| \mathbf{x}^b_{i,2} - \mathbf{x}_{i,0} \right\|} \Bigg), \\
D_{\mathbf{v}_{i,2}} D_{\mathbf{v}_{i,3}} U_i(\mathbf{x}_{i,0}) \leftarrow \text{minmod} \Bigg(& D_{\mathbf{v}_{i,2}} D_{\mathbf{v}_{i,3}} U_i(\mathbf{x}_{i,0}), l^f_{i,2} \frac{D_{\mathbf{v}_{i,3}} U^f_{i,2} - D_{\mathbf{v}_{i,3}} U_i(\mathbf{x}_{i,0})}{\left\| \mathbf{x}^f_{i,2} - \mathbf{x}_{i,0} \right\|}, \\
& l^b_{i,2} \frac{D_{\mathbf{v}_{i,3}} U_i(\mathbf{x}_{i,0}) - D_{\mathbf{v}_{i,3}} U^b_{i,2}}{\left\| \mathbf{x}^b_{i,2} - \mathbf{x}_{i,0} \right\|} \Bigg).
\end{aligned}
\tag{9.32}
$$

The range for the scaling parameters $l^f_{i,k}$ and $l^b_{i,k}$, $k = \{1, 2, 3\}$, is given in (9.21).

Similarly, to limit $D^2_{\mathbf{v}_{i,1}} U_i$, $D_{\mathbf{v}_{i,1}} D_{\mathbf{v}_{i,2}} U_i$, and $D_{\mathbf{v}_{i,1}} D_{\mathbf{v}_{i,3}} U_i$, the first order directional derivatives along $\mathbf{v}_{i,1}$, $\mathbf{v}_{i,2}$, and $\mathbf{v}_{i,3}$ are computed at the cell centroids of Ω_r, Ω_s, Ω_t, Ω_a, Ω_b, and Ω_c (Figure 9.3a), and are used to linearly interpolate the values of the first order directional derivatives at the forward and backward interpolation points $\mathbf{x}^f_{i,1}$ and $\mathbf{x}^b_{i,1}$ as

$$
\begin{aligned}
D_{\mathbf{v}_{i,1}} U^f_{i,1} &= \beta^f_{i,1,1} D_{\mathbf{v}_{i,1}} U_r(\mathbf{x}_{r,0}) + \beta^f_{i,1,2} D_{\mathbf{v}_{i,1}} U_s(\mathbf{x}_{s,0}) + (1 - \beta^f_{i,1,1} - \beta^f_{i,1,2}) D_{\mathbf{v}_{i,1}} U_t(\mathbf{x}_{t,0}), \\
D_{\mathbf{v}_{i,1}} U^b_{i,1} &= \beta^b_{i,1,1} D_{\mathbf{v}_{i,1}} U_a(\mathbf{x}_{a,0}) + \beta^b_{i,1,2} D_{\mathbf{v}_{i,1}} U_b(\mathbf{x}_{b,0}) + (1 - \beta^b_{i,1,1} - \beta^b_{i,1,2}) D_{\mathbf{v}_{i,1}} U_c(\mathbf{x}_{c,0}), \\
D_{\mathbf{v}_{i,2}} U^f_{i,1} &= \beta^f_{i,1,1} D_{\mathbf{v}_{i,2}} U_r(\mathbf{x}_{r,0}) + \beta^f_{i,1,2} D_{\mathbf{v}_{i,2}} U_s(\mathbf{x}_{s,0}) + (1 - \beta^f_{i,1,1} - \beta^f_{i,1,2}) D_{\mathbf{v}_{i,2}} U_t(\mathbf{x}_{t,0}), \\
D_{\mathbf{v}_{i,2}} U^b_{i,1} &= \beta^b_{i,1,1} D_{\mathbf{v}_{i,2}} U_a(\mathbf{x}_{a,0}) + \beta^b_{i,1,2} D_{\mathbf{v}_{i,2}} U_b(\mathbf{x}_{b,0}) + (1 - \beta^b_{i,1,1} - \beta^b_{i,1,2}) D_{\mathbf{v}_{i,2}} U_c(\mathbf{x}_{c,0}), \\
D_{\mathbf{v}_{i,3}} U^f_{i,1} &= \beta^f_{i,1,1} D_{\mathbf{v}_{i,3}} U_r(\mathbf{x}_{r,0}) + \beta^f_{i,1,2} D_{\mathbf{v}_{i,3}} U_s(\mathbf{x}_{s,0}) + (1 - \beta^f_{i,1,1} - \beta^f_{i,1,2}) D_{\mathbf{v}_{i,3}} U_t(\mathbf{x}_{t,0}), \\
D_{\mathbf{v}_{i,3}} U^b_{i,1} &= \beta^b_{i,1,1} D_{\mathbf{v}_{i,3}} U_a(\mathbf{x}_{a,0}) + \beta^b_{i,1,2} D_{\mathbf{v}_{i,3}} U_b(\mathbf{x}_{b,0}) + (1 - \beta^b_{i,1,1} - \beta^b_{i,1,2}) D_{\mathbf{v}_{i,3}} U_c(\mathbf{x}_{c,0}).
\end{aligned}
\tag{9.33}
$$

The directional derivatives $D^2_{\mathbf{v}_{i,1}} U_i$, $D_{\mathbf{v}_{i,1}} D_{\mathbf{v}_{i,2}} U_i$, and $D_{\mathbf{v}_{i,1}} D_{\mathbf{v}_{i,3}} U_i$ are limited by comparing

them to the forward and backward difference along $\mathbf{v}_{i,1}$ as

$$\begin{aligned}
D^2_{\mathbf{v}_{i,1}} U_i(\mathbf{x}_{i,0}) \leftarrow \text{minmod}\Bigg(& D^2_{\mathbf{v}_{i,1}} U_i(\mathbf{x}_{i,0}), l^f_{i,1} \frac{D_{\mathbf{v}_{i,1}} U^f_{i,1} - D_{\mathbf{v}_{i,1}} U_i(\mathbf{x}_{i,0})}{\left\| \mathbf{x}^f_{i,1} - \mathbf{x}_{i,0} \right\|}, \\
& l^b_{i,1} \frac{D_{\mathbf{v}_{i,1}} U_i(\mathbf{x}_{i,0}) - D_{\mathbf{v}_{i,1}} U^b_{i,1}}{\left\| \mathbf{x}^b_{i,1} - \mathbf{x}_{i,0} \right\|} \Bigg), \\
D_{\mathbf{v}_{i,1}} D_{\mathbf{v}_{i,2}} U_i(\mathbf{x}_{i,0}) \leftarrow \text{minmod}\Bigg(& D_{\mathbf{v}_{i,1}} D_{\mathbf{v}_{i,2}} U_i(\mathbf{x}_{i,0}), l^f_{i,1} \frac{D_{\mathbf{v}_{i,2}} U^f_{i,1} - D_{\mathbf{v}_{i,2}} U_i(\mathbf{x}_{i,0})}{\left\| \mathbf{x}^f_{i,1} - \mathbf{x}_{i,0} \right\|}, \\
& l^b_{i,1} \frac{D_{\mathbf{v}_{i,2}} U_i(\mathbf{x}_{i,0}) - D_{\mathbf{v}_{i,2}} U^b_{i,1}}{\left\| \mathbf{x}^b_{i,1} - \mathbf{x}_{i,0} \right\|} \Bigg), \\
D_{\mathbf{v}_{i,1}} D_{\mathbf{v}_{i,3}} U_i(\mathbf{x}_{i,0}) \leftarrow \text{minmod}\Bigg(& D_{\mathbf{v}_{i,1}} D_{\mathbf{v}_{i,3}} U_i(\mathbf{x}_{i,0}), l^f_{i,1} \frac{D_{\mathbf{v}_{i,3}} U^f_{i,1} - D_{\mathbf{v}_{i,3}} U_i(\mathbf{x}_{i,0})}{\left\| \mathbf{x}^f_{i,1} - \mathbf{x}_{i,0} \right\|}, \\
& l^b_{i,1} \frac{D_{\mathbf{v}_{i,3}} U_i(\mathbf{x}_{i,0}) - D_{\mathbf{v}_{i,3}} U^b_{i,1}}{\left\| \mathbf{x}^b_{i,1} - \mathbf{x}_{i,0} \right\|} \Bigg).
\end{aligned} \tag{9.34}$$

To limit $D^2_{\mathbf{v}_{i,3}} U_i$, $D_{\mathbf{v}_{i,3}} D_{\mathbf{v}_{i,1}} U_i$, and $D_{\mathbf{v}_{i,3}} D_{\mathbf{v}_{i,2}} U_i$, the first order directional derivatives along $\mathbf{v}_{i,1}$, $\mathbf{v}_{i,2}$, and $\mathbf{v}_{i,3}$ are computed at the cell centroids of Ω_e, Ω_f, Ω_g, Ω_x, Ω_y, and Ω_z (Figure 9.3c), and are used to linearly interpolate the values of the first order directional derivatives at the forward and backward interpolation points $\mathbf{x}^f_{i,3}$ and $\mathbf{x}^b_{i,3}$ as

$$\begin{aligned}
D_{\mathbf{v}_{i,1}} U^f_{i,3} &= \beta^f_{i,3,1} D_{\mathbf{v}_{i,1}} U_e(\mathbf{x}_{e,0}) + \beta^f_{i,3,2} D_{\mathbf{v}_{i,1}} U_f(\mathbf{x}_{f,0}) + (1 - \beta^f_{i,3,1} - \beta^f_{i,3,2}) D_{\mathbf{v}_{i,1}} U_g(\mathbf{x}_{g,0}), \\
D_{\mathbf{v}_{i,1}} U^b_{i,3} &= \beta^b_{i,3,1} D_{\mathbf{v}_{i,1}} U_x(\mathbf{x}_{x,0}) + \beta^b_{i,3,2} D_{\mathbf{v}_{i,1}} U_y(\mathbf{x}_{y,0}) + (1 - \beta^b_{i,3,1} - \beta^b_{i,3,2}) D_{\mathbf{v}_{i,1}} U_z(\mathbf{x}_{z,0}), \\
D_{\mathbf{v}_{i,2}} U^f_{i,3} &= \beta^f_{i,3,1} D_{\mathbf{v}_{i,2}} U_e(\mathbf{x}_{e,0}) + \beta^f_{i,3,2} D_{\mathbf{v}_{i,2}} U_f(\mathbf{x}_{f,0}) + (1 - \beta^f_{i,3,1} - \beta^f_{i,3,2}) D_{\mathbf{v}_{i,2}} U_g(\mathbf{x}_{g,0}), \\
D_{\mathbf{v}_{i,2}} U^b_{i,3} &= \beta^b_{i,3,1} D_{\mathbf{v}_{i,2}} U_x(\mathbf{x}_{x,0}) + \beta^b_{i,3,2} D_{\mathbf{v}_{i,2}} U_y(\mathbf{x}_{y,0}) + (1 - \beta^b_{i,3,1} - \beta^b_{i,3,2}) D_{\mathbf{v}_{i,2}} U_z(\mathbf{x}_{z,0}), \\
D_{\mathbf{v}_{i,3}} U^f_{i,3} &= \beta^f_{i,3,1} D_{\mathbf{v}_{i,3}} U_e(\mathbf{x}_{e,0}) + \beta^f_{i,3,2} D_{\mathbf{v}_{i,3}} U_f(\mathbf{x}_{f,0}) + (1 - \beta^f_{i,3,1} - \beta^f_{i,3,2}) D_{\mathbf{v}_{i,3}} U_g(\mathbf{x}_{g,0}), \\
D_{\mathbf{v}_{i,3}} U^b_{i,3} &= \beta^b_{i,3,1} D_{\mathbf{v}_{i,3}} U_x(\mathbf{x}_{x,0}) + \beta^b_{i,3,2} D_{\mathbf{v}_{i,3}} U_y(\mathbf{x}_{y,0}) + (1 - \beta^b_{i,3,1} - \beta^b_{i,3,2}) D_{\mathbf{v}_{i,3}} U_z(\mathbf{x}_{z,0}).
\end{aligned} \tag{9.35}$$

The directional derivatives $D^2_{\mathbf{v}_{i,3}} U_i$, $D_{\mathbf{v}_{i,3}} D_{\mathbf{v}_{i,1}} U_i$, and $D_{\mathbf{v}_{i,3}} D_{\mathbf{v}_{i,2}} U_i$ are limited by comparing

them to the forward and backward difference along $\mathbf{v}_{i,3}$ as

$$
\begin{aligned}
D^2_{\mathbf{v}_{i,3}} U_i(\mathbf{x}_{i,0}) \leftarrow \text{minmod} \Bigg(& D^2_{\mathbf{v}_{i,3}} U_i(\mathbf{x}_{i,0}), l^f_{i,3} \frac{D_{\mathbf{v}_{i,3}} U^f_{i,3} - D_{\mathbf{v}_{i,3}} U_i(\mathbf{x}_{i,0})}{\left\| \mathbf{x}^f_{i,3} - \mathbf{x}_{i,0} \right\|}, \\
& l^b_{i,3} \frac{D_{\mathbf{v}_{i,3}} U_i(\mathbf{x}_{i,0}) - D_{\mathbf{v}_{i,3}} U^b_{i,3}}{\left\| \mathbf{x}^b_{i,3} - \mathbf{x}_{i,0} \right\|} \Bigg), \\
D_{\mathbf{v}_{i,3}} D_{\mathbf{v}_{i,1}} U_i(\mathbf{x}_{i,0}) \leftarrow \text{minmod} \Bigg(& D_{\mathbf{v}_{i,3}} D_{\mathbf{v}_{i,1}} U_i(\mathbf{x}_{i,0}), l^f_{i,3} \frac{D_{\mathbf{v}_{i,1}} U^f_{i,3} - D_{\mathbf{v}_{i,1}} U_i(\mathbf{x}_{i,0})}{\left\| \mathbf{x}^f_{i,3} - \mathbf{x}_{i,0} \right\|}, \\
& l^b_{i,3} \frac{D_{\mathbf{v}_{i,1}} U_i(\mathbf{x}_{i,0}) - D_{\mathbf{v}_{i,1}} U^b_{i,3}}{\left\| \mathbf{x}^b_{i,3} - \mathbf{x}_{i,0} \right\|} \Bigg), \\
D_{\mathbf{v}_{i,3}} D_{\mathbf{v}_{i,2}} U_i(\mathbf{x}_{i,0}) \leftarrow \text{minmod} \Bigg(& D_{\mathbf{v}_{i,3}} D_{\mathbf{v}_{i,2}} U_i(\mathbf{x}_{i,0}), l^f_{i,3} \frac{D_{\mathbf{v}_{i,2}} U^f_{i,3} - D_{\mathbf{v}_{i,2}} U_i(\mathbf{x}_{i,0})}{\left\| \mathbf{x}^f_{i,3} - \mathbf{x}_{i,0} \right\|}, \\
& l^b_{i,3} \frac{D_{\mathbf{v}_{i,2}} U_i(\mathbf{x}_{i,0}) - D_{\mathbf{v}_{i,2}} U^b_{i,3}}{\left\| \mathbf{x}^b_{i,3} - \mathbf{x}_{i,0} \right\|} \Bigg).
\end{aligned}
\tag{9.36}
$$

Finally, the modified second order moments $\hat{U}^{l,m}_{i,k}$, $k+l+m = 2$, are computed by substituting the limited second order directional derivatives along $\mathbf{v}_{i,1}$, $\mathbf{v}_{i,2}$, and $\mathbf{v}_{i,3}$ into (9.26)

$$
\begin{aligned}
\hat{U}^{0,0}_{i,2} &= \frac{h^2_{i,3}}{192} \sqrt{\frac{128}{105}} D^2_{\mathbf{v}_{i,3}} U_i, \\
\hat{U}^{1,0}_{i,1} &= \frac{h_{i,3} h_{i,2}}{80} \sqrt{\frac{32}{63}} D_{\mathbf{v}_{i,3}} D_{\mathbf{v}_{i,2}} U_i, \\
\hat{U}^{2,0}_{i,0} &= \frac{h^2_{i,2}}{80} \sqrt{\frac{8}{21}} D^2_{\mathbf{v}_{i,2}} U_i + \frac{h^2_{i,3}}{960} \sqrt{\frac{8}{21}} D^2_{\mathbf{v}_{i,3}} U_i, \\
\hat{U}^{0,1}_{i,1} &= \frac{h_{i,3} h_{i,1}}{48} \sqrt{\frac{4}{21}} D_{\mathbf{v}_{i,3}} D_{\mathbf{v}_{i,1}} U_i + \frac{h_{i,3} h_{i,2}}{360} \sqrt{\frac{4}{21}} D_{\mathbf{v}_{i,3}} D_{\mathbf{v}_{i,2}} U_i, \\
\hat{U}^{0,2}_{i,0} &= \frac{h^2_{i,1}}{30} \frac{1}{\sqrt{14}} D^2_{\mathbf{v}_{i,1}} U_i + \frac{h^2_{i,2}}{540} \frac{1}{\sqrt{14}} D^2_{\mathbf{v}_{i,2}} U_i + \frac{h^2_{i,3}}{720} \frac{1}{\sqrt{14}} D^2_{\mathbf{v}_{i,3}} U_i, \\
\hat{U}^{1,1}_{i,0} &= \frac{h_{i,2} h_{i,1}}{36} \frac{1}{\sqrt{7}} D_{\mathbf{v}_{i,2}} D_{\mathbf{v}_{i,1}} U_i - \frac{h^2_{i,2}}{540} \frac{1}{\sqrt{7}} D^2_{\mathbf{v}_{i,2}} U_i + \frac{h^2_{i,3}}{720} \frac{1}{\sqrt{7}} D^2_{\mathbf{v}_{i,3}} U_i.
\end{aligned}
\tag{9.37}
$$

If all second order directional derivatives have been modified by the limiter, then the linear

moments are limited using the second order moment limiter [23]

$$\begin{aligned}
\hat{U}_{i,1}^{0,0} &\leftarrow \text{minmod}\left(\frac{U_{i,1}^{f}-\overline{U}_i}{\sqrt{10}}, \hat{U}_{i,1}^{0,0}, \frac{\overline{U}_i - U_{i,1}^{b}}{\sqrt{10}}\right),\\
\hat{U}_{i,0}^{1,0} &\leftarrow \text{minmod}\left(\frac{U_{i,2}^{f}-\overline{U}_i}{2\sqrt{5}}, \hat{U}_{i,0}^{1,0}, \frac{\overline{U}_i - U_{i,2}^{b}}{2\sqrt{5}}\right),\\
\hat{U}_{i,0}^{0,1} &\leftarrow \text{minmod}\left(\frac{U_{i,2}^{f}-\overline{U}_i}{2\sqrt{15}}, \hat{U}_{i,0}^{0,1}, \frac{\overline{U}_i - U_{i,2}^{b}}{2\sqrt{15}}\right),
\end{aligned} \tag{9.38}$$

where $\overline{U}_i^n$ is the cell average in Ω_i. The forward and backward interpolation values $U_{i,q}^f$ and $U_{i,q}^b$, $q = \{1,2,3\}$, are linearly interpolated using the cell averages from respective neighboring elements (Figure 9.2). For example, the forward and backward interpolation values along $\mathbf{v}_{i,3}$ are given by

$$\begin{aligned}
U_{i,3}^{f} &= \beta_{i,3,1}^{f}\overline{U}_e + \beta_{i,3,2}^{f}\overline{U}_f + (1-\beta_{i,3,1}^{f}-\beta_{i,3,2}^{f})\overline{U}_g,\\
U_{i,3}^{b} &= \beta_{i,3,1}^{b}\overline{U}_x + \beta_{i,3,2}^{b}\overline{U}_y + (1-\beta_{i,3,1}^{b}-\beta_{i,3,2}^{b})\overline{U}_z,
\end{aligned} \tag{9.39}$$

with $0 \le \beta_{i,3,1}^{f}, \beta_{i,3,2}^{f}, \beta_{i,3,1}^{b}, \beta_{i,3,2}^{b} \le 1$.

9.1.4 Implementation of the moment limiter

As the limiter uses a compact stencil and involves only a set of simple algebraic operations, it is easy to implement. We pre-compute [53] the limiting stencil for each mesh element (Figures 9.2 and 9.3), i.e., for each Ω_i, we store access to the eighteen mesh elements involved in the limiting stencil. We compute and store the constants α in (9.30) and the interpolation weights β in (9.31) and (9.33). For example, with $p = 2$, we

1. Compute higher order derivatives using (9.26).
2. Compute lower order derivatives using (9.28).
3. Compute the directional derivatives along the required direction on neighboring elements using (9.29).
4. Interpolate lower order derivatives at the interpolation points using (9.31) and (9.33).
5. Apply the minmod function.
6. Repeat above steps until a set of unmodified directional derivatives are reached.

9.2 Results

In this section, we present numerical experiments to analyze the performance of the proposed high-order moment limiter. Through convergence studies, we show that the limited solution retains the expected rate of convergence for smooth problems. We also run numerical tests to show the robustness of the proposed limiter in the presence of discontinuities. In all presented cases, time-stepping was performed using an explicit Runge-Kutta method of appropriate order. Finally, unless otherwise stated, the local Lax-Friedrichs flux was used.

9.2.1 Advecting hill.

We solve the scalar advection equation on the domain $\Omega = [-1,1]^3$, with the flux in (1.8) given by $\mathbf{F} = [u,u,u]$. The initial condition is $u_0(x,y,z) = 2.5\exp(\frac{-r^2}{2R^2})$, with $r = \sqrt{(x+0.25)^2+(y+0.25)^2+(z+0.25)^2}$ and $R = 0.15$. The problem is solved until $t = 0.25$ on a series of unstructured tetrahedral meshes $A-D$. Mesh A is the coarsest with 4485 tetrahedra while meshes B-D are obtained by the nested refinement of the preceding mesh. Table 9.1 shows the L_1 errors and the observed convergence rates for the $p = 2$ and $p = 3$ DG approximations with and without limiting. We observe that the limited solutions retain the theoretical rate of convergence.

Mesh	Nb. elems	L1 error			
		p = 2	p = 2 (unlimited)	p = 3	p = 3 (unlimited)
A	4,485	6.24e-02 (-)	6.19e-03 (-)	6.12e-02 (-)	1.47e-03 (-)
B	35,347	1.3e-02 (2.26)	9.44e-04 (2.71)	1.24e-02 (2.3)	1.16e-04 (3.66)
C	271,899	1.1e-03 (3.56)	1.32e-04 (2.86)	8.55e-04 (3.86)	8.25e-06 (3.81)
D	2,178,457	9.99e-05 (3.48)	1.35e-05 (3.29)	2.06e-05 (5.37)	4.17e-07 (4.3)

Table 9.1: L_1 errors for the advecting hill problem for limited and unlimited solutions at $t = 0.25$. Convergence rates are given in parentheses.

9.2.2 Rotating Shapes.

We solve the rotating shapes problem with the flux in (1.8) given by $\mathbf{F} = [-2\pi yu, 2\pi xu, 0]$. The initial condition consists of a hill and a square pulse given by

$$u_0(x,y,z) = \begin{cases} \cos^2(2\pi r), & \text{if } r \le 0.25, \\ 1, & \text{if } \max(|x-0.35|,|y|,|z|) \le 0.25, \\ 0, & \text{otherwise}, \end{cases} \tag{9.40}$$

where $r = \sqrt{(x+0.5)^2 + y^2 + z^2}$. The exact solution is a rotation of the initial condition about the origin. The problem is solved until $t = 1$ on an unstructured mesh of $3,150,670$ tetrahedral elements. Figure 9.5 shows the isolines and the solution profiles at $z = y = 0$, $z = 0, x = 0.5$, and $z = 0, x = 0.55$, obtained using the $p = 1$, $p = 2$, and $p = 3$ approximations with the moment limiter. The quality of the solution is comparable to the results obtained using the moment limiter described in [25] on a 80×80 Cartesian mesh and the high-order moment limiter described in [57] on an unstructured mesh of $12,792$ triangular elements.

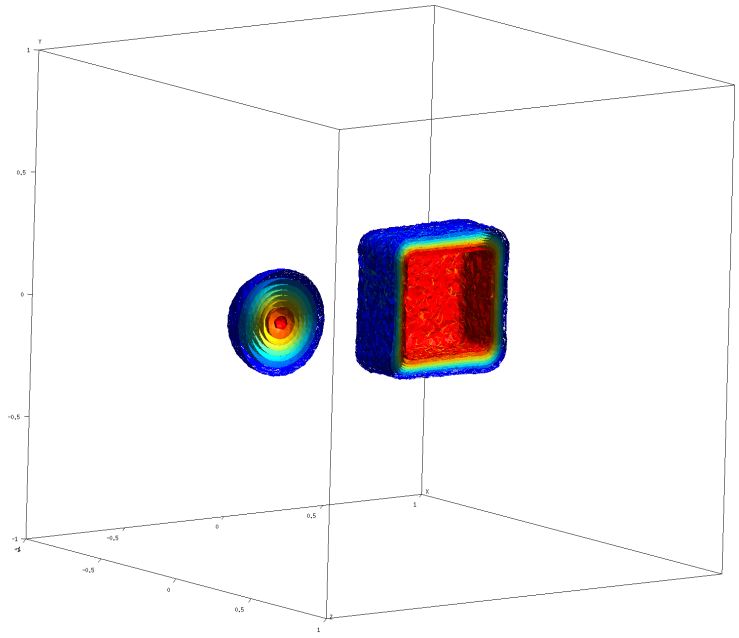

Figure 9.4: Isosurfaces of the limited solution to the rotating shapes problem for $z < 0$ at $t = 1$.

We note that only the third and fourth order schemes capture the peak of the hill well (Figure 9.5c) and not the second order scheme. This is due to a well known phenomenon of

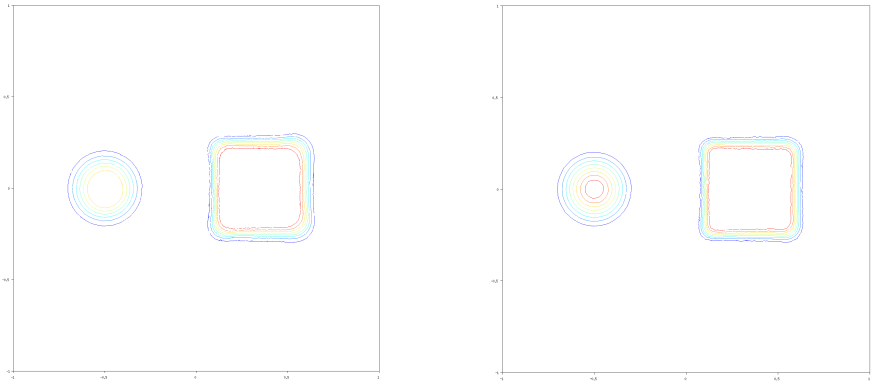

(a) Isolines with second order moment limiter [23].

(b) Isolines with third order moment limiter.

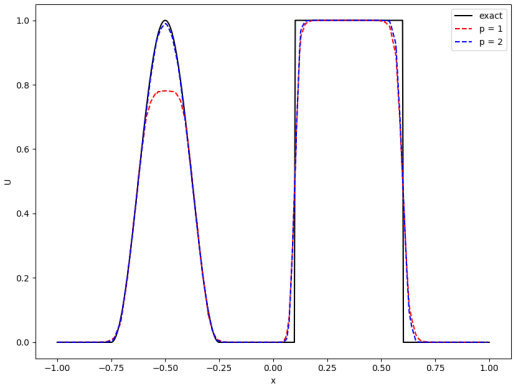

(c) Profile of the solution along $z = 0, y = 0$.

clipping at local extrema by second order limiters. Since the high-order moment limiter is applied hierarchically, the solution is not overlimited for the $p = 2$ and $p = 3$ approximations and the accuracy at the peak is preserved. Further, we observe that all three limiters suppress oscillations near solution discontinuities. Finally, Figure 9.6 shows the isolines of the solutions and solution profiles along $z = y = 0$, $z = 0, x = 0.5$, and $z = 0, x = 0.55$ obtained using the $p = 1$ and $p = 2$ approximations without limiting. We can clearly observe oscillations near the discontinuities for both $p = 1$ and $p = 2$, which severely affect the quality of the solution.

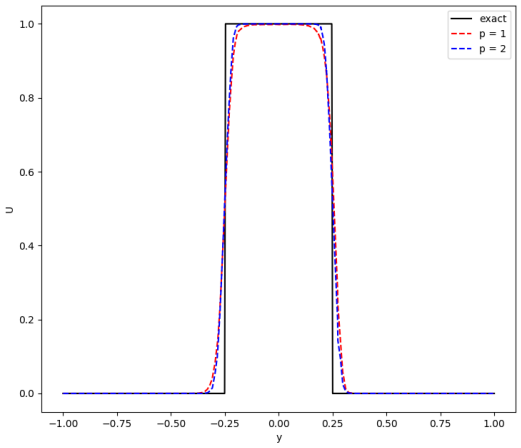

(d) Profile of the solution along $z = 0, x = 0.5$.

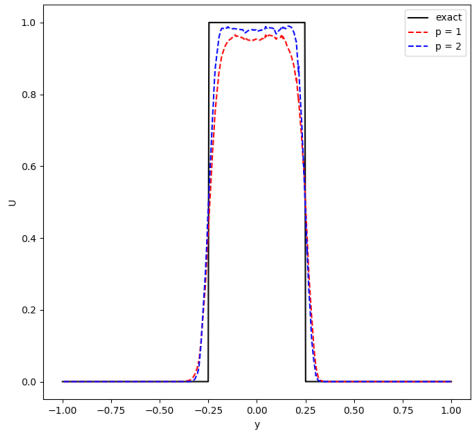

(e) Profile of the solution along $z = 0, x = 0.55$.

Figure 9.5: Rotating shapes at $t = 1$ on an unstructured mesh of $3,150,670$ tetrahedra.

9.2.3 Shock-bubble interaction.

Next, we test the performance of the high-order limiter when applied to a system of non-linear equations, for example, the Euler equations given by

$$\frac{\partial}{\partial t}\begin{pmatrix}\rho\\ \rho u\\ \rho v\\ \rho w\\ E\end{pmatrix}+\frac{\partial}{\partial x}\begin{pmatrix}\rho u\\ \rho u^2+p\\ \rho uv\\ \rho uw\\ (E+p)u\end{pmatrix}+\frac{\partial}{\partial y}\begin{pmatrix}\rho v\\ \rho uv\\ \rho v^2+p\\ \rho vw\\ (E+p)v\end{pmatrix}+\frac{\partial}{\partial y}\begin{pmatrix}\rho w\\ \rho uw\\ \rho vw\\ \rho w^2+p\\ (E+p)w\end{pmatrix}=0, \tag{9.41}$$

where ρ is the density, ρu, ρv and ρw are the x-, y-, and z-direction momenta, E is the energy, and the pressure, p, is given by the equation of state $p = (\gamma-1)\left(E - \frac{\rho}{2}(u^2+v^2+w^2)\right)$. In this example, we simulate the interaction between a Mach 10 shock and a bubble. The initial setup consists of a spherical bubble of radius $R = 0.55$ centered at $(-0.4, 0, 0)$ in the domain $[-1,1]^3$ and incident shock located at $x = -0.95$ (Figure 9.7). Table 9.2 provides the initial incident, quiescent, and bubble states. $\mathbf{U}_B$ and $\mathbf{U}_Q$ respectively denote the initial states inside and outside the bubble, while $\mathbf{U}_I$ gives the state to the right of the left moving shock. Due to the symmetry of the test case, we run the simulation only in a quarter of the original domain, i.e.,$[-1,1]\times[0,1]^2$. The problem is run until $t = 0.125$ on an unstructured mesh of $11,530,455$ tetrahedra.

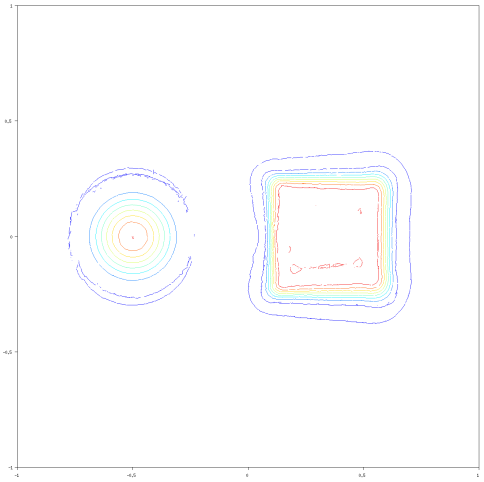

(a) Isolines with $p = 1$.

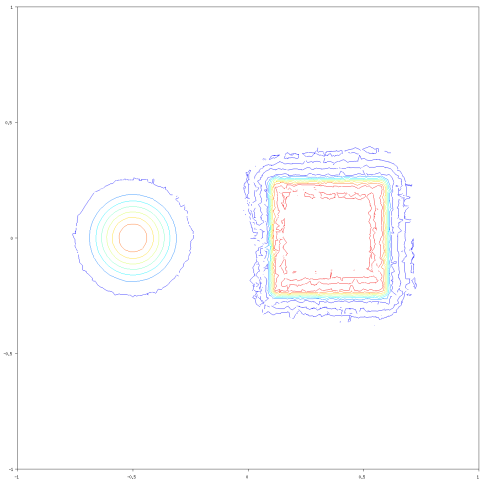

(b) Isolines with $p = 2$.

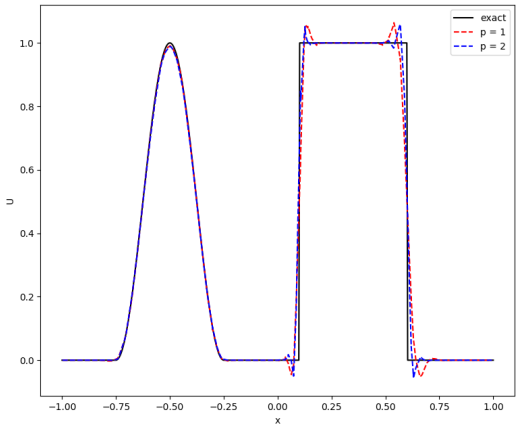

(c) Profile of the solution along $z = 0, y = 0$.

	$\mathbf{U}_Q$	$\mathbf{U}_B$	$\mathbf{U}_I$
ρ	1.4	0.5	8
u	0	0	-8.25
v	0	0	0
w	0	0	0
p	1	1	116.5

Table 9.2: The initial states for the shock-bubble interaction test case.

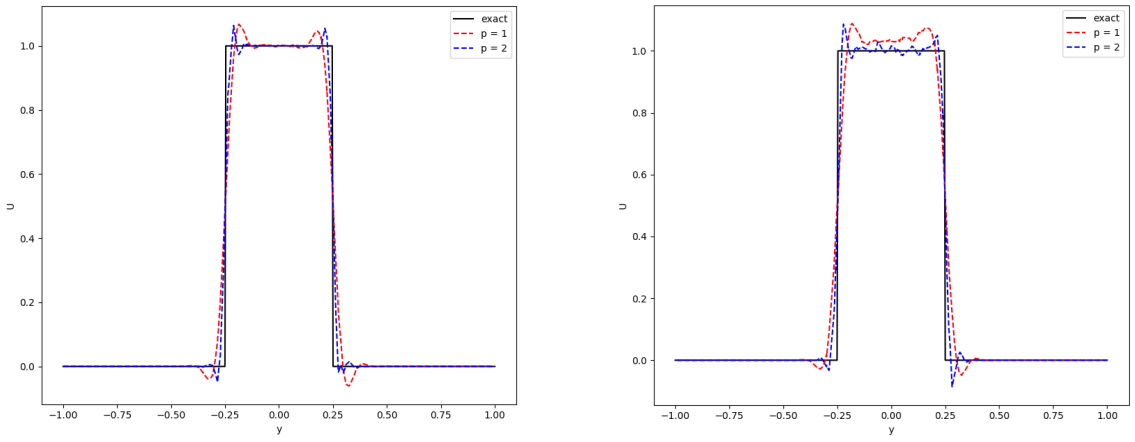

(d) Profile of the solution along $z = 0, x = 0.5$. (e) Profile of the solution along $z = 0, x = 0.55$.

Figure 9.6: Solution of the rotating shapes problem at $t = 1$ without limiting on an unstructured mesh of $3,150,670$ tetrahedra.

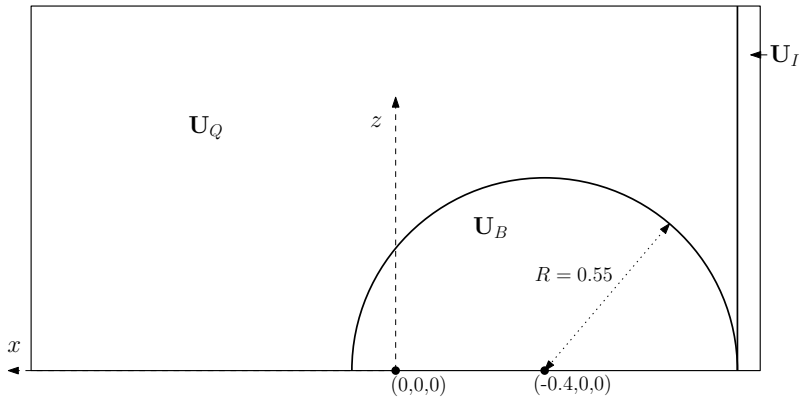

Figure 9.7: Initial setup for the bubble-shock interaction case.

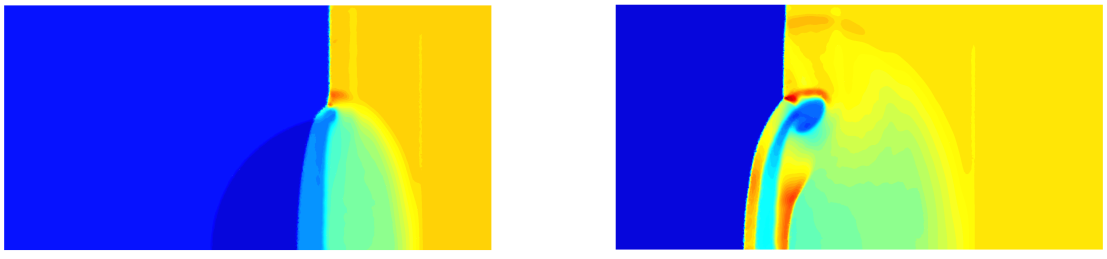

(a) $t = 0.06125$. (b) $t = 0.125$.

Figure 9.9: Density profile along $z = 0.02$ for the bubble shock interaction case using $p = 2$ DG approximation on an unstructured mesh of $11,530,455$ tetrahedra.

(a) $t = 0.06125$. (b) $t = 0.125$.

Figure 9.8: Density profile along $z = 0.02$ for the bubble shock interaction case using $p = 1$ DG approximation on an unstructured mesh of $11,530,455$ tetrahedra.

A cross section of the density on the plane $z = 0.02$ at various times between $t = 0$ and the final time $t = 0.125$ for $p = 1$ and $p = 2$ DG approximations are shown, respectively, in Figures 9.8 and 9.9, demonstrating a complex interaction where the initial bubble is compressed by the shock. Isosurfaces of the density at the final time $t = 0.125$ for $p = 2$ DG approximation are provided in Figure 9.10.

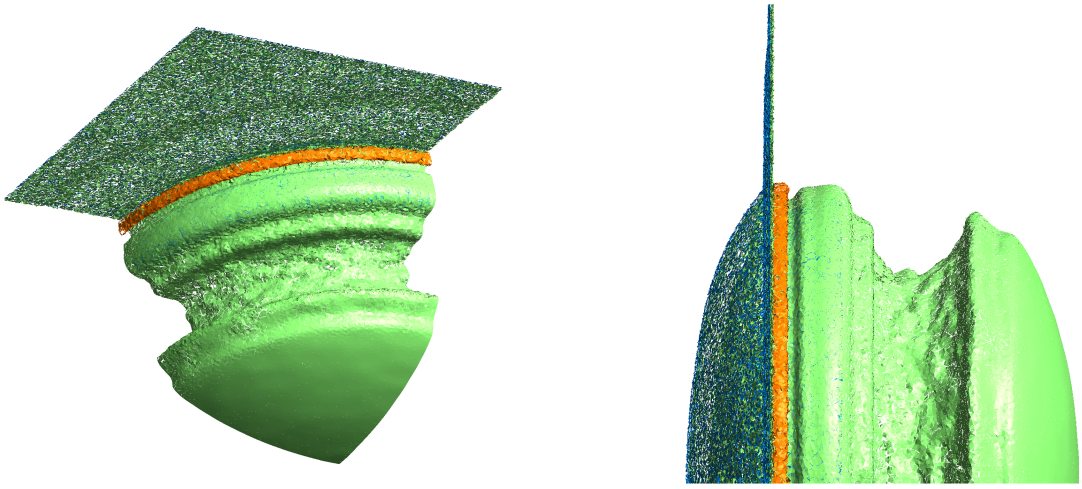

(a) View 1. (b) View 2.

Figure 9.10: Isosurfaces of density for the bubble shock interaction case, at $t = 0.125$ using $p = 2$ DG approximation on an unstructured mesh of $11,530,455$ tetrahedra.

Finally, we perform a walk clock study to check the computational cost of the limiter. The limiter takes about twenty percent of the total run time (Table 9.3) of a parallel multi-GPU implementation of the modal discontinuous Galerkin method [54] and this number is about the same for both orders of approximation.

p	Run time (s)	Limiting time (s)
1	16396.6	2988.47(18.2%)
2	64651.28	13376.95(20.5%)

Table 9.3: Limiting time for the bubble-shock interaction example. The limiting time as a percentage of the total run time is given in parenthesis under "Limiting time".

9.3 Summary

We have presented a high-order moment limiter for the DG method on unstructured tetrahedral meshes. It limits the numerical solution by expressing the solution coefficients (moments) in terms directional derivatives along specific directions and reconstructing the directional derivatives using one-dimensional minmod limiter. The limiting is performed hierarchically, starting with the highest solution coefficients and it stops when the limiter encounters a set of directional derivatives that are not modified by the one-dimensional limiter. This hierarchical implementation avoids overlimiting, especially at solution extrema where second order limiters are known to damage solutions.

Numerical experiments presented in Section 9.2 demonstrate that the DG method equipped with the proposed limiter retains the theoretical convergence rate for smooth solutions and eliminates spurious oscillations in the presence of discontinuities. The proposed limiter has a simple and fixed reconstruction stencil. Despite a complex derivation, the limiter itself consists of a set of simple algebraic operations on solution coefficients. As a result, it takes only a modest percent of the total computing time in a parallel implementation of the modal discontinuous Galerkin method for solution of Euler equations.

Chapter 10

Conclusion

In this thesis, we have presented and implemented efficient limiting techniques for the high-order modal discontinuous Galerkin method on unstructured meshes. In Chapter 2, we proposed and analyzed a class of second order moment limiters for the DG method on adaptively refined triangular meshes. The limiter is an extension of the second order moment limiter proposed in [2] for conforming triangular meshes. We faced unique challenges in extending the limiter to nonconforming meshes as a triangular element in the mesh can share an edge with more than one element. We have proposed a simple algorithm to update the reconstruction neighborhood of elements in an adaptively refined mesh. The algorithm involves updating a vertex database and the vertex-to-element connectivity with every refinement cycle. When implemented on a GPU, the algorithm avoids race conditions as every element is identified uniquely in the database.

In Chapters 3, 5, 6, 7, and 9, we have presented high-order moment limiters for the DG method on triangular, quadrilateral, curvilinear triangular, and tetrahedral meshes. The proposed techniques limit numerical solutions by hierarchically limiting solution coefficients (moments) starting with the highest. The limiters stop when they encounter a set of solution coefficients or corresponding directional derivatives left unchanged by a one-dimensional slope limiter. The hierarchical implementation avoids overlimiting, especially at solution extrema where second-order limiters visibly damage solutions even on reasonably fine meshes.

Through numerical experiments, we demonstrated that the DG method equipped with the proposed limiters retains the $p+1$ convergence rate for smooth solutions and eliminates spurious oscillations in the presence of discontinuities. A major component of the limiters is the choice of the directions in which the numerical solution is limited. The proposed limiting directions nearly uncouple solution coefficients, thus ensuring an easy and quick transformation from solution coefficients to directional derivatives of the solution and back.

This uncoupling of the solution coefficients combined with hierarchical limiting allows us to limit only the moments that exhibit excessive growth and retain the accuracy of the solution.

The proposed limiters have a compact and fixed reconstruction stencil computed during the preprocessing stage. Even though they involve complex derivations, the actual implementation of the limiters consists of a simple set of algebraic operations on solution coefficients and the precomputed constants. As a result, limiting takes up only a modest percent of the total computing time in a parallel implementation of the modal discontinuous Galerkin method on a GPU.

In Chapters 4 and 8, we have presented and analyzed the stability of a family of second-order slope limiters for the DG method on quadrilateral and tetrahedral meshes, respectively. The limiter works by scaling the solution coefficients by a constant multiplier that lies in the interval $[0, 1]$. The limiter bounds the numerical solution at select limiting points on an element by the solution averages in a neighborhood of the element. Further, we derive conditions on the timestep that ensure the numerical solution satisfies a local maximum principle in the means. In this process, we also arrived at a new estimate for the cell size of a quadrilateral element.

Future work involves extending the high-order limiter for the DG method to adaptively refined nonconforming tetrahedral meshes. This can be accomplished since the limiting directions for an element remain the same when a mesh is adaptively refined. It would be interesting to extend the algorithm to update the reconstruction neighborhood, proposed in Chapter 2, to three-dimensional adaptively refined meshes as well as to support multi-GPU platforms. Extending the limiting technique to three-dimensional curvilinear tetrahedral meshes and two-dimensional manifolds would also be of interest. Finally, designing a high-order moment limiter that accounts for entropy stability of solutions of nonlinear conservation laws is an interesting avenue to explore.

References

[1] M. Berger, M. J. Aftosmis, and S. M. Murman. Analysis of slope limiters on irregular grids. *AIAA paper*, 490(2005):1–22, 2005.

[2] A. Giuliani and L. Krivodonova. A moment limiter for the discontinuous Galerkin method on unstructured triangular meshes. *SIAM Journal on Scientific Computing*, 41:A508–A537, 2019.

[3] W. F. Noh. Errors for calculations of strong shocks using an artificial viscosity and artificial heat flux. *Journal of Computational Physics*, 72:78–120, 1987.

[4] R. J. LeVeque. *Finite volume methods for hyperbolic conservation laws*. Cambridge University Press, Cambridge, 2002.

[5] J. Yu and J. S. Hesthaven. A study of several artificial viscosity models within the discontinuous Galerkin framework. *Communications in Computational Physics*, 27(5):1309–1343, 2020.

[6] P. K Sweby. High resolution schemes using flux limiters for hyperbolic conservation laws. *SIAM Journal on Numerical Analysis*, 21(5):995–1011, 1984.

[7] J. S. Hesthaven and T. Warburton. *Nodal discontinuous Galerkin methods : Algorithms, Analysis and Application*. Springer, 2008.

[8] A. Meister, S. Ortleb, and T. Sonar. On spectral filtering for discontinuous Galerkin methods on unstructured triangular grids. *Math. Schriften Kassel*, 2009.

[9] A. Meister, S. Ortleb, and T. Sonar. Application of spectral filtering to discontinuous galerkin methods on triangulations. *Numerical Methods for Partial Differential Equations*, 28(6):1840–1868, 2012.

[10] J. Qiu and C. W. Shu. Runge-Kutta discontinuous Galerkin method using WENO limiters. *Journal of Computational Physics*, 26(3):907–929, 2005.

[11] J. Zhu, X. Zhong, C. W. Shu, and J. Qiu. Runge-Kutta discontinuous Galerkin method using a new type of WENO limiters on unstructured meshes. *Journal of Computational Physics*, 233:3077–3085, 2013.

[12] R. Biswas, K. D. Devine, and J. E. Flaherty. Parallel, adaptive finite element methods for conservation laws. *Applied Numerical Mathematics*, 14(1-3):255–283, 1994.

[13] D. Kuzmin. A vertex-based hierarchical slope limiter for p-adaptive discontinuous Galerkin methods. *Journal of Computational and Applied Mathematics*, 26(3):907–929, 2010.

[14] V. Aizinger, A. Kosík, D. Kuzmin, and B. Reuter. Anisotropic slope limiting for discontinuous Galerkin methods. *International Journal for Numerical Methods in Fluids*, 2017.

[15] A. Harten. High resolution schemes for hyperbolic conservation laws. *Journal of Computational Physics*, 49(3):357–393, 1983.

[16] A. Harten. On a class of high resolution total-variation-stable finite-difference schemes. *SIAM Journal on Numerical Analysis*, 21(1):1–23, 1984.

[17] E. Tadmor. Convenient total variation diminishing conditions for nonlinear difference schemes. *SIAM Journal on Numerical Analysis*, 25(5):1002–1014, 1988.

[18] A. Harten, B. Engquist, S. Osher, and S. Chakravarthy. Uniformly high-order accurate essentially nonoscillatory schemes III. *Journal of Computational Physics*, 71:231–303, 1987.

[19] J. B. Goodman and R. J. LeVeque. On the accuracy of stable schemes for 2D scalar conservation laws. *Mathematics of Computation*, pages 15–21, 1985.

[20] L. Krivodonova and A. Smirnov. On the tvd property of second order methods for 2d scalar conservation laws, 2021.

[21] T. Barth and D. Jespersen. The design and application of upwind schemes on unstructured meshes. *AIAA paper*, pages 89–0366, 1989.

[22] A. Giuliani and L. Krivodonova. Analysis of slope limiters on unstructured triangular meshes. *Journal of Computational Physics*, 374:1–26, 2018.

[23] A. Giuliani and L. Krivodonova. A moment limiter for the discontinuous Galerkin method on unstructured meshes of tetrahedra. *Journal of Computational Physics*, 404:109106, 2020.

[24] S. May and M. Berger. Two-dimensional slope limiters for finite volume schemes on non-coordinate-aligned meshes. *SIAM Journal on Scientific Computing*, 35(5):A2163–A2187, 2013.

[25] L. Krivodonova. Limiters for high-order discontinuous Galerkin methods. *Journal of Computational Physics*, 226(1):879–896, 2007.

[26] A. Burbeau, P. Sagaut, and C-H. Bruneau. A problem-independent limiter for high-order Runge-Kutta discontinuous Galerkin methods. *Journal of Computational Physics*, 169:111–150, 2001.

[27] H. Hajduk, D. Kuzmin, and V. Aizinger. New directional vector limiters for discontinuous Galerkin methods. *Journal of Computational Physics*, 384:308–325, 2019.

[28] M. Yang and Z.J Wang. A parameter–free generalized moment limiter for high-order methods on unstructured grids. *Advances in Applied Mathematics and Mechanics*, 1(4):451–480, 2009.

[29] D. Kuzmin. Slope limiting for discontinuous Galerkin approximations with a possibly non-orthogonal Taylor basis. *International Journal for Numerical Methods in Fluids*, 71(9):1178–1190, 2013.

[30] J. Zhu, C. W. Shu, and J. Qiu. High-order Runge-Kutta discontinuous Galerkin methods with a new type of multi-resolution WENO limiters on tetrahedral meshes. *Communications in Computational Physics*, 29(4):1030–1058, 2021.

[31] M. Dumbser and R. Loubère. A simple robust and accurate a posteriori sub-cell finite volume limiter for the discontinuous Galerkin method on unstructured meshes. *Journal of Computational Physics*, 319:169–199, 2016.

[32] X. Zhang and C.-W. Shu. Maximum-principle-satisfying and positivity-preserving high-order schemes for conservation laws: survey and new developments. *Proceedings of the Royal Society A*, 467:2752–2776, 2011.

[33] X. Zhang and C.-W. Shu. Positivity-preserving high order discontinuous Galerkin schemes for compressible Euler equations with source terms. *Journal of Computational Physics*, 230(4):1238–1248, 2011.

[34] X. Zhang and C.-W. Shu. On positivity-preserving high order discontinuous Galerkin schemes for compressible Euler equations on rectangular meshes. *Journal of Computational Physics*, 229(23):8918–8934, 2010.

[35] Y. Lv and M. Ihme. Entropy-bounded discontinuous Galerkin scheme for Euler equations. *Journal of Computational Physics*, 295:715–739, 2015.

[36] D. Kuzmin. Monolithic convex limiting for continuous finite element discretizations of hyperbolic conservation laws. *Computer Methods in Applied Mechanics and Engineering*, 361:112804, 2020.

[37] D. Kuzmin. Entropy stabilization and property-preserving limiters for p1 discontinuous Galerkin discretizations of scalar hyperbolic problems. *Journal of Numerical Mathematics*, 29(4):307–322, 2021.

[38] D. Kuzmin, H. Hajduk, and A. Rupp. Limiter-based entropy stabilization of semi-discrete and fully discrete schemes for nonlinear hyperbolic problems. *Computer Methods in Applied Mechanics and Engineering*, 389:114428, 2022.

[39] Clawpack Development Team. Clawpack software, 2018. Version 5.5.0.

[40] P. MacNeice, K. M. Olson, C. Mobarry, R. D. Fainchtein, and C. Packer. PARAMESH: A parallel adaptive mesh refinement community toolkit. *Computer physics communications*, 126(3):330–354, 2000.

[41] K. D. Devine and J. E. Flaherty. Parallel, adaptive hp-refinement techniques for conservation laws. *Applied Numerical Mathematics*, 20(4):367–386, 1996.

[42] O. Zanotti and M. Dumbser. A high order special relativistic hydrodynamic and magnetohydrodynamic code with space-time adaptive mesh refinement. *Computer Physics Communications*, 188:110–127, 2015.

[43] A. Giuliani and L. Krivodonova. Adaptive mesh refinement on graphics processing units for applications in gas dynamics. *Journal of Computational Physics*, 381:67–90, 2019.

[44] J. Velechovsky, M. Francois, and T. Masser. Direction-aware slope limiter for three-dimensional cubic grids with adaptive mesh refinement. *Computers and Mathematics with Applications*, 78(2):670–687, 2019.

[45] E. Schall and N. Chauchat. Implicit method and slope limiter in AHMR procedure for high order discontinuous Galerkin methods for compressible flows. *Communications in Nonlinear Science and Numerical Simulation*, 72(1):371–391, 2019.

[46] W. Klieber and B. Rievère. Adaptive simulations of two-phase flow by discontinuous Galerkin methods. *Computer Methods in Applied Mechanics and Engineering*, 196(1):404–416, 2006.

[47] K. Schaal, A. Bauer, P. Chandrashekar, R. Pakmor, C. Klingenberg, and V. Springel. Astrophysical hydrodynamics with a higher order discontinuous Galerkin scheme

and adaptive mesh refinement. *Monthly notices of the Royal Astronomical Society*, 453:4278–4300, 2015.

[48] M. Dubiner. Spectral methods on triangles and other domains. *Journal of Scientific Computing*, 6(4):345–390, 1991.

[49] M. Abramowitz and I. A. Stegun(Eds.). *Handbook of Mathematical Functions*. Dover, New York, 1965.

[50] N. Chalmers and L. Krivodonova. A robust CFL condition for the discontinuous Galerkin method on triangular meshes. *Journal of Computational Physics*, 403:109095, 2020.

[51] H. C. Yee, N. D. Sandham, and M. J. Djomehri. Low-dissipative high-order shock-capturing methods using characteristic-based filters. *Journal of Computational Physics*, 150:199–238, March 1999.

[52] M. Dumbser, O. Zanotti, R. Loubère, and S. Diot. A posteriori subcell limiting of the discontinuous Galerkin finite element method for hyperbolic conservation laws. *Journal of Computational Physics*, 278:47–75, 2014.

[53] Moment limiter pre-processing software, 2019. v1.2, https://www.http://www.math.uwaterloo.ca/~lgk/software.html.

[54] M. Fuhry, A. Giuliani, and L. Krivodonova. Discontinuous Galerkin methods on graphics processing units for nonlinear hyperbolic conservation laws. *International Journal for Numerical Methods in Fluids*, 76(12):982–1003, 2014.

[55] P. D. Lax and X. D. Liu. Solution of two-dimensional Riemann problems of gas dynamics by positive schemes. *Journal of Scientific Computing*, 19:319–340, 1998.

[56] K. Dutt and L. Krivodonova. A moment limiter for the discontinuous Galerkin method on adaptively refined triangular meshes. *Preprint*.

[57] K. Dutt and L. Krivodonova. A high-order moment limiter for the discontinuous Galerkin method on triangular meshes. *Journal of Computational Physics*, 433:110188, 2021.

[58] S. C. Brenner and L. R. Scott. *The mathematical theory of finite element methods*. Springer, 2008.

[59] C. Johnson. *Numerical solutions of partial differential equations by the finite element method*. Cambridge University Press, Cambridge, 1987.

[60] K. Dutt and L. Krivodonova. A high-order moment limiter for the discontinuous Galerkin method on quadrilateral meshes. *Preprint*.

Appendix A

A.1 Fourth order moment limiter on triangles

The $p = 3$ DG approximation on element Ω_i, written as a linear combination of the Dubiner basis, is

$$U_i(r,s) = \sum_{l+k=0}^{3} \hat{U}_{i,k}^{l} \varphi_k^l(r,s). \tag{A.1}$$

The cubic basis functions are given by

$$\begin{aligned}
\varphi_3^0(r,s) &= \sqrt{14}\,(2s+r-1)\left[5\,(2s+r-1)^2 - 3\,(1-r)^2\right],\\
\varphi_2^1(r,s) &= \sqrt{10}\left[3\,(2s+r-1)^2 - (1-r)^2\right](7r-1),\\
\varphi_1^2(r,s) &= 2\sqrt{6}\,(2s+r-1)\left[10 + 30\,(r-1) + 21\,(r-1)^2\right],\\
\varphi_0^3(r,s) &= 8\sqrt{2}r^3 + 36\sqrt{2}r^2\,(r-1) + 24\sqrt{2}r\,(r-1)^2 + 2\sqrt{2}\,(r-1)^3.
\end{aligned} \tag{A.2}$$

Using (3.5) and (3.7), the third order moments can be expressed in terms of the third order directional derivatives along $\mathbf{v}_{i,1}$ and $\mathbf{v}_{i,2}$ as

$$\begin{pmatrix}
h_{i,2}^3 D_{\mathbf{v}_{i,2}}^3 U_i(\mathbf{x}_{i,0}) \\
h_{i,2}^2 h_{i,1} D_{\mathbf{v}_{i,2}}^2 D_{\mathbf{v}_{i,1}} U_i(\mathbf{x}_{i,0}) \\
h_{i,2} h_{i,1}^2 D_{\mathbf{v}_{i,2}} D_{\mathbf{v}_{i,1}}^2 U_i(\mathbf{x}_{i,0}) \\
h_{i,1}^3 D_{\mathbf{v}_{i,1}}^3 U_i(\mathbf{x}_{i,0})
\end{pmatrix} =
\begin{bmatrix}
240\sqrt{14} & 0 & 0 & 0 \\
0 & 168\sqrt{10} & 0 & 0 \\
-12\sqrt{14} & 0 & 168\sqrt{6} & 0 \\
0 & -42\sqrt{10} & 0 & 420\sqrt{2}
\end{bmatrix}
\begin{pmatrix}
\hat{U}_{i,3}^0 \\ \hat{U}_{i,2}^1 \\ \hat{U}_{i,1}^2 \\ \hat{U}_{i,0}^3
\end{pmatrix}. \tag{A.3}$$

Similar to the third order moment limiter described in Section 3.1.3, Chapter 3, we obtain the modified third order moments by limiting the third order directional derivatives along

$\mathbf{v}_{i,1}$ and $\mathbf{v}_{i,2}$. To do this, we first compute second order directional derivatives along $\mathbf{v}_{i,1}$ and $\mathbf{v}_{i,2}$ at the cell centroids of the neighboring cells. For example, to limit $D^3_{\mathbf{v}_{i,1}} U_i$ and $D^2_{\mathbf{v}_{i,1}} D_{\mathbf{v}_{i,2}} U_i$, we compute the second order directional derivatives along $\mathbf{v}_{i,1}$ and $\mathbf{v}_{i,2}$ at the cell centroids of Ω_a, Ω_b, Ω_s, and Ω_t (Figure 3.3a). Consider element Ω_a. Using (3.8), the second order directional derivatives along $\mathbf{v}_{a,1}$ and $\mathbf{v}_{a,2}$ at the cell centroid $\mathbf{x}_{a,0}$ are

$$\begin{aligned}
h^2_{i,a} D^2_{\mathbf{v}_{a,1}} U_a(\mathbf{x}_{a,0}) &= \left(\frac{\sqrt{5}}{2}\right)^2 D^2_{v_1} U_a(\mathbf{r}_0) = 20\sqrt{6}\hat{U}^2_{a,0} - \sqrt{30}\hat{U}^0_{a,2} + 16\sqrt{10}\hat{U}^1_{a,2} \\
&\quad - 40\sqrt{2}\hat{U}^3_{a,0}, \\
h_{a,1} h_{a,2} D^1_{\mathbf{v}_{a,2}} D^1_{\mathbf{v}_{a,1}} U_a(\mathbf{x}_{a,0}) &= \left(\frac{\sqrt{5}}{2}\right) D^1_{v_1} D^1_{v_2} U_a(\mathbf{r}_0) = 30\sqrt{2}\hat{U}^2_{a,1} + 8\sqrt{14}\hat{U}^0_{a,3} + 8\sqrt{6}\hat{U}^2_{a,1}, \\
h^2_{a,2} D^2_{\mathbf{v}_{a,2}} U_a(\mathbf{x}_{a,0}) &= D^2_{v_2} U_a(\mathbf{r}_0) = 12\sqrt{30}\hat{U}^0_{a,2} + 32\sqrt{10}\hat{U}^1_{a,2}.
\end{aligned} \tag{A.4}$$

Then, the second order directional derivatives along $\mathbf{v}_{i,1}$ and $\mathbf{v}_{i,2}$ at $\mathbf{x}_{a,0}$ are computed as

$$\begin{aligned}
D^2_{\mathbf{v}_{i,1}} U_a &= (\alpha^1_{a,1})^2 D^2_{\mathbf{v}_{a,1}} U_a + 2\alpha^1_{a,1}\alpha^1_{a,2} D_{\mathbf{v}_{a,1}} D_{\mathbf{v}_{a,2}} U_a + (\alpha^1_{a,2})^2 D^2_{\mathbf{v}_{a,2}} U_a, \\
D^1_{\mathbf{v}_{i,1}} D^1_{\mathbf{v}_{i,2}} U_a &= \alpha^1_{a,1}\alpha^2_{a,1} D^2_{\mathbf{v}_{a,1}} U_a + \left(\alpha^1_{a,1}\alpha^2_{a,2} + \alpha^1_{a,2}\alpha^2_{a,1}\right) D^1_{\mathbf{v}_{a,1}} D^1_{\mathbf{v}_{a,2}} U_a + \alpha^1_{a,2}\alpha^2_{a,2} D^2_{\mathbf{v}_{a,2}} U_a, \\
D^2_{\mathbf{v}_{i,2}} U_a &= (\alpha^2_{a,1})^2 D^2_{\mathbf{v}_{a,1}} U_a + 2\alpha^2_{a,1}\alpha^2_{a,2} D_{\mathbf{v}_{a,1}} D_{\mathbf{v}_{a,2}} U_a + (\alpha^2_{a,2})^2 D^2_{\mathbf{v}_{a,2}} U_a,
\end{aligned} \tag{A.5}$$

where the coefficients α are obtained from

$$\mathbf{v}_{i,1} = \alpha^1_{a,1}\mathbf{v}_{a,1} + \alpha^1_{a,2}\mathbf{v}_{a,2}, \quad \mathbf{v}_{i,2} = \alpha^2_{a,1}\mathbf{v}_{a,1} + \alpha^2_{a,2}\mathbf{v}_{a,2}. \tag{A.6}$$

In a similar way, the directional derivatives along $\mathbf{v}_{i,1}$ and $\mathbf{v}_{i,2}$ are computed at the cell centroids of Ω_s, Ω_t, and Ω_b. The computed values at the cell centroids are used to linearly interpolate the values of second order directional derivatives at the forward and backward interpolation points $\mathbf{x}^f_{i,1}$ and $\mathbf{x}^b_{i,1}$

$$\begin{aligned}
D^2_{\mathbf{v}_{i,1}} U^f_{i,1} &= \beta^f_{i,1} D^2_{\mathbf{v}_{i,1}} U_s(\mathbf{x}_{s,0}) + (1-\beta^f_{i,1}) D^2_{\mathbf{v}_{i,1}} U_t(\mathbf{x}_{t,0}), \\
D^2_{\mathbf{v}_{i,1}} U^b_{i,1} &= \beta^b_{i,1} D^2_{\mathbf{v}_{i,1}} U_a(\mathbf{x}_{a,0}) + (1-\beta^b_{i,1}) D^2_{\mathbf{v}_{i,1}} U_b(\mathbf{x}_{b,0}), \\
D_{\mathbf{v}_{i,1}} D_{\mathbf{v}_{i,2}} U^f_{i,1} &= \beta^f_{i,1} D_{\mathbf{v}_{i,1}} D_{\mathbf{v}_{i,2}} U_s(\mathbf{x}_{s,0}) + (1-\beta^f_{i,1}) D_{\mathbf{v}_{i,1}} D_{\mathbf{v}_{i,2}} U_t(\mathbf{x}_{t,0}), \\
D_{\mathbf{v}_{i,1}} D_{\mathbf{v}_{i,2}} U^b_{i,1} &= \beta^b_{i,1} D_{\mathbf{v}_{i,1}} D_{\mathbf{v}_{i,2}} U_a(\mathbf{x}_{a,0}) + (1-\beta^b_{i,1}) D_{\mathbf{v}_{i,1}} D_{\mathbf{v}_{i,2}} U_b(\mathbf{x}_{b,0}), \\
D^2_{\mathbf{v}_{i,2}} U^f_{i,1} &= \beta^f_{i,1} D^2_{\mathbf{v}_{i,2}} U_s(\mathbf{x}_{s,0}) + (1-\beta^f_{i,1}) D^2_{\mathbf{v}_{i,2}} U_t(\mathbf{x}_{t,0}), \\
D^2_{\mathbf{v}_{i,2}} U^b_{i,1} &= \beta^b_{i,1} D^2_{\mathbf{v}_{i,2}} U_a(\mathbf{x}_{a,0}) + (1-\beta^b_{i,1}) D^2_{\mathbf{v}_{i,2}} U_b(\mathbf{x}_{b,0}).
\end{aligned} \tag{A.7}$$

The third order directional derivatives $D^3_{\mathbf{v}_{i,1}} U_i$, $D^2_{\mathbf{v}_{i,2}} D_{\mathbf{v}_{i,1}} U_i$, and $D^2_{\mathbf{v}_{i,1}} D_{\mathbf{v}_{i,2}} U_i$ are limited by comparing them to the forward and backward differences along $\mathbf{v}_{i,1}$ multiplied by the parameters $l^f_{i,1}$ and $l^b_{i,1}$

$$
\begin{aligned}
D^3_{\mathbf{v}_{i,1}} U_i(\mathbf{x}_{i,0}) \leftarrow \text{minmod} \Bigg(& D^3_{\mathbf{v}_{i,1}} U_i(\mathbf{x}_{i,0}), l^f_{i,1} \frac{D^2_{\mathbf{v}_{i,1}} U^f_{i,1} - D^2_{\mathbf{v}_{i,1}} U_i(\mathbf{x}_{i,0})}{\left\| \mathbf{x}^f_{i,1} - \mathbf{x}_{i,0} \right\|}, \\
& l^b_{i,1} \frac{D^2_{\mathbf{v}_{i,1}} U_i(\mathbf{x}_{i,0}) - D^2_{\mathbf{v}_{i,1}} U^b_{i,1}}{\left\| \mathbf{x}^b_{i,1} - \mathbf{x}_{i,0} \right\|} \Bigg), \\
D^2_{\mathbf{v}_{i,1}} D_{\mathbf{v}_{i,2}} U_i(\mathbf{x}_{i,0}) \leftarrow \text{minmod} \Bigg(& D^2_{\mathbf{v}_{i,1}} D_{\mathbf{v}_{i,2}} U_i(\mathbf{x}_{i,0}), l^f_{i,1} \frac{D_{\mathbf{v}_{i,1}} D_{\mathbf{v}_{i,2}} U^f_{i,1} - D_{\mathbf{v}_{i,1}} D_{\mathbf{v}_{i,2}} U_i(\mathbf{x}_{i,0})}{\left\| \mathbf{x}^f_{i,1} - \mathbf{x}_{i,0} \right\|}, \\
& l^b_{i,1} \frac{D_{\mathbf{v}_{i,1}} D_{\mathbf{v}_{i,2}} U_i(\mathbf{x}_{i,0}) - D_{\mathbf{v}_{i,1}} D_{\mathbf{v}_{i,2}} U^b_{i,1}}{\left\| \mathbf{x}^b_{i,1} - \mathbf{x}_{i,0} \right\|} \Bigg), \\
D^2_{\mathbf{v}_{i,2}} D_{\mathbf{v}_{i,1}} U_i(\mathbf{x}_{i,0}) \leftarrow \text{minmod} \Bigg(& D^2_{\mathbf{v}_{i,2}} D_{\mathbf{v}_{i,1}} U_i(\mathbf{x}_{i,0}), l^f_{i,1} \frac{D^2_{\mathbf{v}_{i,2}} U^f_{i,1} - D^2_{\mathbf{v}_{i,2}} U_i(\mathbf{x}_{i,0})}{\left\| \mathbf{x}^f_{i,1} - \mathbf{x}_{i,0} \right\|}, \\
& l^b_{i,1} \frac{D^2_{\mathbf{v}_{i,2}} U_i(\mathbf{x}_{i,0}) - D^2_{\mathbf{v}_{i,2}} U^b_{i,1}}{\left\| \mathbf{x}^b_{i,1} - \mathbf{x}_{i,0} \right\|} \Bigg).
\end{aligned}
\tag{A.8}
$$

The range for the scaling parameters $l^f_{i,k}$ and $l^b_{i,k}$, $k = \{1, 2\}$, is given in (3.22). Similarly, the second order directional derivatives along $\mathbf{v}_{i,1}$ and $\mathbf{v}_{i,2}$ are computed at the cell centroids of Ω_j, Ω_k, Ω_m, and Ω_n. The second order directional derivatives at the forward and backward interpolation points $\mathbf{x}^f_{i,2}$, and $\mathbf{x}^b_{i,2}$ (Figure 3.3b) are linearly interpolated using the found values. They in turn are used to limit the third order directional derivatives $D^3_{\mathbf{v}_{i,2}} U_i$, $D^2_{\mathbf{v}_{i,2}} D_{\mathbf{v}_{i,1}} U_i$ and $D^2_{\mathbf{v}_{i,1}} D_{\mathbf{v}_{i,2}} U_i$, similar to (A.8).

Finally, the modified third order moments $\hat{U}^3_{i,0}$, $\hat{U}^2_{i,1}$, $\hat{U}^1_{i,2}$, and $\hat{U}^0_{i,3}$ are computed by substituting the limited third order directional derivatives $D^3_{\mathbf{v}_{i,1}} U_i$, $D^2_{\mathbf{v}_{i,1}} D^1_{\mathbf{v}_{i,2}} U_i$, $D_{\mathbf{v}_{i,1}} D^2_{\mathbf{v}_{i,2}} U_i$,

and $D^3_{\mathbf{v}_{i,2}} U_i$ into (A.3)

$$
\begin{aligned}
\hat{U}^0_{i,3} &= \frac{h^3_{i,2}}{240\sqrt{14}} D^3_{\mathbf{v}_{i,2}} U_i, \\
\hat{U}^1_{i,2} &= \frac{h^2_{i,2} h_{i,1}}{168\sqrt{10}} D^2_{\mathbf{v}_{i,2}} D_{\mathbf{v}_{i,1}} U_i, \\
\hat{U}^2_{i,1} &= \frac{h_{i,2} h^2_{i,1}}{168\sqrt{6}} D_{\mathbf{v}_{i,2}} D^2_{\mathbf{v}_{i,1}} U_i + \frac{h^3_{i,2}}{3360\sqrt{14}} D^3_{\mathbf{v}_{i,2}} U_i, \\
\hat{U}^3_{i,0} &= \frac{h^3_{i,1}}{420\sqrt{2}} D^3_{\mathbf{v}_{i,1}} U_i + \frac{h^2_{i,2} h_{i,1}}{1680\sqrt{2}} D^2_{\mathbf{v}_{i,2}} D_{\mathbf{v}_{i,1}} U_i.
\end{aligned}
\tag{A.9}
$$

If all the third order directional derivatives are modified by the limiter, then we hierarchically apply the third order moment limiter, and so on, until we reach either a set of directional derivatives that are not limited or the zeroth order moment.

Appendix B

B.1 Third order moment limiter on quadrilaterals

The third order DG approximation on a quadrilateral element Ω_i, written as a linear combination of Legendre tensor product basis (1.25), is

$$U_i = \sum_{j=0,k=0}^{2} \hat{U}_{i,j}^{k} \varphi_j^k(\zeta, \eta). \tag{B.1}$$

The constant and linear basis functions are given in (6.24) and the quadratic basis functions are

$$\begin{aligned}
&\varphi_2^0 = \frac{\sqrt{5}}{4}(3\zeta^2 - 1), \quad \varphi_0^2 = \frac{\sqrt{5}}{4}(3\eta^2 - 1), \\
&\varphi_2^1 = \frac{\sqrt{15}}{4}(3\zeta^2 - 1)\eta, \quad \varphi_1^2 = \frac{\sqrt{15}}{4}\zeta(3\eta^2 - 1), \\
&\varphi_2^2 = \frac{5}{8}(3\zeta^2 - 1)(3\eta^2 - 1).
\end{aligned} \tag{B.2}$$

The derivatives of U_i along the directions $v_1 = (1,0)$ and $v_2 = (0,1)$ in the canonical space are

$$
\begin{aligned}
U_{i,\zeta} &= \frac{\sqrt{3}}{2}\hat{U}^0_{i,1} + \frac{3}{2}\hat{U}^1_{i,1}\eta + \frac{3\sqrt{5}}{2}\hat{U}^0_{i,2}\zeta + \frac{3\sqrt{15}}{2}\hat{U}^1_{i,2}\zeta\eta + \frac{\sqrt{15}}{4}\hat{U}^2_{i,1}(3\eta^2-1) + \frac{15}{4}\hat{U}^2_{i,2}\zeta(3\eta^2-1),\\
U_{i,\eta} &= \frac{\sqrt{3}}{2}\hat{U}^1_{i,0} + \frac{3}{2}\hat{U}^1_{i,1}\zeta + \frac{3\sqrt{5}}{2}\hat{U}^2_{i,0}\eta + \frac{3\sqrt{15}}{2}\hat{U}^2_{i,1}\zeta\eta + \frac{\sqrt{15}}{4}\hat{U}^1_{i,2}(3\zeta^2-1) + \frac{15}{4}\hat{U}^2_{i,2}(3\zeta^2-1)\eta,\\
U_{i,\zeta\zeta} &= \frac{3\sqrt{3}}{2}\hat{U}^0_{i,2} + \frac{3\sqrt{15}}{2}\hat{U}^1_{i,2}\eta + \frac{15}{4}\hat{U}^2_{i,2}(3\eta^2-1),\\
U_{i,\eta\eta} &= \frac{3\sqrt{3}}{2}\hat{U}^2_{i,0} + \frac{3\sqrt{15}}{2}\hat{U}^2_{i,1}\zeta + \frac{15}{4}\hat{U}^2_{i,2}(3\zeta^2-1),\\
U_{i,\zeta\eta} &= \frac{3}{2}\hat{U}^1_{i,1} + \frac{3\sqrt{15}}{2}\hat{U}^1_{i,2}\zeta + \frac{3\sqrt{15}}{2}\hat{U}^2_{i,1}\eta + + \frac{45}{2}\hat{U}^2_{i,2}\zeta\eta, \quad U_{i,\zeta\zeta\zeta} = 0, \quad U_{i,\eta\eta\eta} = 0,\\
U_{i,\zeta\zeta\eta} &= \frac{3\sqrt{15}}{2}\hat{U}^1_{i,2} + \frac{45}{2}\hat{U}^2_{i,2}\eta, \quad U_{i,\zeta\eta\eta} = \frac{3\sqrt{15}}{2}\hat{U}^2_{i,1} + \frac{45}{2}\hat{U}^2_{i,2}\zeta, \quad U_{i,\zeta\zeta\eta\eta} = \frac{45}{2}\hat{U}^2_{i,2},
\end{aligned}
\tag{B.3}
$$

Using (1.19), (1.20), (1.22), and by applying chain rule, the derivatives in (B.3) can be expressed in terms of the derivatives of U_i in the physical space as

$$
\begin{aligned}
U_{i,\zeta} &= U_{i,x}x_\zeta + U_{i,y}y_\zeta, \quad U_{i,\eta} = U_{i,x}x_\eta + U_{i,y}y_\eta,\\
U_{i,\zeta\zeta} &= U_{i,xx}x_\zeta^2 + U_{i,yy}y_\zeta^2 + 2U_{i,xy}x_\zeta y_\zeta, \quad U_{i,\eta\eta} = U_{i,xx}x_\eta^2 + U_{i,yy}y_\eta^2 + 2U_{i,xy}x_\eta y_\eta,\\
U_{i,\zeta\eta} &= U_{i,xx}x_\zeta x_\eta + U_{i,yy}y_\zeta y_\eta + U_{i,xy}(x_\eta y_\zeta + x_\zeta y_\eta) + U_{i,x}C_{i,x3} + U_{i,y}C_{i,y3},\\
U_{i,\zeta\zeta\zeta} &= U_{i,xxx}x_\zeta^3 + U_{i,yyy}y_\zeta^3 + 3U_{i,xxy}x_\zeta^2 y_\zeta + 3U_{i,xyy}x_\zeta y_\zeta^2,\\
U_{i,\eta\eta\eta} &= U_{i,xxx}x_\eta^3 + U_{i,yyy}y_\eta^3 + 3U_{i,xxy}x_\eta^2 y_\eta + 3U_{i,xyy}x_\eta y_\eta^2,\\
U_{i,\zeta\zeta\eta} &= U_{i,xxx}x_\zeta^2 x_\eta + U_{i,yyy}y_\zeta^2 y_\eta + U_{i,xxy}\left(2x_\zeta y_\zeta x_\eta + x_\zeta^2 y_\eta\right) + U_{i,yyx}\left(2x_\zeta y_\zeta y_\eta + y_\zeta^2 y_\eta\right)\\
&\quad + 2\{U_{i,xx}C_{i,x3}x_\zeta + U_{i,yy}C_{i,y3}y_\zeta + U_{i,xy}\left(C_{i,y3}x_\zeta + C_{i,x3}y_\zeta\right)\},\\
U_{i,\zeta\eta\eta} &= U_{i,xxx}x_\eta^2 x_\zeta + U_{i,yyy}y_\eta^2 y_\zeta + U_{i,xxy}\left(2x_\eta y_\eta x_\zeta + x_\eta^2 y_\zeta\right) + U_{i,yyx}\left(2x_\eta y_\eta y_\zeta + y_\eta^2 y_\zeta\right)\\
&\quad + 2\{U_{i,xx}C_{i,x3}x_\eta + U_{i,yy}C_{i,y3}y_\eta + U_{i,xy}\left(C_{i,y3}x_\eta + C_{i,x3}y_\eta\right)\}.
\end{aligned}
\tag{B.4}
$$

Consider the following vectors on the physical element Ω_i

$$
\mathbf{v}_{i,1} = (C_{i,x1}, C_{i,y1}), \quad \mathbf{v}_{i,2} = (C_{i,x2}, C_{i,y2}), \quad \mathbf{v}_{i,3} = (C_{i,x3}, C_{i,y3}). \tag{B.5}
$$

We can write $\mathbf{v}_{i,3}$ in terms of the other two vectors as

$$
\mathbf{v}_{i,3} = \alpha^1_{i,\mathbf{v}_{i,3}}\mathbf{v}_{i,1} + \alpha^2_{i,\mathbf{v}_{i,3}}\mathbf{v}_{i,2}. \tag{B.6}
$$

Denote the sth directional derivative along the directions $\mathbf{v}_{i,1}$ and $\mathbf{v}_{i,2}$, evaluated at the centroid $\mathbf{x}_{i,0}$, as

$$D^q_{\mathbf{v}_{i,1}} D^{s-q}_{\mathbf{v}_{i,2}} U_i = \frac{\partial^s U_i}{\partial^q \mathbf{v}_{i,1} \partial^{s-q} \mathbf{v}_{i,2}}, \ 0 \le q \le s. \tag{B.7}$$

Using (B.4), the directional derivatives along $\mathbf{v}_{i,1}$ and $\mathbf{v}_{i,2}$ evaluated at the centroid $\mathbf{x}_{i,0}$ of Ω_i can be computed as

$$\begin{aligned}
D_{\mathbf{v}_{i,1}} U_i &= U_{i,\zeta}\Big|_{(0,0)}, \quad D_{\mathbf{v}_{i,2}} U_i = U_{i,\eta}\Big|_{(0,0)}, \\
D^2_{\mathbf{v}_{i,1}} U_i &= U_{i,\zeta\zeta}\Big|_{(0,0)}, \quad D^2_{\mathbf{v}_{i,2}} U_i = U_{i,\eta\eta}\Big|_{(0,0)}, \\
D_{\mathbf{v}_{i,1}} D_{\mathbf{v}_{i,2}} U_i &= U_{i,\zeta\eta}\Big|_{(0,0)} - \{\alpha^1_{i,\mathbf{v}_{i,3}} D_{\mathbf{v}_{i,1}} U_i + \alpha^2_{i,\mathbf{v}_{i,3}} D_{\mathbf{v}_{i,2}} U_i\}, \\
D^3_{\mathbf{v}_{i,1}} U_i &= U_{i,\zeta\zeta\zeta}\Big|_{(0,0)}, \quad D^3_{\mathbf{v}_{i,2}} U_i = U_{i,\eta\eta\eta}\Big|_{(0,0)}, \\
D^2_{\mathbf{v}_{i,1}} D_{\mathbf{v}_{i,2}} U_i &= U_{i,\zeta\zeta\eta}\Big|_{(0,0)} - 2\{\alpha^1_{i,\mathbf{v}_{i,3}} D^2_{\mathbf{v}_{i,1}} U_i + \alpha^2_{i,\mathbf{v}_{i,3}} D_{\mathbf{v}_{i,1}} D_{\mathbf{v}_{i,2}} U_i\}, \\
D_{\mathbf{v}_{i,1}} D^2_{\mathbf{v}_{i,2}} U_i &= U_{i,\zeta\eta\eta}\Big|_{(0,0)} - 2\{\alpha^1_{i,\mathbf{v}_{i,3}} D_{\mathbf{v}_{i,1}} D_{\mathbf{v}_{i,2}} U_i + \alpha^2_{i,\mathbf{v}_{i,3}} D^2_{\mathbf{v}_{i,2}} U_i\}.
\end{aligned} \tag{B.8}$$

We start limiting at the highest solution coefficient, i.e., $\hat{U}^2_{i,2}$. Consider the directional derivative $D^2_{v_1} D_{v_2} U_i$, which from (B.3) can be written as

$$D^2_{v_1} D_{v_2} U_i = \frac{3\sqrt{15}}{2} \hat{U}^1_{i,2} + \frac{45}{2} \hat{U}^2_{i,2} \zeta, \tag{B.9}$$

i.e., $\hat{U}^2_{i,2}$ is proportional to the gradient of $D^2_{v_1} D_{v_2} U_i$ along $\eta = 0$. Therefore, we can find the limited value of $\hat{U}^2_{i,2}$ by computing the forward and backward difference of $D^2_{v_1} D_{v_2} U_i$ along $\mathbf{v}_{i,1}$. To do so, we first find the value of $D^2_{v_1} D_{v_2} U_i$ at the forward and backward interpolation points $\mathbf{x}^f_{i,1}$ and $\mathbf{x}^b_{i,1}$. Let's first consider the forward interpolation point $\mathbf{x}^f_{i,1}$. Using (6.7), (6.8), and (B.4), $D^2_{v_1} D_{v_2} U_i$ at $\mathbf{x}^f_{i,1}$ can be written as

$$D^2_{v_1} D_{v_2} U_i = D^2_{\mathbf{v}^{1,f}_{i,\zeta}} D_{\mathbf{v}^{1,f}_{i,\eta}} U_i + 2 D_{\mathbf{v}_{i,3}} D_{\mathbf{v}^{1,f}_{i,\zeta}} U_i. \tag{B.10}$$

Next, we compute the directional derivatives on the right hand side of (B.10) at the cell centroids of the neighboring elements Ω_j and Ω_k. Consider the element Ω_k (Figure B.1b).

Using (6.10), the derivatives $D^2_{\mathbf{v}^{1,f}_{i,\zeta}} D_{\mathbf{v}^{1,f}_{i,\eta}} U_k$ and $D_{\mathbf{v}_{i,3}} D_{\mathbf{v}^{1,f}_{i,\zeta}} U_k$ can be written in terms of the derivatives along $\mathbf{v}_{k,1}$ and $\mathbf{v}_{k,2}$ as

$$\begin{aligned} D^2_{\mathbf{v}^{1,f}_{i,\zeta}} D_{\mathbf{v}^{1,f}_{i,\eta}} U_k &= \left(\alpha^{1,f}_{k,\zeta} D_{\mathbf{v}_{k,1}} + \beta^{1,f}_{k,\zeta} D_{\mathbf{v}_{k,2}}\right)^2 \left(\alpha^{1,f}_{k,\eta} D_{\mathbf{v}_{k,1}} + \beta^{1,f}_{k,\eta} D_{\mathbf{v}_{k,2}}\right) U_k \\ D_{\mathbf{v}_{i,3}} D_{\mathbf{v}^{1,f}_{i,\zeta}} U_k &= \left(\alpha^{1,f}_{k,3} D_{\mathbf{v}_{k,1}} + \beta^{1,f}_{k,3} D_{\mathbf{v}_{k,2}}\right) \left(\alpha^{1,f}_{k,\zeta} D_{\mathbf{v}_{k,1}} + \beta^{1,f}_{k,\zeta} D_{\mathbf{v}_{k,2}}\right) U_k, \end{aligned} \tag{B.11}$$

where the derivatives along $\mathbf{v}_{k,1}$ and $\mathbf{v}_{k,2}$ at $\mathbf{x}_{k,0}$ can be computed using (B.8) and (B.3). Next, we compute the derivatives $D^2_{\mathbf{v}^{1,f}_{i,\zeta}} D_{\mathbf{v}^{1,f}_{i,\eta}} U_j$ and $D_{\mathbf{v}_{i,3}} D_{\mathbf{v}^{1,f}_{i,\zeta}} U_j$ at the cell centroid $\mathbf{x}_{j,0}$ of Ω_j and linearly interpolate the value of $D^2_{v_1} D_{v_2} U_i$ at $\mathbf{x}^f_{i,1}$ using the computed values at the cell centroids as

$$D^2_{v_1} D_{v_2} U_i(\mathbf{x}^f_{i,1}) = \beta^f_{i,1} D^2_{v_1} D_{v_2} U_k + (1 - \beta^f_{i,1}) D^2_{v_1} D_{v_2} U_j. \tag{B.12}$$

In a similar fashion, we can estimate the value of $D^2_{v_1} D_{v_2} U_i$ at the backward interpolation

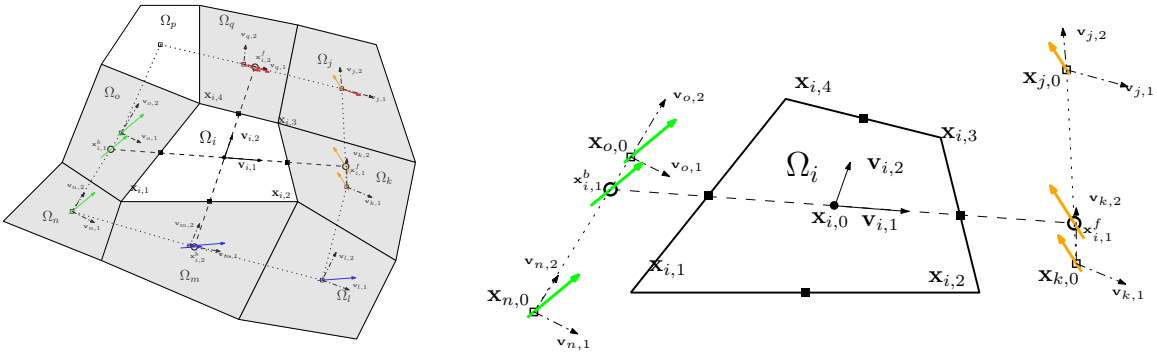

(a) Reconstruction stencil for high-order moments

(b) Reconstruction stencil along $\mathbf{v}_{i,2}$

Figure B.1: Reconstruction stencil for moment limiter on quadrilateral mesh.

point $\mathbf{x}^b_{i,1}$ as

$$D^2_{v_1} D_{v_2} U_i(\mathbf{x}^b_{i,1}) = \beta^b_{i,1} D^2_{v_1} D_{v_2} U_n + (1 - \beta^b_{i,1}) D^2_{v_1} D_{v_2} U_o. \tag{B.13}$$

Finally, we compute the limited solution coefficient $\tilde{U}^2_{i,2}$ by plugging the forward and back-

ward differences into (6.15) as

$$\tilde{U}^2_{i,2} \leftarrow \text{minmod}\left(\hat{U}^2_{i,2}, l^f_{i,1}\frac{1}{|\zeta^f_{i,1}|}\left(\frac{2D^2_{v_1}D_{v_2}U_i(\mathbf{x}^f_{i,1})}{45} - \frac{1}{\sqrt{15}}\hat{U}^1_{i,2}\right), l^b_{i,1}\frac{1}{|\zeta^b_{i,1}|}\left(\frac{1}{\sqrt{15}}\hat{U}^1_{i,2} - \frac{2D^2_{v_1}D_{v_2}U_i(\mathbf{x}^b_{i,1})}{45}\right)\right). \tag{B.14}$$

Next, consider the directional derivative $D_{v_1}D^2_{v_2}U_i$, which from (B.3) can be written as

$$D_{v_1}D^2_{v_2}U_i = \frac{3\sqrt{15}}{2}\hat{U}^2_{i,1} + \frac{45}{2}\hat{U}^2_{i,2}\zeta, \tag{B.15}$$

i.e., $\hat{U}^2_{i,2}$ is proportional to the gradient of $D_{v_1}D^2_{v_2}U_i$ along $\zeta = 0$. Following the steps outlined above for $D^1_{v_1}D_{v_2}U_i$, we compute the limited solution coefficient $\tilde{U}^2_{i,2}$ from the forward and backward differences of $D_{v_1}D^2_{v_2}U_i$ along $\mathbf{v}_{i,2}$ as

$$\tilde{U}^2_{i,2} \leftarrow \text{minmod}\left(\tilde{U}^2_{i,2}, l^f_{i,2}\frac{1}{|\eta^f_{i,2}|}\left(\frac{2D_{v_1}D^2_{v_2}U_i(\mathbf{x}^f_{i,2})}{45} - \frac{1}{\sqrt{15}}\hat{U}^2_{i,1}\right), l^b_{i,2}\frac{1}{|\eta^b_{i,2}|}\left(\frac{1}{\sqrt{15}}\hat{U}^2_{i,1} - \frac{2D_{v_1}D^2_{v_2}U_i(\mathbf{x}^b_{i,2})}{45}\right)\right). \tag{B.16}$$

If $\hat{U}^2_{i,2}$ is modified, then we compute the limited coefficients $(\tilde{U}^2_{i,1},\ \tilde{U}^1_{i,2})$. Consider the directional derivative $D^2_{v_2}U_i$, which from (B.3), after ignoring the contribution from higher order solution coefficients, can be written as

$$D^2_{v_2}U_i = \frac{3\sqrt{3}}{2}\hat{U}^2_{i,0} + \frac{3\sqrt{15}}{2}\hat{U}^2_{i,1}\zeta, \tag{B.17}$$

i.e., $\hat{U}^2_{i,1}$ is proportional to the gradient of $D^2_{v_2}U_i$ along $\eta = 0$. Following the steps outlined above for $D^1_{v_1}D_{v_2}U_i$, we can compute the limited solution coefficient $\tilde{U}^2_{i,1}$ from the forward and backward differences of $D^2_{v_2}U_i$ along $\mathbf{v}_{i,1}$ as

$$\tilde{U}^2_{i,1} \leftarrow \text{minmod}\left(\hat{U}^2_{i,1}, l^f_{i,1}\frac{1}{|\zeta^f_{i,1}|}\left(\frac{2D^2_{v_2}U_i(\mathbf{x}^f_{i,1})}{3\sqrt{15}} - \frac{1}{\sqrt{5}}\hat{U}^2_{i,0}\right), l^b_{i,1}\frac{1}{|\zeta^b_{i,1}|}\left(\frac{1}{\sqrt{5}}\hat{U}^2_{i,0} - \frac{2D^2_{v_2}U_i(\mathbf{x}^b_{i,1})}{3\sqrt{15}}\right)\right). \tag{B.18}$$

Next, consider the directional derivative $D_{v_1}D_{v_2}U_i$, which from (B.3) can be written as

$$D_{v_1}D_{v_2}U_i = \frac{3}{2}\hat{U}^1_{i,1} + \frac{3\sqrt{15}}{2}\hat{U}^1_{i,2}\zeta + \frac{3\sqrt{15}}{2}\hat{U}^2_{i,1}\eta + \frac{45}{2}\hat{U}^2_{i,2}\zeta\eta, \tag{B.19}$$

i.e., $\hat{U}^2_{i,1}$ is proportional to the gradient of $D_{v_1}D_{v_2}U_i$ along $\eta = 0$. Therefore, we compute the limited solution coefficient $\tilde{U}^2_{i,1}$ from the forward and backward differences of $D_{v_1}D_{v_2}U_i$ along $\mathbf{v}_{i,2}$ as

$$\begin{aligned}\tilde{U}^2_{i,1} \leftarrow \text{minmod}\Bigg(&\tilde{U}^2_{i,1}, l^f_{i,2}\frac{1}{|\eta^f_{i,2}|}\left(\frac{2D_{v_1}D_{v_2}U_i(\mathbf{x}^f_{i,2})}{3\sqrt{15}} - \frac{1}{\sqrt{15}}\hat{U}^1_{i,1}\right),\\ &l^b_{i,2}\frac{1}{|\eta^b_{i,2}|}\left(\frac{1}{\sqrt{15}}\hat{U}^1_{i,1} - \frac{2D_{v_1}D_{v_2}U_i(\mathbf{x}^b_{i,2})}{3\sqrt{15}}\right)\Bigg).\end{aligned} \tag{B.20}$$

Similarly, we compute the limited solution coefficient $\tilde{U}^1_{i,2}$ as

$$\begin{aligned}\tilde{U}^1_{i,2} \leftarrow \text{minmod}\Bigg(&\hat{U}^1_{i,2}, \frac{l^f_{i,1}}{|\zeta^f_{i,1}|}\left(\frac{2D_{v_1}D_{v_2}U_i(\mathbf{x}^f_{i,1})}{3\sqrt{15}} - \frac{1}{\sqrt{15}}\hat{U}^1_{i,1}\right),\\ &\frac{l^b_{i,1}}{|\zeta^b_{i,1}|}\left(\frac{1}{\sqrt{15}}\hat{U}^1_{i,1} - \frac{2D_{v_1}D_{v_2}U_i(\mathbf{x}^b_{i,1})}{3\sqrt{15}}\right)\Bigg)\\ \tilde{U}^1_{i,2} \leftarrow \text{minmod}\Bigg(&\tilde{U}^1_{i,2}, \frac{l^f_{i,2}}{|\eta^f_{i,2}|}\left(\frac{2D^2_{v_1}U_i(\mathbf{x}^f_{i,2})}{3\sqrt{15}} - \frac{1}{\sqrt{5}}\hat{U}^0_{i,2}\right), \frac{l^b_{i,2}}{|\eta^b_{i,2}|}\left(\frac{1}{\sqrt{5}}\hat{U}^0_{i,2} - \frac{2D^2_{v_1}U_i(\mathbf{x}^b_{i,2})}{3\sqrt{15}}\right)\Bigg).\end{aligned} \tag{B.21}$$

If both $\hat{U}^2_{i,1}$ and $\hat{U}^1_{i,2}$ are modified, then we compute the limited coefficients $(\tilde{U}^2_{i,0},\ \tilde{U}^0_{i,2})$ as

$$\begin{aligned}\tilde{U}^0_{i,2} \leftarrow \text{minmod}\Bigg(&\hat{U}^0_{i,2}, \frac{l^f_{i,1}}{|\zeta^f_{i,1}|}\left(\frac{2D_{v_1}U_i(\mathbf{x}^f_{i,1})}{3\sqrt{5}} - \frac{1}{\sqrt{15}}\hat{U}^0_{i,1}\right), \frac{l^b_{i,1}}{|\zeta^b_{i,1}|}\left(\frac{1}{\sqrt{15}}\hat{U}^0_{i,1} - \frac{2D_{v_1}U_i(\mathbf{x}^b_{i,1})}{3\sqrt{5}}\right)\Bigg)\\ \tilde{U}^2_{i,0} \leftarrow \text{minmod}\Bigg(&\hat{U}^2_{i,0}, \frac{l^f_{i,2}}{|\eta^f_{i,2}|}\left(\frac{2D_{v_2}U_i(\mathbf{x}^f_{i,2})}{3\sqrt{5}} - \frac{1}{\sqrt{5}}\hat{U}^1_{i,0}\right), \frac{l^b_{i,2}}{|\eta^b_{i,2}|}\left(\frac{1}{\sqrt{5}}\hat{U}^1_{i,0} - \frac{2D_{v_2}U_i(\mathbf{x}^b_{i,2})}{3\sqrt{5}}\right)\Bigg).\end{aligned} \tag{B.22}$$

If both $\hat{U}^2_{i,0}$ and $\hat{U}^0_{i,2}$ are modified, then we proceed with the second order limiter described in Section 6.1.4, Chapter 6.